SYNTHETIC APERTURE DIGITAL BEAMSTEERING ARRAY FOR GLOBAL POSITIONING SYSTEM INTERFERENCE MITIGATION: A STUDY ON ARRAY TOPOLOGY

A Thesis

by

JOEL K. HARMS

Submitted to the Office of Graduate and Professional Studies of
Texas A&M University
in partial fulfillment of the requirements for the degree of

MASTER OF SCIENCE

Chair of Committee,	Gregory Huff
Committee Members,	Henry Pfister
	Paul Gratz
	Steve Liu
Head of Department,	Chanan Singh

August 2014

Major Subject: Electrical Engineering

ABSTRACT

The Global Positioning System (GPS) satellite navigation system is deeply intertwined with civilian everyday life. Unfortunately for the civilians that use the system, the GPS system is vulnerable to external interference. Antenna arrays with Direction of Arrival (DoA) signal identification and beamsteering provide a very effective technique for mitigating directional interference by moving the antenna gain toward the Signal of Interest (SOI) or away from the Signal not of Interest (SNOI), however, such systems are typically too large to integrate or require more processing capabilities than civilian devices are able to provide. Synthetic aperture arrays are a means to reduce the array size but provide a similar interference protection with a smaller processing capability overhead. This thesis assists in array selection by providing simulated gains of different switched antenna arrays. The Uniform Circular Array (UCA), rectangular array, random array, random full aperture, random sequential, ring (UCA random hybrid) topologies are evaluated. In a pure synthetic beamsteering system in the presence of continuous wave (CW) interference, it is determined that array topology has marginal impact on Signal to Interference Noise Ratio (SINR) as each array's results show very similar performance. With the two CW scenarios in the absence of null steering, the UCA maintains the highest performance using the smallest number of antenna elements.

DEDICATION

I dedicate my work to my family and friends. To my parents who gave words of encouragement, assisted with document reviews, and who exercised extended patience while I completed my degree. To my graduate coworkers and friends at Texas A&M whose study sessions, research problem solving discussions, and distractions away from studies proved invaluable. Last but not least, to my four legged friend who shared the highs and lows of my life.

ACKNOWLEDGEMENTS

I would like to thank my committee members for their expertise and time. A special thanks to Dr. Greg Huff for his countless hours of discussion, reading, and patience throughout the entire process of topic selection, research, and documentation. Thank you Dr. Henry Pfister, Dr. Paul Gratz, and Dr. Steve Liu for serving on my committee.

I would also like to acknowledge Sandia National Laboratories for assisting with equipment and funding to complete my research.

TABLE OF CONTENTS

Page

LIST OF FIGURES

FIGURE Page

LIST OF TABLES

TABLE Page

1. INTRODUCTION

The proliferation of Global Positioning System (GPS) enabled or enhanced devices into civilian everyday life makes the system ubiquitous and compounds the effects of the system's performance degradation or absence. Performance degradation or absence is the result of external interference, whether deliberate or unintentional. Irrespective of the level of sophistication in an attack, the deliberate assault can be divided into civilian and military objectives. Militaristic goals consist of denial of navigation services to opposing forces and creating confusion/lessening their effectiveness. Financial incentives, terrorism, or protection of personal privacy are common civilian attack justifications[38][1]. Most end users rely on small inexpensive GPS receivers to access the satellite constellation's positioning service. This is due to the physical size limitations and funding constraints when compared to military applications. Despite Direction of Arrival (DoA)'s potential shortcomings with a sophisticated adversary without cryptographic techniques, the multi-antenna system is one of the best defenses for detecting and mitigating an attack. However, due to the size, weight, processing requirements, and budgetary overhead of a multi-antenna system, the implementation of such a system is limited. Synthetic aperture techniques when properly applied can help find a compromise between performance and the other limiting factors to assist in broadening the market for DoA mitigation integration. The remainder of the chapter will discuss the types of attacks, the sophistication of different attack vectors, detail society's reliance on GPS, provide real-world examples of known attacks, describe research topic goals, identify related literature, and explain the research contributions.

1.1 Interference

The civilian section of the Navigation System with Timing and Ranging (NAVSTAR), better known as GPS, is a known periodic, unassociated, unauthenticated, low amplitude broadcast communication scheme operating on frequencies and spreading codes that are publicly known. This makes the system vulnerable to the affects of external interference and deliberate attack via jamming or spoofing. Jamming is a simplistic subset of the category spoofing. The goal of a purposeful attack is a Denial of Service (DoS) by preventing the system from obtaining a position lock (jamming) or feeding the receiver erroneous time and location information (spoofing)[41]. Jamming is either an accidental occurrence due to out of band frequency components or an intentional action designed to prevent the receiver from acquiring, tracking, or navigating. Spoofing attempts to fool the receiver into a false position, velocity, or time information, known as PVT, by acting as fake navigation satellites with a stronger signal output than the legitimate Satellite Vehicles (SVs)[38].

1.2 Level of Sophistication

The level of interference can be classified as unintentional interference to a purposeful orchestrated assault where the threat is one of three categories: simplistic, intermediate, and sophisticated.

Simplistic or unsophisticated attacks are the most rudimentary, however, probabilistically speaking, the most prevalent as they require the smallest resources and cost to perpetrate. These attacks use signals that are orders of magnitude larger than their legitimate counterparts. The transmitted signals lack synchronization between legitimate SVs resulting in a mismatch of phase, frequency, and navigation message data[25]. In the pure spoofing case, the transmitted signals are often generated using a GPS signal generator where the signal generator's output tends to make each

replica satellite signal of equal strength with constant timing between each artificial signal[41]. A higher magnitude signal can effectively act as a jammer causing the receiver to loose tracking lock. Upon the receiver loosing satellite tracking lock, the attacker can attempt to cause the receiver to reacquire using the simulator's information or continue jamming. A jamming continuance would prevent the receiver from reacquiring legitimate satellite signals[18]. Meaconing, or recording an authentic signal at a certain location and time for subsequent playback, would also fall under this category[30]. This requires a device even less complex than a GPS simulator.

An intermediate attack increases the complexity of the unsophisticated attack and the difficulty of defending by coupling the capability of tracking legitimate GPS signals with the spoofers locality to mimic the satellites in all respects from code, phase, frequency, and navigation data, with variable signal strength relative to the authentic signals. The receiver-spoofer attacker may also have the capability to compensate for geometric offsets between the attacker and the target's antenna[25]. In addition, these systems tend to be more portable[18]. The spoofer uses the genuine satellite signals to estimate its own Position, Velocity, and Time (PVT) and then uses that information to generate counterfeit signals. The attack is orchestrated by allowing the target to obtain a tracking lock, each channel of the receiver-spoofer aligns its correlation peak with the genuine signal. As the attack proceeds the counterfeit signal is gradually increased above the power level of the legitimate signal. Once the targets starts to utilize the spoofed signals the attacker can tweak the strength, phase, frequency, and navigation message of the replica signal to control the victim[18].

A sophisticated attack is similar to the intermediate attack except the stakes are raised again by incorporating multiple antennas and potentially multiple receiver-spoofers. The attackers are able to vary the carrier phase for each output antenna to

provide a measure of directionality and imitate multiple transmission sources[25]. In the multiple receiver-spoofer instance, the attackers share a common oscillator through a communication link to align their clocks similar to the legitimate constellation[18]. The attack is designed to thwart DoA detection and mitigation methods. Depending on the number of sources and their direction of attack, the only known defense is cryptographic authentication[18].

1.3 Attack Vectors

The 2001 United States of America (US) Department of Transportation's Volpe report and professor Humphrey's 2012 congressional testimony[17] highlight the potential targets to transportation, communication, commerce, and energy and the consequences from a targeted attack.

1.3.1 Aircraft

The potential effect on commercial aircraft by an attack on GPS may not be that profound due to the existence of legacy navigation equipment that is used in tandem, providing a valuable position cross-check. However, depending on the implementation for an aircraft's autopilot, a risk may still remain. When autopilot is engaged the aircraft's course depends largely on the Inertial Measurement Unit (IMU) with GPS assisting to correct for bias drifts. As a pilot relies mostly on alerts, the computer or pilot may not be aware of an error that builds up over a period of time.

As more Unmanned Aerial Vehicles (UAVs) enter the global airspace with less stringent requirements for their avionic suite, an attack on this vector may be more profound[17].

1.3.2 Maritime

Marine craft rely on GPS for positioning information and to correct the bias of their IMUs. An attack on this sector could lead shipping vessels astray or into falsely believing they are in navigable waters. Either case could result in significant financial loss or an environmental disaster[17].

1.3.3 Surface Transportation

Surface transportation targets consists of automotive and rail. The consequences from an attack on GPS to the automobile transportation system would not be catastrophic as it would hinder handheld or OEM navigation equipment. This could thwart an employer's tracking of cargo or employee movements, as well as law enforcement's high-tech vehicle monitoring and surveillance activities. As automated systems become more prevalent, such as the Google car that rely on such systems for navigation, the affects of an attack on this sector would become more severe.

The stakes are higher for rail transportation as management is provided through positive train control systems that actively report a train's location and display this information on control center computers. An attack could result in train engineers and control center monitors believing that a train is moving along a different track leading to a collision[17].

1.3.4 Communications

Many communication systems such as the Internet and cellular networks rely on GPS for precise time and synchronization. Cellular telephony systems deploying Code Division Multiple Access (CDMA) communication rely on the precise time provided by GPS for synchronization to prevent adjacent towers from interfering with each other and enable tower-to-tower call hand-off. If adjacent tower time deviates by

more than 10 micro seconds the hand-off to and from that tower is disrupted, which affects overall network throughput[34]. Interrupting this synchronization would cause disruption and potentially interfere with E911 location services[17].

1.3.5 Banking and Finance

Most global financial exchanges are operated by computerized systems that require nanosecond time stamping. To accommodate this requirement, GPS has been integrated to supply a synchronized time stamping mechanism in the stock exchange data centers and co-located facilities. The vast majority of the trading volume on major exchanges $(50 - 70\%)$ is accounted for by automated transactions. The automatic and high frequency nature of the high frequency traders has the potential to compound the effect of an attack on GPS in the vicinity of exchange data centers[17].

Exasperating the potential problem, automatic teller machines also use GPS for time synchronization to counteract fraud and prevent insufficient funds withdrawals. Without synchronized timestamped financial transactions, geospatial separated financial transactions might permit insufficient withdrawals from accounts that indicated they were in good standing.

1.3.6 Energy Distribution

GPS time is used as a synchronized timestamping mechanism for Phasor Measurement Units (PMUs), which are devices used to monitor and control the electrical power grid. PMUs measure the phase angles of electricity surging through the electrical grid, and an attack on GPS could cause spurious variations in their measurements. Such variations would impact the power flow or stability estimates and have the potential to cause operators or automatic monitors to take incorrect or unnecessary compensation and control actions, such as powering-up or shutting down generators[17].

1.4 Threats Realized

The following reports or demonstrations clearly indicate the importance of tightening the security surrounding the civilian version of GPS.

As reported by The Economist, in 2013 the London Stock Exchange experienced a GPS blackout everyday for up to 10 minutes. Navigation of automobiles in the area and exchange timestamps were affected. A private firm monitoring such events attributed the attacks to a weak dashboard jammer in a nearby moving vehicle. The target of the attack, as reported by the private watchdog group, was the driver's unspecified employer. The attack was not targeted at the financial exchange or surrounding area; instead the driver was attempting to avoid their employer's attempts to track the driver's location[11].

A year prior to the events in London, researchers from the University of Texas at Austin completed a demonstration for the Department of Homeland Security at White Sands Missile Range whereby they demonstrated the ability to hijack a civilian drone by spoofing the aircraft with false global positioning system information[33]. Unfortunately, literature found to date on this event did not indicate what defenses existed, if any. The attack vehicle was an in-house directional spoofing system developed by Humphrey. Humphrey's congressional testimony on the subject indicated that the GPS receiver on the demonstration target operated on a single frequency utilizing the L1 band and possessed an integrity checking methodology known as Receiver Autonomous Integrity Monitoring (RAIM)[17]. In its standard form, RAIM is a methodology to assess the integrity of a received global positioning signal. The methodology functions by requiring at least one signal in addition to the minimum number of signals required for a position, velocity, and time computation. It uses the extra signal to examine for outliers that differ significantly from the expected

pseudorange value. Some variants extend RAIM to also exclude the faulty signal from the PVT computation[25]. Standard RAIM is ineffective against GPS spoofing because the spoofer generates a fully self-consistent ensemble of signals, thus there are no outliers[17].

Another attack made headlines in 2013 when Humphrey used a GPS spoofing device in a maritime example to capture a yacht's GPS receiver. The captured receiver caused the crew to adjust the vessel's course while still indicating a straight trajectory that did not require adjustment. The yacht was called the White Rose of Drachs, and the test took place near Italy in international waters[44].

1.5 Objective

The prior examples illustrate the threat to civilian GPS due to its proliferation into society. To improve the performance of a civilian receiver in a jamming environment, this research seeks to:

- Construct a research platform that aids in the understanding of the operation of the GPS system that permits continued expansion and that addresses the issue of GPS vulnerability to outside interference.
- Utilize a switched feed antenna network to create a synthetic aperture with a GPS system.
- Evaluate the effectiveness of different array spatial topologies, as well as, the number of active elements in the synthetic array on the accuracy of the DoA signal estimation algorithm Multiple Signal Classification (MUSIC).
- Obtain a direction of arrival estimation and compute the signal gains produced by digital beamsteering.

1.6 Related Literature

Prior literature shows the application of beamsteering and spatial nulling to combat interference on standard phased arrays and synthetic aperture arrays after obtaining a DoA of the Signal of Interest (SOI) and the interference Signal not of Interest (SNOI). It also shows the application of switched antenna feed networks to create a synthetic aperture array.

To maximize antenna performance in the presence of multiple types of satellite generated SOI and external interference, Lu, et al., investigate the application of a semi-spherical array made of concentric Uniform Circular Array (UCA) array elements that lie parallel to the XY plane and that are spatially offset in the positive Z axis. The incident angle for pseudolites and GPS SVs are obtained using the Capon DoA estimation technique. This information is then fed into an unspecified beemsteering/null-steering algorithm to obtain an array pattern that focuses on the combination of the two types of SVs while attenuating interference sources. Although a quantitative Signal to Noise Ratio (SNR) comparison is not provided, the array plots indicate a gain in the presence of uniformly spaced SOI and uniformly non-competing interference sources or SNOI[24].

To combat interference using standard phased arrays, Li, et al., uses an antenna array with adaptive beamsteering and spatial nulling to improve GPS's performance in the presence of continuous wave (CW) interference. An adjustable steering algorithm changes between null steering and beamsteering depending on the proximity of the interference to the Coarse Acquisition (C/A) spectral lines[22].

Chen, et al., investigate the application of a multi-receiver Controlled Reception Pattern Antenna (CRPA) antenna array on jamming immunity to CDMA and CW interference. The system uses MVDR adaptive beamsteering. Although the paper

mostly discusses the software parallel architecture implementation, a demonstration of the CRPA array was performed to show the gains made in the presence of jamming interference sources[7].

Charvat, et al., show the application of a synthetic aperture array created through a switched network instead of relying on the source's trajectory. They incorporate an antenna switched feed network coupled with Time Division Multiplexing (TDM) to create a synthetic aperture radar system for a Uniform Linear Array (ULA) to create an Ultra Wideband (UWB) radar system with a center frequency of 3 GHz. By using the switched feed network to create a synthetic aperture they are able to reduce the number of elements required by a similar phased array with a comparable center frequency and beamwidth[6].

Although not specifically tied to synthetic arrays, Cheng and Lee introduce the concept of antenna array with pattern diversity through a switch network at each antenna feed to improve DoA estimation reliability. They work to reduce the number of required array elements when using the delay-and-sum DoA estimation technique. The advantage of the delay-and-sum technique is that it is computationally fast and does not require eigenvalue decomposition; however, it requires many array elements to obtain high resolution results. An antenna pattern switching technique is proposed, analyzed, and tested to verify that a reduction in the required array elements is achieved. Information is provided to show the improvement in accuracy as the number of antenna elements in the ULA is increased[9].

In Global Navigation Satellite System (GNSS) literature on synthetic aperture arrays Broumandan, et al., analyze the DoA estimation technique UCA-MUSIC in a synthetic aperture array created by a synthesized UCA. The UCA was synthesized using a single antenna located on the end of a lever that was spun in a circle. The lever was rotated with a certain angular velocity and sampled at a certain periodicity

to create the UCA synthetic aperture. The paper also analyzed the effect of several implementation dependent errors and created a field trial where the system was used to determine the DoA of a jammer [4].

In a similar manner, Pany investigated the use of a UCA synthetic aperture array to mitigate the effects of multipath in GNSS applications. The article notes the system's effectiveness at combating near-range multipath. By using an unspecified DoA beamsteering algorithm selectivity of the antenna beam was created to focus on the source and reject multipath signals incident on the array[29].

Lin, et al., build upon the work by Broumandan[4] by analyzing the performance of several different methods of DoA, as well as, addressing the problem of incorporating adaptive beam forming techniques using linear, circular, and rectangular arrays[23].

Soloviev, et al., investigated the application of frequency based multiple beamsteering combined with a synthetic antenna array to mitigate jamming interference. The frequency based Fast Fourier Transform (FFT) algorithm was designed to provide an open loop tracking of the legitimate GNSS signals, identify signal sources, and provide jamming immunity. A further reduction was hypothesized by incorporating a synthetic aperture array. A real-world test was constructed to confirm their hypothesis[36]. Soloviev, et al., contribute to the state of the art by incorporating a different version of DoA estimation with a synthetic aperture.

Relying on the sources trajectory and adding polarization diversity into the mix, Dehghanian, Broumandan, Zaheri, and Nielsen investigate the combination of spatial and polarization diversity in a dual-polarized synthetic antenna array for GNSS. This paper departs from the traditional continuous movement sampling of a synthetic array to a stop-measure-go procedure that still relies on the user's trajectory to provide it with spatial diversity despite using two antennas[10].

Prior literature shows that the combination of a switched antenna feed network synthetic aperture antenna array to combat interference in GNSS applications, regardless of the array configuration, is unpublished.

1.7 Contributions

This work departs from mechanically based synthetic UCAs previously used in synthetic aperture GNSS applications[4][23]. The research instead generates the synthetic aperture through a switching antenna feed network that allows for more complex array configurations, such as the random array[5], and lessens the dependence on the antenna platform trajectory to improve spatial diversity. By introducing a switched network, the synthetic array's spatial diversity is not entirely defined by the sources trajectory or lack thereof. The effectiveness of the type of array and the size of the array was evaluated by using the accuracy of the resultant DoA estimation compared to the true DoA and the processing gain after digital beamsteering. The thesis also discusses using signal correlation to recover the phase of a signal incident on an antenna array.

2. COMMUNICATION SYSTEMS

This chapter introduces the fundamental communication theory behind GPS which includes Binary Phase Shift Keying (BPSK) and statistical correlation used in Pseudo Random Noise (PRN) sequences for Direct Sequence Spread Spectrum (DSSS) and phase determination. In-Phase and Quadrature (IQ) phase determination, noise power, and signal quality metrics are also introduced to provide sufficient background for later chapters.

2.1 Modulation

Communication modulation is the process of encoding user data onto a carrier frequency for transmission where the amount of information or channel capacity over a noisy channel is governed by Shannon's channel capacity theorem[16]. The underlying encoding process can largely be decomposed from the methods known as amplitude, frequency, and phase modulation. This paper is mostly concerned about phase modulation, where the process of modulating data using phase is known as Phase Shift Keying (PSK).

2.1.1 Phase Shift Keying (PSK)

PSK is used in many practical applications such as satellite, cellular communications, and wireless local area networks[16]. PSK modulation works by encoding the transmitted data into n discrete phases α, typically given as

$$\alpha_i(t) = \frac{2\pi i}{n} \quad i = 1, \ldots, n \tag{2.1}$$

Integration of the discrete phases into a modulation carrier with angular velocity ω_0 yields the transmitted signal in Equation 2.2.

$$s(t) = \mathrm{a}\cos(\omega_0 t + \alpha_i(t)) \tag{2.2}$$

2.1.2 Binary Phase Shift Keying (BPSK)

BPSK is a digital communication modulation scheme that is a subset of PSK and uses the phase discrepancy of two sinusoids to represent the data in the transmitted message. The set of phases or the number of possible phase offset combinations is restricted to two, giving it the binary name. In BPSK modulation two finite energy signals $s_0(t)$ and $s_1(t)$ are separated out of phase by π radians are employed to represent the encoded data bit 0 and bit 1 over an arbitrary bit time T_{data}[16]. The result is that the Radio Frequency (RF) carrier sinusoid is multiplexed between a zero phase shift or a phase shift of π radians depending on whether a binary data value of 0 or 1 is conveyed[20].

$$s_0(t) = \mathrm{a}\, p(t)\cos(2\pi f_c t) : \mathrm{bit}\, 0 \tag{2.3}$$

$$s_1(t) = \mathrm{a}\, p(t)\cos(2\pi f_c t + \pi) : \mathrm{bit}\, 1 \tag{2.4}$$

Decomposing BPSK Equation 2.3, a is the signal amplitude, $p(t)$ is the bit pulse shape, and $\cos(2\pi f_c t)$ is the carrier. Using this notation, the carrier frequency-bit duration product $f_c \cdot T_{data}$ is assumed to be a positive integer, and the carrier frequency f_c is an integer multiple of the bit rate $1/T_{data}$. The bit rate is the interval of time representing the value of one data bit. A diagram of BPSK modulated data is shown in Figure 2.1. Alternately, BPSK can be represented by multiplying two time domain waveforms consisting of an unmodulated RF carrier and a data waveform,

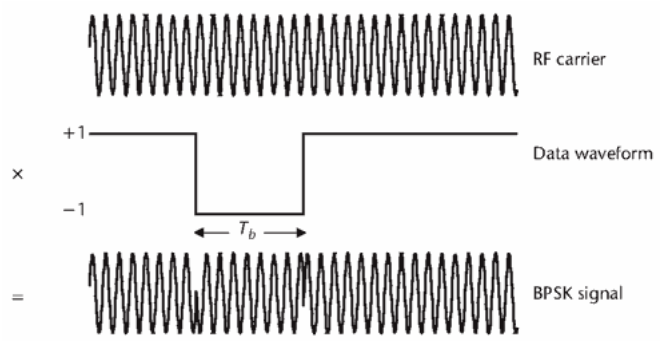

Figure 2.1: Binary Phase Shift Keying[20]

whose values are non-return to zero positive and negative ones for each successive bit interval. The bit interval is $T_{data} = 1/R_{data}$ seconds, where R_{data} is data rate (bps)[20].

Depending on the phases selected to represent the modulated data, a BPSK signal can be represented in terms of an amplitude modulated system $f_{AM}(t) = \mathrm{a}(t)\cos(2\pi f_c t)$ instead of a phase modulated system $f_{BPSK}(t) = \cos(2\pi f_c t + \alpha(t))$. This is worth noting as many textbooks or papers, such as *A Software- Defined GPS and Galileo Receiver: A Single-Frequency Approach*[3], use this notation. If the amplitude modulated signal maintains binary states, $\mathrm{a}(t),\ \mathrm{a} \in \{-1, 1\}$, then under certain conditions $f_{AM}(t) = f_{BPSK}(t)$.

$$\mathrm{a}(t)\cos(2\pi f_c t) = \cos(2\pi f_c t + \theta\alpha(t)) \tag{2.5}$$

$$= \cos(2\pi f_c t)\cos(\theta\alpha(t)) - \sin(2\pi f_c t)\sin(\theta\alpha(t)) \tag{2.6}$$

$$= \cos(2\pi f_c t)\cos\Big(\frac{\pi}{2} + \theta\alpha(t)\Big) - \sin(2\pi f_c t)\sin\Big(\frac{\pi}{2} + \theta\alpha(t)\Big) \tag{2.7}$$

$$= \sin(\theta\alpha(t))\cos(2\pi f_c t) + \cos(\theta\alpha(t))\sin(2\pi f_c t) \tag{2.8}$$

$$= \sin(\theta\alpha(t))\cos(2\pi f_c t) \tag{2.9}$$

If $\theta \Rightarrow \pi/2$ then $f_{AM}(t) = f_{BPSK}(t)$ via Equation 2.10.

$$\mathrm{a}(t)\cos(2\pi f_c t) = \cos\Big(2\pi f_c t + \frac{\pi}{2}(1+\alpha(t))\Big) \tag{2.10}$$

Regardless of how the transmitted signal is constructed, BPSK is based on the phase discrepancy of two signals carrying data; therefore, the demodulation process requires accurate knowledge of the carrier frequency and the current phase at receiver end. To recover the carrier frequency, a special frequency recovery loop is used in the receiver[19].

2.2 Correlation

Correlation is a measure of how close the composition of two input signals are relative to one another. From statistics, correlation is defined as the covariance of two signals over the product of their respective standard deviations, where σ is used to represent the standard deviation or square root of the variance. This is shown in mathematical notation in Equation 2.12[2]:

$$\rho_{XY} = corr(X,Y) \tag{2.11}$$

$$= \frac{cov(X,Y)}{\sigma_X \sigma_Y} \tag{2.12}$$

$$= \frac{E[(X-\mu_X)(Y-\mu_Y)]}{\sigma_X \sigma_Y} \tag{2.13}$$

A derivative of correlation is the term cross-correlation, which refers to the situation where the correlation input variables are the same; thus, ρ_{XY} is equivalent to ρ_{XX}. This provides a measure of how closely related a signal's structure is to the remaining portions of the same signal. Covariance, as shown in Equation 2.14, is the statistical expectation of the product of the differences of X and Y by their

respective expectation[2].

$$cov(X,Y) = E[(X - E[X])(Y - E[Y])] \tag{2.14}$$

$$= E[XY] - E[X]E[Y] \tag{2.15}$$

Variance σ^2 is a very similar concept to covariance, however, only one variable is used. Therefore, variance is the statistical expectation of the square of the difference of X from its expectation, refer to Equation 2.17.

$$var(X) = cov(X,X) \tag{2.16}$$

$$= E[(X - E[X])(X - E[X])] \tag{2.17}$$

$$= E[XX] - E[X]E[X] \tag{2.18}$$

$$= E[X^2] - E[X]^2 \tag{2.19}$$

$E[X]$ represents the statistical expectation of the quantity X, where the expectation is defined in the discrete case as the sum of the product of X by its probability p_i. The sum of all probabilities $\sum p_i = 1$[2]. Refer to Equation 2.20 for the definition of expectation in mathematical notation.

$$E[X] = \sum_{i=-\infty}^{\infty} X_i p_i \tag{2.20}$$

Depending on the application, expressing the expectation, covariance, or correlation in matrix form may be desirable. The bold lowercase variables, such as $\vec{\mathbf{x}}$ represent vectors while bold uppercase variables are used to distinguish between matrices, such as $\mathbf{R}$. When the expectation or the variance of the random signal is unknown, signal processing techniques often approximate the correlation as the

following, where N is the number of elements in $\vec{\mathbf{x}}$ over the time interval T[8].

$$\boldsymbol{\rho}_{XY} \approx \mathbf{R}_{XY} \tag{2.21}$$

$$\mathbf{R}_{XY} = E[\vec{\mathbf{x}}(t)\vec{\mathbf{y}}(t)] = \frac{1}{N}\sum_{t=0}^{T}\vec{\mathbf{x}}(t)\vec{\mathbf{x}}^{H}(t) = \frac{1}{N}\mathbf{X}^{H}\mathbf{X} \tag{2.22}$$

2.2.1 Continuous Time Correlation

Convolution is a mathematical property that shows the amount of overlap of two signals as one signal traverses or shifts past the other from $-\infty \leq t \leq \infty$. Mathematically in the continuous time case convolution is defined as the integral of the two signals with a time delay or lag in the second signal. This is more easily seen in mathematical notation as in Equations 2.23 – 2.25.

$$x(t) * y(t) = (x * y)(t) \tag{2.23}$$

$$= \int_{-\infty}^{\infty} x(\tau)y^{*}(t-\tau)\ d\tau \tag{2.24}$$

$$= \int_{-\infty}^{\infty} y(\tau)x^{*}(t-\tau)\ d\tau \tag{2.25}$$

Correlation, as discussed in Section 2.2, can also be calculated as the convolution of two signals with a time reversal of the second signal. In the continuous time case this yields:

$$R_{xy}(t) = x(t) * y(-t) \tag{2.26}$$

$$= \int_{-\infty}^{\infty} x(\tau)y^{*}(\tau-t)\ d\tau \tag{2.27}$$

$$= \int_{-\infty}^{\infty} y(\tau)x^{*}(\tau-t)\ d\tau \tag{2.28}$$

Correlation of periodic functions through convolution reduces to the following:

$$R_{xy}(t) = x(t) * y(-t) \tag{2.29}$$

$$= \frac{1}{T}\int_0^T x(\tau)y^*(\tau - t)\ d\tau \tag{2.30}$$

$$= \frac{1}{T}\int_0^T y(\tau)x^*(\tau - t)\ d\tau \tag{2.31}$$

By multiplying by the reciprocal of K, the limits of the periodic correlation can be scaled to $-\frac{1}{2} \leq R_{xy}(t) \leq \frac{1}{2}$ over the time interval $-\infty < t < \infty$, where K is expressed as[35]:

$$K = \frac{1}{T_0}\int_{\frac{-T_0}{2}}^{\frac{T_0}{2}} x^2(\tau)\ d\tau$$

$$R_{xy}(t) = \frac{1}{K}\frac{1}{T_0}\int_{\frac{-T_0}{2}}^{\frac{T_0}{2}} x(\tau)x(\tau - t)\ d\tau$$

2.2.2 Discrete Time Correlation

As in the continuous time case, correlation exists in discrete time and is defined by replacing the integral with a summation over sampled time where n is used to specify the sample index. For indexes when either of the signals is not defined, the appropriate signal is zero padded. Equation 2.32 shows discrete time convolution[35].

$$x(l) * y(l) = \sum_{n=0}^{N-1} x(n)y(l - n) \tag{2.32}$$

Discrete time correlation is similarly defined by time reversal of the second signal:

$$R_{xy}(l) = x(l) * y(-l) \tag{2.33}$$

$$= \frac{1}{N} \sum_{n=0}^{N-1} x(n) y^*(n-l) \tag{2.34}$$

Discrete time convolution for periodic functions uses a property called circular convolution where the sample indexes for locations at which the signal is not defined wrap around to the beginning or the end of the signal instead of zero padding. Although circular convolution can be performed on non-periodic functions, circular convolution is required to parallel continuous time periodic convolution. Discrete time circular convolution uses the modulo operator to wrap the signal around undefined indexes and is defined as[35]:

$$x(l) \circledS y(l) = \frac{1}{N} \sum_{n=0}^{N-1} x(n) y^*((l-n)_N) \tag{2.35}$$

Discrete time circular correlation and subsequent scaling are defined in Equations 2.36 – 2.38.

$$R_{xy}(l) = x(l) \circledS y(-l) \tag{2.36}$$

$$= \frac{1}{N} \sum_{n=0}^{N-1} x(n) y^*((n-l)_N) \tag{2.37}$$

Discrete Time Circular Correlation with scaling after applying the scaling constant

K is[35]:

$$R_{xy}(l) = x(l) \circledS y(l) = \frac{1}{KN} \sum_{n=0}^{N-1} x(n)y((n-l)_N), \tag{2.38}$$

$$K = \frac{1}{N} \sum_{n=0}^{N-1} x(n)x((n)_N) \tag{2.39}$$

2.3 Pseudo Random Noise (PRN)

Unlike random noise processes such as Gaussian or uniform distributions, a PRN process appears random but in reality is a repeating sequence. A PRN waveform over one period is commonly referred to as a PRN sequence or PRN code. Since the PRN sequence is repetitive it has a period where the interval of time between transitions in the PRN waveform is referred to as the chip period, T_{chip}. The reciprocal of the chip period is known as the chipping rate, R_{chip}. The waveform sequence over one chip period is known as the chip or spreading symbol[20].

Many different types of PRN sequences exist, but arguably the most important ones are the maximal sequences, also called maximal-length sequences. Maximal-length PRN sequences can be generated by Linear Feedback Shift Registers (LFSRs) and are called maximal-length because they are periodic and generate a sequence that is the length of shift register chain. With an n stage LFSR, the period of the PRN sequence is $N = 2^n - 1$ chips. Different sequences can be generated by a monic binary irreducible primitive polynomial $h(x)$, as shown in Equation 2.40. The polynomial coefficients, h_i, are the feedback tap coefficients of the LFSR. A coefficient of one indicates that a feedback to the input exists at stage i[16].

$$h(x) = 1 + h_1x + h_2x^2 + \cdots + h_{n-1}x^{n-1} + x^n, \quad h_i \epsilon \{0, 1\} \tag{2.40}$$

Gold codes are created using the sum of two maximal-length sequences. Gold codes, after the discoverer's namesake, were first presented by Robert Gold in 1967. From a communication perspective Gold codes maintain two important correlation properties, nearly zero correlation and cross-correlation[3].

$$R_{ik}(l) = \sum_{n=0}^{N-1} C_i(n)C_k(l+n) \approx 0 \quad \text{for all } m. \tag{2.41}$$

$$R_{kk}(l) = \sum_{n=0}^{N-1} C_k(n)C_k(l+n) \approx 0 \quad \text{for } |m| \geq 1. \tag{2.42}$$

The cross-correlation maintains a nearly zero value except for the zero lag; in other words, the sequence perfectly overlaps itself.

2.4 Spread Spectrum Modulation

As a product of the time-frequency domain relationship, Spread Spectrum modulation combines a PRN sequence known both to the sender and the receiver with the data or the carrier to widen the transmitted signal's spectral density. Widening the spectral density reduces the effectiveness of external interference or potential eavesdropping.

Historically, spread spectrum modulation originated from military applications. The first patent on what would eventually become spread spectrum appeared around 1938 by G. Guanella on the topic of radar[19]. The earliest works in data transmission using spread spectrum were primarily aimed at speech masking and communication protection. Spread spectrum protects a signal's integrity by reducing the effectiveness of a jamming signal. This is accomplished by spreading or increasing the modulated signal bandwidth so that the bandwidth is significantly larger than the bandwidth of the narrowband counterpart of the transmitted message signal. To jam a spread spectrum signal the jammer must distribute its fixed transmitted power over a larger

bandwidth thus lowering the magnitude of the jammer's power spectral density and correspondingly the jamming power is smaller in the message bandwidth[16].

There are two types of spread spectrum signals Frequency Hopping Spread Spectrum (FHSS) and DSSS[16].

2.4.1 Frequency Hopping Spread Spectrum (FHSS)

FHSS rapidly switches among several carrier frequencies using the PRN sequence in the frequency selection process.

2.4.2 Direct Sequence Spread Spectrum (DSSS)

DSSS is an extension of BPSK or other PSK modulation techniques with its main feature consisting of a PRN sequence or spreading waveform. A DSSS system consists of binary data modulated onto a finite periodic binary PRN sequence with a length of N chips[16]. A depiction of the DSSS physical construction is shown in Figure 2.2. The rate at which the chipping sequence changes is a function of the

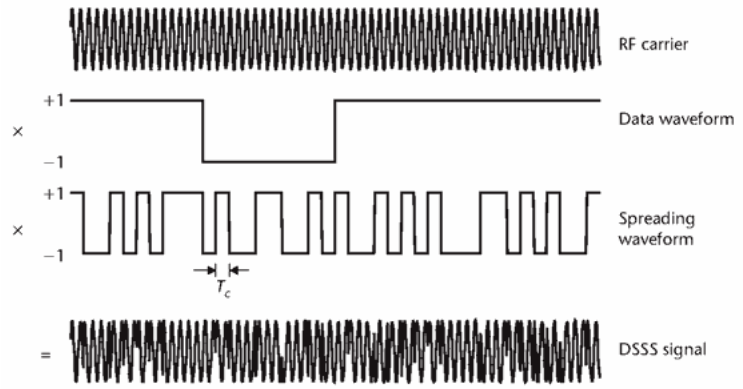

Figure 2.2: Signal Modulation Decomposition[20]

data bit rate and the number of N chips in the sequence as shown in Equation 2.43.

$$R_{chip} = \frac{1}{T_{chip}} = N \cdot R_{data} \tag{2.43}$$

Where the bit rate, R_{data} is defined as the reciprocal of the bit time T_{data}, therefore $R_{data} = 1/T_{data}$.

Since the spreading code is a function of the time interval of a bit period, the DSSS output is generated by replicating each data bit N times and modulo-2 adding the replicated data bits with the N chip repeating PRN sequence. The result of the modulo-2 addition or exclusive-or operation on the replicated data bit value is for a whole chipping sequence when the data is a binary 0 the unmodified PRN sequence is transmitted, and when the data bit is a binary 1 the complement of the PRN sequence is transmitted shown in Table 2.1.

Table 2.1: Exclusive OR Logic Output

Input (A)	**Input (B)**	**Output (C)**
0	0	0
0	1	1
1	0	1
1	1	0

Often the data values are scaled such that $0 \Rightarrow 1$ and $1 \Rightarrow -1$. After scaling the data in such a manner the exclusive-or operation mimics multiplication as shown in Table 2.2.

Table 2.2: 'Exclusive OR' Multiplication

Input (A)	**Input (B)**	**Output (C)**
-1	-1	1
-1	1	-1
1	-1	-1
1	1	1

After the combination, the output of the modulo-2 adder is fed to the PSK modulator to produce a DSSS signal where the bandwidth of the new signal is N times the bandwidth of the narrowband PSK signal. The N bit chip sequence or spreading factor is often called the processing gain of the spread spectrum signal[16]. Formally, the processing gain for DSSS is defined as[35]:

$$G_p = \frac{R_{chip}}{R_{data}} \tag{2.44}$$

where R_{chip} is the chipping rate and R_{data} is the data rate.

Demodulation of the DSSS signal is accomplished by first despreading the received signal by multiplying it by a time synchronized replica of the common PRN code. The despread signal after multiplication is returned to a narrowband form and can be demodulated by conventional means. The despreading operation in addition to narrowing the band of the desired data signal simultaneously spreads the received jamming signal power over a bandwidth much larger than the data bandwidth. It is worth noting that the despreading process provides no advantage with respect to white noise due to fact that the spectrum of white noise is theoretically infinite. Thus spreading an infinite spectrum is not feasible as the spectrum remains infi-

nite. Therefore, the performance of a DSSS signal to White Gaussian Noise (WGN) channel is identical to performance of its narrowband counterpart[16].

2.4.3 Code Division Multiple Access (CDMA)

CDMA is a DSSS multiple access modulation technique that is commonly used in commercial and military communication systems. CDMA operates under the same principles as DSSS but multiplexes multiple users by restricting the user space to the same carrier frequency and by using unique spreading sequences with low cross-correlation for each user. Low cross-correlation codes that are commonly used include Gold, Kasami, and phase-offset maximal sequences[16].

2.5 Phase Detection

Digitization is a common aspect of signal recovery and is performed by an Analog to Digital Converter (ADC). The received signal $y(t) = \mathrm{a}(t)\cos(2\pi f_c t + \alpha(t))$ after sampling at a frequency of f_s and substituting $t = nf_s$ yields a digitized signal.

$$y(n) = \sum_{n=-\infty}^{\infty} \mathrm{a}(nf_s)\cos(2\pi f_c n f_s + \alpha(nf_s)) \tag{2.45}$$

Although the digitized signal is mathematically characterized by Equation 2.45, in reality the sampling process of the ADC only captures discrete amplitudes at the sampling intervals in time. Therefore, the phase component $\alpha(t)$ of the signal is lost. This leads to the acquisition of the magnitude $\|A(t)e^{j(2\pi f_c t+\alpha(t))}\|_2$ instead of the amplitude $\|A(t)e^{j2\pi f_c t}\|_2$ and phase $\alpha(t)$ of the signal. Without additional circuitry or other recovery techniques the phase component of the signal is lost in the sampling process. One common phase recovery technique is known as IQ.

2.5.1 In-Phase and Quadrature (IQ)

In-Phase and Quadrature operates from the premise of Euler's formula, reference Equation 2.46, where a signal can be decomposed into its real $\Re = \cos(\alpha)$ and imaginary $\Im = \sin(\alpha)$ parts.

$$e^{j\alpha} = \cos(\alpha) + j\sin(\alpha) \tag{2.46}$$

$$\alpha = \tan^{-1}\left(\frac{\Im}{\Re}\right) \tag{2.47}$$

$$= \tan^{-1}\left(\frac{\sin(\alpha)}{\cos(\alpha)}\right) \tag{2.48}$$

By simultaneously multiplying or mixing the waveform received by the antenna by $\cos(\alpha)$ and $\sin(\alpha)$ the real and imaginary components of Euler's formula are realized as shown in Figure 2.3. After obtaining the real and imaginary parts, a trigonometric operation of inverse tangent yields the phase of the signal at its time of digitization. Using the IQ technique to recover the signal phase can take place pre or post digitization. Pre-digitization requires two digitizers to recover both branches.

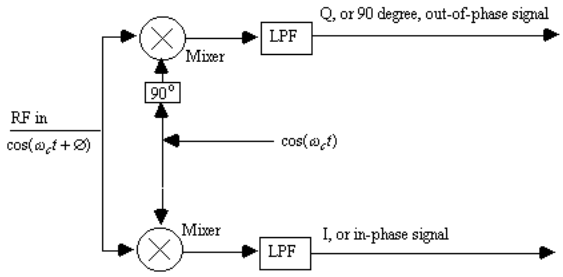

Figure 2.3: In-Phase and Quadrature Signal Generation[13]

Application the trigonometric identity $\cos(\alpha)\cos(\beta) = \frac{1}{2}(\cos(\alpha-\beta) + \cos(\alpha+\beta))$

for the in-phase branch allows the substitution:

$$IF_I(t) = \mathrm{a}(t)\cos(2\pi f_c t - \alpha(t))\cos(2\pi f_{LO} t) \tag{2.49}$$

$$= \frac{1}{2}\mathrm{a}(t)\cos(2\pi f_c(t) - \alpha(t) - 2\pi f_{LO} t) + \frac{1}{2}\mathrm{a}(t)\cos(2\pi f_c(t) - \alpha(t) + 2\pi f_{LO} t) \tag{2.50}$$

$$= \frac{1}{2}\mathrm{a}(t)\cos(2\pi(f_c - f_{LO})t - \alpha(t)) + \frac{1}{2}\mathrm{a}(t)\cos(2\pi(f_c + f_{LO})t - \alpha(t)) \tag{2.51}$$

After low pass filtering to remove the high frequency content $f_c + f_{LO}$ this yields the in-phase signal:

$$I(t) = \frac{1}{2}\mathrm{a}(t)\cos(2\pi(f_c - f_{LO})t - \alpha(t)) \tag{2.52}$$

In a similar manner to obtain the in-phase component, using the trigonometric identity $\cos(\alpha)\sin(\beta) = \frac{1}{2}(\sin(\alpha+\beta) - \sin(\alpha-\beta))$ allows the substitution for quadrature branch:

$$IF_Q(t) = \mathrm{a}(t)\cos(2\pi f_c t - \alpha(t))\sin(2\pi f_{LO} t) \tag{2.53}$$

$$= \frac{1}{2}\mathrm{a}(t)\sin(2\pi f_c(t) - \alpha(t) + 2\pi f_{LO} t) - \frac{1}{2}\mathrm{a}(t)\sin(2\pi f_c(t) - \alpha(t) - 2\pi f_{LO} t) \tag{2.54}$$

$$= \frac{1}{2}\mathrm{a}(t)\sin(2\pi(f_c + f_{LO})t - \alpha(t)) - \frac{1}{2}\mathrm{a}(t)\sin(2\pi(f_c - f_{LO})t - \alpha(t)) \tag{2.55}$$

After low pass filtering to remove the high frequency $f_c + f_{LO}$ content leaves the

quadrature component:

$$Q(t) = \frac{1}{2}\,\mathrm{a}(t)\sin(2\pi(f_c - f_{LO})t - \alpha(t)) \tag{2.56}$$

If the carrier f_c and the local oscillator f_{LO} are perfectly matched the filtered in-phase and quadrature signals further cancellation is allowed.

$$\begin{aligned}
\alpha(t) &= \tan^{-1}\left(\frac{Q(t)}{(t)}\right) && (2.57)\\
&= \tan^{-1}\left(\frac{\frac{1}{2}\,\mathrm{a}(t)\sin(2\pi(f_c - f_{LO})t - \alpha(t))}{\frac{1}{2}\,\mathrm{a}(t)\cos(2\pi(f_c - f_{LO})t - \alpha(t))}\right) && (2.58)\\
&= \tan^{-1}\left(\frac{\sin(2\pi(f_c - f_{LO})t - \alpha(t))}{\cos(2\pi(f_c - f_{LO})t - \alpha(t))}\right) && (2.59)\\
&= \tan^{-1}\left(\frac{\sin(-\alpha(t))}{\cos(-\alpha(t))}\right) && (2.60)
\end{aligned}$$

2.6 Signal Performance Metrics

The SNR is a measure of the ratio between the signal power and the noise power, and the ratio is a metric to the quality of a signal[35].

$$\mathrm{SNR} = \frac{P_s}{P_n} \tag{2.61}$$

The ratio is more commonly displayed in decibels.

$$\mathrm{SNR}_{dB} = 10\log_{10}\left(\frac{P_s}{P_n}\right) \tag{2.62}$$

Another performance measure is the Signal to Interference Noise Ratio (SINR) ratio, which is defined as the power of the signal to the combined power of the

interference and noise.

$$\text{SINR} = \frac{P_s}{P_i + P_n} \tag{2.63}$$

2.6.1 Energy and Power Signals

The energy of a signal is defined as the magnitude of the signal squared integrated from $-\infty \leq t \leq \infty$[35]

$$E_x = \int_{-\infty}^{\infty} |x(t)|^2 dt = \int_{-\infty}^{\infty} |X(f)|^2 df \tag{2.64}$$

Power is a derivative of energy and is defined as the time average of the signal energy[35].

$$P_x = \lim_{T\to\infty} \frac{1}{T} \int_{-T/2}^{T/2} x^2(t) dt \tag{2.65}$$

For a periodic signal or for computing the instantaneous power over the interval T, the limit is dropped forming Equation 2.66.

$$P_x = \frac{1}{T} \int_{-T/2}^{T/2} x^2(t) dt = \int_{-\infty}^{\infty} \lim_{T\to\infty} \frac{1}{T} |X_T(f)|^2 df \tag{2.66}$$

2.6.2 Noise Power

The noise power is a composite of thermal radiation, electronic noise, galactic noise, and other sources. The noise spectral density of thermal noise with a noise reference temperature of $T_0^\circ = 290$ K yields[35]:

$$N_0 = \kappa T_0^\circ = 1.38 \times 10^{-23} \times 290 = 4.00 \times 10^{-21} W/Hz \tag{2.67}$$

where κ is equal to the Boltzmann constant = $1.3806488 \times 10^{-23}$ $\text{m}^2\text{kg/s}^2\text{K}$.

The total output noise power flowing into a load is a function of noise spectral

density in Equation 2.67 multiplied by the bandwidth of the signal with all components of the network at the effective noise temperature T°_{sys}[35]:

$$N_{out} = G_{sys}\kappa T^{\circ}_{sys} W \tag{2.68}$$

where W is the bandwidth in Hz, and G_{sys} is the system gain. The system temperature T°_{sys} is a combination of the antenna temperature T°_{ant} and the composite temperature T°_{comp} of the multiple series network elements[35].

$$T^{\circ}_{sys} = T^{\circ}_{ant} + T^{\circ}_{comp} \tag{2.69}$$

Composite noise can be formed via noise figure or noise temperature where all variables are in ratios[35]:

$$T^{\circ}_{comp} = T^{\circ}_{1} + \frac{T^{\circ}_{2}}{G_1} + \frac{T^{\circ}_{3}}{G_1 G_2} + \cdots + \frac{T^{\circ}_{n}}{G_1 G_2 \cdots G_{n-1}} \tag{2.70}$$

$$F_{comp} = F_1 + \frac{F_2 - 1}{G_1} + \frac{F_3 - 1}{G_1 G_2} + \cdots + \frac{F_n - 1}{G_1 G_2 \cdots G_{n-1}} \tag{2.71}$$

The noise figure F is given as the ratio of SNR in and out of the network. The noise figure is formally defined in Equation 2.72.

$$F = \frac{SNR_{in}}{SNR_{out}} \tag{2.72}$$

The effective noise temperature of receiver or network describes the translation between noise figure and noise temperature[35].

$$T^{\circ} = (F - 1)T^{\circ}_{0} \tag{2.73}$$

3. GLOBAL NAVIGATION SATELLITE SYSTEM (GNSS) CONCEPT

A brief introduction into radio navigation is provided, which shows the underlying principles behind the GPS navigation system and why multiple satellite signals arriving from different locations must be received and processed in parallel. The complexity of the GPS operation is shown. Also, an overview of the GPS signal structure and receiver is constructed to give a framework for which any defense or interference mitigation must be made.

3.1 Radio Navigation

Using basic geometry, the position of an unknown point in space can be derived if both the locations of additional points, as well, as their respective distance to the unknown position are known. The number of additional known points must be of sufficient quantity to solve the number of variable unknowns; with generality, this is the dimension of the geometry plus one[20].

In one dimensional space, the axis forms a line where the location of all point sources are known, but the user location on the line is unknown. From the unknown location U, if the position and distance to point F_1 are known the solution for the location of U provides two solutions on the line; one solutions matches the unknown location and the other solution provides a false position. If the location and distance to another point F_2 is known, the position of U is uniquely determined. If the known points are fog horns with clocks perfectly synchronized with the user, the distance between the user and the fog horn can be calculated by measuring the propagation time of each foghorn's sound wave as it travels toward the user. This result is summarized in Table 3.1.

Table 3.1: Radio Navigation: 1 Dimensional Space

Number of Sources	**Position Outcome**
1	Two Points
2	One Point
3	One Point with Time

Extending the foghorn concept into two dimensional space, if only one reference F_1 exists then the calculation of the potential locations of U forms a circle with F_1 at the center as shown in Figure 3.1. The addition of second reference F_2, as shown in

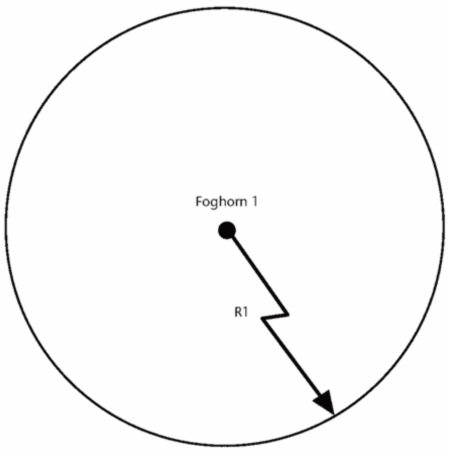

Figure 3.1: 2D Radio Navigation with Single Beacon[20]

Figure 3.2, narrows the possible solutions to two points formed by the intersection of two circles. Extrapolating the navigation calculation to a third reference F_3 provides the unique solution as indicated in Figure 3.3.

The previous discussion operated under the assumption that the point sources

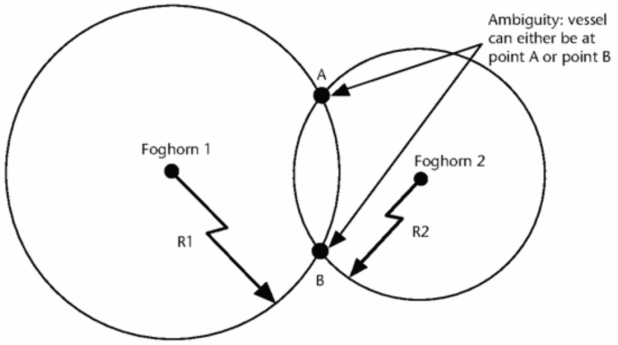

Figure 3.2: 2D Radio Navigation with Dual Beacons[20]

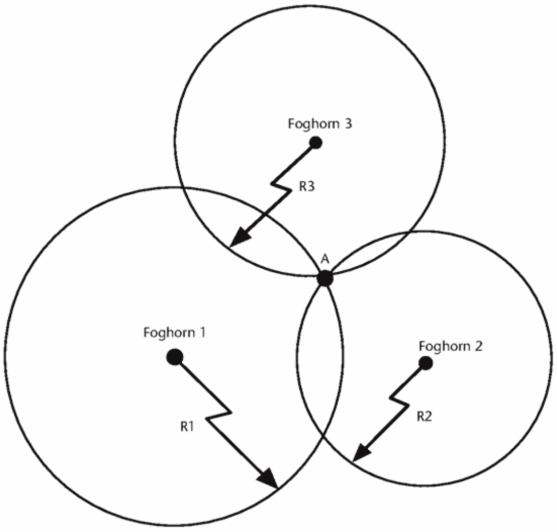

Figure 3.3: 2D Radio Navigation with Triple Beacons[20]

(fog horns) and the user had perfectly synchronized clocks. In practical situations this assumption is not valid due to different clock drift rates and biases. The error associated with the clock leaves an ambiguity in the position determination and requires an additional point source to help resolve the clock error by calculating system time. Figure 3.4 shows the effect of the position determination using dashed lines to indicate the numerical solution position verses the solid lines that align with

the true position. The position determination verses the number of point sources is summarized in Table 3.2.

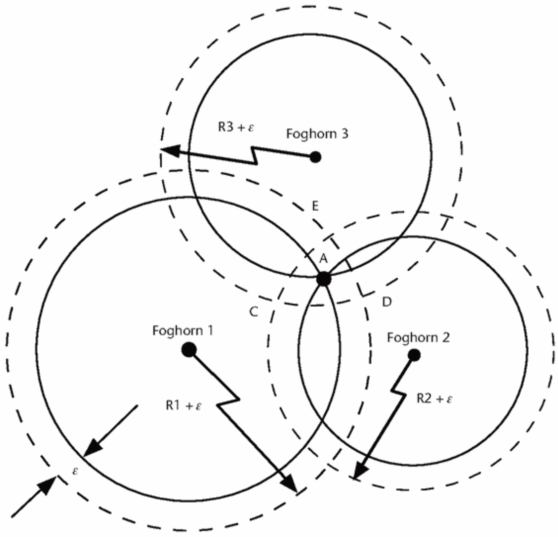

Figure 3.4: 2D Radio Navigation with Triple Beacons and Signal Error[20]

Table 3.2: Radio Navigation: 2 Dimensional Space

Number of Sources	**Position Outcome**
1	Circle Circumference
2	Two Points
3	One Point
4	One Point with Time

With only one reference F_1, in three dimensional space, the solution for all possible outcomes of the unknown position U are a sphere with F_1 at the center. With two reference locations, F_2 provides sufficient information to narrow the search to the intersection of two spheres forming an ellipsoid. With three references, the solution

for U given the position and distances to $\{F_1, F_2, F_3\}$ are two points in space shown in Figure 3.5. A fourth reference F_4 supplies the remaining information to provide a unique location with the synchronized clock condition, and a fifth reference F_5 allows the removal of the synchronized clocks. The position determination is summarized in Table 3.3.

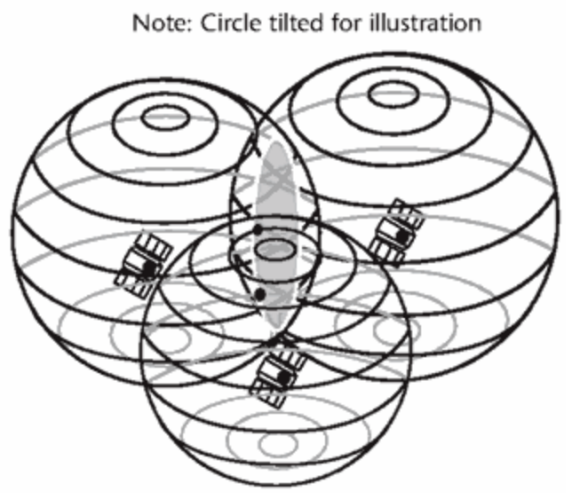

Figure 3.5: 3D Radio Navigation with Triple Beacons[20]

Table 3.3: Radio Navigation: 3 Dimensional Space

Number of Sources	**Position Outcome**
1	Sphere
2	Oval
3	Two Points
4	One Point
5	One Point with Time

Given the possible situation that in three dimensional space the system is under-

determined, where the number of known locations is less than the number required for a unique solution, a position can still be derived operating under certain assumptions. A reduced accuracy position can be obtained by using the statistical probability of the user's position. When a navigation solution calculates two outcomes with a position near the Earth's surface and a position in the upper atmosphere or beyond, most users will operate close to the Earth's surface. This allows the secondary solution to be disregarded. A further reduction in signal sources can be made if a larger tolerance to accuracy errors is allowed by not correcting for clock synchronization errors[20].

3.2 Global Navigation Satellite System (GNSS)

In Global Navigation Satellite Systems (GNSSs) the known positions or foghorns in the illustrative example are the navigation satellite's location on their respective orbital trajectory, and the known distance is the distance from each satellite to the unknown user's position.

Similar to the fog horn, each satellite sends a signal at time t_{si}, which propagates to the receiver and is received sometime later at time t_u. By simultaneously measuring the satellites's respective signal at a certain instance in time and comparing it with the time of the received signal the distances from the unknown user position to the satellites is determined by equating the time derivative of velocity[40]. The distance between the user and the satellite i with a propagation velocity constant c equaling the speed of light is[39]:

$$\rho_{iT} = c(t_u - t_{si}) \tag{3.1}$$

In other words, the distance between the user and the satellites is calculated by the travel time of the radio waves from the satellite when the satellite position is

known. The value ρ_{iT} is referred to as the true pseudorange. The true pseudorange is difficult to obtain from the satellite to the user due to inconsistences in the signal measurement. One such inconsistency is the unknown clock bias and drift between the user and the satellites. The clock time on the satellite $t_{si}^{'}$ and the clock time on the user's receiver $t_{u}^{'}$ are related to the true time by[39]:

$$t_{si}^{'} = t_{si} + \Delta b_i t_{u}^{'} = t_u + b_{ut} \tag{3.2}$$

where Δb_i is the satellite clock error, and b_{ut} is the user clock bias error. The pseudorange is also affected by other disturbances such as the ionosphere, the troposphere, and relativity to name a few. Adjusting equation 3.1 for these effects yields:

$$\rho_i = \rho_{iT} + \Delta D_i - c(\Delta b_i - b_{ut}) + c(\Delta T_i + \Delta I_i + v_i + \Delta v_i) \tag{3.3}$$

where ΔD_i is the satellite position error effect on range; ΔT_i is the tropospheric delay error; ΔI_i is the ionospheric delay error; v_i is the receiver measurement noise error; and Δv_i is the relativistic time correction[39].

To calculate position when the receiver clock is unsynchronized to the satellite's onboard clock, it is necessary to have an over-determined system where the number of signal transmitters exceeds the number of unknown dimensions by one. Therefore, contact to at least four satellites is required to determine longitude, latitude, altitude, and time[40].

3.3 Global Positioning System (GPS)

The GPS Global Navigation Satellite System is an example of radio navigation position determination using time propagation delay of the incident radio waves for distance and the satellite's broadcast position for the satellite's location information.

The GPS program was developed by the US Department of Defense (DoD) after its approval in December of 1973. Five years after its approval the first satellite was launched into orbit on February 22, 1978[40]. By August of 1993, the constellation was complete with 24 satellites in orbit, and in December of that same year, Full Operational Capability (FOC) was achieved. The Federal Aviation Agency (FAA) declared GPS ready for aviation use in February 1994 starting the civilian dependency on the system[39]. The constellation is composed of a variety of satellite variation which are managed by the 50^{th} Space Wing of the United States Air Force (USAF)[40].

The NAVSTAR GPS is a GNSS comprised of three segments: the control, space, and user segments. The control segment is responsible for the monitoring and maintenance of the space segment. The space segment consists of the satellite constellation and their transmitted signals. The user segment consists of the end user receiver navigation equipment.

3.3.1 Control Segment

The GPS control segment consist of a Master Control Station (MCS) located in Colorado and five monitoring stations located throughout the Earth near the equator. The control segment is responsible for[40]:

- Observing the movement of the satellites and compute orbital data (ephemeris)
- Monitoring satellite clocks and predicting their behavior
- Synchronizing onboard satellite time
- Relaying precise orbital data from the satellites
- Relaying approximate orbital data of all satellites
- Relaying status information (satellite health, clock errors, etc.)

- Overseeing selective availability artificial accuracy distortion of the civilian signal deactivated in May 2, 2000 and the capability to regionally or globally reactivate

3.3.2 Space Segment

The space segment consists of the satellite constellation and the signals they transmit. The constellation is constructed to permit 6 orbital planes with a total of 32 operational satellites orbiting at a Medium Earth Orbit (MEO) of $20,180$ km. The orbits are inclined at $55°$ to the equator, and each satellite has a period of approximately 12 hours. [40]. Although, the constellation was designed to accommodate 32 operational satellites the space segment currently contains 31 with several spares[27]. A depiction of the satellite constellation is made in Figure 3.6.

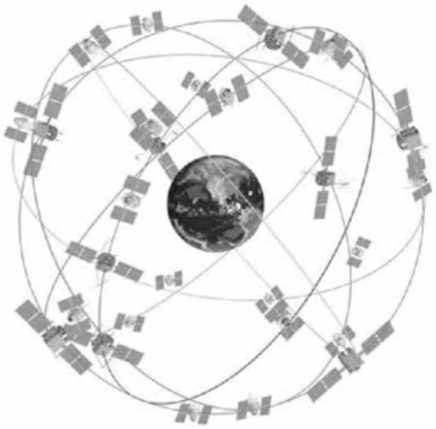

Figure 3.6: Satellite Constellation[20]

Each SV is identified by a unique PRN code that is added onto its navigation data signal. Signal recovery occurs by correlating a replica code associated with each satellite with the received signal. Due to the Doppler Effect caused by a relative

difference in velocity between the user and the satellites, the transmitted signal can be out of phase from their original form by as much as $\pm 6000Hz$. In addition, clock synchronization mismatch causes an unknown code phase. Determination of the signal travel time and data recovery requires the use of an exact frequency and code; therefore, a search of all possible frequency shifts and code phases is required to obtain a doppler-code match.[40]

3.3.3 Signal Structure

The GPS signal structure consists of a carrier, a modulator, a spreading sequence, and navigation data for specific codes. The signal structure can be broken into two groups or classification based on the access permissions. These groups are the civilian and the restricted segment.

3.3.4 Civilian Segment

The civilian segment, known as the Standard Positioning Service (SPS), is a non-encrypted, freely available service that consists of the L1 C/A code. The L1 C/A operates at a carrier of $1575.42MHz$ and uses BPSK modulation.

The GPS constellation is currently undergoing a moderation plan that will augment the civilian segment by adding the L2 Civil-Moderate (CM), L2 Civil-Long (CL), and the L5 emergency codes. However, due to the incomplete state of the modernization program, L1 C/A is the only fully operational and reliable service for civilian use[20].

3.3.5 Restricted Segment

The restricted segment is a Precision Positioning Service (PPS) for the US military and other authorized users. The restricted segment is comprised of the L1 P, L2 P, L1 M, and L2 M codes. Originally the unencrypted PPS, known as P code, was

available to the public until January 31, 1994 when encryption was enabled. The code provided higher accuracy through the absence of Selective Availability (SA) and a longer chipping sequence. The P code is a repeating truncated code that operates at a chipping rate of 10.23 Mega bits per second (Mbps) and repeats every 266 days[12]. Following standard cryptography notation, the encrypted P code is known as P(Y). The encrypted variant remains exactly the same as the unencrypted P code but requires a decryption key to prevent access from unauthorized users.

3.3.6 Pseudo Random Noise (PRN) Codes

As a means of individual satellite identification, signal propagation time estimation, jamming suppression, and frequency reuse, each SV continually transmits a unique PRN signature.

The L1 C/A code is a truncated 1023 bit repeating Gold PRN number sequence which is uniquely assigned to each satellite[40]. The C/A code defines 37 sequences, but only 36 of the codes are mutually exclusive and non-overlapping. Each code has a chip rate of 1.023 Mbps. The chip period, or the period at which the 1023 sequence repeats, is 1 ms[12]. The C/A code is generated using two 10 bit LFSRs, G_1 and G_2, where the taps to the second register G_2 control which of the 37 spreading sequences is generated. The LFSR feedback polynomials are shown in Equations 3.4 and 3.5. By selecting a combination of two of the taps from G_2 each unique code is created[3]. For reference the C/A code generater is shown in Figure 3.7.

$$G_1(x) = 1 + x^3 + x^{10} \tag{3.4}$$

$$G_2(x) = 1 + x^2 + x^3 + x^6 + x^8 + x^9 + x^{10} \tag{3.5}$$

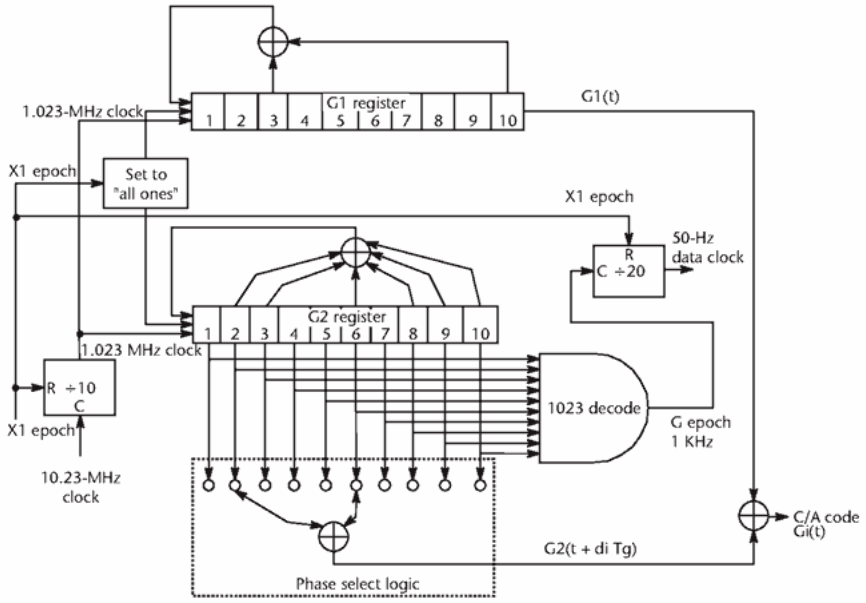

Figure 3.7: Coarse Acquisition (C/A) Code Generator[20]

3.3.7 Message Structure

The navigation message contains information to aid GPS receivers in tracking valid satellites and obtaining a PVT solution. This is accomplished through the use of a satellite almanac to aid the acquisition process, satellite health to help determine satellites that should be avoided, broadcast ephemeris containing the coordinates of the SV to allow the calculation of the user's position, and correction parameters such as satellite clock correction and ionosphere and troposphere atmospheric model parameters to improve the accuracy of the PVT solution[12].

The entire message contains $37,500$ bits and is generated at a rate of 50 bits per second (bps) translating into a total of 12.5 minutes for complete transmission. The message is segmented into 25 groups, called frames, each $1,500$ bits. Each frame is further divided into 5 subframes of 300 bits that each contain different information[12]. Encoded in each of the 25 navigation data frames are sections de-

voted to GPS broadcast orbital information and almanac. The broadcast orbit, also known as broadcast ephemeris, represents the perturbed satellite orbit but is given in the form of predicted orbital parameters. The broadcast ephemeris records are updated by the MCS every hour. The almanac provides a less accurate version of the ephemeris information, but is useful during the acquisition phase. By predicting the satellite visibility over the horizon at a particular location and time from the almanac information, the acquisition loop can reduce the satellite search space that effectively improves the efficiency of the acquisition process. Ephemeris and almanac data is publicly available from the U.S. Coast Guard Navigation Center and Crustal Dynamics Data Information System [12]. The navigation payload structure is depicted in Figure 3.8.

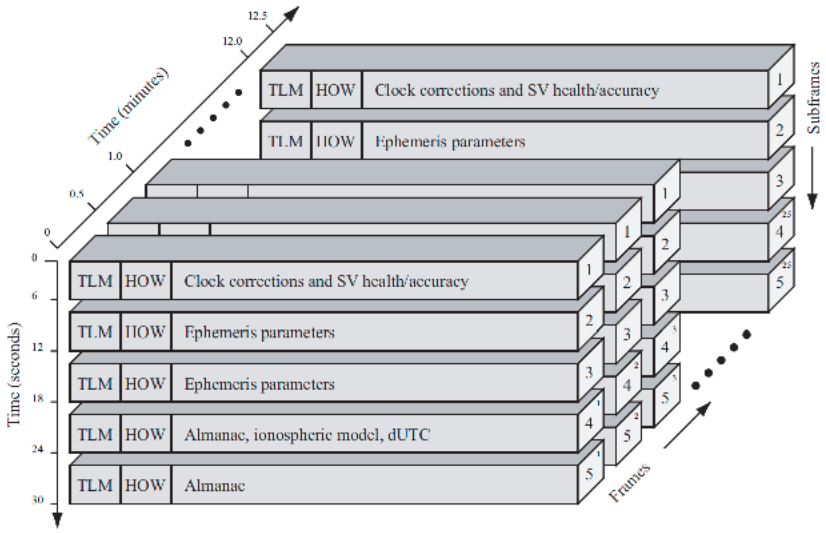

Figure 3.8: NAVSTAR GPS Data Payload[3]

The Telemetry Word (TLM) starts the sequence of every single subframe. It contains an 8 bit preamble with the binary sequence 10001011 that is used for syn-

chronization purposes, followed by 16 bits of reserved data specified by authorized users, and ends with a 6 bit parity. Immediately following the TLM is the 17 bit Handover Word (HOW) that contains the start time of the next subframe using GPS Time of Week (TOW). The TOW count begins at 0 starting at the beginning of the GPS week (transition period from Saturday $23:59:59$ hours to Sunday $00:00:00$ hours) and is increased by a value of 1 every 6 seconds. As there are $604,800$ seconds in a week, the count runs from 0 to $100,799$ before returning to 0[40]. The remaining portions of the message contain the ephemeris, almanac, correction parameters, and SV health. After the data payload is formed it is prepared for modulation and subsequent transmission.

3.4 Modulation

Prior to modulation, the C/A PRN code containing each SV's identification number is modulo 2 added, or binary exclusive-ored, onto the navigation data discussed in section 3.3.7. After the spreading process is complete, the GPS C/A code uses BPSK to modulate the satellite's navigation message and identification sequence onto the airwaves[20]. As previously mentioned in section 2.1.2, BPSK imposes two discrete phase shifts on the carrier sine wave that are aligned with the data's binary value. For reference, a diagram of BPSK modulated data is shown in Figure 2.1. Figure 2.2 shows hows the navigation data payload is superimposed with the PRN spreading sequence, then combined with the carrier waveform to complete the construction of the satellite signal.

Due to each SV's limited transmission power and the energy loss due to propagation, the modulated L1 C/A code has a maximum signal strength on earth's surface of -153 dBW and a minimum signal level of -160 dBW. This can be seen relative to the noise floor in Figure 3.9[40].

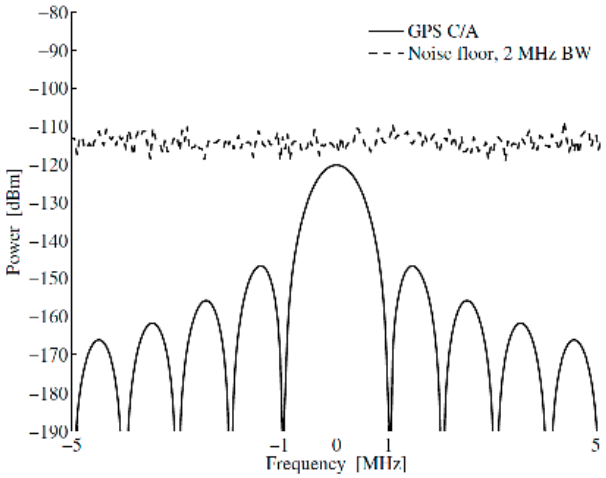

Figure 3.9: Coarse Acquisition (C/A) Signal to Noise Floor[3]

3.5 User Segment

The user segment consists of the end user equipment that is designed to receive and process the GPS signal to compute a navigation solution. The following sections describe the construction and the stages required to demodulate the satellite signals and compute a position solution. This section helps build the framework for which any interference defense is based.

3.5.1 Receiver Concepts

The GPS signals impinging on the navigation receiver will proceed through a number of stages before a final navigation solution is computed provided a sufficient number of satellites are in view of the receiver. The stages progress through the following flow[39], which is better summarized in graphical form in Figure 3.10.

1. Antenna
2. RF chain

3. Digitization via an ADC

4. Acquisition

5. Tracking

6. Bit Synchronization and subframe identification

7. Ephemeris and pseudorange calculation

8. Satellite positions

9. User PVT

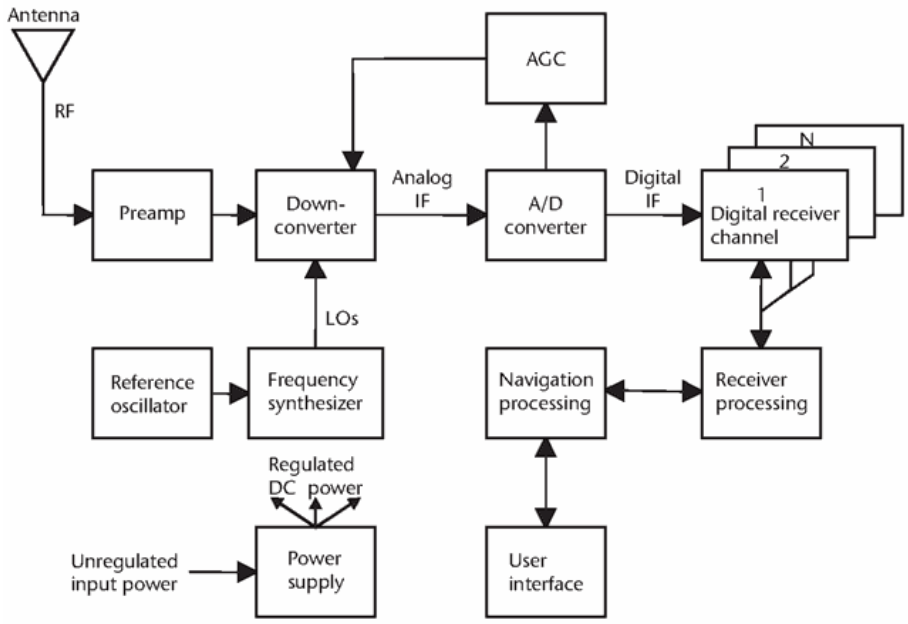

Figure 3.10: Receiver Block Diagram[20]

3.5.2 Signal Reception and Demodulation

The GPS satellite signal is received by a Right Hand Cross Polarization (RHCP) capable antenna. Such an antenna usually provides hemispherical (i.e. above the

horizon) gain coverage to limit multipath and other types of interference. After receiving the satellite signal through the antenna, it proceeds through a series of conditioning operations in the RF front end to amplify, filter, and down-mix the signal to a lower center frequency.

The first stage after reception is amplification by a low noise preamplifier, which also sets the noise figure of the receiver discussed in Section 2.6.2. Prior to down-mixing, a passive bandpass filter may exist to minimize out-of-band interference. Then the signal is down-converted to an Intermediate Frequency (IF) through the process of mixing. Mixing is the process of multiplying a frequency component, in this case the carrier, by a local oscillator after an anti-aliasing filter to produce an intermediate frequency. Depending on the frequency of the local oscillator, the IF can either cause an upshift or a downshift in frequency. Usually after another round of filtering, the IF is digitized by an ADC with Automatic Gain Control (AGC). The digitized IF is then processed by the receiver channels' acquisition, tracking, and navigation routines[20].

It is worth noting that a signal's doppler frequency and PRN phase are preserved through the mixing process. Therefore, the necessary components for DoA estimation are not altered by down-mixing; only the carrier center frequency is lowered.

3.5.3 Receiver Types

Two different types of GPS receivers exist, the Application Specific Integrated Circuit (ASIC) and Software Defined Radio (SDR). Although the two receivers platforms perform the same function, the manner in which they operate is radically different. The ASIC receiver is a custom electronic circuit that typically implements the RF front end and processing components in hardware. The SDR variant implements typical hardware functionality such as mixers, filters, demodulators, detectors

in software after the signal is digitized using a generic processor, Digital Signal Processor (DSP) or reconfigurable logic. The SDR receiver typically has the advantage over the ASIC due to the reconfiguration capability. A GPS SDR is shown in Figure 3.11. In either case, after amplification, down-mixing, and filtering, the next stage

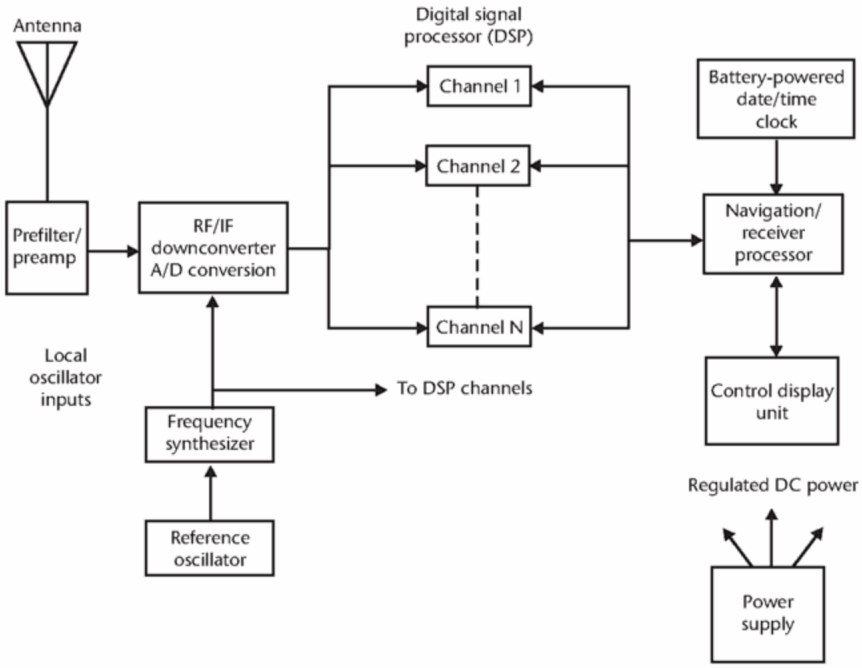

Figure 3.11: Software Defined Radio Receiver Block Diagram[20]

is to start the demodulation process. In order to demodulate the signal, the exact PRN phase must be found. The phase is found in part of a process called acquisition and the information is later used during the tracking phase to maintain signal lock.

3.5.4 Acquisition

The acquisition process is a more generalized or coarse version of the tracking process whose purpose is to identify SVs and aid the tracking loops by providing an approximation of the frequency and code phase. Signal acquisition and tracking is

a two-dimensional (carrier Doppler and code phase) signal replication process based on the principles of correlation. When a satellite signal is first received there is an unknown doppler shift on the carrier created by the respective movement of the satellites to the receiver. In addition, with an unknown distance to the satellite and the absence of a synchronized clock between the satellites and the receiver, an unknown PRN code phase exists. After dividing the frequency spectra into bins, a search of the two dimensional frequency code space is required to recover the incoming signal[20]. This can be seen in Figure 3.12.

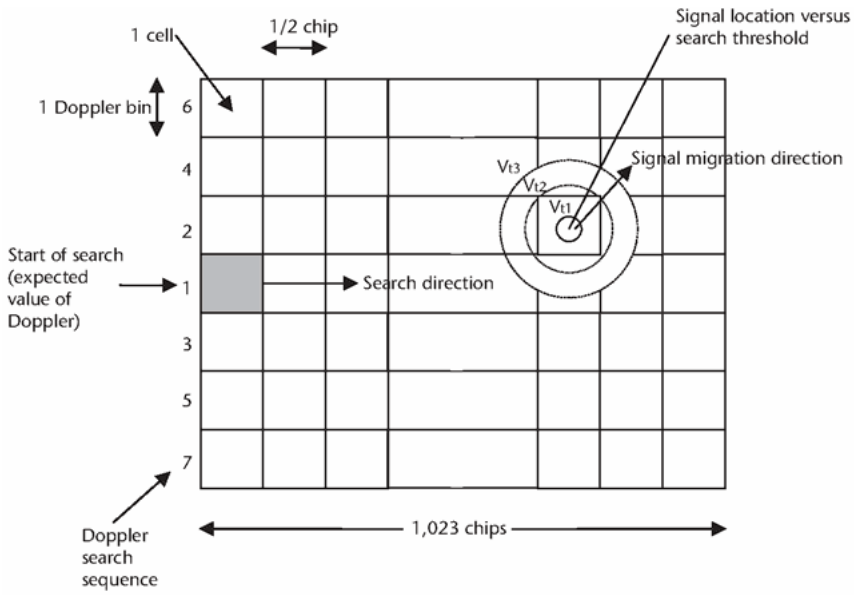

Figure 3.12: Acquisition Frequency Doppler and Code Phase Search[20]

By the properties of correlation, when the GPS receiver replica code phase matches the phase of the incoming satellite vehicle (i.e. the codes are aligned in time) maximum correlation is achieved. However, if the phase of the code replica deviates from the SV code phase by more than 1 chip on either side minimum cor-

relation is achieved. In practice the GPS creates three code replicas: an early, a prompt (aligned time), and a late versionkaplan2006understanding. The effect of the replica alignment with the incoming signal is depicted in Figure 3.13.

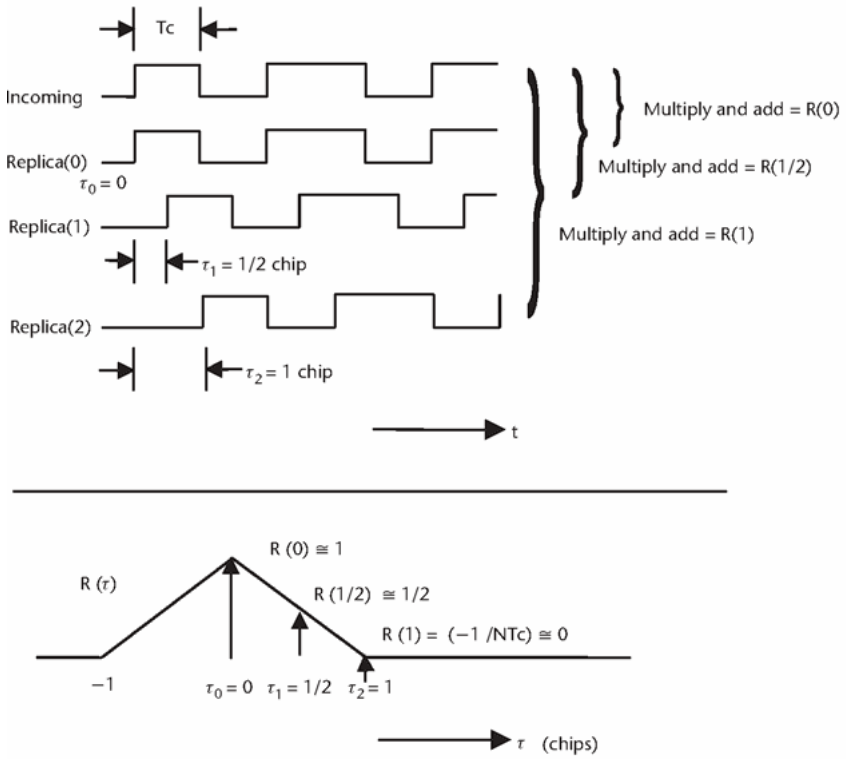

Figure 3.13: Early, Prompt, Late Signal Correlation[20]

By a similar process, GPS receiver replicates the carrier frequency plus Doppler shift of the various SVs to detect the carrier phase dimension. Carrier phase lock is usually achieved by this method[20].

3.5.5 Tracking

In the carrier Doppler frequency dimension, the GPS receiver accomplishes carrier matching or carrier wipe off by first searching for the carrier Doppler frequency

of the desired SV and then tracking the SV carrier Doppler state. Using the generalized frequency and code phase from the acquisition phase, the receiver improves its estimation of the frequency and code by first searching for the phase of the desired SV then tracking the code state. This is accomplished by adjusting the nominal spreading code chip rate of the receiver replica PRN code to compensate for the Doppler-induced effect caused by Line of Sight (LoS) dynamics and the receiver's frequency offset in its reference oscillator with respect to the specified frequency. The tracking process is depicted in Figure 3.14.

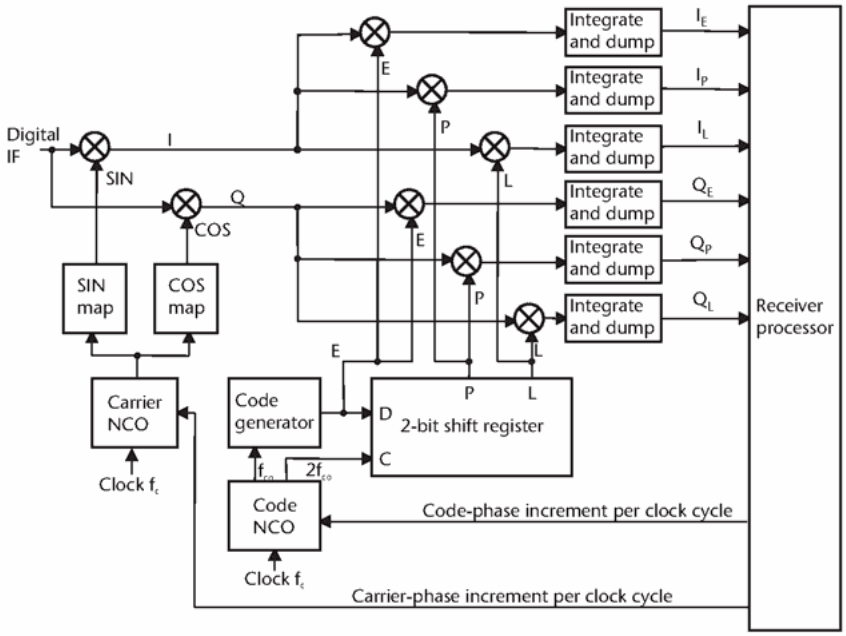

Figure 3.14: Tracking Loop[20]

If a signal was successfully acquired through the replication of the SV code and frequency carried out during the search process but later loses tracking of the SV frequency then the receiver subsequently loses code track as well[20]. Thus the

acquisition process must start over and the tracking SV process will resume pending successful reacquisition.

3.5.6 Decoding

After first acquiring a satellite signal then increasing the accuracy of the frequency and code phase through the tracking process, the receiver moves onto the decoding phase. The decoding phase starts by first synchronizing to the data bit transition boundaries. Once the boundary is obtained and several data bits are accumulated, the decoding proceeds into the frame synchronization phase. During this phase the preamble contained in the TLM is sought after as this marks the beginning of each subframe. After successful frame synchronization and accumulation of 300 bits of a subframe, parity is checked to ensure the navigation data's integrity[20].

3.5.7 Position, Velocity, and Time (PVT) Determination

After a successful subframe integrity check, the system proceeds to use the information in the subframe to assist in the pseudorange calculation. The range or distance between the GPS receiver and the GPS satellite is known as the pseudorange. More precisely, the pseudorange is the distance between the antenna center of the GPS receiver and the antenna center of the GPS satellite. Methods of determining distance include pseudorange and carrier phase measurements[12]. The reader is left to other literature for a detailed discussion of this process.

4. ANTENNA PHASED ARRAYS

Previous chapters provided sufficient background on how the GPS constellation and receivers operate and the modulation scheme used for satellite identification and transmission. This chapter will introduce the model assumptions used in the antenna component of the research, discuss available diversity techniques that improve signal reception, describe the incident signal phasing relative to the reference array element mathematics, explain the subspace estimation techniques that are fundamental to the DoA algorithm used, show how beamsteering and synthetic aperture antenna arrays operate, and define directivity, which is measure of beam pattern concentration and performance.

4.1 Model Assumptions

The following discussion and subsequent results in Chapter 5 rely on certain model assumptions. Some of these assumptions are based on the principles of an isotropic radiator. An isotropic radiator is an ideal radiator where the antenna transmission or reception pattern is represented by a unity sphere and has the same physical properties in all directions. Being a unity sphere, the gain of the element is one. The model assumptions consist of an isotropic and linear transmission medium, far-field condition, narrowband criterion, Additive White Gaussian Noise (AWGN) channel, and the absence of mutual coupling, which are summarized by Chen, et al., below[8]:

Isotropic and linear transmission medium implies that the d signal wavefronts impinging onto the N element antenna array do not change with DoA of signals, and that the signals traveling through the medium received by any element of the array can be computed as a linear superposition of d signal wavefronts generated by the d sources.

Far-field condition allows the d signal wavefronts to be approximated as a planar wavefront where the wavefront arrives at all N antenna elements at an equal direction of propagation. This assumption is realized by making the distance between the signal sources and the array significantly larger than the dimension D of the array. A general guideline for the far-field approximation is that the distance is larger than $2D^2/\lambda$ with D being the dimension of the array and λ being the wavelength of the signals[8].

Narrowband criterion requires that each of the d signal sources have the same carrier frequency f_c and that the Fourier transform of the data frequency contents are concentrated around the center of the carrier. The source signals are considered narrowband as long as their amplitudes, $\mathrm{a}_i(t)$, and information-bearing phases, $\alpha_i(t)$, vary slowly with respect to the time, τ, for the waves to propagate from one antenna element to another. The slowly varying requirement ensures that most of the data frequency contents fulfill the Fourier transform requirement of being within the vicinity of the carrier frequency and that the information bearing sequences can be approximated as $\mathrm{a}_i(t-\tau) \approx \mathrm{a}_i(t)$ and $\alpha_i(t-\tau) \approx \alpha_i(t)$. Therefore:

$$s_i(t) = \mathrm{a}_i(t-\tau)\cos(2\pi f_c t + \alpha_i(t-\tau)), \quad 0 < i < d-1$$

$$s_i(t) \approx \mathrm{a}_i(t)\cos(2\pi f_c t + \alpha_i(t)), \quad 0 < i < d-1$$

AWGN channel is assumed to be a spatially uncorrelated random process with zero mean and a common variance σ_N^2 at all antenna array elements; in other words, an additive complex white Gaussian random process[8].

4.2 Diversity

The fundamental concept behind combating destructive interference in RF applications, called diversity, lies in arranging several independent transmission channels or branches. The purpose of the independent channels is to jointly process the signal branches in a manner that makes the higher SNR ratio branches more influential compared with the weaker branches on overall system performance. Diversity of a system can take several forms[19]:

Spacial diversity, also known as antenna diversity, creates several independent propagation pathways by using multiple antennas. Such a configuration is not limited to use in only transmission or reception but is applicable on both sides.

Pattern diversity uses two or more co-located antennas with different radiation patterns to discriminate the angle space with directional beams to achieve a higher gain over a single omnidirectional element.

Polarization diversity exploits the different polarization profiles of multipath waves. An example application might consist of two antennas, one horizontally polarized and one vertically polarized.

Frequency diversity is based on the concept of the channel coherence bandwidth. This notion determines the frequency range within which fading is considered flat, i.e. distortion of signal frequency components is strongly dependent. Transmitting the same signal simultaneously at carriers whose frequencies are offset by coherence bandwidth or more creates diversity branches.

Time diversity exploits the time-variance of the multipath pattern. Since the time moments are spaced apart by the coherence time or more, the fading patterns

may be treated as independent retransmission replicas with the same information. When selected at the appropriate time intervals this creates diversity branches.

Analysis of GPS as described in section 3.3 permits the application of each different type of diversity in certain situations and to varying degrees. As the GPS structure uses RHCP some gains may be made through the use of polarization diversity assuming that any interference source in linearly polarized. Due to the incomplete roll out of the civilian SPS L2 CL and L2 CM, non-PPS systems must rely on the L1 C/A service. This severely hinders if not prohibits the application of frequency diversity for civilian use. However, spacial diversity with an adequate element layout can mimic pattern diversity and is less limiting with regard to application despite its obvious disadvantage of a larger, more complex, and more costly footprint.

For the remainder of this thesis spatial diversity is assumed, and the spatial diversity is used as a building block without prohibiting the addition of polarization, time, or frequency diversity at a later time.

4.3 Direction of Arrival (DoA)

DoA, as the name implies, is the angle of a signal incident on a point in space. To better understand how the impinging signal relates to the antenna position a coordinate system is required to give a frame of reference.

4.3.1 Coordinate System

Using the three dimensional spherical coordinate system shown in Figure 4.1 the azimuth is defined as the angle ϕ in the XY plane measured counter clockwise at the origin from the positive X axis. Elevation is the angel θ measured between the positive Z axis and the XY plane.

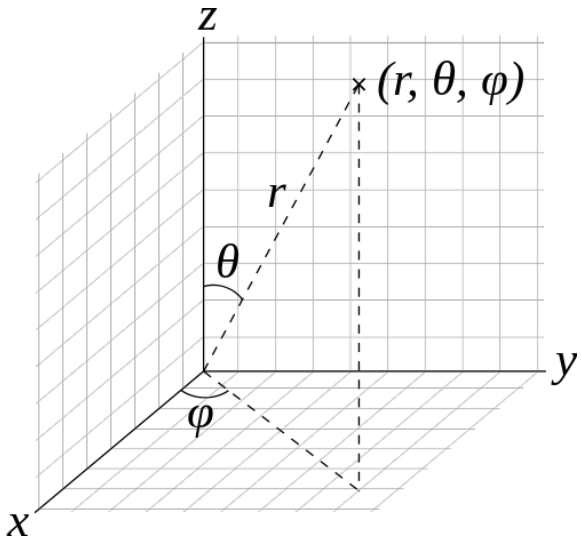

Figure 4.1: 3D Spherical Coordinates[1]

Therefore, any point n from in three dimensional space can be described by the spherical coordinate system using the notation:

$$\vec{\mathbf{r_n}} = r_n\hat{\mathbf{r}} + \theta_n\hat{\boldsymbol{\theta}} + \phi_n\hat{\boldsymbol{\phi}} \tag{4.1}$$

Similarly after a conversion, the same point n can be described by the Cartesian coordinate system:

$$\vec{\mathbf{r_n}} = x_n\hat{\mathbf{x}} + y_n\hat{\mathbf{y}} + z_n\hat{\mathbf{z}} \tag{4.2}$$

Applying this concept to GNSS, the XY plane is tangent to the earth's surface. The positive Z axis is the zenith at an angle $\theta = 0^\circ$ and the horizon is located at θ of 90°. If the N points in three dimensional space represent an antenna array in the far field condition (the phase difference is ≈ 0 so the impinging signal can be approximated by a plane wave) then the coordinates (x_n, y_n, z_n) are the phase center of nth antenna element in array with respect to the origin for $n = 0, 1, 2, \ldots$. The origin can be viewed as a reference element $\vec{\mathbf{r_e}} = 0\hat{\mathbf{x}} + 0\hat{\mathbf{y}} + 0\hat{\mathbf{z}}$ which does not need

to contain one of the n antenna elements. The signal from the M^{th} satellite S_m can be described by its angle of arrival from the vector formed between the point source and the origin. The angle ϕ_m is the azimuth and θ_m is the elevation angle measured from the zenith and is represented by[32]:

$$\vec{\mathbf{s}}_m = \sin(\theta_m)\cos(\phi_m)\hat{\mathbf{x}} + \sin(\theta_m)\sin(\phi_m)\hat{\mathbf{y}} + \cos(\theta_m)\hat{\mathbf{z}} \tag{4.3}$$

4.3.2 Incident Signal Phasing

As the incident signal $\vec{\mathbf{s}}_m$ impinges on the antenna array a phase offset occurs as the signal propagates across the array elements. If Δr is the distance the impinging waveform must travel from the element $\vec{\mathbf{r_n}}$ to the reference element $\vec{\mathbf{r_e}}$, τ is the time of propagation, then Φ_{nm} is the angle formed between the element $\vec{\mathbf{r}}_n$ and the incident signal. Distance is the time derivative of velocity. After variable rearrangement this leads to to following summarization:

$$\tau = \frac{\Delta r}{v} \tag{4.4}$$

$$v = \lambda_m f_m \tag{4.5}$$

$$\Delta r = d_{nm}\cos(\Phi_{nm}) \tag{4.6}$$

Given that the vector formed between the element and reference element can be expressed as $\vec{\mathbf{r}}_n - \vec{\mathbf{r}}_e = \Delta x_n\hat{\mathbf{x}} + \Delta y_n\hat{\mathbf{y}} + \Delta z_n\hat{\mathbf{z}}$ then the angle Φ_{nm} can be expressed as the dot product of the resultant vectors. After substitution and simplification this

yields the time delay:

$$\cos(\Phi_{nm}) = \frac{(\vec{\mathbf{r}}_n - \vec{\mathbf{r}}_e)\cdot \vec{\mathbf{s}}_m}{\|\vec{\mathbf{r}}_n - \vec{\mathbf{r}}_e\|\|\vec{\mathbf{s}}_m\|} \tag{4.7}$$

$$\cos(\Phi_{nm}) = \frac{\Delta x_n \sin(\theta_m)\cos(\phi_m) + \Delta y_n \sin(\theta_m)\sin(\phi_m) + \Delta z_n \cos(\theta_m)}{d_{nm}} \tag{4.8}$$

$$\tau = d_{nm}\left(\frac{\Delta x_n \sin(\theta_m)\cos(\phi_m) + \Delta y_n \sin(\theta_m)\sin(\phi_m) + \Delta z_n \cos(\theta_m)}{d_{nm}\lambda_m f_m}\right) \tag{4.9}$$

$$\tau = \frac{\Delta x_n \sin(\theta_m)\cos(\phi_m) + \Delta y_n \sin(\theta_m)\sin(\phi_m) + \Delta z_n \cos(\theta_m)}{\lambda_m f_m} \tag{4.10}$$

The time delay derivation proves useful when mathematically describing the mth satellite signal. Due to the narrowband data assumption in Section 4.1, the incident satellite signal on the array can be approximated by:

$$S_m(t) = \mathrm{a}(t-\tau_m)\cos(2\pi f_m(t-\tau_m) + \alpha_m) \tag{4.11}$$

$$S_m(t) \approx \mathrm{a}(t)\cos(2\pi f_m t + \alpha_m - 2\pi f_m \tau_m) \tag{4.12}$$

$$S_m(t) \approx \mathrm{a}(t)\cos\Bigg(2\pi f_m t + \alpha_m - 2\pi\frac{\Delta x_n \sin(\theta_m)\cos(\phi_m) + \Delta y_n \sin(\theta_m)\sin(\phi_m) + \Delta z_n \cos(\theta_m)}{\lambda_m}\Bigg) \tag{4.13}$$

$$S_m(t) \approx \mathrm{a}(t)\cos(2\pi f_m t + \alpha_m - \beta(\Delta x_n \sin(\theta_m)\cos(\phi_m) + \Delta y_n \sin(\theta_m)\sin(\phi_m) + \Delta z_n \cos(\theta_m))) \tag{4.14}$$

where $\beta = 2\pi/\lambda_m = 2\pi f_m/c$ and c is velocity of light. The difference in phase between satellite S_m's signal incident on element r_n in the array and reference element $\vec{\mathbf{r_e}}$ is described by:

$$\alpha_{nm} = \beta(\Delta x_n \sin(\theta_m)\cos(\phi_m) + \Delta y_n \sin(\theta_m)\sin(\phi_m) + \Delta z_n \cos(\theta_m)) \tag{4.15}$$

Using the real portion of Euler's formula, the satellite signal S_m can be reconstructed in phasor notation:

$$S_m(t) = \Re\Big\{ \mathrm{a}(t) e^{j(2\pi f_m t + \alpha_m)} \cdot e^{-j(\beta(\Delta x_n \sin(\theta_m)\cos(\phi_m) + \Delta y_n \sin(\theta_m)\sin(\phi_m) + \Delta z_n \cos(\theta_m)))} \Big\} \tag{4.16}$$

$$S_m(t) = \Re\Big\{ \mathrm{a}(t) e^{j(2\pi f_m t + \alpha_m)} e^{-j\alpha_{nm}} \Big\} \tag{4.17}$$

The incident signal and each element in array are assumed to be co-polarized so that polarization mismatch and subsequent loss do not occur upon reception of the signal. The modulation of the incident satellite signal is represented by its baseband complex envelope $\mathrm{a}(t)$. The non-corrupted signal $s(t)$ at output terminal of array manifold will be[32]:

$$S_m(t) = \mathrm{a}(t) \sum_{n=0}^{N-1} g_{na}(\theta_m, \phi_m, f_0) e^{j\alpha_{nm}} \tag{4.18}$$

where $g_{na}(\theta_m, \phi_m, f_0)$ is gain of nth array element along direction specified by (θ_m, ϕ_m). In practice the array gain $g_{na}(\theta_m, \phi_m, f_0)$ may not be the same for all elements. For optimum performance, it is necessary to accurately account for phase and amplitude weight contribution differences due to non-ideal construction techniques through calibration.

Operating under the assumption that all elements have identical radiation patterns and the same RHCP axial ratio then $S_m(t)$ can be simplified to:

$$S_m(t) = \mathrm{a}_m(t) g_a(\theta_m, \phi_m, f_0) f(\theta_m, \phi_m) \tag{4.19}$$

The term $f(\theta_m, \phi_m)$ is called the array factor; it determines the ratio of the received

signal at the array output to the signal at a central reference element. Following the assumption that all antenna elements have isotropic radiators from Section 4.1, Equation 4.19 can further be reduced to[32]:

$$S_m(t) = \mathrm{a}_m(t) f(\theta_m, \phi_m) \tag{4.20}$$

The satellite signal S_m impinging on the antenna array is received by all N elements and using equal weight combining is described by the sum:

$$S_m(t) = \mathrm{a}_m(t) \sum_{n=0}^{N-1} e^{j\alpha_{nm}} \tag{4.21}$$

In practice there are multiple signals. Following the superposition of signal waveforms blends the multiple signals and noise to form a vector of a single element over time interval leads to:

$$\vec{\mathbf{x}}_n(t) = \sum_{m=0}^{M-1} \mathrm{a}_m(t) e^{j\alpha_{nm}} + n_n(t) \tag{4.22}$$

Compressing Equation 4.22 to account for all N array elements provides a matrix solution:

$$\mathbf{x}(t) = \sum_{n=0}^{N-1} \sum_{m=0}^{M-1} \mathrm{a}_m(t) e^{j\alpha_{nm}} + n_n(t) \tag{4.23}$$

Although Equation 4.23 provides an accurate description of the physical process it does not blend itself to efficient modern computing. When compared to signal at the reference element, the phase differences can be represented in terms of a steering vector $\vec{\mathbf{a}}(\alpha_m)$. The steering vector describes the phase shift of the received signal due to the spatial separation of the array elements in vector or matrix form. The M

satellite signals over a snapshot t are described individually by the vector $\vec{\mathbf{S}}_m(t)$ and in entirety by the matrix $\mathbf{s}$. The matrix operations provide mathematical convenience but are also an optimized computing operation.

$$\vec{\mathbf{a}}(\alpha_m) = \begin{bmatrix} e^{j\alpha_{0m}} & e^{j\alpha_{1m}} & e^{j\alpha_{2m}} & \dots & e^{j\alpha_{(N-1)m}} \end{bmatrix}^T \tag{4.24}$$

$$\mathbf{a} = \begin{bmatrix} \vec{\mathbf{a}}(\alpha_0) & \vec{\mathbf{a}}(\alpha_1) & \cdots & \vec{\mathbf{a}}(\alpha_{M-1}) \end{bmatrix} \tag{4.25}$$

$$\vec{\mathbf{S}}_m(t) = \begin{bmatrix} S_m(0) & S_m(1) & \cdots & S_m(t-1) \end{bmatrix} \tag{4.26}$$

$$\mathbf{s} = \begin{bmatrix} \vec{\mathbf{S}}_0(t) & \vec{\mathbf{S}}_1(t) & \cdots & \vec{\mathbf{S}}_{M-1}(t) \end{bmatrix}^T \tag{4.27}$$

The matrix product of $\mathbf{a}$ and $\mathbf{s}$ with an additive noise or interference term describe the received signals incident on the array:

$$\mathbf{x}(t) = \begin{bmatrix} \vec{\mathbf{a}}(\alpha_0) & \vec{\mathbf{a}}(\alpha_1) & \cdots & \vec{\mathbf{a}}(\alpha_{M-1}) \end{bmatrix} \begin{bmatrix} \vec{\mathbf{S}}_0(t) \\ \vec{\mathbf{S}}_1(t) \\ \vdots \\ \vec{\mathbf{S}}_{M-1}(t) \end{bmatrix} + \mathbf{n}(t) \tag{4.28}$$

4.3.3 Subspace Estimation Techniques

Given a signal correlation matrix $\mathbf{R}_{ss}$, a noise common variance of σ_N^2, and an identity matrix $\mathbf{I}_M$ with rank M, the input data signal's covariance matrix takes the form[8]:

$$\mathbf{R}_{xx} = E[\vec{\mathbf{x}}(t)\vec{\mathbf{x}}^H(t)] \tag{4.29}$$

$$= \mathbf{A}\mathbf{R}_{ss}\mathbf{A}^H + \sigma_N^2\mathbf{I}_M \tag{4.30}$$

Given that the solution to the eigenvalue equation for $\mathbf{R}_{xx}$, reference Equation 4.31,

$$|\mathbf{R}_{xx} - \lambda_i \mathbf{I}_M| = 0 \tag{4.31}$$

produces the eigenvalues $\lambda_0, \cdots, \lambda_{(M-1)}$ and assuming that $\mathbf{A}\mathbf{R}_{ss}\mathbf{A}^H$ has the eigenvalues e_i, then the eigenvalues of e_i after substitution of and equating:

$$\left|\mathbf{A}\mathbf{R}_{ss}\mathbf{A}^H + \sigma_N^2 \mathbf{I}_M - \lambda_i \mathbf{I}_M\right| = 0 \tag{4.32}$$

yields:

$$e_i = \lambda_i - \sigma_N^2 \tag{4.33}$$

The matrix $\mathbf{A}$ is composed of steering vectors that are linearly independent, thus the matrix has full column rank. With incident signals that are not highly correlated, the signal correlation matrix $\mathbf{R}_{ss}$ is nonsingular. With these two conditions the number of incident signals d is less than the number of elements in the antenna array M and the matrix $\mathbf{A}\mathbf{R}_{ss}\mathbf{A}^H$ is positive semidefinite with rank d. This leads to the $M - d$ eigenvalues, e_i of $\mathbf{A}\mathbf{R}_{ss}\mathbf{A}^H$ are zero and are equal to the noise variance. This implies that using the number of elements in the array and the multiplicity of the smallest eigenvalue the number of incident signals is determined by $d = M - k$. The eigenvector associated with the particular eigenvalue λ_i, denoted as $\mathbf{q}_i$, satisfies:

$$(\mathbf{R}_{xx} - \lambda_i \mathbf{I}_M)\mathbf{q}_i = 0, i = d, d+1, \cdots, M-1 \tag{4.34}$$

for the eigenvectors associated with $M - d$ smallest eigenvalues. This is seen in

Equation 4.35.

$$(\mathbf{R}_{xx} - \sigma_i \mathbf{I}_M)\mathbf{q}_i = \mathbf{A}\mathbf{R}_{ss}\mathbf{A}^H\mathbf{q}_i + \sigma_N^2\mathbf{I}_M\mathbf{q}_i - \sigma_N^2\mathbf{q}_i \tag{4.35}$$

$$= \mathbf{A}\mathbf{R}_{ss}\mathbf{A}^H\mathbf{q}_i = 0 \tag{4.36}$$

Since $\mathbf{A}$ full rank and $\mathbf{R}_{ss}$ nonsingular, this implies that $\mathbf{A}^H\mathbf{q}_i = 0$. This means the eigenvectors associated with $M - d$ smallest eigenvalues are orthogonal to the d steering vectors that make up A. Thus:

$$\{\mathbf{a}(\theta_i), \ldots, \mathbf{a}(\theta_{d-1})\} \perp \{\mathbf{q}(\theta_d), \ldots, \mathbf{q}(\theta_{M-1})\} \tag{4.37}$$

Since the eigenvectors are orthogonal, one can estimate the steering vectors associated with the received signals by finding the steering vectors, which are orthogonal to $M - d$ eigenvectors associated with the eigenvalues of $\mathbf{R}_{xx}$ that are approximately equal to σ_N^2. This shows that eigenvectors of $\mathbf{R}_{xx}$ belong to either two orthogonal subspaces, one being principal or signal subspace and the other non principal or noise subspace.

4.3.3.1 Covariance Matrices

In the physical world, signals received by the antenna array are noise-corrupted where the noises are normally uncorrelated. The uncorrupted signals received by the different array elements are correlated as they originate from same sources. The spatial covariance matrix defined as:

$$\mathbf{R}_{xx} = E[\vec{\mathbf{x}}(t)\vec{\mathbf{x}}^H(t)] = \mathbf{A}\mathbf{R}_{ss}\mathbf{A}^H + \sigma_N^2\mathbf{I}_M \tag{4.38}$$

where $\vec{\mathbf{x}}(t)$ is the noise corrupted array signal snapshot at time t, $E[]$ is statistical expectation, $\mathbf{R}_{ss} = E[\vec{\mathbf{s}}(t)\vec{\mathbf{s}}^H(t)]$ is the signal covariance matrix, $\vec{\mathbf{s}}(t)$ is the signal snapshot at time t, and σ_N^2 is common variance of the noises.

Due to the difficulty in finding the exact covariance matrix $\mathbf{R}_{xx}$ from the limited number of data sets received and processed by the array, an estimation is made under the assumption that the random noises are ergodic. This allows the statistical expectation to be replaced by a time average[8]. This yields the time averaged estimate of data covariance matrix $\mathbf{R}_{xx}$:

$$\mathbf{R}_{xx} \approx \hat{\mathbf{R}}_{xx} \tag{4.39}$$

$$\hat{\mathbf{R}}_{xx} = \frac{1}{T}\sum_{t=0}^{T-1} \vec{\mathbf{x}}(t)\vec{\mathbf{x}}^H(t) \tag{4.40}$$

$$= \frac{1}{T}\mathbf{X}^H\mathbf{X} \tag{4.41}$$

where the noise corrupted array signal over a snapshot interval is represented as the matrix:

$$\mathbf{X} = \begin{bmatrix} \vec{\mathbf{x}}(0) & \vec{\mathbf{x}}(1) & \cdots & \vec{\mathbf{x}}(N-1) \end{bmatrix}^T \tag{4.42}$$

and $\vec{\mathbf{x}}(t), t = 0, 1, \ldots, T-1$ are the different snapshots in time.

4.3.3.2 Multiple Signal Classification (MUSIC)

To form the noise subspace used in determining the DoA, a matrix containing the noise eigenvectors is created:

$$\mathbf{V}_n = \begin{bmatrix} \mathbf{q}_{d+i} & \cdots & \mathbf{q}_M \end{bmatrix} \tag{4.43}$$

Since the steering vectors corresponding to signal components are orthogonal to noise subspace eigenvectors, $\mathbf{a}^H(\theta,\phi)\mathbf{V}_n\mathbf{V}_n^H\mathbf{a}(\theta,\phi) = 0$ for $\theta = \theta_i, \phi = \phi_i$ corresponding to

DoA of incoming signal. By taking the inverse, the spectrum is created where the d largest peaks correspond to the DoA estimates of the multiple impinging signals on the antenna array:

$$P_{MUSIC}(\theta, \phi) = \frac{1}{\mathbf{a}^H(\theta, \phi)\mathbf{V}_n\mathbf{V}_n^H\mathbf{a}(\theta, \phi)} \tag{4.44}$$

The MUSIC direction of arrival estimation algorithm can be broken down into five steps[8]:

1. Collect input samples $\mathbf{x}(t_n)$ and estimate input covariance matrix:
   $\hat{\mathbf{R}}_{xx} = \frac{1}{T}\mathbf{X}^H\mathbf{X}$
2. Perform eigenvalue decomposition on $\hat{\mathbf{R}}_{xx}$:
   $\hat{\mathbf{R}}_{xx}\mathbf{V} = \mathbf{V}\mathbf{\Lambda}, \{\mathbf{\Lambda} = \text{diag}\{\lambda_0, \ldots, \lambda_{M-1}\} | \lambda_0 \geq \lambda_1 \geq \ldots \geq \lambda_{M-1}\}$
3. Estimate the multiplicity of the k smallest eigenvalues λ_{min} and the number of signals d:
   $d = M - k$
4. Form the noise space matrix and compute MUSIC spectrum:
   $$\mathbf{V}_n = \begin{bmatrix} \mathbf{q}_{d+1} & \cdots & \mathbf{q}_M \end{bmatrix}$$
   $$P_{MUSIC}(\theta, \phi) = \frac{1}{\mathbf{a}^H(\theta, \phi)\mathbf{V}_n\mathbf{V}_n^H\mathbf{a}(\theta, \phi)}$$
5. Locate the d largest peaks of $P_{MUSIC}(\theta, \phi)$ to obtain DoA estimates

4.4 Beamsteering

Beamsteering, also known as beamforming, is the process of steering one or more high-gain antenna beams toward a SOI while using antenna nulling to steer the antenna beam way from a SNOI using the spatial separation or antenna spatial diversity. The mechanics behind the steering can utilize a change in the array pattern

in addition to changing its orientation. By increasing gain in the direction of the SOI the SNR ratio increases, and conversely by moving the effective antenna pattern away from SNOI the external interference decreases[32].

In a parallel concept to the signal arrival on the antenna array being represented by a steering vector that describes the phase shifts of the impinging signal on the array, the same principal concept of a steering vector allows the main beam of the antenna array to be steered in the direction (θ_s, ϕ_s) of SOI using a complex weight vector $\mathbf{w}$ that contains both a magnitude and phase. Instead of describing the phase shifts of the incoming signal, the beamsteering weight signal vector describes the necessary phase shifts to move the main antenna beam in the desired direction, adjust the side lobes[32], and combine the signal from the array elements to form a single output signal $y(t)$[8]. Several types of combining techniques exist with equal weighting being the most simplistic. With equal weighting the weight vector's magnitude is uniform from element to element.

Beamsteering consists of two types: conventional and adaptive. In a conventional beamsteering environment the steering vector and subsequent antenna array pattern are stationary. In the adaptive configuration the steering vector and subsequent antenna pattern adjust to changes in the environment affecting the received signals.

In either case, the weight vector $\mathbf{w}$ requires a slight modification of the phasing description when compared to α_{nm} in Equation 4.15. A change in variable from m to i is made to reflect that the phasing equation is not limited to the M satellite

signals but can be used to steer in the direction of SOI or away.

$$\beta = \frac{2\pi}{\lambda_i} = \frac{2\pi f_i}{c} \tag{4.45}$$

$$\mu_{ni} = \beta(\Delta_{x_n}\sin(\theta_i)\cos(\phi_i) + \Delta_{y_n}\sin(\theta_i)\sin(\phi_i) + \Delta_{z_n}\cos(\theta_i)) \tag{4.46}$$

$$\vec{\mathbf{w}}(\mu_{ni}) = \begin{bmatrix} w_{0i}e^{j\mu_{0i}} & w_{1i}e^{j\mu_{1i}} & w_{2i}e^{j\mu_{2i}} & \cdots & w_{(N-1)i}e^{j\mu_{(N-1)i}} \end{bmatrix}^T \tag{4.47}$$

To recover a single signal i, the weight vector is composed of a single phasing vector as shown below:

$$\mathbf{w} = \begin{bmatrix} \vec{\mathbf{w}}(\mu_{ni}) \end{bmatrix} \tag{4.48}$$

$$\vec{\mathbf{y}}(t) = \mathbf{w}^H\mathbf{x}(t) \tag{4.49}$$

If multiple signals are recovered at once then the weight vector $\mathbf{w}$ is extended to include all the SOI. As long as the SOI does not exceed the number of antenna elements N the matrix mathematics hold:

$$\mathbf{w} = \begin{bmatrix} \vec{\mathbf{w}}(\mu_{n0}) & \vec{\mathbf{w}}(\mu_{n1}) & \cdots & \vec{\mathbf{w}}(\mu_{(N-1)1}) \end{bmatrix} \tag{4.50}$$

$$\mathbf{y}(t) = \mathbf{w}^H\mathbf{x}(t) \tag{4.51}$$

4.4.1 Digital Beamsteering

In analog beamsteering the steering vectors are implemented and controlled via attenuators and phase shifters in the RF section between the antenna elements. Further analog processing or subsequent combining may occur before digitation of the signal through a single ADC. Analogous to analog beamsteering, digital beamsteering transforms an effective array pattern through numerical computations of the weight

vector changing the magnitude and phase of each digitized array element.

Digital beamsteering has the advantages of a more simplistic RF front end with the cost of an ADC at the end of each antenna element chain. Analog beamsteering can remain completely analog or only require one ADC if combining is completed before digitization. The total averaged output power over T snapshots of the array[26]:

$$P(\mathbf{w}(t)) = \frac{1}{T}\sum_{t=0}^{T-1}|y(t)|^2 = \frac{1}{T}\sum_{t=0}^{T-1}\mathbf{w}^H\mathbf{x}(t)\mathbf{x}^H(t)\mathbf{w} = \mathbf{w}(t)^H\hat{\mathbf{R}}_{xx}\mathbf{w}(t) \tag{4.52}$$

4.5 Array Factor

The array factor provides an equivalence radiation pattern produced by the combination of the individual antenna elements. The complex array factor or array pattern function for N isotropic point sources $\mathbf{r}_n$ is described by[43]:

$$F(\theta,\phi) = \sum_n I_n e^{jk\hat{\mathbf{r}}\cdot\mathbf{r}_n} \tag{4.53}$$

where I_n is the relative complex excitation to the nth element, $k = 2\pi/\lambda$, $\hat{\mathbf{r}} = \sin(\theta)\cos(\phi)\hat{\mathbf{x}} + \sin(\theta)\sin(\phi)\hat{\mathbf{y}} + \cos(\theta)\hat{\mathbf{z}}$ is the position vector of the observation point, and $\mathbf{r}_n$ is the position vector of the nth antenna element. By sweeping (θ,ϕ) from $\{\theta|0 \geq \theta > 2\pi\}$ and $\{\phi|-\frac{\pi}{2} \geq \phi \geq \frac{\pi}{2}\}$ respectively, a three dimensional array pattern is obtained. The pattern is modified via beamsteering, referring to Section 4.4, by adding an additional term to Equation 4.53 shown below[5]:

$$F(\theta,\phi) = \sum_n I_n e^{jk\hat{\mathbf{r}}\cdot\mathbf{r}_n}e^{-jk\boldsymbol{\mu}_m} \tag{4.54}$$

This is reduced to:

$$F(\theta,\phi) = \sum_n I_n e^{jk(\hat{\mathbf{r}}\cdot\mathbf{r}_n-\boldsymbol{\mu}_m)} \tag{4.55}$$

4.6 Synthetic Aperture Array

One of the key limitations of constructing hardware-based phased arrays is that a narrowing of the array beamwidth requires an increase in the physical size of the array. This limitation can be overcome by applying synthetic array principles. Generation of a synthetic GNSS antenna array is conceptually similar to Synthetic Aperture Radar (SAR) where antenna motion is utilized to increase the antenna aperture and azimuthal resolution. The synthetic array is synthesized by observing an antenna through samples at different locations in time. The sampling process requires the samples to be taken a certain distance apart, in general a half-wavelength, to reduce aliasing effects, which are then combined for array processing[36]. During the data collection process, the receiver collects the impinging signal with different phases at different instances in time using the sampling process occurring while the antenna is repositioned or after[4].

The sampling process collected by the antenna can be divided into batches of M equal parts. If the communication channel remains stationary during the data collection interval then the sample blocks used for beam steering and DoA estimation (spatial signal processing) can be asynchronous in time, as shown in Figure 4.2. The stationary communication channel permits the synthetic aperture array sampling[23]. Figure 4.3 provides a better understanding how a stationary object creates a synthetic array of a moving object by sampling at different instances in time and combining the samples during processing.

A synthetic array has the benefit of not being affected by inter-channel phases, gains and mutual coupling between antenna elements. Therefore, a single element synthetic array does not require calibration. The number of antenna elements affects the accuracy of the DoA estimation. A larger quantity of effective elements

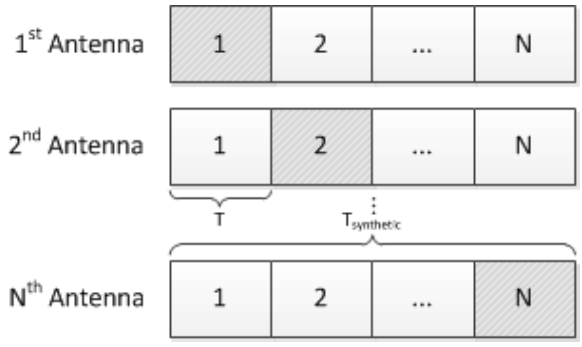

Figure 4.2: Synthetic Aperture Sampling

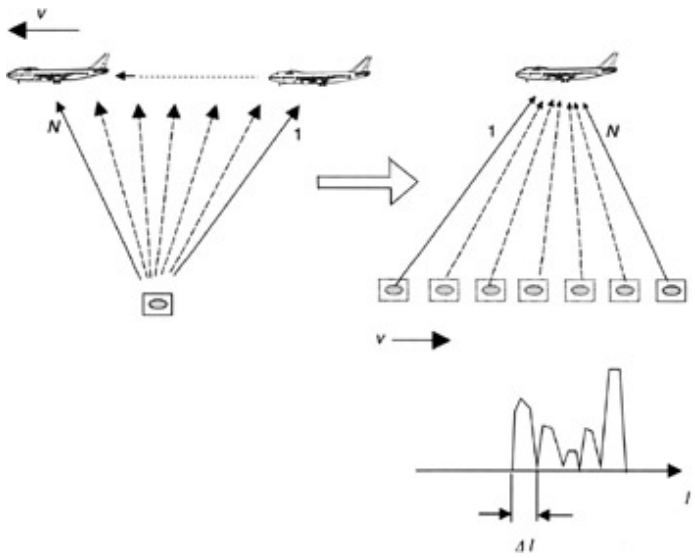

Figure 4.3: Synthetic Aperture[42]

results in an increased estimation accuracy. The Cramer-Rao lower bound criteria of DoA estimation predicts that if the distance among the sensors is long then the estimation accuracy is improved, however, antenna aliasing limits the sensors to half of wavelength. Also, the narrow-band assumption further restricts the diameter of the array[4].

4.7 Directivity

Directivity of an antenna is defined as ratio of the power radiated in one direction to the radiated power of an omnidirectional antenna in same direction when both antennas radiate the same total power. In essence, directivity is the measure of radiated power in a certain direction compared to a reference element. Antenna directivity is an important system parameter as it is related to antenna gain. Antenna gain in a certain direction is a product of the directivity of the antenna and of the antenna efficiency[8]. Maximum directivity D is a measure of the concentration of the main beam and is defined as the maximum power over the average power of the antenna.

$$D = \frac{P(\theta,\phi)|_{\max}}{P_{ave}} \tag{4.56}$$

$$P_{\max}(\theta,\phi) = U(\theta,\phi)|_{\max} \tag{4.57}$$

$$P_{ave} = \frac{1}{4\pi}\int_0^{2\pi}\int_0^{\pi} U(\theta,\phi)\sin(\theta)d\theta d\phi \tag{4.58}$$

$$D = \frac{U(\theta,\phi)|_{\max}}{\frac{1}{4\pi}\int_0^{2\pi}\int_0^{\pi} U(\theta,\phi)\sin\theta d\theta d\phi} \tag{4.59}$$

where the power is a function of the radiation intensity $U(\theta, \phi)$[8]. After normalization the maximum directivity changes[21].

$$D = \frac{4\pi}{\int_0^{2\pi}\int_0^{\pi} \frac{U(\theta,\phi)}{U(\theta,\phi)_{max}} \sin(\theta) d\theta \; d\phi} \tag{4.60}$$

$$P_n(\theta, \phi) = \frac{U(\theta, \phi)}{U(\theta, \phi)_{max}} \tag{4.61}$$

$$D = \frac{4\pi}{\int_0^{2\pi}\int_0^{\pi} P_n(\theta, \phi) \sin(\theta) d\theta \; d\phi} \tag{4.62}$$

For antenna arrays the radiation intensity is a function of the array factor where the radiation intensity is $U_{tot}(\theta, \phi) = |AF(\theta, \phi)|^2 U(\theta, \phi)$[28]. After substitution, the maximum directivity of an antenna array is controlled by the absolute value of the array factor squared.

$$D = \frac{4\pi}{\int_0^{2\pi}\int_0^{\pi} |F_n(\theta, \phi)|^2 \sin(\theta) d\theta \; d\phi} \tag{4.63}$$

5. CONTRIBUTIONS

5.1 Phase Detection

Due to standard digitization practices, as an incoming signal arrives at the antenna center and traverses through the RF front end the phase component of the signal is lost. Without additional circuitry or other recovery techniques the phase component of the signal is lost in the sampling process. One common phase recovery technique is known as IQ, however method is not without its short comings.

5.1.1 In-Phase and Quadrature (IQ)

To obtain the phase by IQ, discussed in Section 2.5.1, the phase component $\phi(t)$ is better described by the time delayed signal on each array element compared to the reference is described by:

$$\tau_i = \frac{1}{c}(\delta_{x_i}\sin(\theta)\cos(\phi) + \delta_{y_i}\sin(\theta)\sin(\phi) + \delta_{z_i}\cos(\theta)) \tag{5.1}$$

$$s_i(t) = \mathrm{a}(t-\tau_i)\sin(2\pi f_c(t-\tau_i)) \tag{5.2}$$

Following a similar procedure, the IQ components of the time delayed signal applying the trigonometric identity $\sin(\alpha)\cos(\beta) = \frac{1}{2}(\sin(\alpha+\beta)+\sin(\alpha-\beta))$ for

the quadrature branch are respectively described by:

$$IF_{Q_i}(t) = \mathrm{a}(t-\tau_i)\sin(2\pi f_c(t-\tau_i))\cos(2\pi f_{LO}t) \tag{5.3}$$

$$= \frac{1}{2}\mathrm{a}(t-\tau_i)\sin(2\pi f_c(t-\tau_i)+2\pi f_{LO}t)+ \frac{1}{2}\mathrm{a}(t-\tau_i)\sin(2\pi f_c(t-\tau_i)-2\pi f_{LO}t) \tag{5.4}$$

$$= \frac{1}{2}\mathrm{a}(t-\tau_i)\sin(2\pi(f_c+f_{LO})t-2\pi f_c\tau_i)+ \frac{1}{2}\mathrm{a}(t-\tau_i)\sin(2\pi(f_c-f_{LO})t-2\pi f_c\tau_i) \tag{5.5}$$

After low pass filtering to remove the high frequency $f_c + f_{LO}$ content leaves the quadrature component:

$$Q_i(t) = \frac{1}{2}\mathrm{a}(t-\tau_i)\sin(2\pi(f_c-f_{LO})t-2\pi f_c\tau_i) \tag{5.6}$$

In a similar manner to obtain the in-phase component, using the trigonometric identity $\sin(\alpha)\sin(\beta) = \frac{1}{2}(\cos(\alpha-\beta)-\cos(\alpha+\beta))$ allows the substitution for in-phase branch:

$$IF_{I_i}(t) = \mathrm{a}(t-\tau_i)\sin(2\pi f_c(t-\tau_i))\sin(2\pi f_{LO}t) \tag{5.7}$$

$$= \frac{1}{2}\mathrm{a}(t-\tau_i)\cos(2\pi f_c(t-\tau_i)-2\pi f_{LO}t)- \frac{1}{2}\mathrm{a}(t-\tau_i)\cos(2\pi f_c(t-\tau_i)+2\pi f_{LO}t) \tag{5.8}$$

$$= \frac{1}{2}\mathrm{a}(t-\tau_i)\cos(2\pi(f_c-f_{LO})t-2\pi f_c\tau_i)- \frac{1}{2}\mathrm{a}(t-\tau_i)\cos(2\pi(f_c+f_{LO})t-2\pi f_c\tau_i) \tag{5.9}$$

After low pass filtering to remove the high frequency content $f_c + f_{LO}$ this yields the

in-phase signal:

$$I_i(t) = \frac{1}{2}\,\mathrm{a}(t-\tau_i)\cos(2\pi(f_c - f_{LO})t - 2\pi f_c\tau_i) \tag{5.10}$$

If the carrier f_c and the local oscillator f_{LO} are perfectly matched the filtered in-phase and quadrature signals allow a further cancellation.

$$\begin{aligned}
\phi_i(t) &= \tan^{-1}\frac{Q_i(t)}{I_i(t)} && (5.11)\\
&= \tan^{-1}\frac{\frac{1}{2}\,\mathrm{a}(t-\tau_i)\sin(2\pi(f_c - f_{LO})t - 2\pi f_c\tau_i)}{\frac{1}{2}\,\mathrm{a}(t-\tau_i)\cos(2\pi(f_c - f_{LO})t - 2\pi f_c\tau_i)} && (5.12)\\
&= \tan^{-1}\frac{\sin(2\pi(f_c - f_{LO})t - 2\pi f_c\tau_i)}{\cos(2\pi(f_c - f_{LO})t - 2\pi f_c\tau_i)} && (5.13)\\
&= \tan^{-1}\frac{\sin(-2\pi f_c\tau_i)}{\cos(-2\pi f_c\tau_i)} && (5.14)
\end{aligned}$$

However, when the local oscillator f_{LO} is unable to match the phase of the carrier f_c no cancellation occurs, and the recovered phase is equal to $\phi_i(t) = 2\pi(f_c - f_{LO})t - 2\pi f_c\tau_i$. This results in an oscillating error or bias on the actual phase at a frequency of $f_c - f_{LO}$. If the oscillation is slow subspace processing techniques may be able to still function with relatively little error. However, a fast oscillation makes the processing techniques unusable.

5.1.2 Correlation Based Phase Determination and Recovery

For the periodic function incident signal $x(t) = \cos(\omega t)$ and the local signal replica $y(t) = \cos(\omega t)$ with perfectly aligned frequency and phase their correlation,

described by Equation 5.15, is maximum with zero lag between them.

$$R_{xy}(t) = \frac{1}{2\pi}\int_0^{2\pi} x(\tau)y^*(\tau - t)\ d\tau \tag{5.15}$$

$$= \frac{1}{2\pi}\int_0^{2\pi} \cos(\omega\tau)\cos(\omega(\tau - t))\ d\tau \tag{5.16}$$

$$R_{xy_{max}} = \max\{R_{xy}|0 \leq t \leq 2\pi\} = R_{xy}(0) \tag{5.17}$$

If the periodic function incident signal $\bar{x}(t) = \cos(\omega t)$ and the local signal replica $\bar{y}(t) = \cos(\omega t - \alpha)$ with perfectly aligned frequency differ by a phase α then their maximum correlation is no longer described by the zeroth lag. Maximum correlation is achieved when the lag is equivalent to the phase over the angular velocity as described by:

$$R_{\bar{x}\bar{y}}(t) = \frac{1}{2\pi}\int_0^{2\pi} \bar{x}(\tau)\bar{y}^*(\tau - t)\ d\tau \tag{5.18}$$

$$= \frac{1}{2\pi}\int_0^{2\pi} \cos(\omega\tau)\cos(\omega(\tau - t) - \alpha)\ d\tau \tag{5.19}$$

$$R_{xy}(0) = R_{\bar{x}\bar{y}}(t) \tag{5.20}$$

$$\frac{1}{2\pi}\int_0^{2\pi} \cos(\omega\tau)\cos(\omega(\tau - t))\ d\tau = \frac{1}{2\pi}\int_0^{2\pi} \cos(\omega\tau)\cos(\omega(\tau - t) - \alpha)\ d \tag{5.21}$$

$$\omega\tau = \omega\tau - \omega t - \alpha \tag{5.22}$$

$$\omega t = -\alpha \tag{5.23}$$

Therefore, if both the angular velocity ω and the correlation lag t are known then the phase α can be calculated.

As seen previously, convolution or correlation of periodic functions is a form of

circular convolution. This allows the transformation into the discrete domain.

$$\bar{x}(n) = \cos(\omega n) \tag{5.24}$$

$$\bar{y}(n) = \cos(\omega n - \alpha) \tag{5.25}$$

$$R_{xy}(l) = \frac{1}{KN} \sum_{n=0}^{N-1} \cos(\omega n) \cos(\omega (n-l)_N - \alpha), l \in \mathbb{N} \tag{5.26}$$

$$\Rightarrow \omega l = -\alpha \tag{5.27}$$

In the discrete domain, the maximum resolution or accuracy tied to the sampling frequency.

$$Res_{max} = \omega T_s = 2\pi f_c T_s \tag{5.28}$$

The initial examination of the phase recovery through correlation of signals between a reference antenna element assumed that all signals were sampled at RF due to the phase shift in the signal induced by using the heterodyne process to convert the signal to baseband. Provided an infinitely fast ADC exists or at least one able to provide the desired precision or resolution and an ability to separate the signals to appear that only one source is incident on the array, one can recover the phase of the incident signal using correlation to determine the lag associated with the maximum correlation. From the lag associated with the maximum correlation and the angular velocity ω, one can recover the phase from Equation 5.27 with the error or precision dependent on the sampling frequency $f_s = 1/T_s$

5.2 The Measurement System

The measurement system platform consists of a GN3Sv3 developed by the University of Colorado at Boulder with a single Antenna Factor L1 SH series antenna

front end. The GN3Sv3 is a GPS and GNSS SDR front end with known support for SoftGPS[31], a software-defined GPS and Galileo receiver. The SDR was used to down-mix the satellite signal and oversample the C/A code by a factor of 16. For processing the GPS signal recorded by the GN3Sv3, a heavily modified version of the SoftGPS SDR was used. The stock code generated by Plausinaitis[31] was augmented to incorporate the GN3Sv2 and GN3Sv3[14] changes before any user modifications were made. The GN3Sv3 is depicted if Figure 5.1.

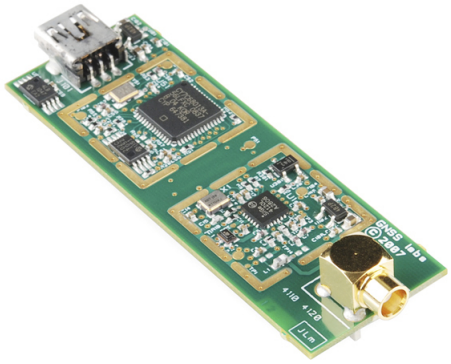

Figure 5.1: GN3Sv3 Software Defined Radio Front End[37]

The SDR front end was used to sample real-world (not simulated) GPS data. Due to hardware limitations and time constraints the sampled data was used to generate the simulated GPS data for the antenna array by pulling out the carrier frequency, code frequency, code offset, PRN, direction of arrival, and navigation data for each indecent signal. This information was used in the reconstruction of the signal for the simulation. The SVs recovered along with their DoA are shown in Figure 5.2, and their exact coordinates are listed in Table 5.1.

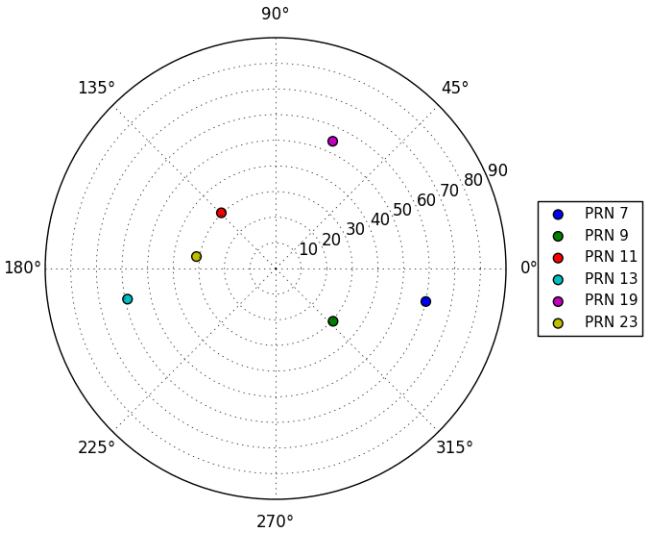

Figure 5.2: Signal of Interest (SOI) Nominal Direction of Arrival (DoA)

Table 5.1: Signal of Interest (SOI) Nominal Direction of Arrival (DoA)

PRN #	**Elevation** (θ)	**Azimuth** (ϕ)
7	60.0821	347.6239
9	30.4455	317.4980
11	30.3415	134.3163
13	59.0587	191.6564
19	54.3909	65.7848
23	31.2717	171.4422

5.2.1 Global Positioning System (GPS) Synthetic Aperture Array

The importance of a stationary communication channel for a synthetic aperture array was previously in Section 4.6. Unfortunately, the GPS propagation channel is not stationary due to the non-static position of the GNSS SVs and the differing clock drifts of the satellite and receiver clocks. To perform spatial processing, thus permitting a synthetic aperture sampling, the phase and Doppler changes due to the

satellite motion and clock drifts must be compensated prior to de-correlation and subsequent beamsteering. Provided that the location of the antenna is known at the sampling intervals, the satellite motion and clock drift rate can be compensated using the recovered ephemeris information provided that the navigation data is wiped off prior to synthetic array processing. Even if the navigation data is wiped off for synthetic array processing, the navigation data can be obtained from a sign estimate of the prompt correlator output at the post-correlation level following the tracking phase. At the pre-correlation level, external navigation data aiding is required[23]

To satisfy the stationary communication system criterion after compensating for phase and Doppler changes, there are several periodicities that might be used for creating the synthetic aperture array which are as follows.

- PRN code (every 1ms for C/A)
- Data pseudo periodic (every 12.5 minutes)
- Data header (every 6 sec)
- Telemetry Word (TLM)
  - 8 bit preamble
  - 16 bit reserved
  - 6 bit parity

Given the C/A PRN code's high periodicity, ease of synchronization, low processing overhead, and unique identifying signature it makes an ideal choice. As the C/A PRN repeats every 1 ms, synchronization must be maintained between the spreading sequence and the synthetic aperture antenna array. Due to the navigation data rate, a data bit is only guaranteed to maintain stable for 20 code cycles; this imposes an

upper limit on the maximum sample size for the synthetic array to maintain stationarity without data wipe-off. By performing navigation data wipe-off post correlation and feeding back the sign estimate post signal combining and beamsteering, it is possible of surpass the restriction imposed by the data rate on the maximum number of antenna elements in a sample and the maximum dwell time. Removing the maximum element restriction makes it possible to achieve higher accuracy DoA at the expense of higher system complexity.

Provided that the GPS receiver system is not fixed to a stationary position, the spatial diversity in a single antenna synthetic aperture system is dictated by the system's trajectory or lack thereof. This restriction is better illustrated in figure 5.3. By incorporating multiple antennas or a multiple antenna switched feed network in

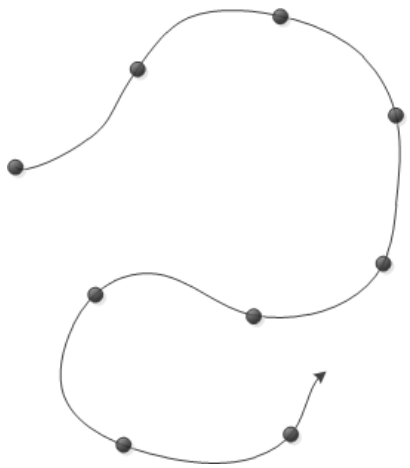

Figure 5.3: Trajectory of Synthetic Aperture Single Antenna

the synthetic aperture array the trajectory restriction is removed. The absence of a trajectory requirement extends the system to stationary position applications as well. Figure 5.4 provides a visualization of how spatial diversity is improved over the

single antenna design.

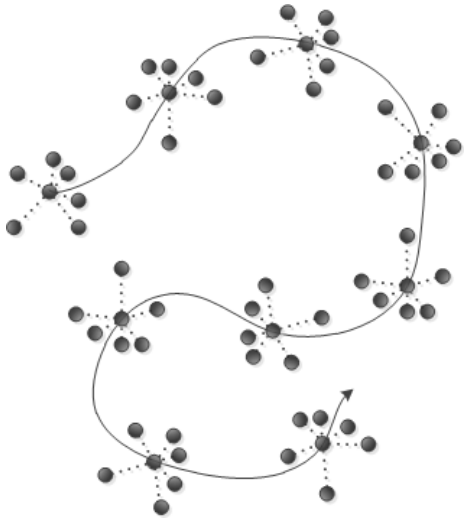

Figure 5.4: Trajectory of Synthetic Aperture Multiple Antennas

Using the switched feed antenna network permits the use of a single GPS receiver. The antennas are switched in a cyclic or semi-cyclic manner to build up the synthetic aperture array data matrix. Figure 5.5 provides a conceptual diagram of the switch feed antenna front end in conjunction with the receiver system.

5.2.2 Beamsteering

Because the system uses signal processing to emulate the effective aperture or antenna array pattern, assuming that each combined signal can be separated into its individual SOI, then it is possible to beamsteer a highly directive beam in one direction at a time but simultaneously for all SOI. In analog beamsteering the array pattern would have to simultaneously point in all the directions related to the SOI, otherwise all of the SOIs would not simultaneously be received. This restriction is removed when performing pure digital beamsteering.

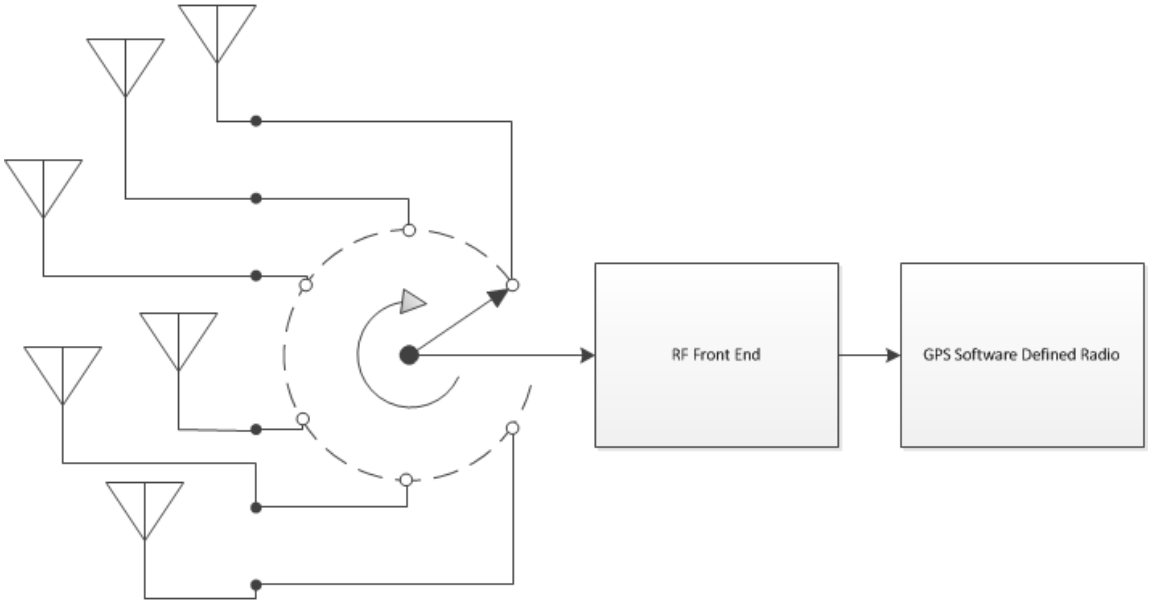

Figure 5.5: Synthetic Switched Array Block Diagram Overview

5.2.3 Detailed System

Figure 5.6 provides more details into the inter workings of the SDR synthetic aperture receiver after putting all of the pieces together: synthetic array switched network, direction finding algorithm components, and the receiver.

5.3 Evaluation Scenarios

Several scenarios ranging from element spacing, to interference position, to noise level were considered in the evaluation of the effectiveness of the different array types.

5.3.1 Array Element Spacing

Simulations varying the array spacing from λ, $\lambda/2$, $\lambda/4$, and $\lambda/10$ were performed, where aliasing occurs with element spacing over $\lambda/2$. This provides a gauge of performance from both ends of the element spacing spectrum.

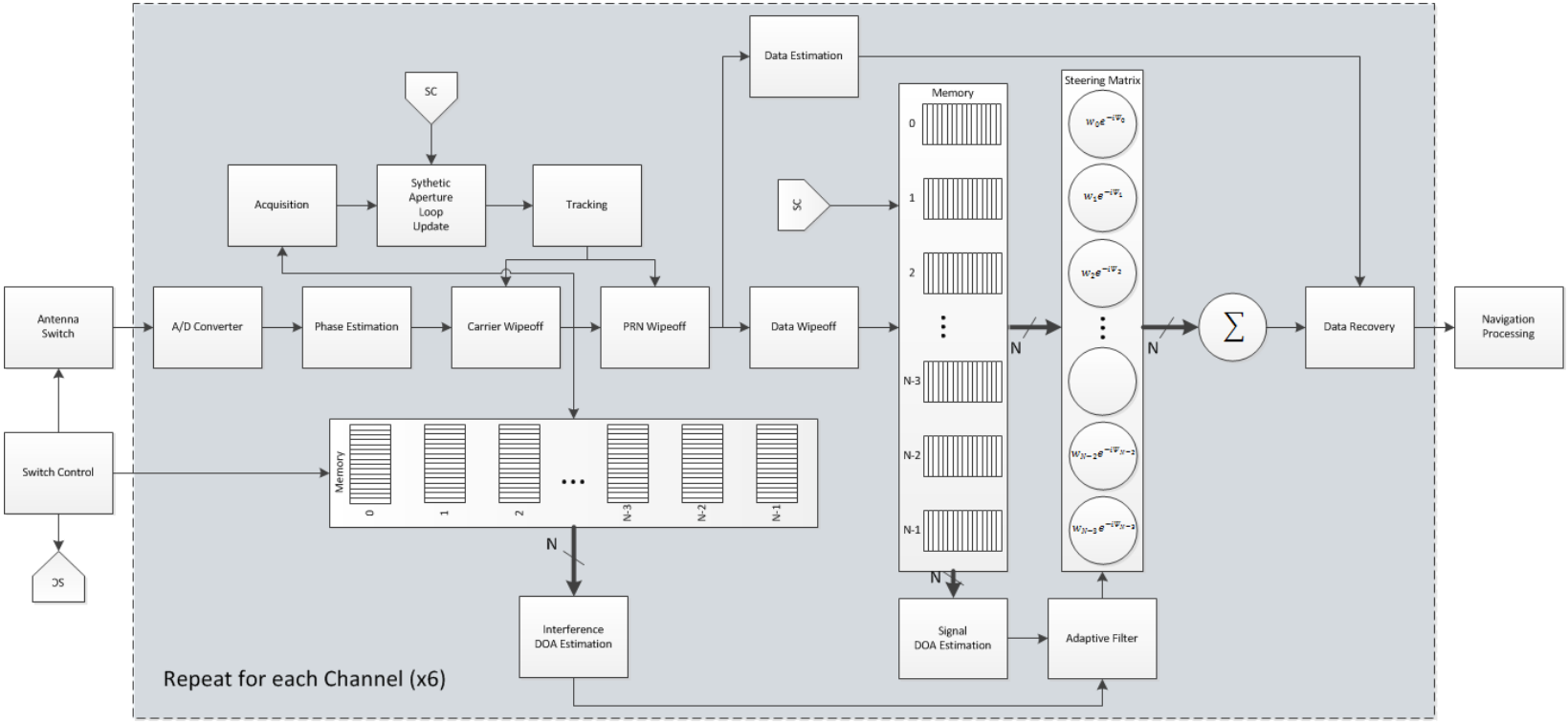

Figure 5.6: Synthetic Switched Array Receiver Block Diagram

5.3.2 Noise Level

The noise level was evaluated at two different levels using complex AWGN. A noise temperature of 513 K, a typical effective noise temperature for a receiver[15], over a 6 MHz bandwidth was the control. A second elevated noise temperature of 2052 K, or four times a typical temperature, was also used.

5.3.3 Interference Position

The interference scenarios consisted of two different models. The first model was orchestrated as a CW jammer low on the horizon to mimic a simplistic non-airborne interference source. The second scenario combines two different tests the immunity of DoA and beamsteering to directional interference: in the relative proximity to a legitimate signal; and to an overhead interference source. The low on the horizon CW_0 jammer is located at $\theta_{int} = 70.0°, \phi_{int} = 140.0°$. The jammer's relative proximity to the legitimate signal sources is depicted in Figure 5.7 and Table 5.2.

Table 5.2: Signal of Interest (SOI) Nominal Direction of Arrival (DoA) for CW_0

PRN #	**Elevation** (θ)	**Azimuth** (ϕ)
7	60.0821	347.6239
9	30.4455	317.4980
11	30.3415	134.3163
13	59.0587	191.6564
19	54.3909	65.7848
23	31.2717	171.4422
CW	70.0000	140.0000

The second interference model consists of a CW_1 jammer located at $\theta_{int} = 65.5°, \phi_{int} = 342.0°$, which is shown in Figure 5.8 and Table 5.3.

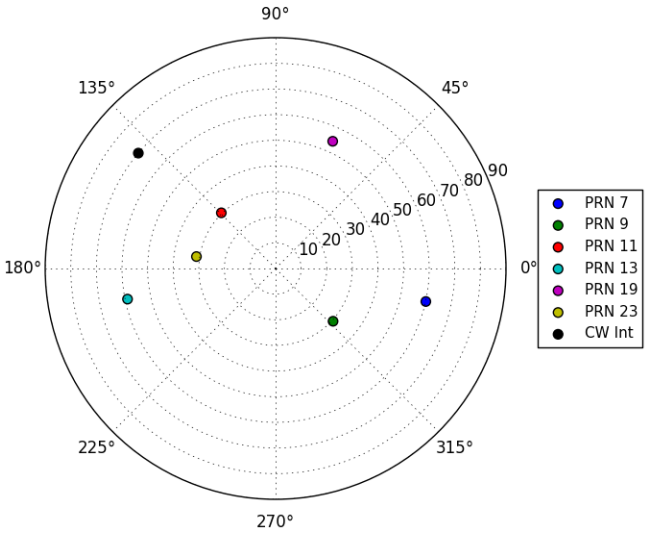

Figure 5.7: Signal of Interest (SOI) and CW_0 Interference Nominal Direction of Arrival (DoA)

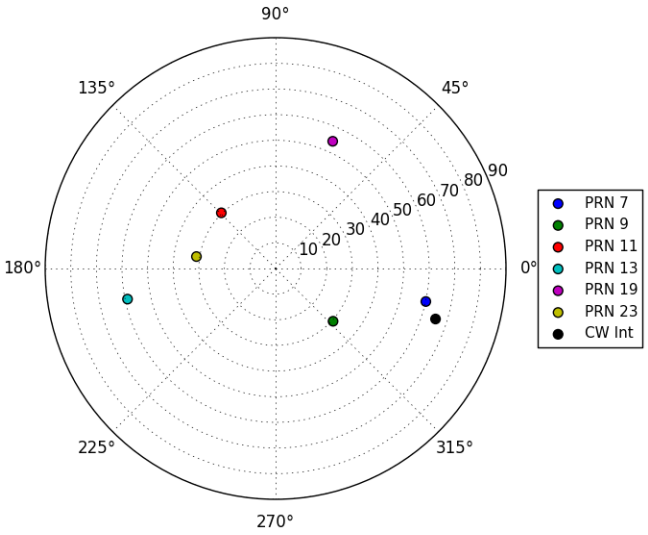

Figure 5.8: Signal of Interest (SOI) and CW_1 Interference Nominal Direction of Arrival (DoA)

Table 5.3: Signal of Interest (SOI) Nominal Direction of Arrival (DoA) for CW_1

PRN #	**Elevation** (θ)	**Azimuth** (ϕ)
7	60.0821	347.6239
9	30.4455	317.4980
11	30.3415	134.3163
13	59.0587	191.6564
19	54.3909	65.7848
23	31.2717	171.4422
CW	65.5000	342.5000

5.4 Expected Results

In the worst case, an oversampled 3 dB spread GPS signal power $P_{3\text{dB}}$ of -158.5 dBW across 16 MHz was calculated to be -130.5 dBW. After a 6 MHz bandpass filter, the remaining signal power was -130.656 dBW. The noise, as described in Section 2.6.2, at a noise temperature of 513 K and a bandwidth of 6 MHz was -133.6177 dBW. The CW interference power was -120 dBW aligned with the spectral power of the spread spectrum spreading sequence. Following the DSSS processing gain from Section 2.4.2, the processing gain assuming an ideal low pass filter is described by

$$P_g = \frac{BW_{chip}}{BW_{data}} \tag{5.29}$$

$$P_g = \frac{6 \text{ MHz}}{100 \text{ Hz}} = 60,000 = 47.78 \text{ dB} \tag{5.30}$$

The despreading process shifts the DSSS signal into the data bandwidth. Since the spread signal power is equivalent to the despread signal power in the data bandwidth there is no change in signal power. Signal power from satellite m after de-

spreading is mathematically equivalent to:

$$P_m = \frac{1}{T}\sum_{t=0}^{T-1}\left|\sum_{n=0}^{N-1} \mathrm{a}(t)e^{(2\pi f_m t)}e^{j(\mu_{nm}-\alpha_{nm})}\right|^2 \tag{5.31}$$

$$P_m = -130.656\text{dBW} \tag{5.32}$$

where μ_{nm} is the beamsteering direction and α_{nm} is the incident signal direction of origin. With infinite Gaussian noise the despreading will not achieve any processing gain; however, the processing gain is achieved during the despreading process of the narrowband noise by effectively lowering the noise floor.

$$P_{N_{100\text{ Hz}}} = \frac{1}{T}\sum_{t=0}^{T-1}\frac{1}{P_g}\left|\sum_{n=0}^{N-1} N_0 e^{j(\mu_{nm}-\gamma nm)}\right|^2 \tag{5.33}$$

$$P_{N_{100\text{ Hz}}} = -133.6177 - 47.78 = -181.3977\text{dBW} \tag{5.34}$$

In a similar manner, the narrowband interference power is also lowered by the despreading process.

$$P_I = \frac{1}{T}\sum_{t=0}^{T-1}\frac{1}{P_g}\left|\sum_{n=0}^{N-1} I(t)e^{j(2\pi f_i t)}e^{j(\mu_{nm}-\iota_n)}\right|^2 \tag{5.35}$$

$$P_I = -120 - 47.78 = -167.78\text{dBW} \tag{5.36}$$

In the worst case assuming directional noise with a DoA equivalent to the signal of interest, equal weight combining, and given that the DoA angle α_{nm} equals the

beamsteering angle μ_{nm} gives a SNR of:

$$\text{SNR} = \frac{\frac{1}{T}\sum_{t=0}^{T-1}\left|\sum_{n=0}^{N-1}\text{a}(t)e^{(2\pi f_m t)}e^{j(\mu_{nm}-\alpha_{nm})}\right|^2}{\frac{1}{T}\sum_{t=0}^{T-1}\frac{1}{P_g}\left|\sum_{n=0}^{N-1}N_0 e^{j(\mu_{nm}-\gamma_{nm})}\right|^2} \tag{5.37}$$

$$\text{SNR} = \frac{\sum_{t=0}^{T-1}\left|\sum_{n=0}^{N-1}\text{a}(t)e^{(2\pi f_m t)}e^{j(0)}\right|^2}{\sum_{t=0}^{T-1}\frac{1}{P_g}\left|\sum_{n=0}^{N-1}N_0 e^{j(0)}\right|^2} \tag{5.38}$$

$$\text{SNR} = \frac{\sum_{t=0}^{T-1}\left|N\,\text{a}(t)e^{(2\pi f_m t)}\right|^2}{\sum_{t=0}^{T-1}\frac{1}{P_g}|NN_0|^2} \tag{5.39}$$

$$\text{SNR} = \frac{\sum_{t=0}^{T-1}\left|\text{a}(t)e^{(2\pi f_m t)}\right|^2}{\sum_{t=0}^{T-1}\frac{1}{P_g}|N_0|^2} \tag{5.40}$$

$$\text{SNR} = -130.656 + 181.3977 = 50.7417\text{dBW} \tag{5.41}$$

SINR, in the worst case, assuming directional noise γ_{nm}, with directional CW interference from angle ι_n, using equal weight combining, and given that the DoA angle α_{nm} is equal to the beamsteering angle μ_{nm} yields:

$$\text{SINR} = \frac{\frac{1}{T}\sum_{t=0}^{T-1}\left|\sum_{n=0}^{N-1}\text{a}(t)e^{j(2\pi f_m t)}e^{j(\mu_{nm}-\alpha_{nm})}\right|^2}{\frac{1}{T}\sum_{t=0}^{T-1}\frac{1}{P_g}\left|\sum_{n=0}^{N-1}N_0 e^{j(\mu_{nm}-\gamma_{nm})}+I(t)e^{j(2\pi f_i t)}e^{j(\mu_{nm}-\iota_n)}\right|^2} \tag{5.42}$$

$$\text{SINR} = \frac{\sum_{t=0}^{T-1}\left|\sum_{n=0}^{N-1}\text{a}(t)e^{j(2\pi f_m t)}e^{j(0)}\right|^2}{\sum_{t=0}^{T-1}\frac{1}{P_g}\left|\sum_{n=0}^{N-1}N_0 e^{j(0)}+I(t)e^{j(2\pi f_i t)}e^{j(\mu_{nm}-\iota_n)}\right|^2} \tag{5.43}$$

$$\text{SINR} = \frac{\sum_{t=0}^{T-1}\left|N\,\text{a}(t)e^{j(2\pi f_m t)}\right|^2}{\sum_{t=0}^{T-1}\frac{1}{P_g}\left|NN_0+\sum_{n=0}^{N-1}I(t)e^{j(2\pi f_i t)}e^{j(\mu_{nm}-\iota_n)}\right|^2} \tag{5.44}$$

As this is the worse case, it is expected that in situations without directional noise from the signal of interest that the array gain will improve both the SNR and the SINR.

5.5 Polar Contour

The array factor is the physical representation of an antenna array's effective antenna pattern. This is typically depicted in the form of a polar radiation pattern such as the pattern of a 20 element UCA in Figure 5.9 from the direction $\phi = 0°$ sweeping $\frac{-\pi}{2} \leq \theta \leq \frac{\pi}{2}$ across the sky. This cross section is a slice of the three

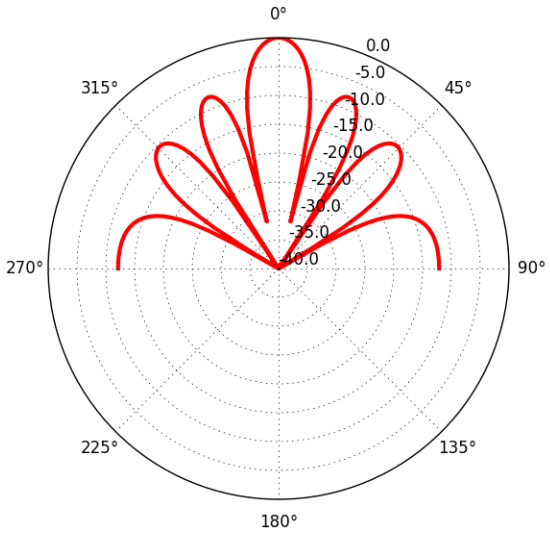

Figure 5.9: Array Factor 20 Element UCA $\theta = 0 - \frac{\pi}{2}$, $\phi = 0$ Radians in Polar Decibel Form

dimensional antenna pattern shown in Figure 5.10 for all directions of $0 \leq \phi \leq 2\pi$ and $0 \leq \theta \leq \frac{\pi}{2}$. Another representation of the three dimensional array factor is the polar contour plot. The polar contour plot is a top down view (perpendicular over the XY plane) of the three dimensional plot where the magnitude of array pattern is represented by a colored contour mapping. The azimuth ϕ is depicted by the angle formed between 0 and the polar radius, where the elevation θ is represented by the magnitude of the polar radius. An example for the same 20 element UCA is shown

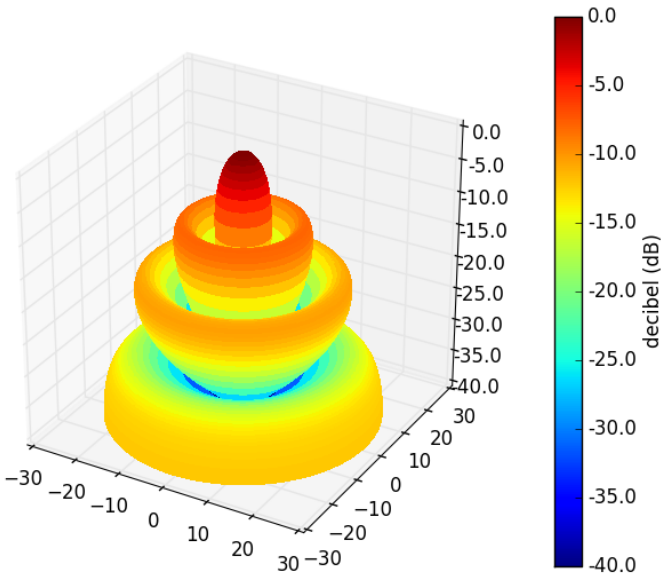

Figure 5.10: Array Factor 20 Element UCA in 3D Decibel Form

in Figure 5.11. As the polar contour plot a is convenient method for conveying 3D directional information it was the primary graphic method used for the remainder of the thesis.

5.6 Phased Arrays

For evaluating the effectiveness of the synthetic aperture digital beamsteering six different array methodologies were used: the UCA, which is commonly used in DoA; a rectangular array; a random array; a random full aperture; a random sequential array; and a ring array that combines the UCA and random arrays.

5.6.1 Uniform Circular Array (UCA)

A UCA array is composed of elements that are equally spaced along the perimeter of a circle. To create a UCA the maximum tolerance allowed between antenna

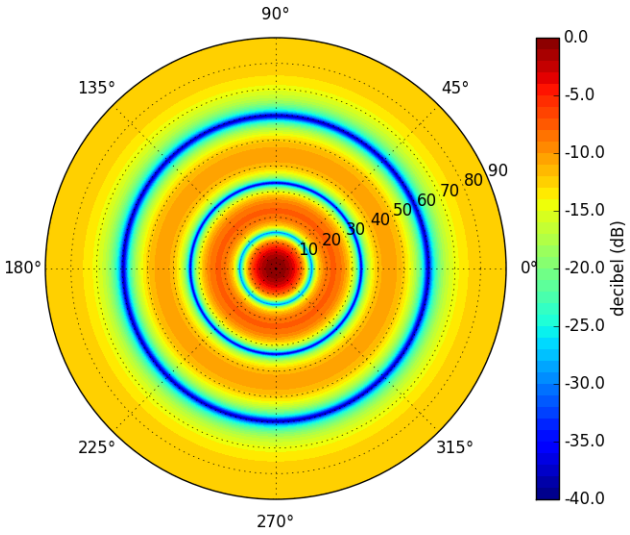

Figure 5.11: Array Factor 20 Element UCA in Polar Contour Decibel Form

elements is T_{max}. Using the maximum tolerance to inscribe a perimeter around the center of each array element results in a circle with a radius half of the tolerance or $T_{max}/2$. If the elements are placed as close to one another as possible this leaves the distance between adjacent elements as the specified tolerance. Placing the elements as close to one another as possible yields an angle between the antenna phase center as $\theta = 2\pi/n$ where n is the number of elements. If T_{max} is the distance between two adjacent elements and θ is the corresponding angle then the circle radius can be derived by using the Law of Cosines $a^2 = b^2 + c^2 - 2bc\cos(A)$. The lowercase scripts are the lengths of the sides of a triangle and the uppercase script is the angle of the opposite length bearing the same character. The resulting circle radius is calculated

as follows:

$$\begin{aligned} T_{max}^2 &= r^2 + r^2 - 2rr\cos(\theta) \\ &= 2r^2\big(1 - \cos(\theta)\big) \\ r &= \sqrt{\frac{T_{max}^2}{2(1 - \cos(\theta))}} \end{aligned} \tag{5.45}$$

5.6.1.1 UCA Element Configuration

Following the array placement described in Section 5.6.1 where $T_{max} = \lambda/2$ for array sizes of 5, 10, 15, 20, 30, 40, and 50 result in the configurations shown in Figures 5.12 - 5.18.

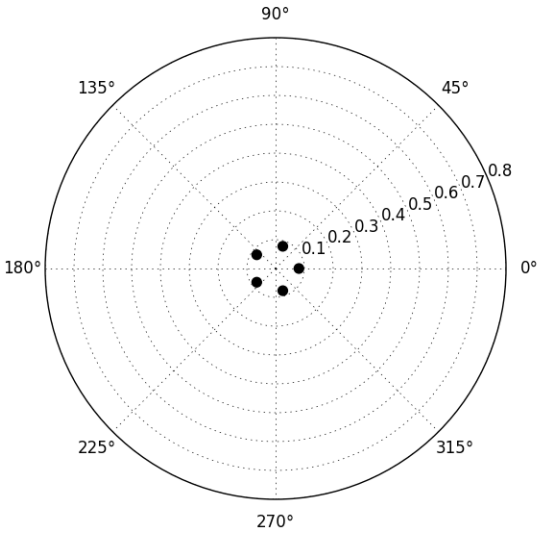

Figure 5.12: UCA 5 Element Configuration in Meters

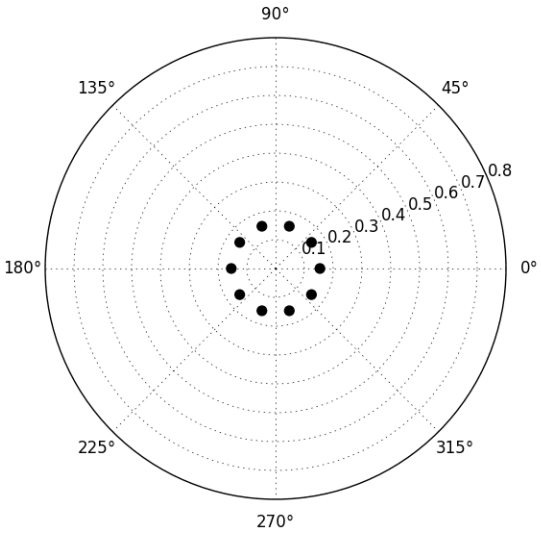

Figure 5.13: UCA 10 Element Configuration in Meters

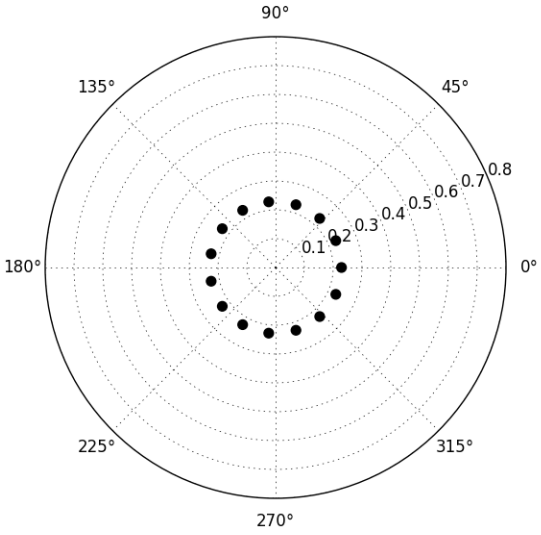

Figure 5.14: UCA 15 Element Configuration in Meters

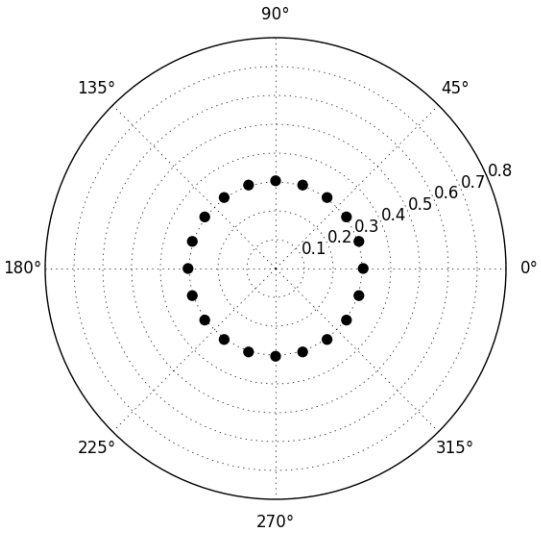

Figure 5.15: UCA 20 Element Configuration in Meters

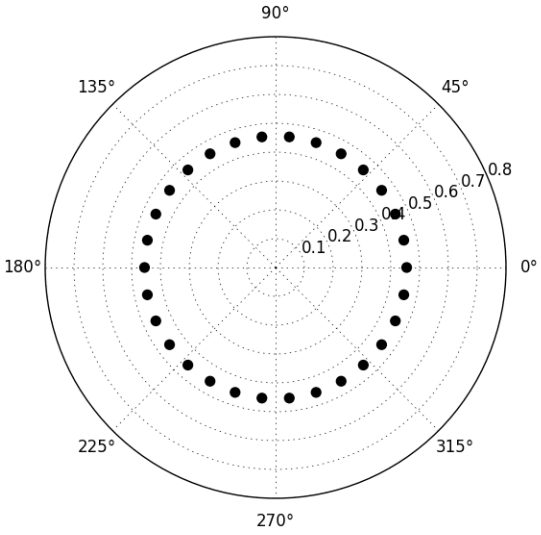

Figure 5.16: UCA 30 Element Configuration in Meters

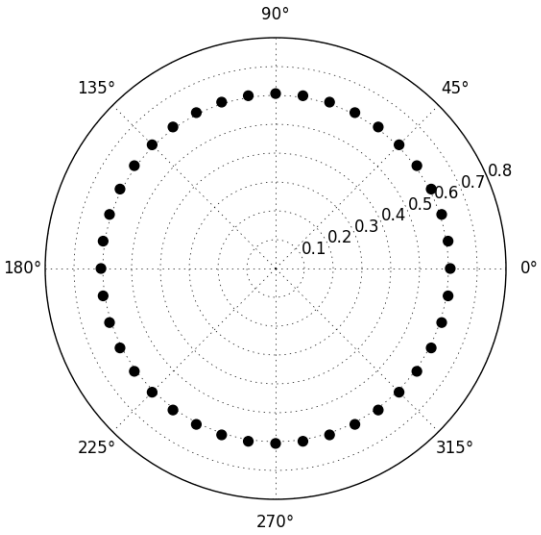

Figure 5.17: UCA 40 Element Configuration in Meters

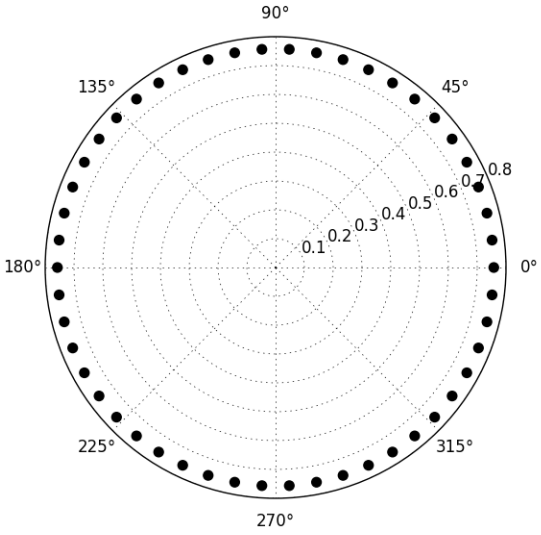

Figure 5.18: UCA 50 Element Configuration in Meters

5.6.1.2 Array Size

The circular area encompassed by the array from 2 elements to 50 in m^2 is shown in Figure 5.19. As expected the array size increases with additional elements and is highest for the maximum tolerance $T_{max} = \lambda$.

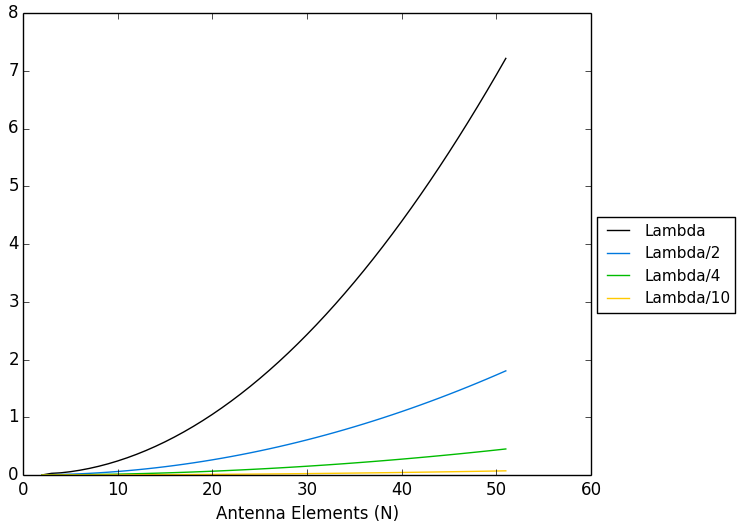

Figure 5.19: Array Size for λ, $\lambda/2$, $\lambda/4$, $\lambda/10$ Array Spacing in Circular Area in m^2 for UCA

5.6.1.3 Directivity

Directivity is a measure of the concentration of an array beam. The directivity for the UCA is shown in Figure 5.20. As expected the directivity increases for all tolerances of T_{max} simulated.

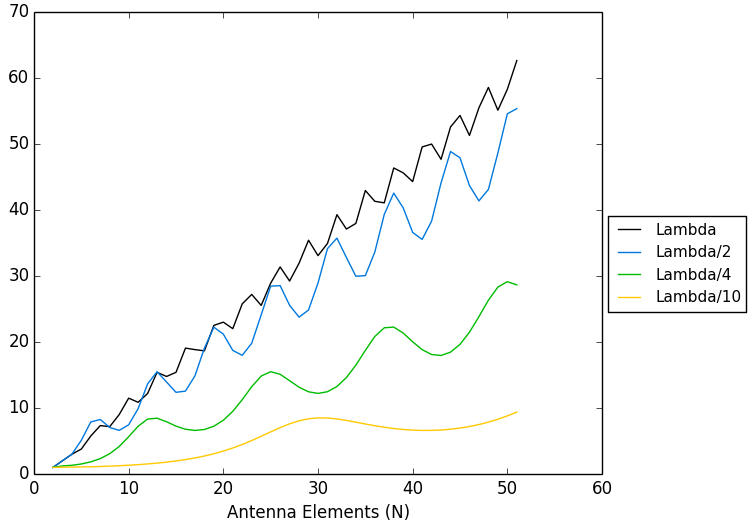

Figure 5.20: Directivity for λ, $\lambda/2$, $\lambda/4$, $\lambda/10$ Array Spacing for UCA

5.6.1.4 Uniform Circular Array (UCA) Array Factor

The UCA is characterized by ring structure as depicted in Figures 5.21 - 5.33 for a tolerance of $T_{max} = \lambda/2$. The ring structure created by beamsteering a single element in the direction of $(\theta, \phi) = (60.0821, 374.6239)$ is also shown in Figures 5.22 - 5.34. The focus of the main beam mirrors the increase in directivity shown in Figure 5.20 as the number of elements is increased.

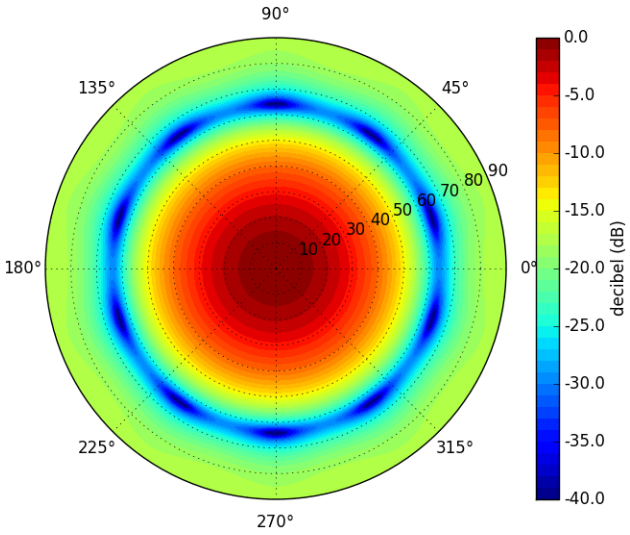

Figure 5.21: Array Factor Contour of 5 Element UCA in Decibels

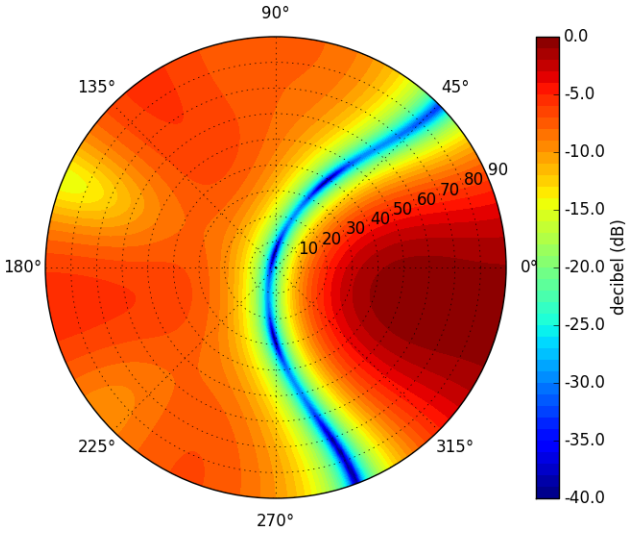

Figure 5.22: Array Factor Contour of 5 Element UCA with Beamsteering in Decibels

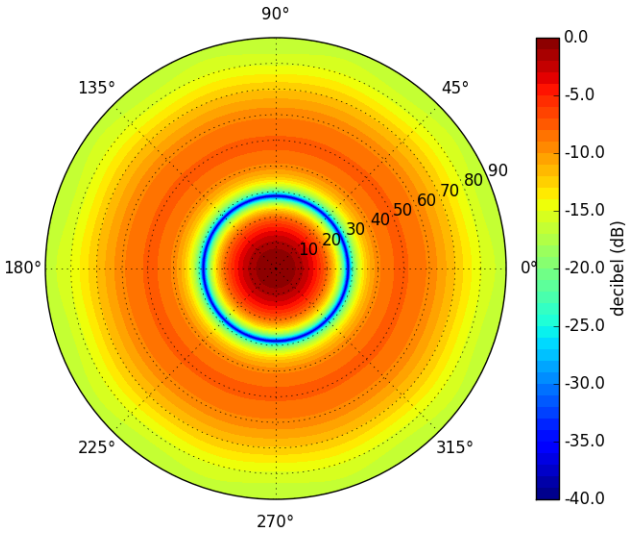

Figure 5.23: Array Factor Contour of 10 Element UCA in Decibels

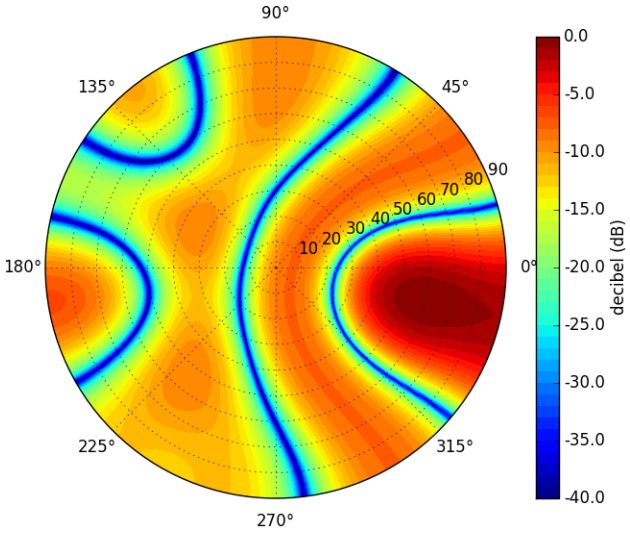

Figure 5.24: Array Factor Contour of 10 Element UCA with Beamsteering in Decibels

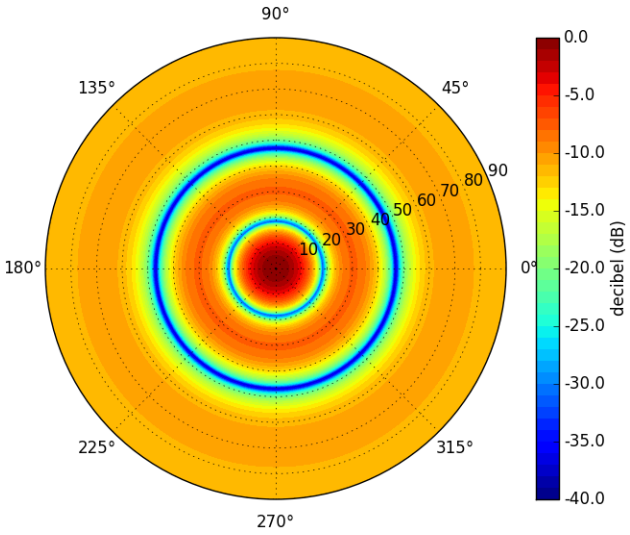

Figure 5.25: Array Factor Contour of 15 Element UCA in Decibels

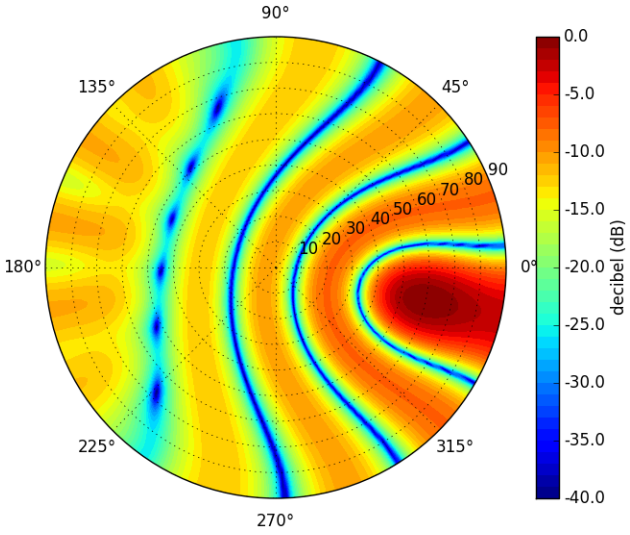

Figure 5.26: Array Factor Contour of 15 Element UCA with Beamsteering in Decibels

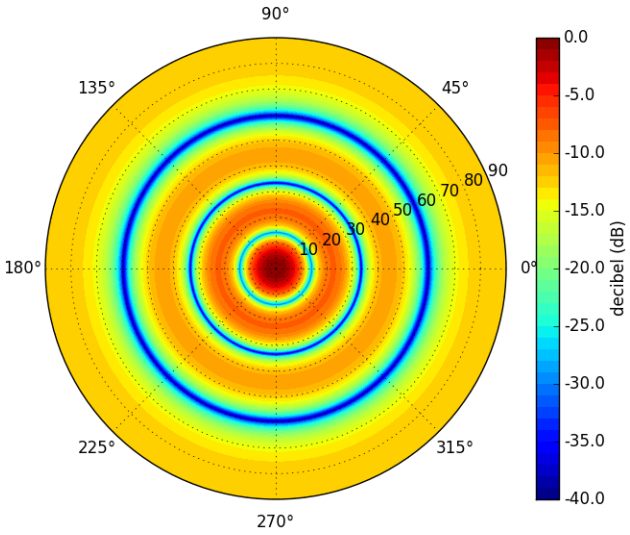

Figure 5.27: Array Factor Contour of 20 Element UCA in Decibels

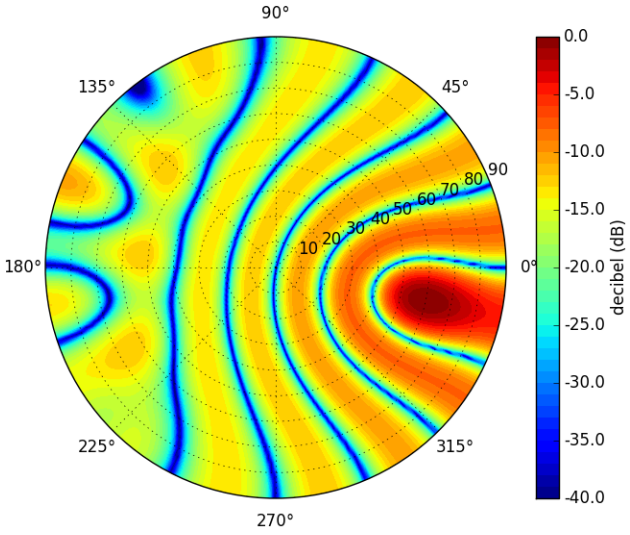

Figure 5.28: Array Factor Contour of 20 Element UCA with Beamsteering in Decibels

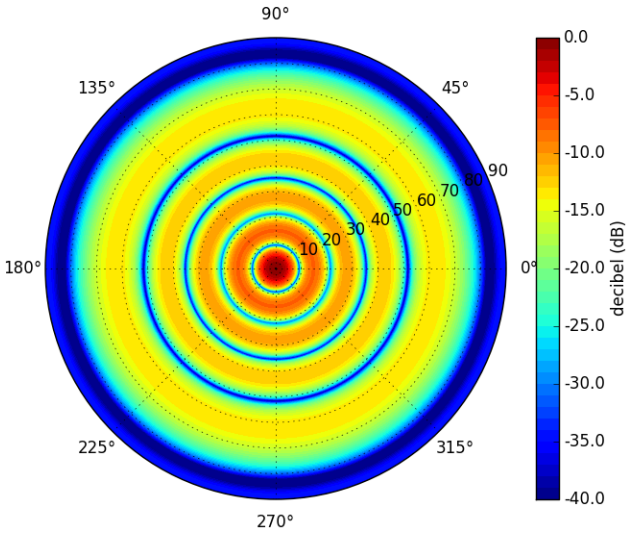

Figure 5.29: Array Factor Contour of 30 Element UCA in Decibels

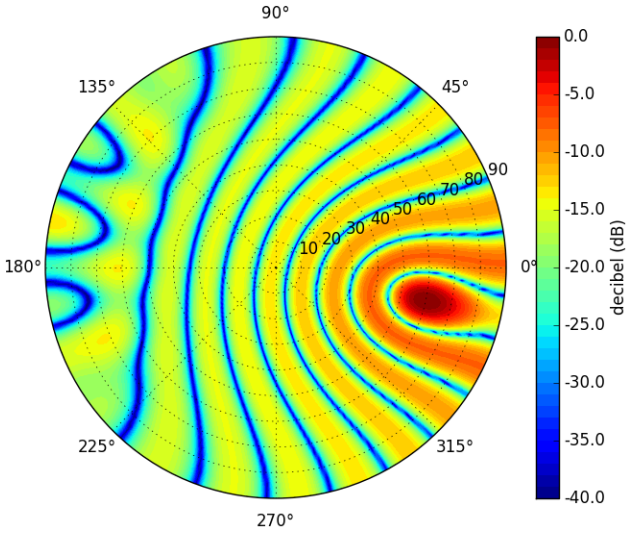

Figure 5.30: Array Factor Contour of 30 Element UCA with Beamsteering in Decibels

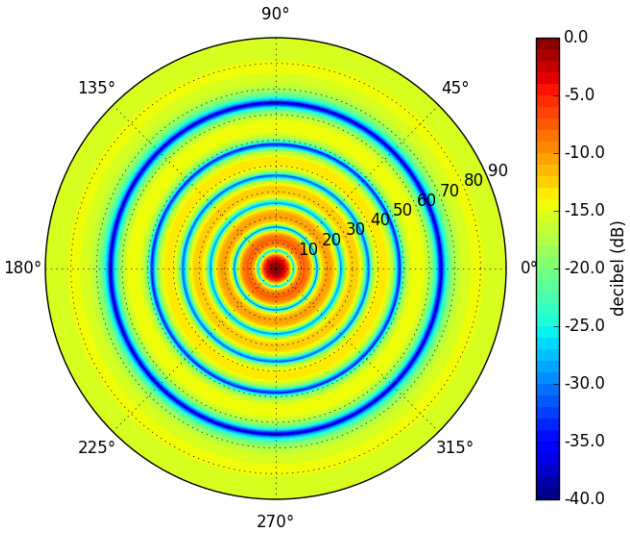

Figure 5.31: Array Factor Contour of 40 Element UCA in Decibels

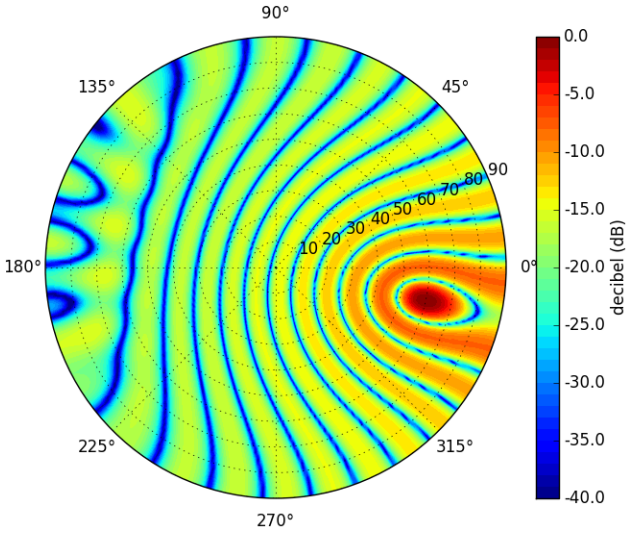

Figure 5.32: Array Factor Contour of 40 Element UCA with Beamsteering in Decibels

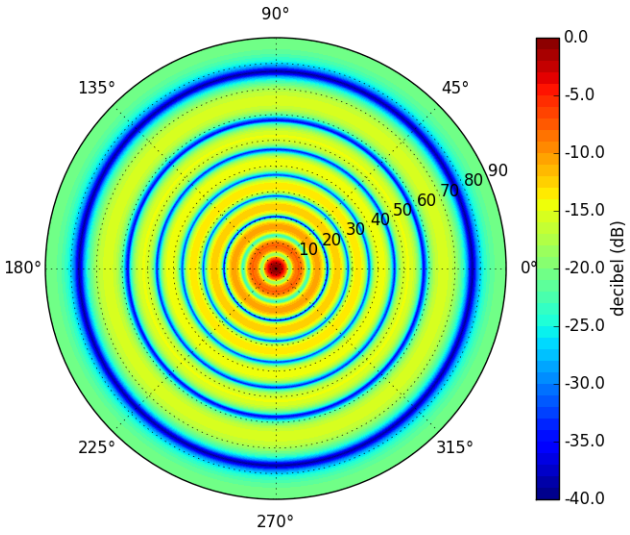

Figure 5.33: Array Factor Contour of 50 Element UCA in Decibels

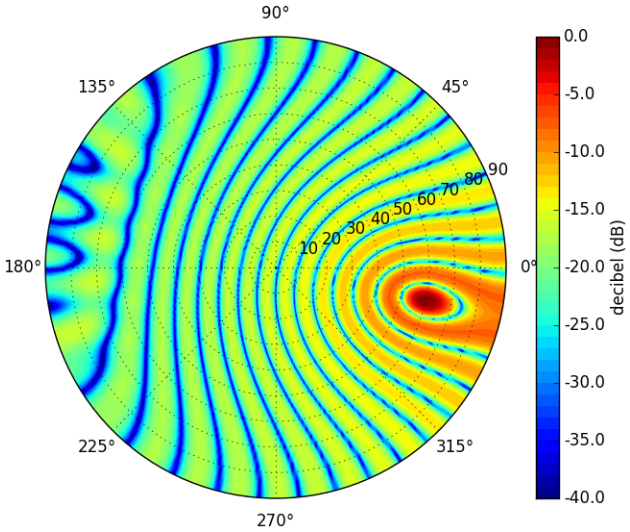

Figure 5.34: Array Factor Contour of 50 Element UCA with Beamsteering in Decibels

5.6.1.5 Uniform Circular Array Direction of Arrival

The MUSIC DoA estimation algorithm processed the synthetic aperture array data after despreading each incident signal with its PRN sequence and prior to combining or beamsteering. The results from the MUSIC algorithm are shown in Figures 5.35 - 5.41. A peak detection algorithm was used to determine the predicted signal direction of origin. The figures show that an increase in the number of elements improves or narrows the spatial resolution of the peak.

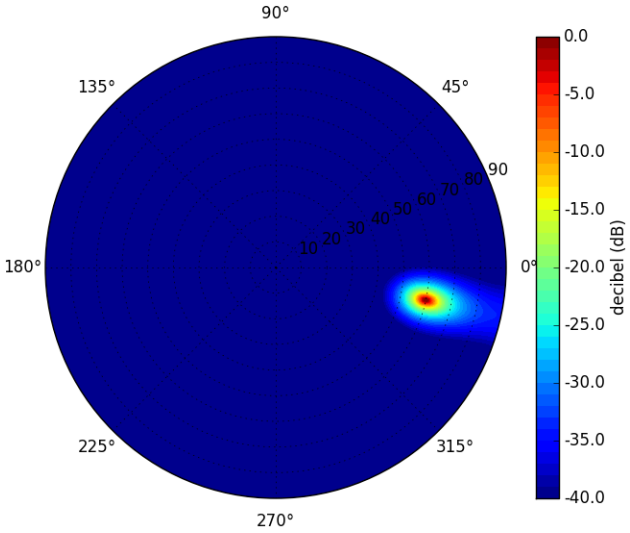

Figure 5.35: PRN_7 DoA of 5 Element UCA in Decibels

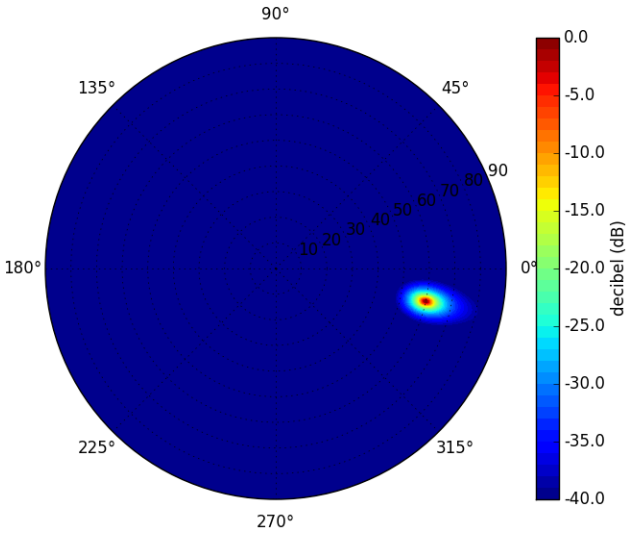

Figure 5.36: PRN_7 DoA of 10 Element UCA in Decibels

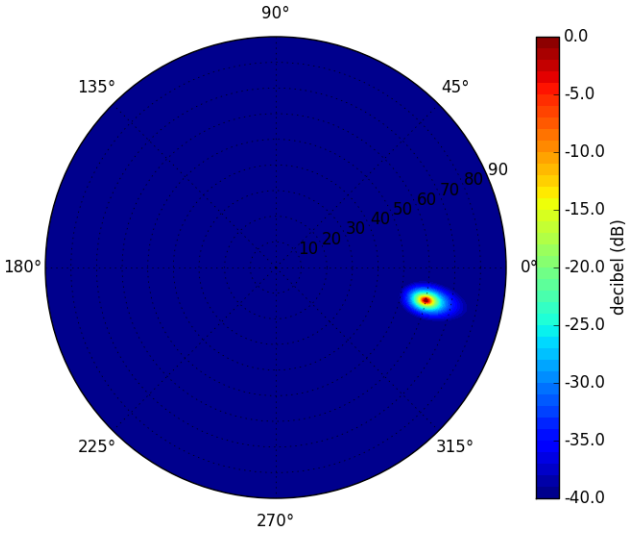

Figure 5.37: PRN_7 DoA of 15 Element UCA in Decibels

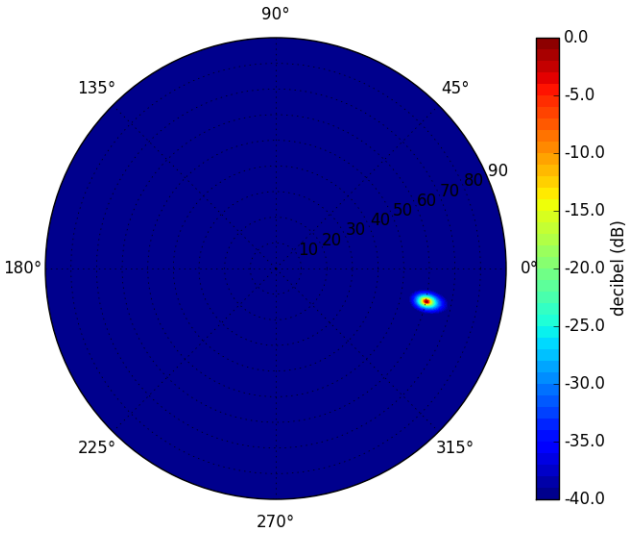

Figure 5.38: PRN_7 DoA of 20 Element UCA in Decibels

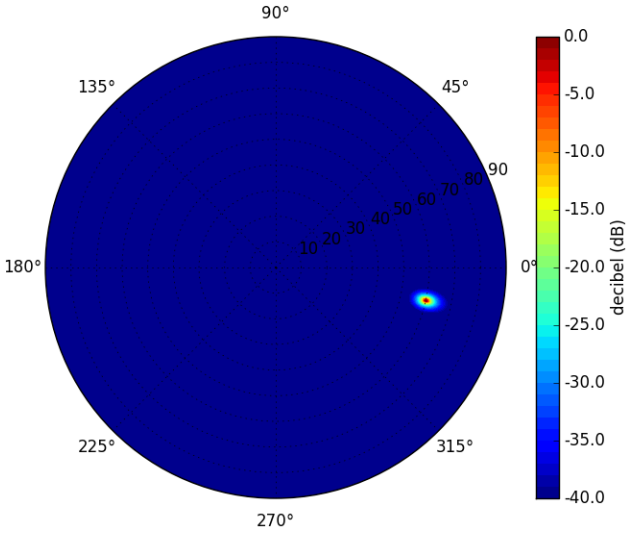

Figure 5.39: PRN_7 DoA of 30 Element UCA in Decibels

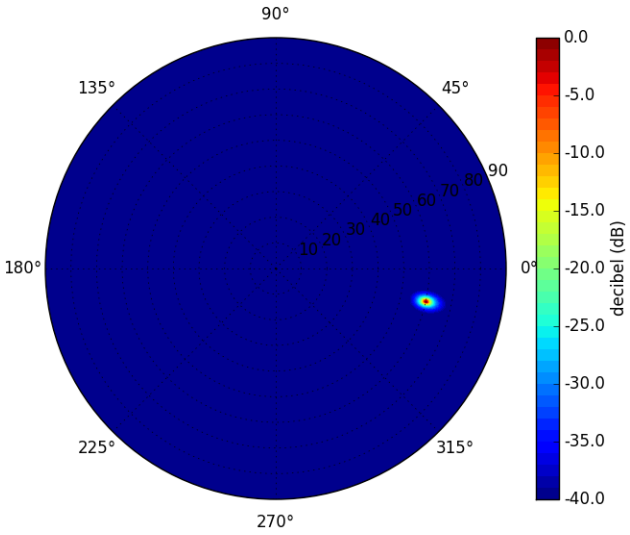

Figure 5.40: PRN_7 DoA of 40 Element UCA in Decibels

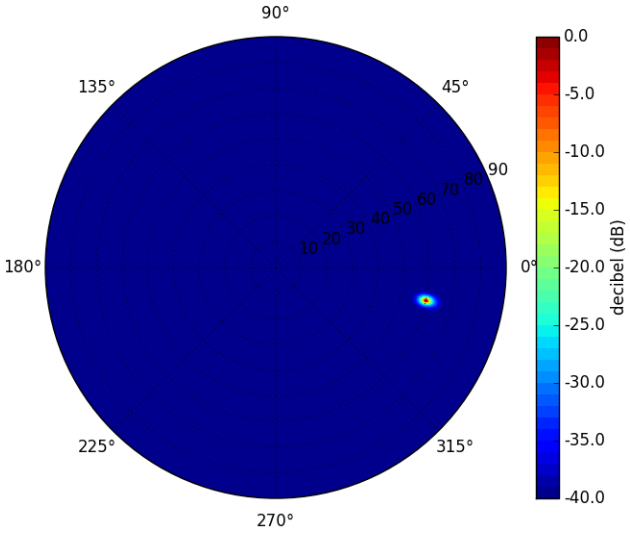

Figure 5.41: PRN_7 DoA of 50 Element UCA in Decibels

5.6.1.6 *Uniform Circular Array (UCA) Direction of Arrival*

Figure 5.42 shows the DoA error under CW interference CW_0 and CW_1, where CW_0 is near the horizon and CW_1 is near a satellite signal. Regardless of the presence of interference or the interference's proximity to the signal source the DoA error flattens around an array of size 10 for MUSIC with a tolerance of .5°.

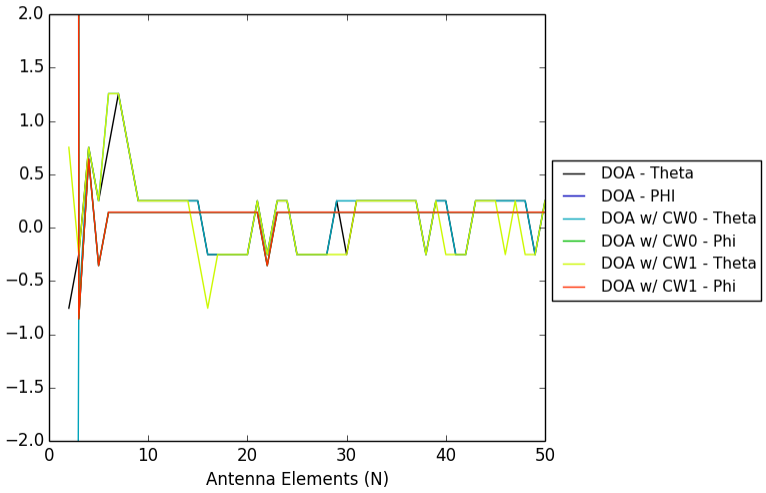

Figure 5.42: DoA error for different interference sources for $\lambda/2$ spacing

5.6.1.7 *Nominal SNR and SINR Comparison*

A comparison of the SNR and SINR ratios is made under ideal or nominal DoA information from signal PRN_7 for beamsteering, MUSIC DoA information from signal PRN_7, and all signals of interest DoA generated by MUSIC estimation averaged together. The comparison occurred at $\lambda/2$ spacing, and the results are shown in Figure 5.43 and Figure 5.44. From these two graphs, it is apparent that the DoA

error generated by the MUSIC algorithm is very small; this is shown by the PRN_7 signal tracking the nominal or ideal signal as the number array elements increased. The averaged signal power shows that all six signals of interest follow PRN_7 with a small variance.

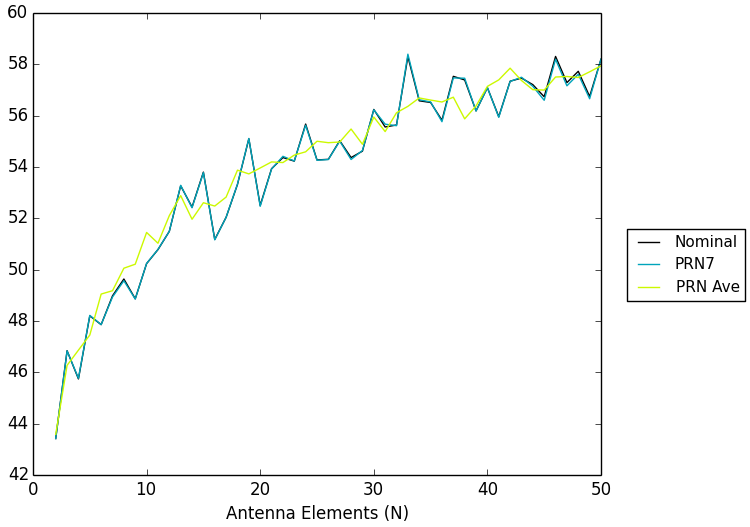

Figure 5.43: UCA SNR for Nominal, PRN_7, and Averaged PRN Signal DoA at $\lambda/2$ Spacing

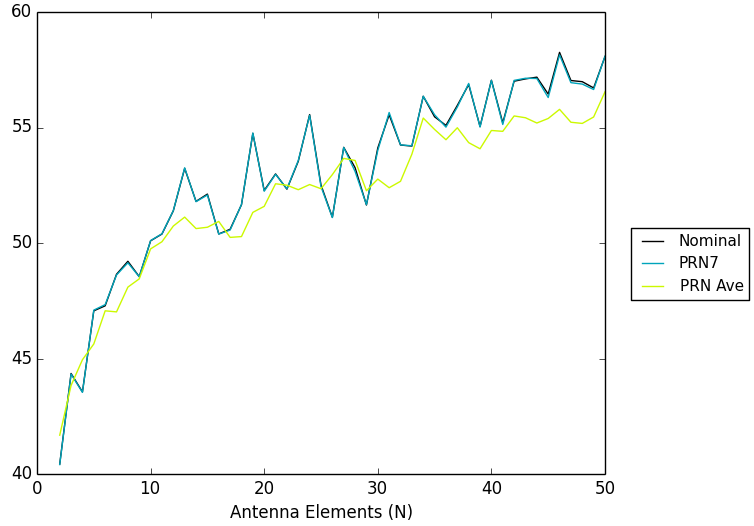

Figure 5.44: UCA SINR for Nominal, PRN_7, and Averaged PRN Signal DoA at $\lambda/2$ Spacing, with CW_0 Interference

5.6.1.8 Noise Level Comparison

The noise level was evaluated for $\lambda/2$ spacing with a noise temperature of 513 K and 2052 K with interference source CW_0. The SNR and SINR are shown in Figure 5.45 and Figure 5.46 respectively. A higher noise floor has a negative impact on the SNR and SINR, but the size of the array has a limited impact on complex AWGN as expected. The two noise curves are identical only differing in magnitude.

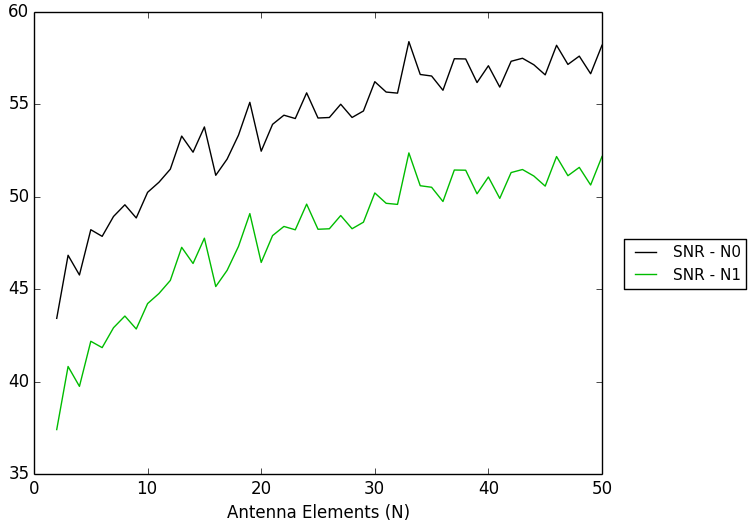

Figure 5.45: UCA SNR for noise levels N_0 and N_1 at $\lambda/2$ spacing

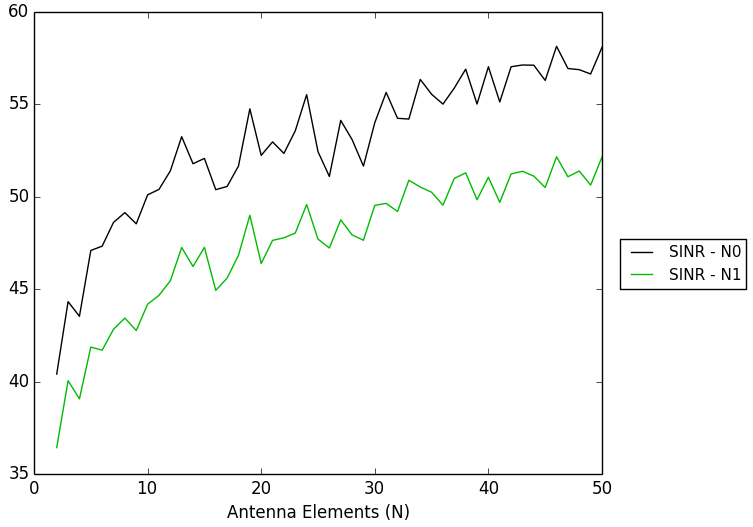

Figure 5.46: UCA SINR for noise levels N_0 and N_1 at $\lambda/2$ spacing

5.6.1.9 *Interference Position Comparison*

Figure 5.47 shows the SINR under CW interference CW_0 and CW_1, where CW_0 is near the horizon, and CW_1 is near a satellite signal. The interference source near the satellite signal has a smaller gain as expected. When beamsteering near the signal of interest, a highly focused pattern is moved near the interference source placing it near a gain rather than a null. This results in increased interference power and a decreased SINR.

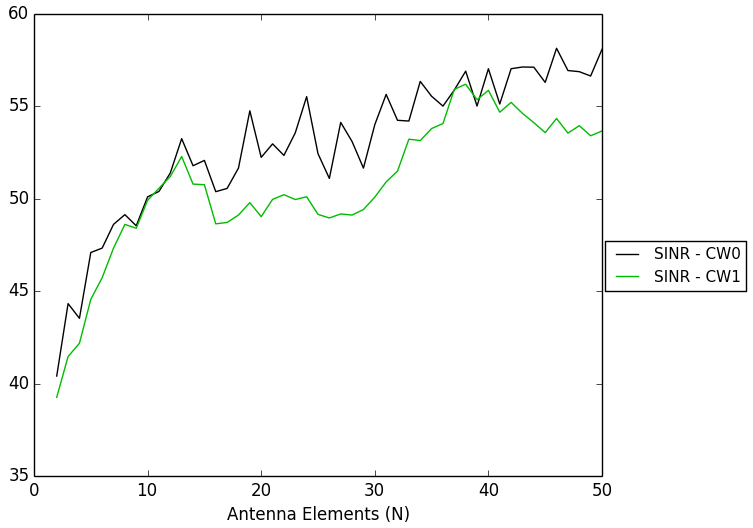

Figure 5.47: UCA SINR for Different Interference Sources at $\lambda/2$ Spacing

5.6.1.10 *Array Inter-Element Spacing Comparison*

A little surprising is the effect of the array spacing or lack of a significant effect on the SNR and SINR ratios respectively for λ, $\lambda/2$, $\lambda/4$, $\lambda/10$ array spacing. The SNR and SINR ratios are captured in Figure 5.48 and Figure 5.49. The comparable

ratios are likely the result of the communication despreading process selecting only the signal of interest. The presence of one signal would cause aliasing or a decrease in directivity to have a marginal affect.

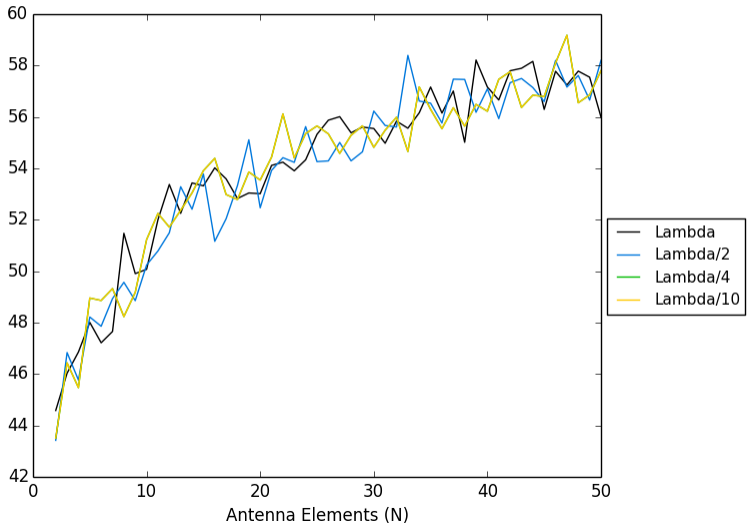

Figure 5.48: UCA SNR for λ, $\lambda/2$, $\lambda/4$, $\lambda/10$ spacing

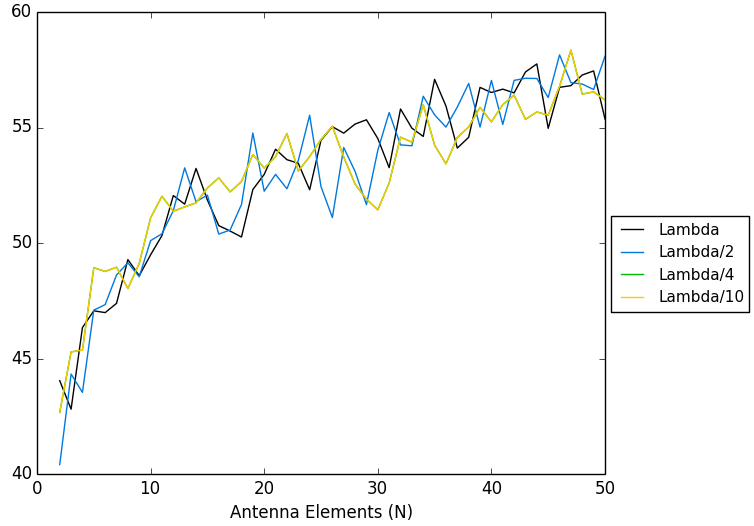

Figure 5.49: UCA SINR for λ, $\lambda/2$, $\lambda/4$, $\lambda/10$ spacing

5.6.2 Rectangular Array

A rectangular array is comprised of antenna elements uniformly spaced on a hatched grid with a certain element height and width. To create a rectangular array, the maximum tolerance allowed between antenna elements is T_{max}. The elements were placed on a rectangular grid of spacing equal at the maximum tolerance T_{max} allowed between antenna elements. Starting at the origin, elements were added to the array in a counter clockwise spiral pattern where the first non-origin element occurred at T_{max} on the positive X axis. The methods used in array placement are portrayed in the Algorithm 1.

5.6.2.1 Rectangular Element Configuration

Following the array placement described in Section 5.6.2 where $T_{max} = \lambda/2$ for array sizes of 5, 10, 15, 20, 30, 40, and 50 result in the configurations shown in Figures 5.50 - 5.56.

Algorithm 1 Rectangular Array Element Placement

```
1: for ii = 2 : n do
2:     if direction == 'right' then
3:         position(1) = position(1) + 1
4:         if counter == right then
5:             direction =' up'
6:             counter = 0
7:             right = right + 2
8:         end if
9:     else if direction == 'up' then
10:        position(2) = position(2) + 1
11:        if counter == up then
12:            direction =' left'
13:            counter = 0
14:            up = up + 2
15:        end if
16:    else if direction == 'left' then
17:        position(1) = position(1) − 1
18:        if counter == left then
19:            direction =' down'
20:            counter = 0
21:            left = left + 2
22:        end if
23:    else if direction == 'down' then
24:        position(2) = position(2) − 1
25:        if counter == down then
26:            direction =' right'
27:            counter = 0
28:            down = down + 2
29:        end if
30:    end if
31:    X(ii) = position(1)
32:    Y(ii) = position(2)
33:    counter = counter + 1
34: end for
```

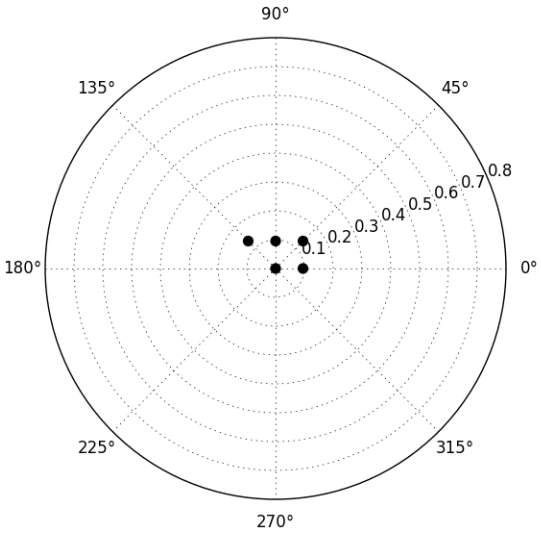

Figure 5.50: Rectangular Array 5 Element Configuration

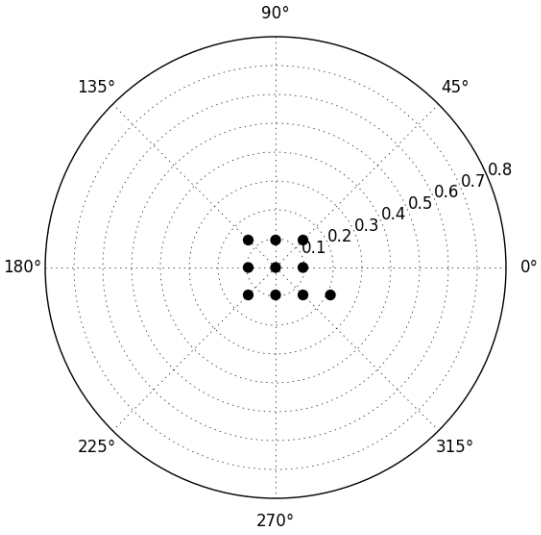

Figure 5.51: Rectangular Array 10 Element Configuration

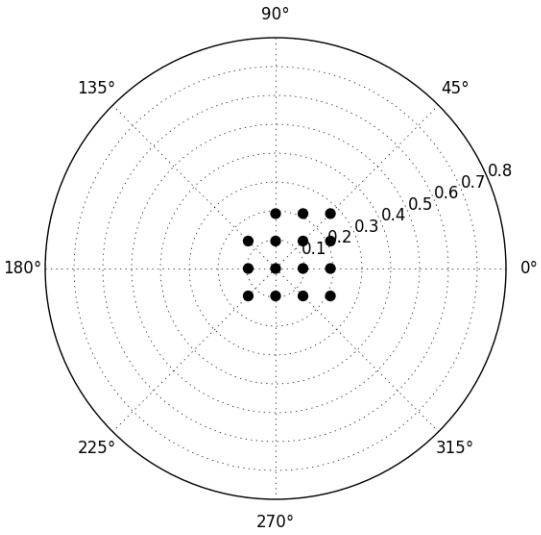

Figure 5.52: Rectangular Array 15 Element Configuration

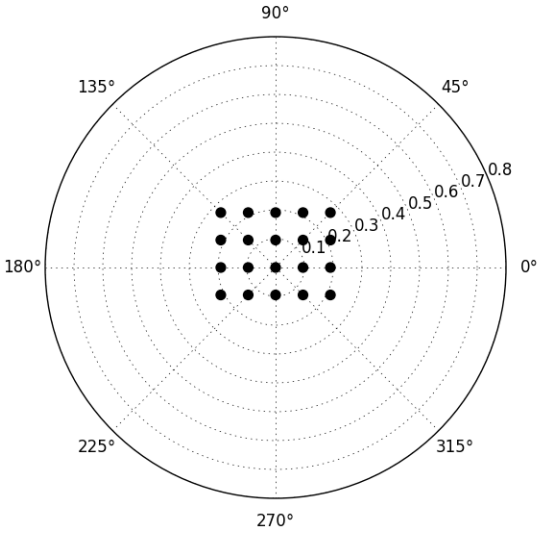

Figure 5.53: Rectangular Array 20 Element Configuration

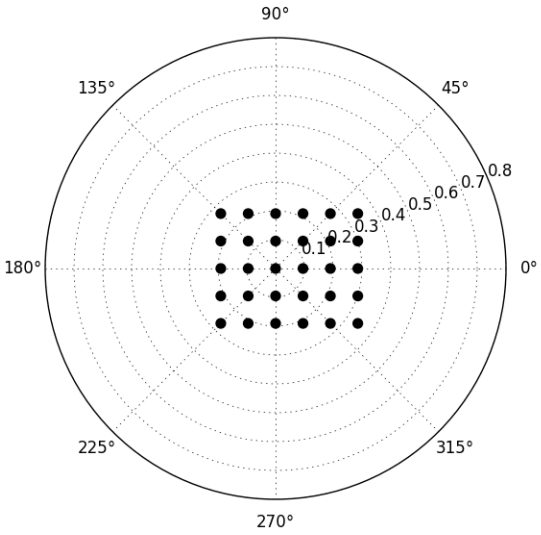

Figure 5.54: Rectangular Array 30 Element Configuration

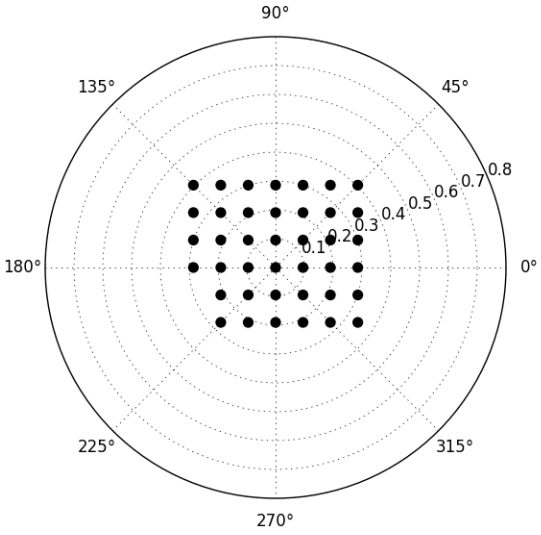

Figure 5.55: Rectangular Array 40 Element Configuration

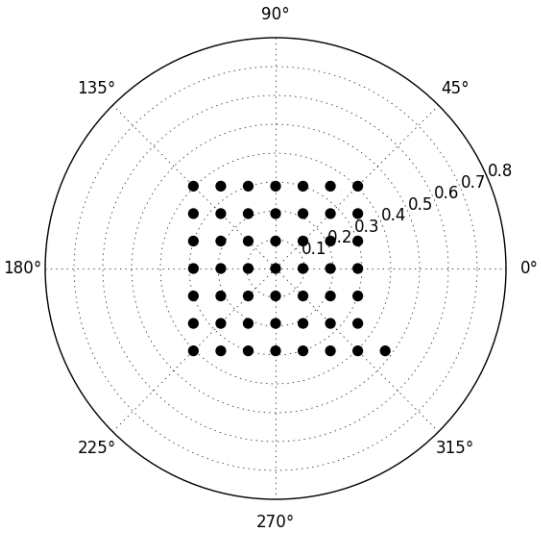

Figure 5.56: Rectangular Array 50 Element Configuration

5.6.2.2 Array Size

The circular area encompassed by the array from 2 elements to 50 in m^2 is shown in Figure 5.57. As expected the array size increases with additional elements and is highest for the maximum tolerance $T_{max} = \lambda$.

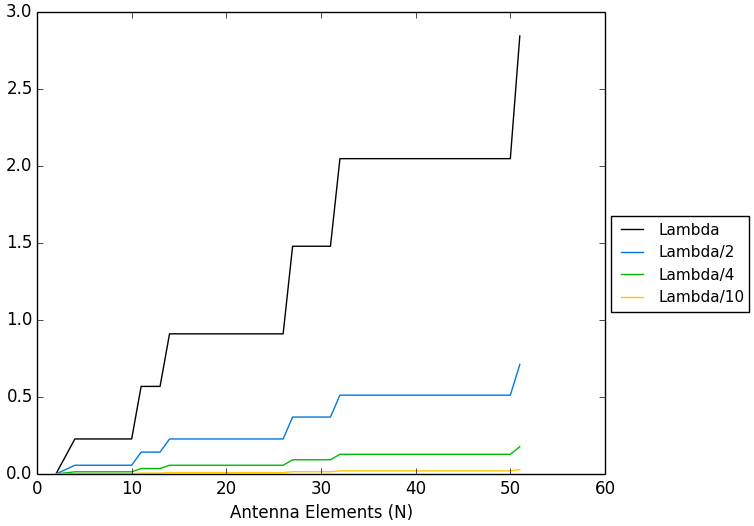

Figure 5.57: Array Size for λ, $\lambda/2$, $\lambda/4$, $\lambda/10$ Array Spacing in Circular Area in m^2 for Rectangular Array

5.6.2.3 Directivity

Directivity is a measure of the concentration of an array beam. The directivity for the Rectangular Array is shown in Figure 5.58. As expected the directivity increases for all tolerances of T_{max} simulated.

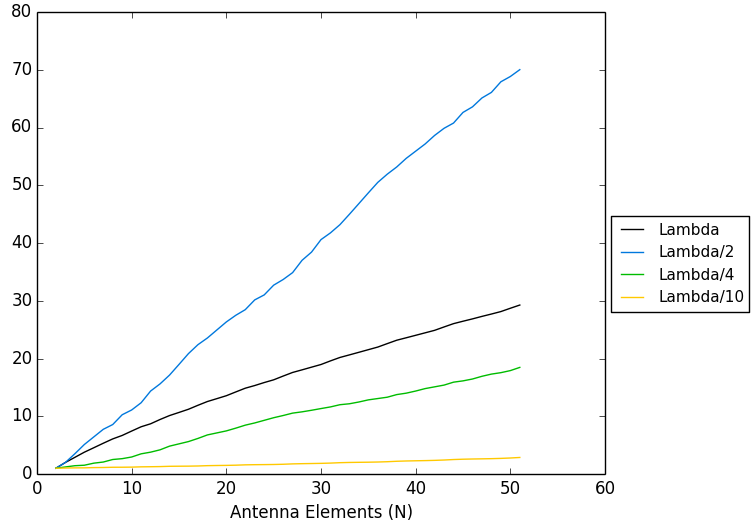

Figure 5.58: Directivity for λ, $\lambda/2$, $\lambda/4$, $\lambda/10$ Array Spacing for Rectangular Array

5.6.2.4 Rectangular Array Factor

The Rectangular Array is characterized by repeating cross structure as depicted in Figures 5.59 - 5.71 for a tolerance of $T_{max} = \lambda/2$. The cross structure beamsteered in the direction of $(\theta, \phi) = (60.0821, 374.6239)$ of a single signal is also shown in Figures 5.60 - 5.72. The focus of the main beam mirrors the increase in directivity shown in Figure 5.58.

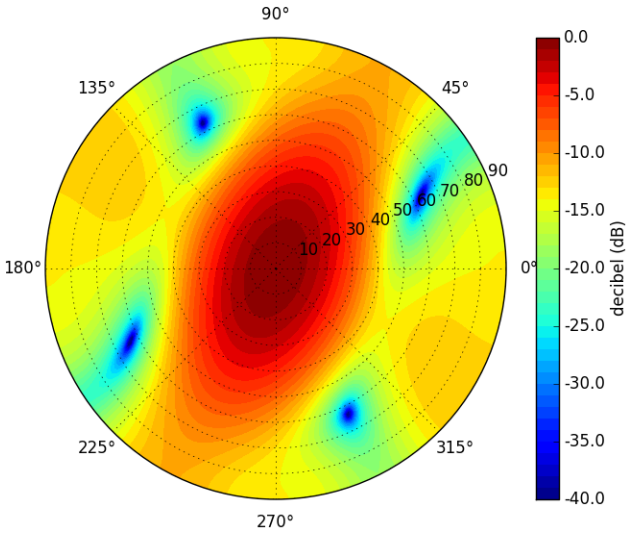

Figure 5.59: Array Factor Contour of 5 Element Rectangular Array in Decibels

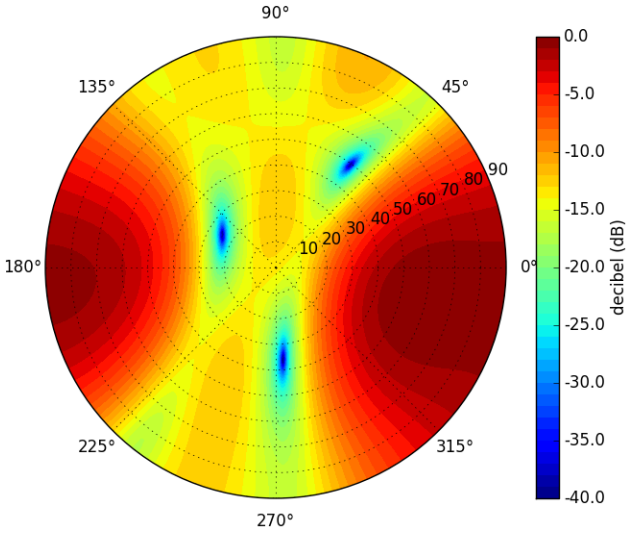

Figure 5.60: Array Factor Contour of 5 Element Rectangular Array with Beamsteering in Decibels

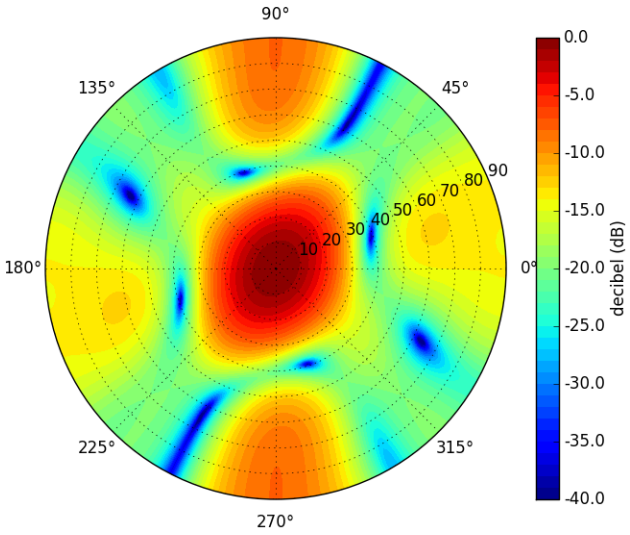

Figure 5.61: Array Factor Contour of 10 Element Rectangular Array in Decibels

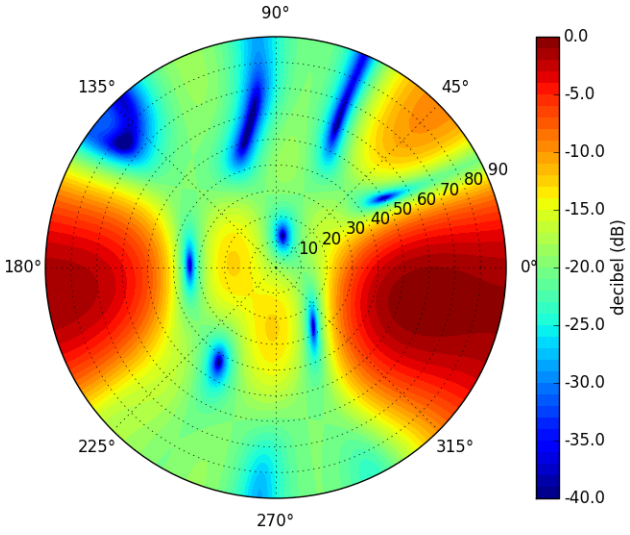

Figure 5.62: Array Factor Contour of 10 Element Rectangular Array with Beam-steering in Decibels

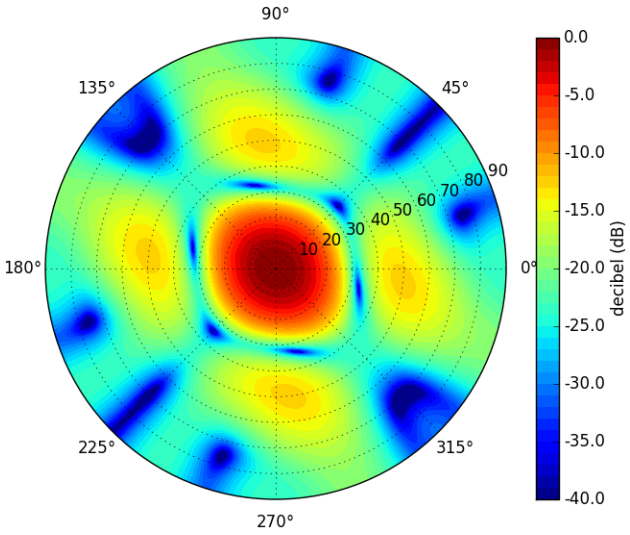

Figure 5.63: Array Factor Contour of 15 Element Rectangular Array in Decibels

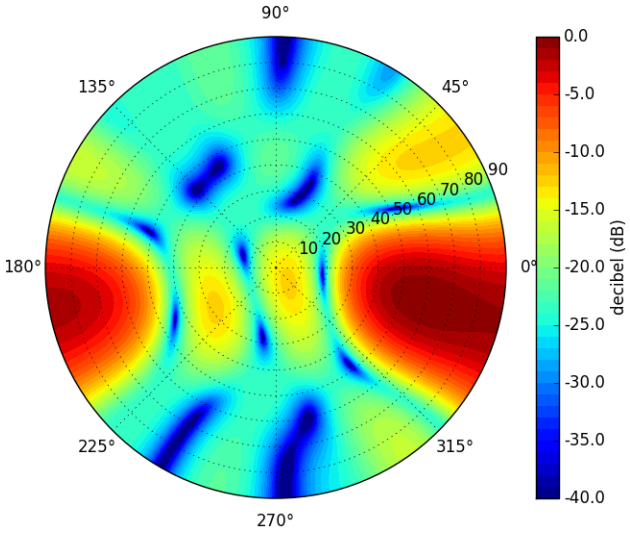

Figure 5.64: Array Factor Contour of 15 Element Rectangular Array with Beam-steering in Decibels

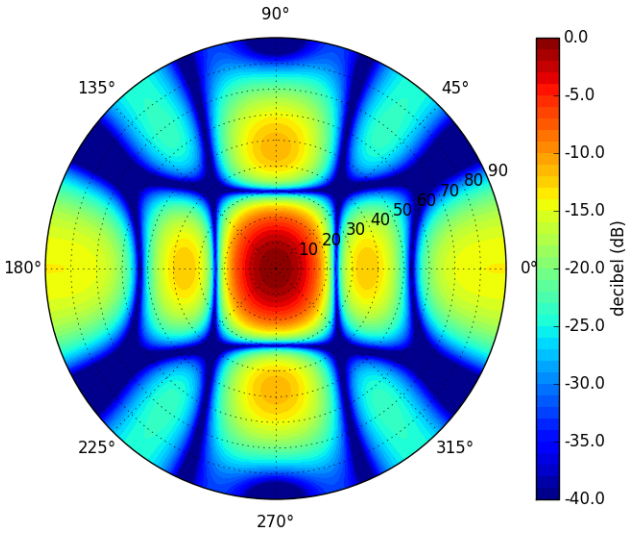

Figure 5.65: Array Factor Contour of 20 Element Rectangular Array in Decibels

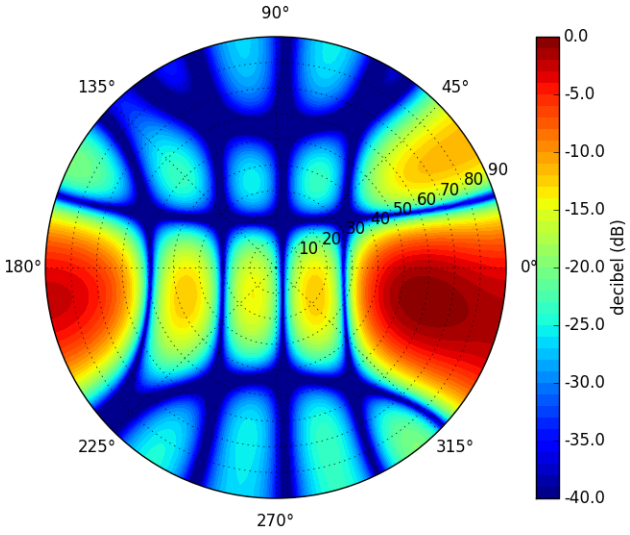

Figure 5.66: Array Factor Contour of 20 Element Rectangular Array with Beam-steering in Decibels

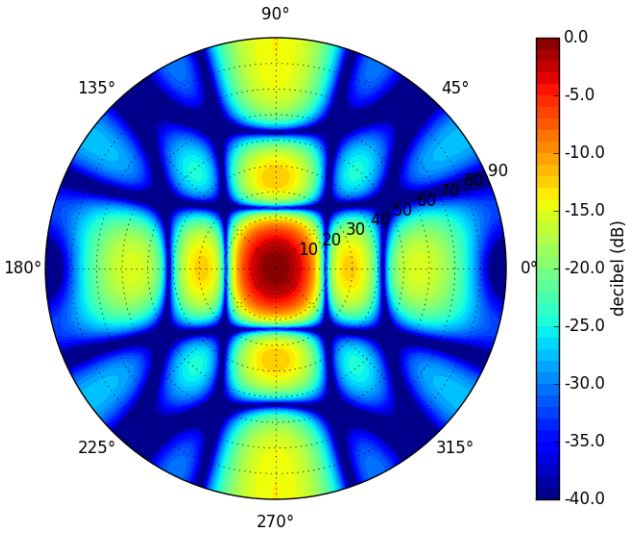

Figure 5.67: Array Factor Contour of 30 Element Rectangular Array in Decibels

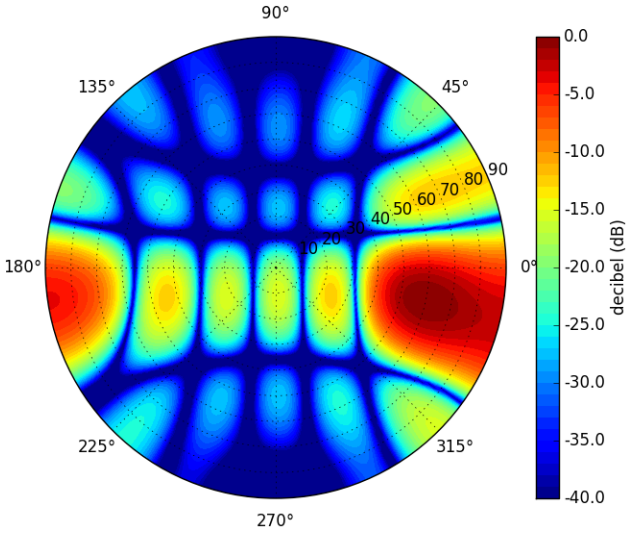

Figure 5.68: Array Factor Contour of 30 Element Rectangular Array with Beam-steering in Decibels

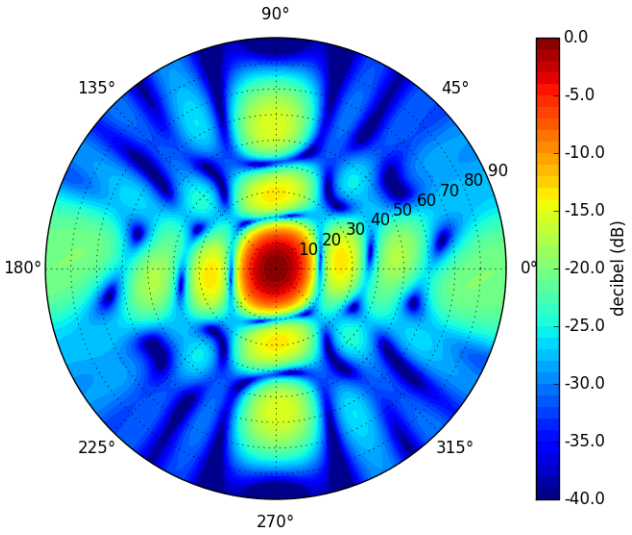

Figure 5.69: Array Factor Contour of 40 Element Rectangular Array in Decibels

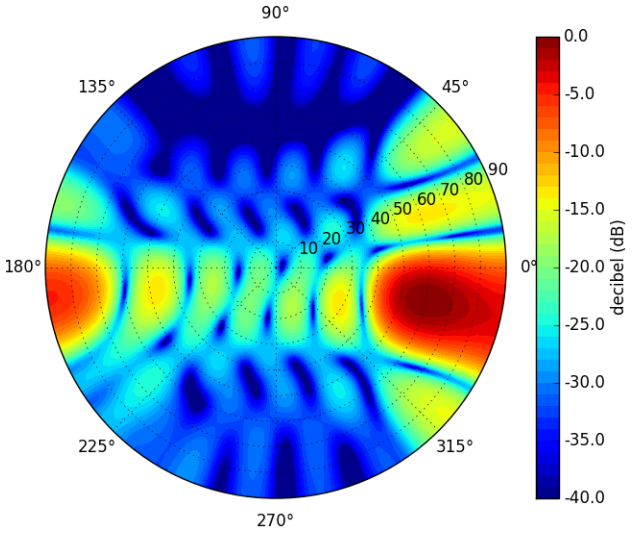

Figure 5.70: Array Factor Contour of 40 Element Rectangular Array with Beam-steering in Decibels

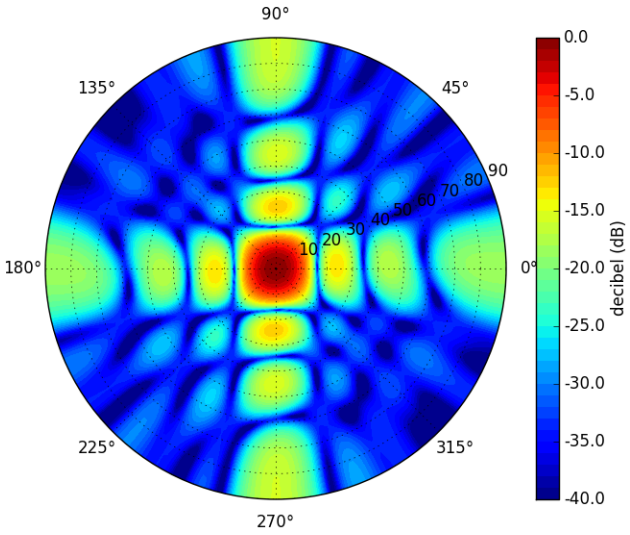

Figure 5.71: Array Factor Contour of 50 Element Rectangular Array in Decibels

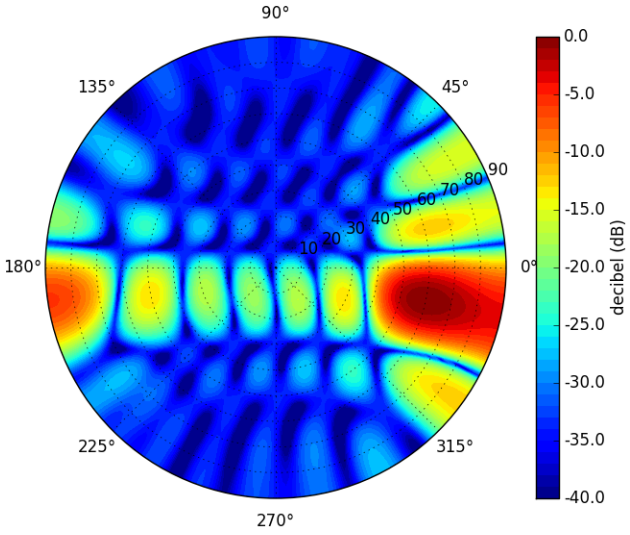

Figure 5.72: Array Factor Contour of 50 Element Rectangular Array with Beam-steering in Decibels

5.6.2.5 *Rectangular Direction of Arrival*

The MUSIC DoA estimation algorithm processed the synthetic aperture array data after despreading each incident signal with its PRN sequence and prior to combining or beamsteering. A peak detection algorithm was used to determine the predicted signal direction of origin. The figures show that an increase in the number of elements improves or narrows the spatial resolution of the peak. Figure 5.73 shows the DoA error under CW interference CW_0 and CW_1, where CW_0 is near the horizon and CW_1 is near a satellite signal. Regardless of the presence of interference or the interference's proximity to the signal source, the DoA error flattens around an array of size 15 mirroring the number of elements improving or narrowing the directivity as the array size is increased.

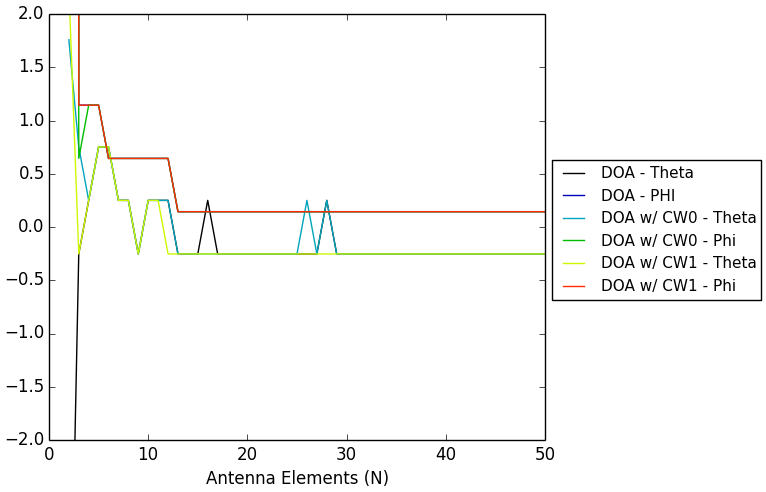

Figure 5.73: DoA error for different interference sources for $\lambda/2$ spacing

5.6.2.6 Nominal SNR and SINR Comparison

A comparison of the SNR and SINR ratios under ideal or nominal DoA information from signal PRN_7 for beamsteering, MUSIC DoA information from signal PRN_7, and all signals of interest DoA generated by MUSIC estimation averaged together is constructed. The comparison occurred at $\lambda/2$ spacing, and the results are shown in Figure 5.74 and Figure 5.75. From these two graphs it is apparent that the DoA error generated by the MUSIC algorithm is very small; given by the PRN_7 signal closely tracks the nominal or ideal signal as the number array elements increased. The averaged signal power shows that all six signals of interest follow PRN_7 with a small variance.

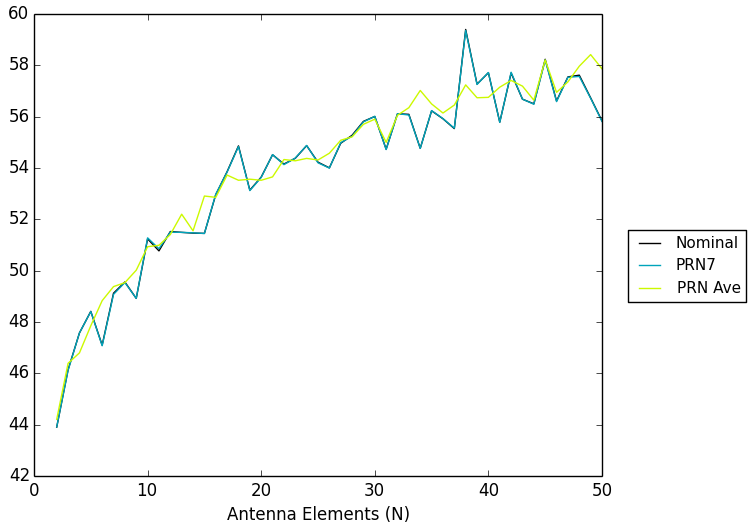

Figure 5.74: Rectangular Array SNR for Nominal, PRN_7, and Averaged PRN Signal DoA at $\lambda/2$ Spacing

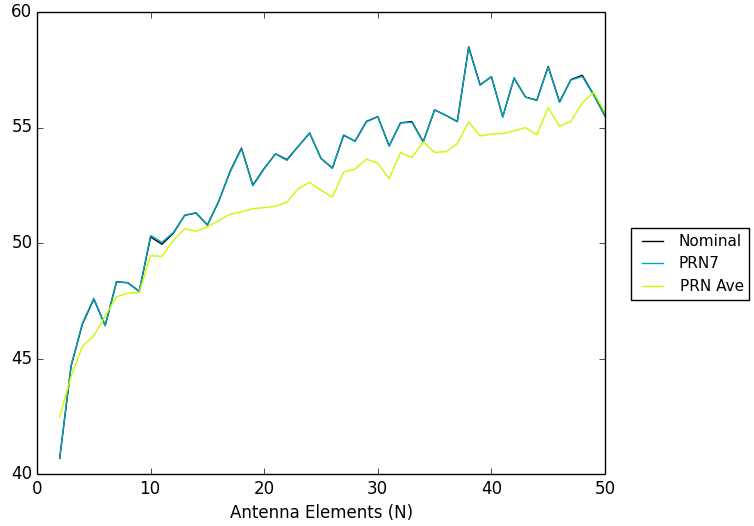

Figure 5.75: Rectangular Array SINR for Nominal, PRN_7, and Averaged PRN Signal DoA at $\lambda/2$ Spacing, with CW_0 Interference

5.6.2.7 Noise Level Comparison

The noise level was evaluated for $\lambda/2$ spacing with a noise temperature of 513 K and 2052 K and interference source CW_0. The SNR and SINR are shown in Figure 5.76 and Figure 5.77 respectively. From the figures it is apparent that a higher noise floor has a negative impact on the SNR and SINR, but the size of the array has a limited impact on complex AWGN as expected. The two noise curves are identical only differing in magnitude. The decrease in SNR and SINR for an array size near 5 elements at high noise is likely caused by a large main beam and the existence of a large sidelobe.

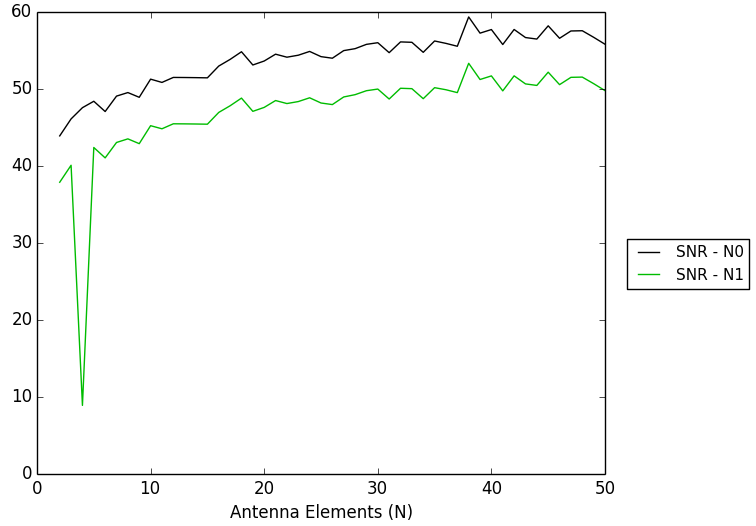

Figure 5.76: Rectangular Array SNR for noise levels N_0 and N_1 at $\lambda/2$ spacing

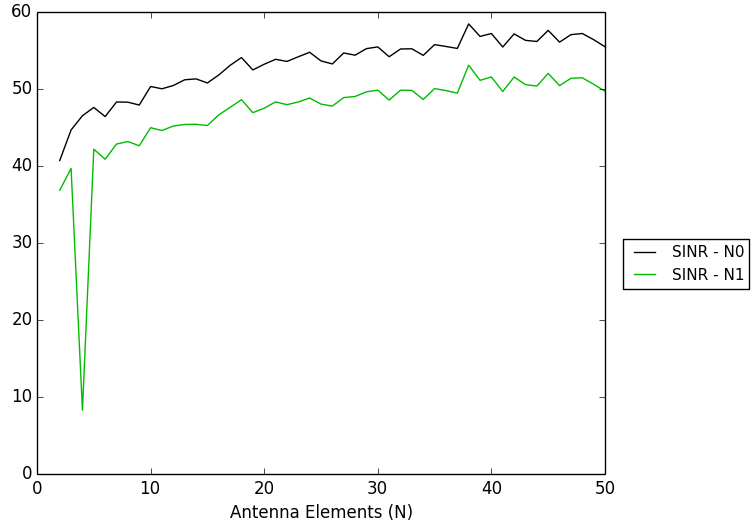

Figure 5.77: Rectangular Array SINR for noise levels N_0 and N_1 at $\lambda/2$ spacing

5.6.2.8 *Interference Position Comparison*

Figure 5.78 shows the SINR under CW interference CW_0 and CW_1, where CW_0 is near the horizon and CW_1 is near a satellite signal. The interference source near the satellite signal has a smaller gain as expected. When beamsteering near the signal of interest a highly focused pattern is moving near the interference source placing it near a gain rather than a null. This results in increased interference power and a decreased SINR.

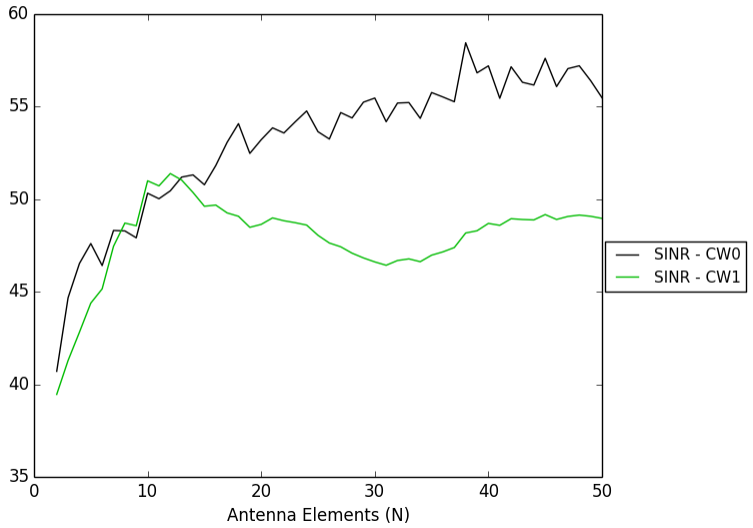

Figure 5.78: Rectangular Array SINR for Different Interference Sources at $\lambda/2$ Spacing

5.6.2.9 *Array Inter-Element Spacing Comparison*

The effect on the SNR and SINR ratios respectively for λ, $\lambda/2$, $\lambda/4$, $\lambda/10$ array spacing is captured in Figure 5.79 and Figure 5.80. The comparable ratios are likely the result of the communication despreading process selecting only the signal of

interest. The presence of one signal would cause aliasing or a decrease in directivity to have a marginal affect. In the scenario with CW and a small array spacing of $\lambda/10$ a decrease in SINR occurred as the array size increased. The cause for this decrease is likely a smaller directivity compared to the other array spacings and aliasing placing sidelobes near the interference source.

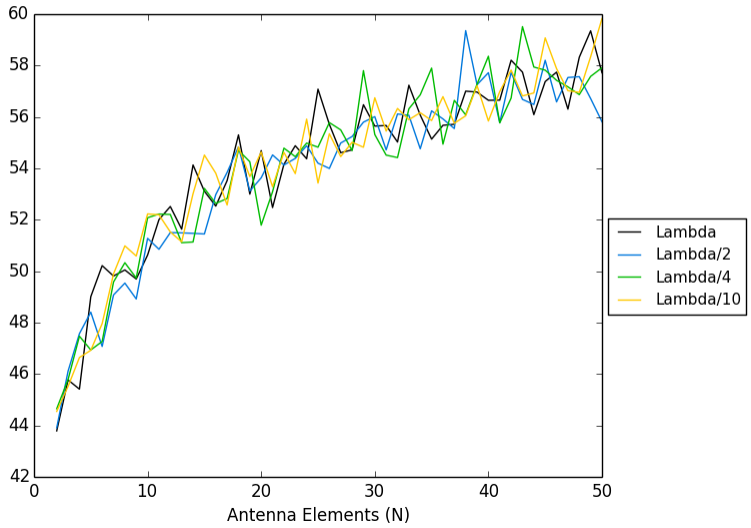

Figure 5.79: Rectangular Array SNR for λ, $\lambda/2$, $\lambda/4$, $\lambda/10$ spacing

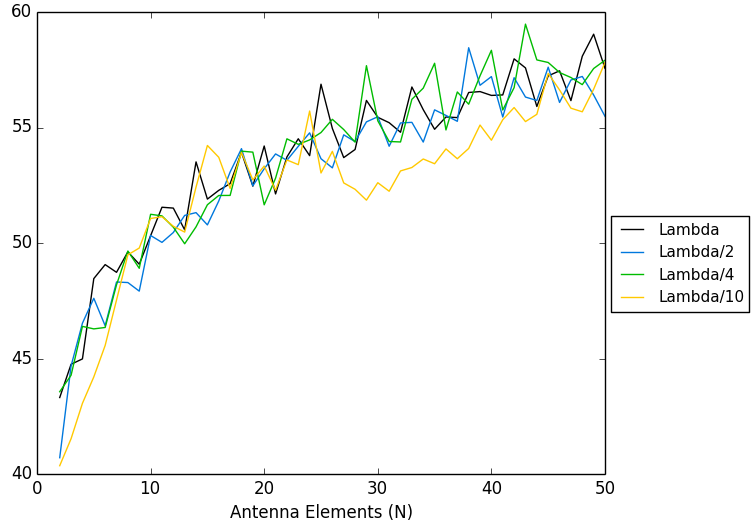

Figure 5.80: Rectangular Array SINR for λ, $\lambda/2$, $\lambda/4$, $\lambda/10$ spacing

5.6.3 Random Sequential Array Placement

The sequential random array is constructed using randomly placed elements using a uniformly distributed random process according to a maximum T_{max} and minimum T_{min} spacing tolerance. The difference between the random array and random sequential array is that the random sequential array for an array of size N maintains the prior placement of all $N-1$ antenna elements. This is accomplished by reseeding the random number generate to the same value at the start of every array generation regardless of the array size and following the same method to calculate the maximum radius specified by the UCA in Equation 5.45. As with the random array, the tolerance criterion requires that at least one element is within T_{max} and no closer than T_{min} as shown by $T_{min} \leq \|A(r_i - A(r,\theta)\|_2, \theta_i) \leq T_{max}$. The Algorithm 2 explains how the array is generated using the tolerance parameters.

Algorithm 2 RandomSequential Array Element Placement

for ii = 2:n **do**
  $\theta_r = \frac{2\pi}{ii}$
  $d = \frac{\lambda}{2}$
  $r = \sqrt{\frac{d^2}{2(1-\cos(\theta_r))}}$
  while not tolerance **do**
    $\vec{\theta} = rand \cdot 2\pi$
    $\vec{r} = rand \cdot r$
    $\vec{X} = \vec{r} \cdot \cos(\vec{\theta})$
    $\vec{Y} = \vec{r} \cdot \sin(\vec{\theta})$
    $\vec{Z} = \vec{0}$
  end while
end for

5.6.3.1 Random Sequential Element Configuration

Following the array placement described in Section 5.6.3 where $T_{max} = \lambda/2$ for array sizes of 5, 10, 15, 20, 30, 40, and 50 result in the configurations shown in Figures 5.81 - 5.87.

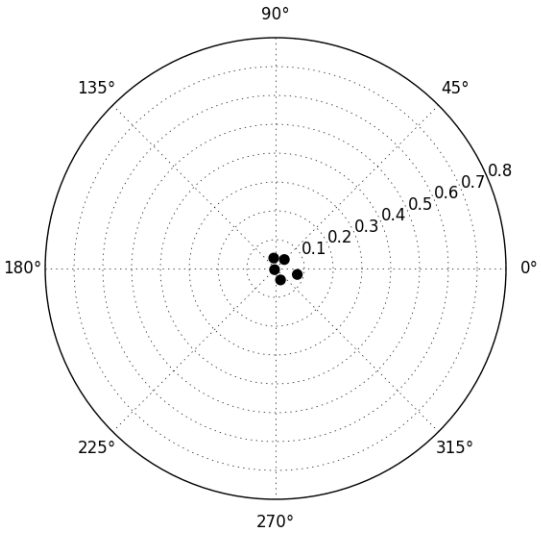

Figure 5.81: Random Sequential 5 Element Configuration

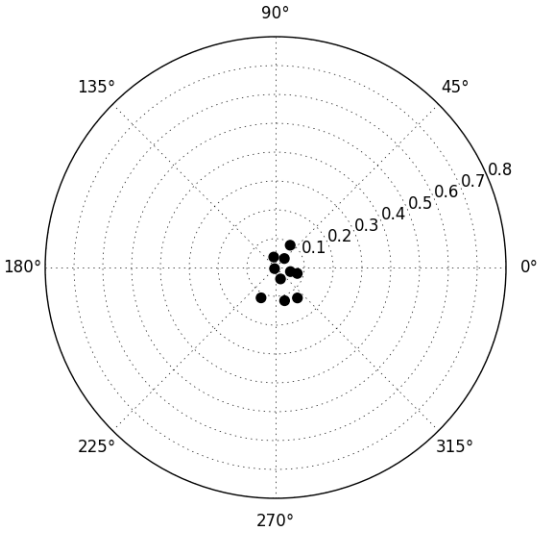

Figure 5.82: Random Sequential 10 Element Configuration

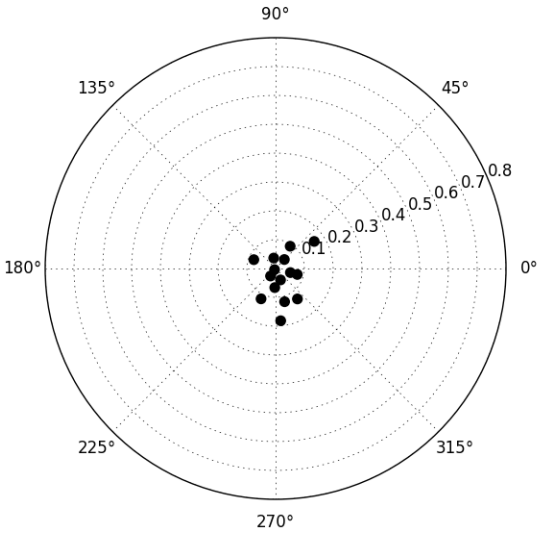

Figure 5.83: Random Sequential 15 Element Configuration

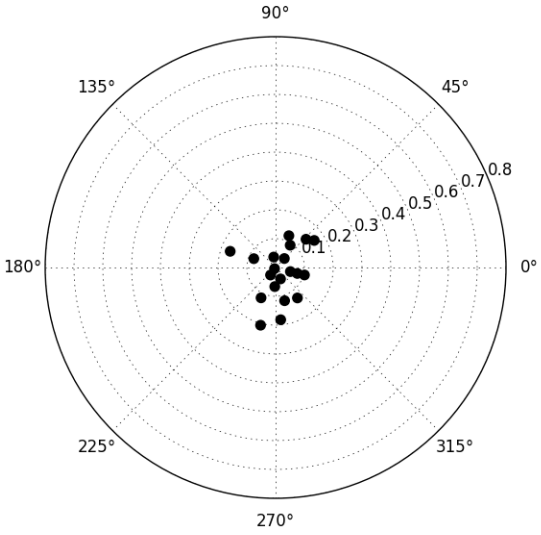

Figure 5.84: Random Sequential 20 Element Configuration

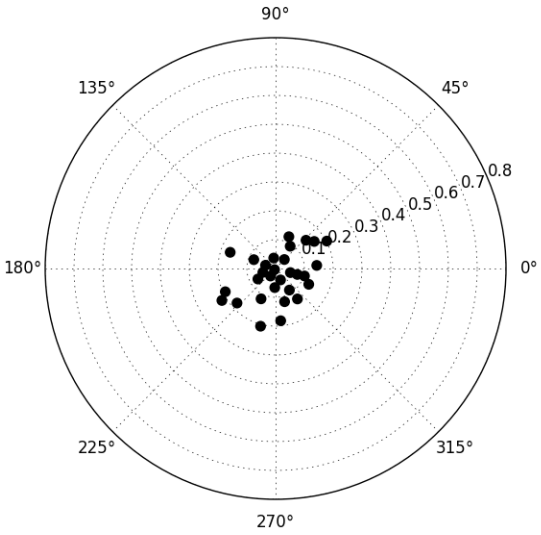

Figure 5.85: Random Sequential 30 Element Configuration

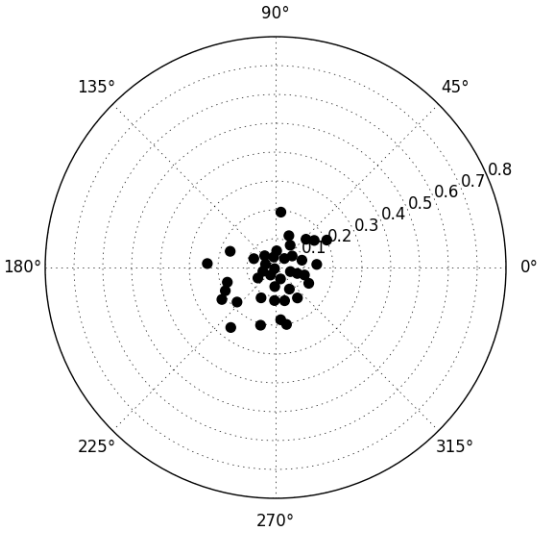

Figure 5.86: Random Sequential 40 Element Configuration

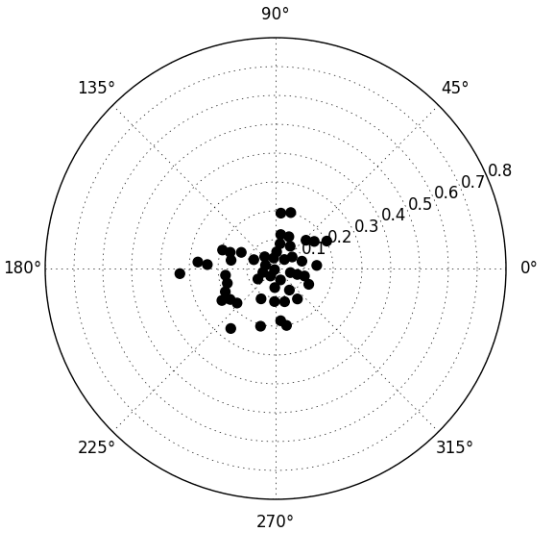

Figure 5.87: Random Sequential 50 Element Configuration

5.6.3.2 Array Size

The circular area encompassed by the array from 2 elements to 50 in m^2 is shown in Figure 5.88. As expected the array size increases with additional elements and is highest for the maximum tolerance $T_{max} = \lambda$.

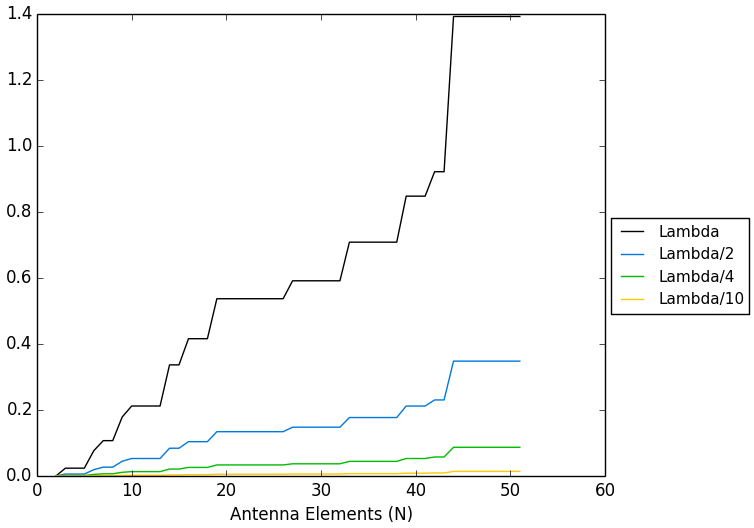

Figure 5.88: Array Size for λ, $\lambda/2$, $\lambda/4$, $\lambda/10$ Array Spacing in Circular Area in m^2 for Random Sequential Array

5.6.3.3 Directivity

Directivity is a measure of the concentration of an array beam. The directivity for the Random Sequential Array is shown in Figure 5.89. As expected the directivity increases for all tolerances of T_{max} simulated.

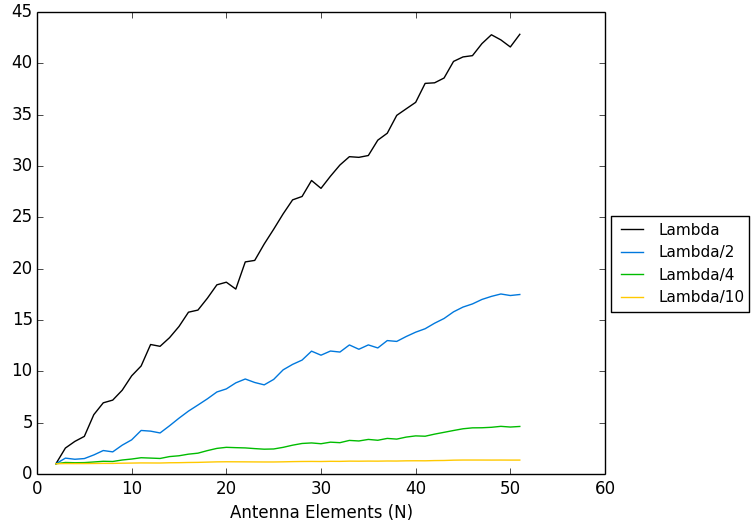

Figure 5.89: Directivity for λ, $\lambda/2$, $\lambda/4$, $\lambda/10$ Array Spacing for Random Sequential Array

5.6.3.4 Random Sequential Array Factor

The Random Sequential Array is characterized by a main beam with non-uniform null structure as depicted in Figures 5.90 - 5.102 for a tolerance of $T_{max} = \lambda/2$. The main beam was beamsteered in the direction of $(\theta, \phi) = (60.0821, 374.6239)$ of a single source as shown in Figures 5.91 - 5.103. The focus of the main beam mirrors the increase in directivity shown in Figure 5.89.

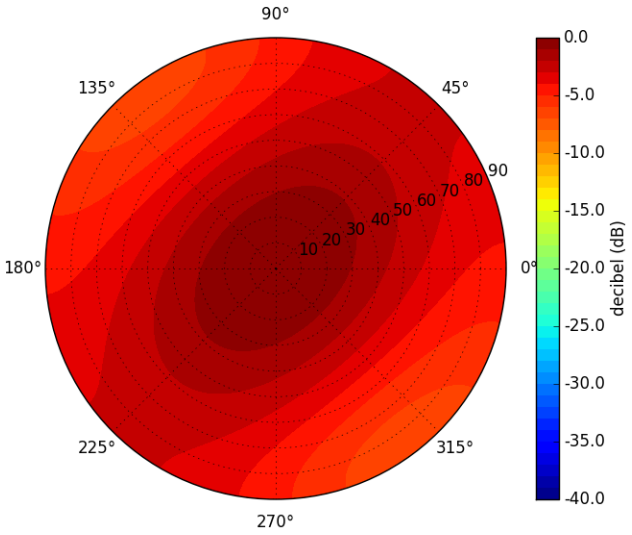

Figure 5.90: Array Factor Contour of 5 Element Random Sequential Array in Decibels

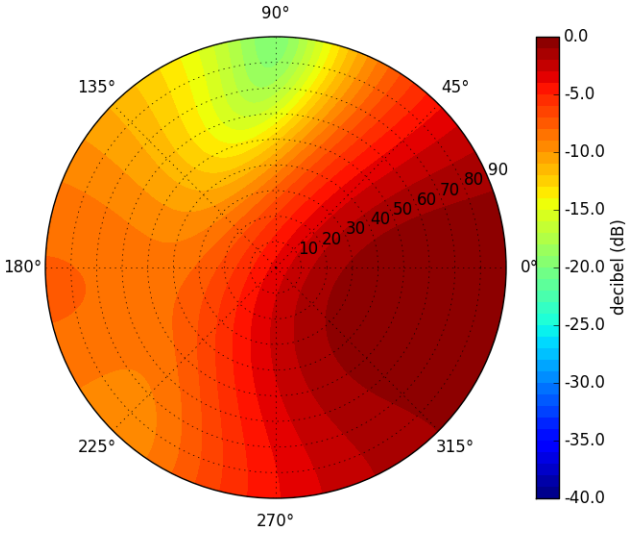

Figure 5.91: Array Factor Contour of 5 Element Random Sequential Array with Beamsteering in Decibels

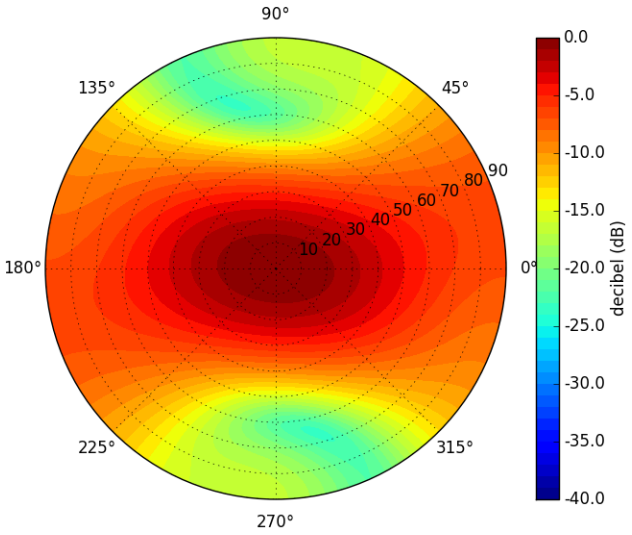

Figure 5.92: Array Factor Contour of 10 Element Random Sequential Array in Decibels

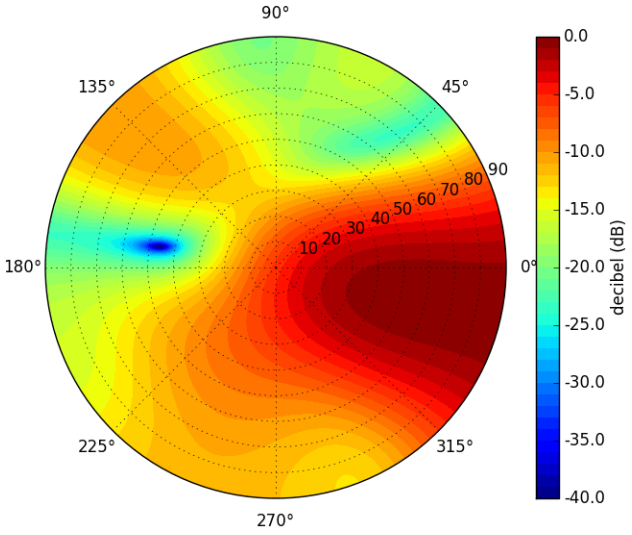

Figure 5.93: Array Factor Contour of 10 Element Random Sequential Array with Beamsteering in Decibels

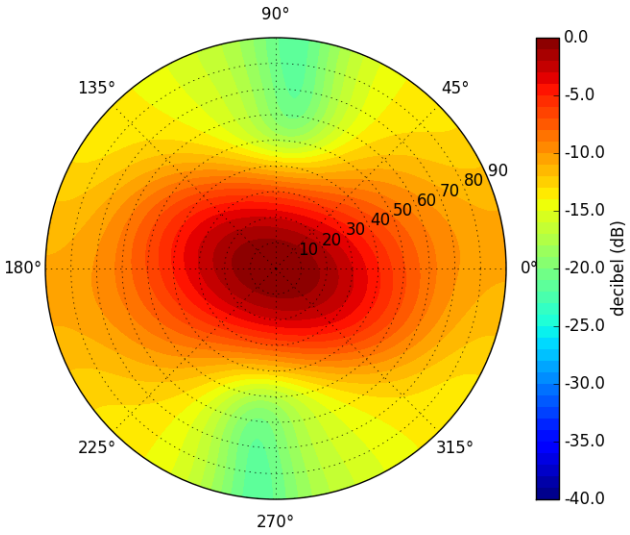

Figure 5.94: Array Factor Contour of 15 Element Random Sequential Array in Decibels

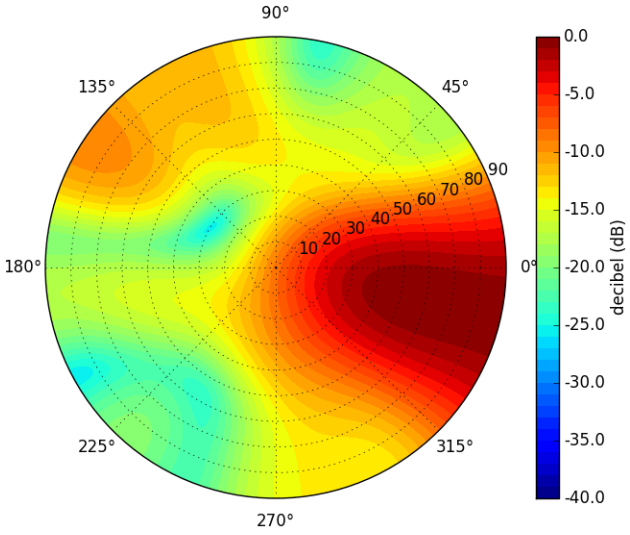

Figure 5.95: Array Factor Contour of 15 Element Random Sequential Array with Beamsteering in Decibels

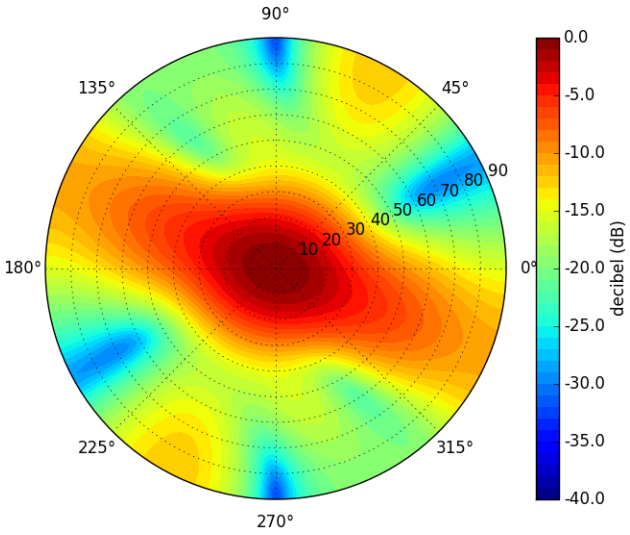

Figure 5.96: Array Factor Contour of 20 Element Random Sequential Array in Decibels

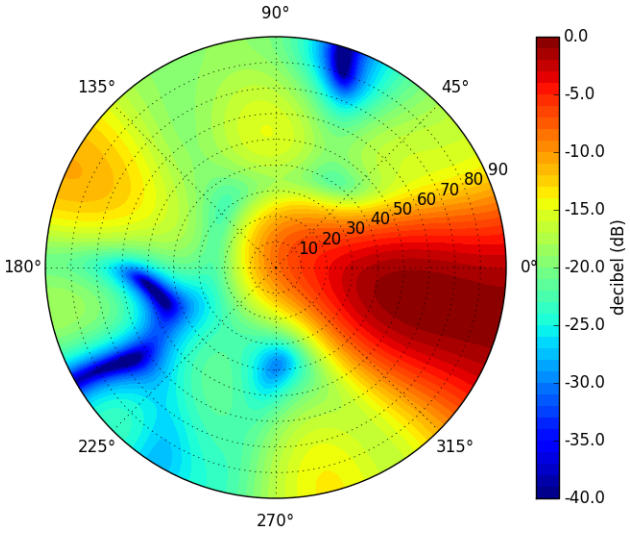

Figure 5.97: Array Factor Contour of 20 Element Random Sequential Array with Beamsteering in Decibels

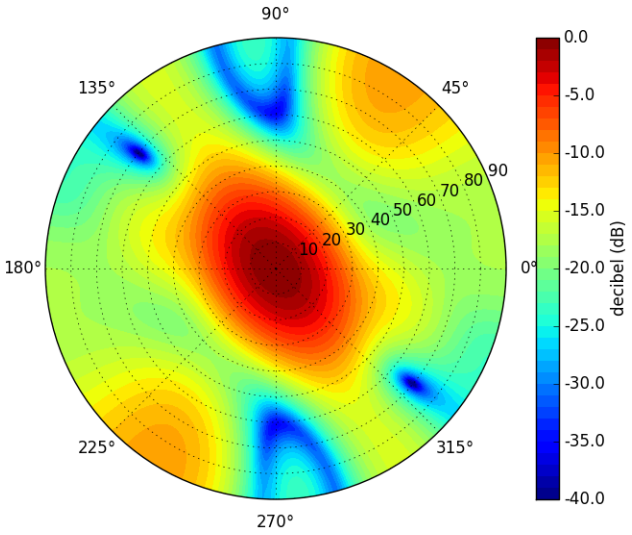

Figure 5.98: Array Factor Contour of 30 Element Random Sequential Array in Decibels

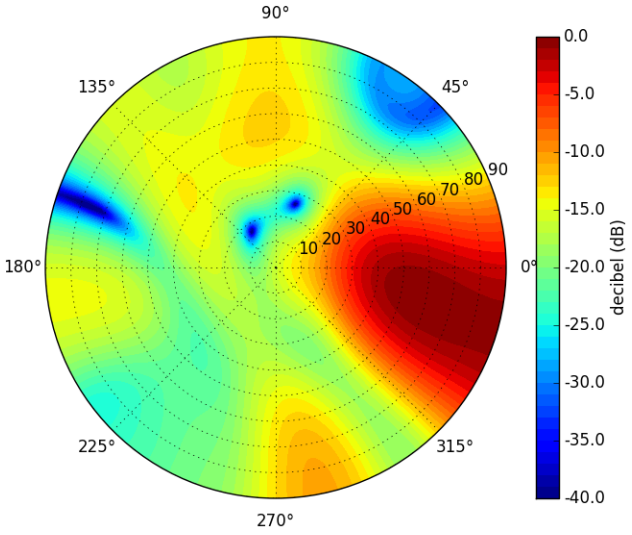

Figure 5.99: Array Factor Contour of 30 Element Random Sequential Array with Beamsteering in Decibels

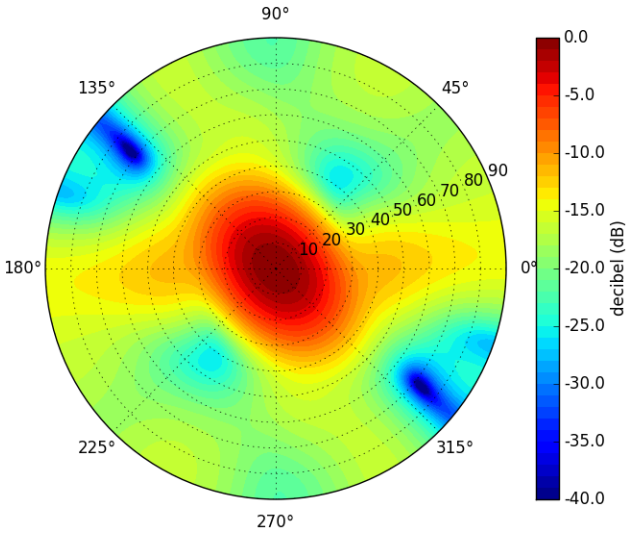

Figure 5.100: Array Factor Contour of 40 Element Random Sequential Array in Decibels

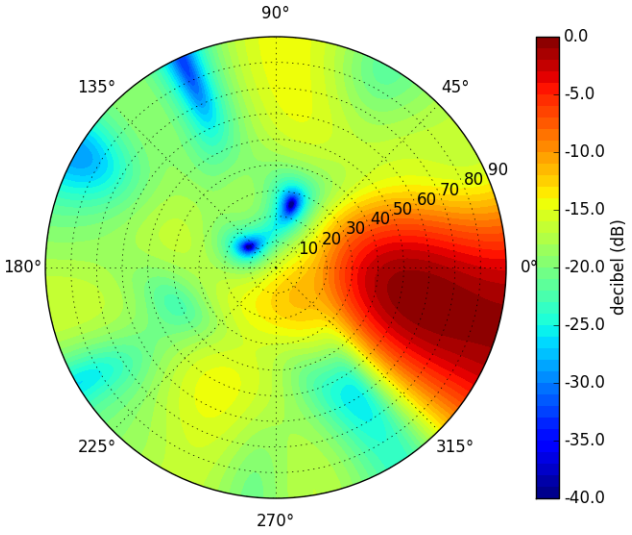

Figure 5.101: Array Factor Contour of 40 Element Random Sequential Array with Beamsteering in Decibels

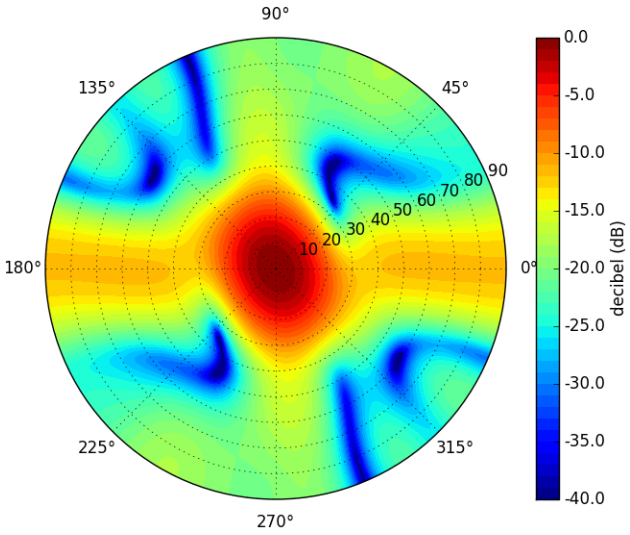

Figure 5.102: Array Factor Contour of 50 Element Random Sequential Array in Decibels

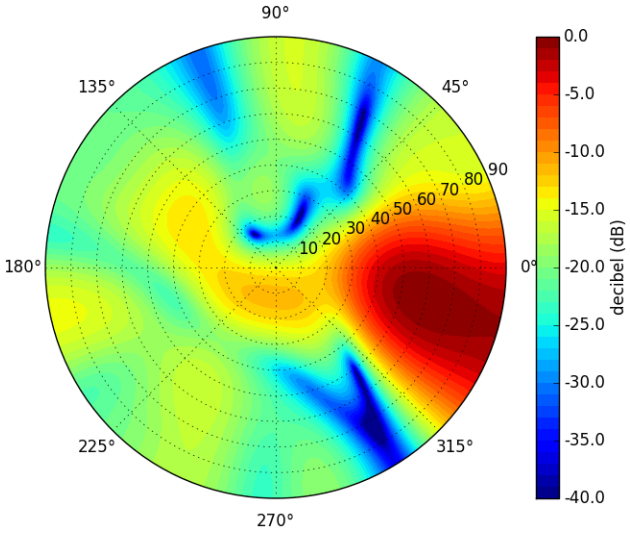

Figure 5.103: Array Factor Contour of 50 Element Random Sequential Array with Beamsteering in Decibels

5.6.3.5 Random Sequential Direction of Arrival

The MUSIC DoA estimation algorithm processed the synthetic aperture array data after despreading each incident signal with its PRN sequence and prior to combining or beamsteering. A peak detection algorithm was used to determine the predicted signal direction of origin. Figure 5.104 shows the DoA error under CW interference CW_0 and CW_1, where CW_0 is near the horizon and CW_1 is near a satellite signal using an algorithm maximum resolution of .5°. Regardless of the presence of interference or the interference's proximity to the signal source, the DoA error flattens around an array of size 25. The decrease in error mirrors the directivity improvement as the number of elements is increased.

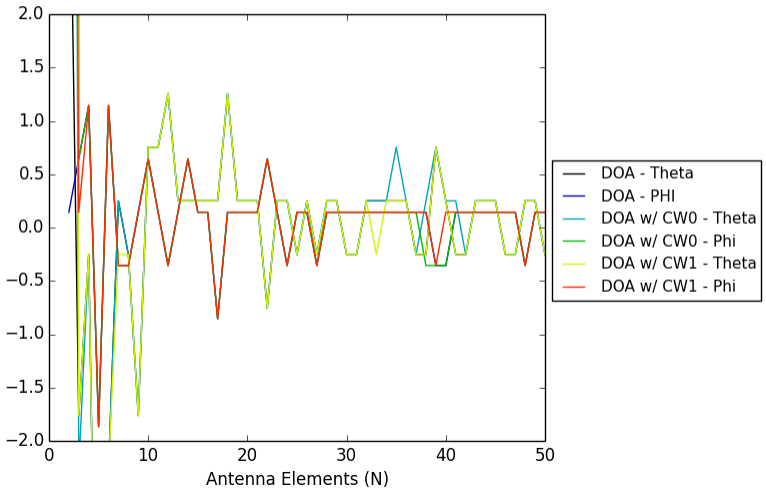

Figure 5.104: DoA error for different interference sources for $\lambda/2$ spacing

5.6.3.6 Nominal SNR and SINR Comparison

A comparison of the SNR and SINR ratios under ideal or nominal DoA information from signal PRN_7 for beamsteering, MUSIC DoA information from signal PRN_7, and all signals of interest DoA generated by MUSIC estimation averaged together. The comparison occurred at $\lambda/2$ spacing, and the results are shown in Figure 5.105 and Figure 5.106. From these two graphs it is apparent that the DoA error generated by the MUSIC algorithm is very small shown by the PRN_7 signal closely tracking the nominal or ideal signal as the number array elements increased. The averaged signal power shows that all six signals of interest follow PRN_7 with a small variance.

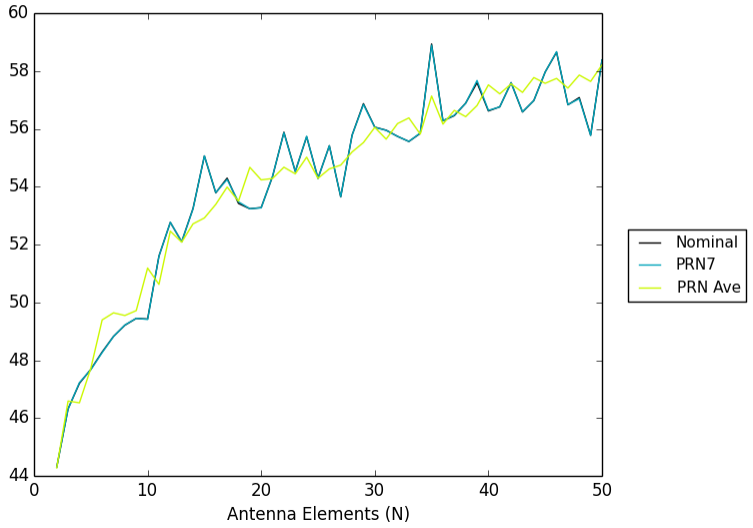

Figure 5.105: Random Sequential Array SNR for Nominal, PRN_7, and Averaged PRN Signal DoA at $\lambda/2$ Spacing

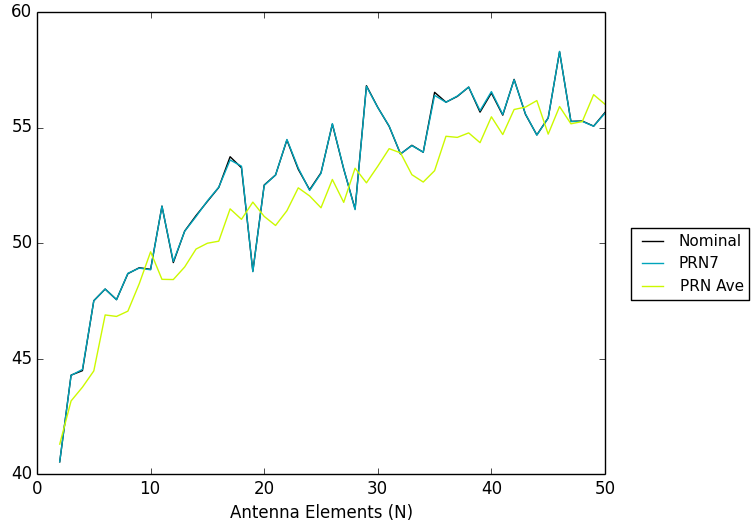

Figure 5.106: Random Sequential Array SINR for Nominal, PRN_7, and Averaged PRN Signal DoA at $\lambda/2$ Spacing, with CW_0 Interference

5.6.3.7 Noise Level Comparison

The noise level was evaluated for $\lambda/2$ spacing with at a noise temperature of 513 K and 2052 K with interference source CW_0. The SNR and SINR are shown in Figure 5.107 and Figure 5.108 respectively. From the figures it is apparent that a higher noise floor has a negative impact on the SNR and SINR, but the size of the array has a limited impact on complex AWGN as expected. The two noise curves are identical only differing in magnitude.

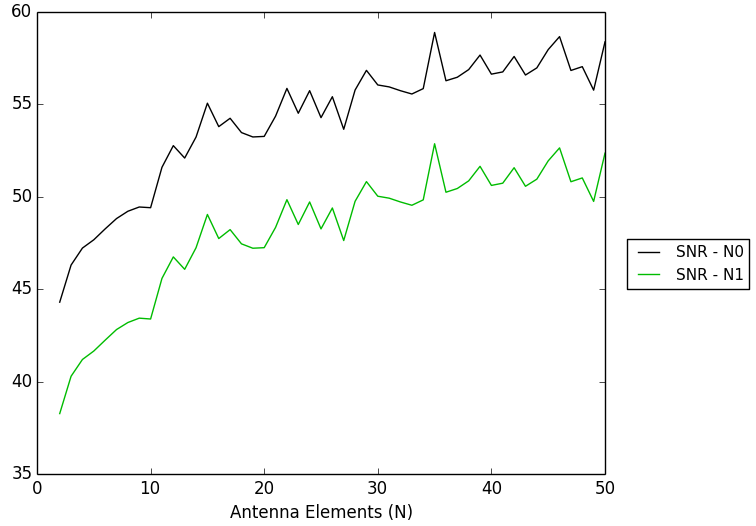

Figure 5.107: Random Sequential Array SNR for noise levels N_0 and N_1 at $\lambda/2$ spacing

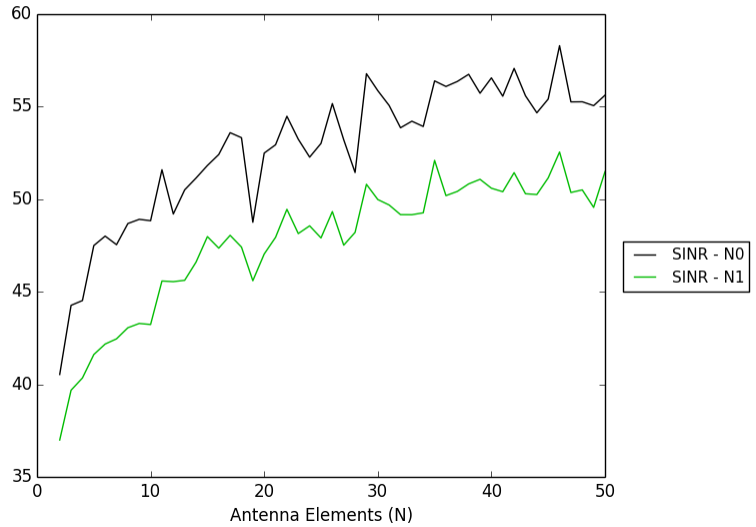

Figure 5.108: Random Sequential Array SINR for noise levels N_0 and N_1 at $\lambda/2$ spacing

5.6.3.8 Interference Position Comparison

Figure 5.109 shows the SINR under CW interference CW_0 and CW_1, where CW_0 is near the horizon and CW_1 is near a satellite signal. The interference source near the satellite signal has a smaller gain as expected. When beamsteering near the signal of interest a highly focused pattern is moving near the interference source placing it near a gain rather than a null. This results in increased interference power and a decreased SINR. The decrease in SINR for CW_1 is likely the result of the main beam being steering closer to the interference source as the number of elements increased.

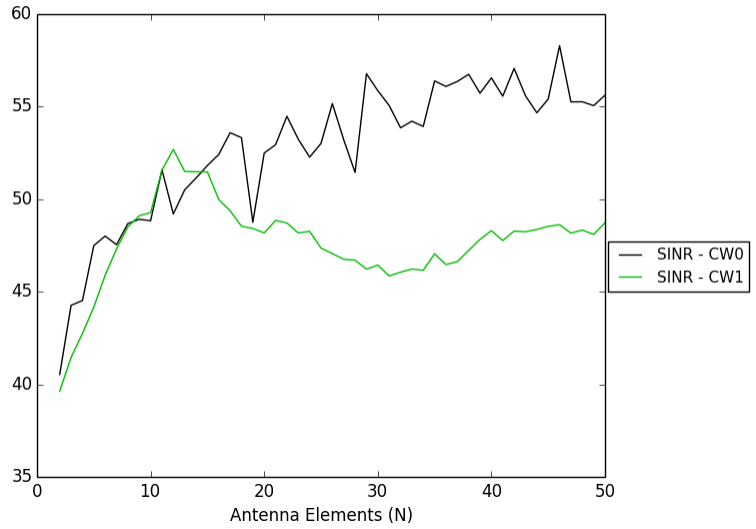

Figure 5.109: Random Sequential Array SINR for Different Interference Sources at $\lambda/2$ Spacing

5.6.3.9 Array Inter-Element Spacing Comparison

The effect on the SNR and SINR ratios respectively for λ, $\lambda/2$, $\lambda/4$, $\lambda/10$ array spacing is shown in Figure 5.110 and Figure 5.111 respectively. The comparable

ratios are likely the result of the communication despreading process selecting only the signal of interest. In the scenario with CW and a small array spacing of $\lambda/10$ a decrease in SINR occurred as the array size increased. The cause for this decrease is likely a smaller directivity compared to the other array spacings and aliasing placing sidelobes near the interference source.

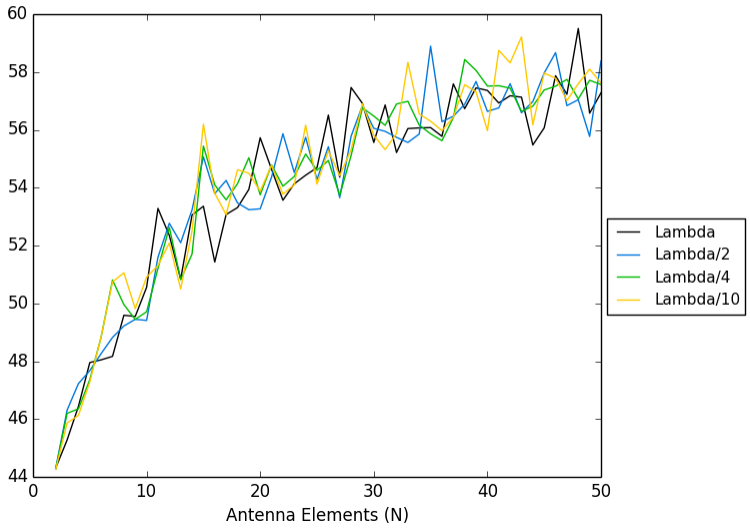

Figure 5.110: Random Sequential Array SNR for λ, $\lambda/2$, $\lambda/4$, $\lambda/10$ spacing

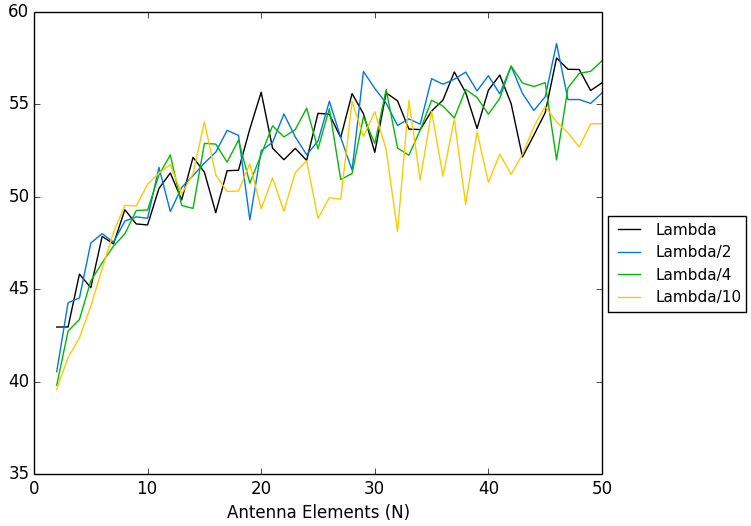

Figure 5.111: Random Sequential Array SINR for λ, $\lambda/2$, $\lambda/4$, $\lambda/10$ spacing

5.6.4 Random Array Placement

The random array is made of antenna elements that are randomly placed using a uniformly distributed random number within a circle of a certain radius where elements are placed no farther apart than a maximum tolerance T_{max} and no closer than a minimum tolerance T_{min} shown by $T_{min} \leq \|A(r_i - A(r,\theta)\|_2, \theta_i) \leq T_{max}$. The circle radius was determined using the same formula for the UCA as described in Equation 5.45. After element generation shown in Equation 5.46 and Equation 5.47, the coordinates were converted from Polar to Cartesian coordinates, and the

tolerance was verified.

$$\vec{\theta} = rand(n) \cdot 2\pi \tag{5.46}$$

$$\vec{r} = rand(n) \cdot r \tag{5.47}$$

$$\vec{X} = \vec{r} \cdot \cos(\vec{\theta}) \tag{5.48}$$

$$\vec{Y} = \vec{r} \cdot \sin(\vec{\theta}) \tag{5.49}$$

$$\vec{Z} = \vec{0} \tag{5.50}$$

5.6.4.1 Random Element Configuration

Following the array placement described in Section 5.6.4 where $T_{max} = \lambda/2$ for array sizes of 5, 10, 15, 20, 30, 40, and 50 result in the configurations shown in Figures 5.112 - 5.118.

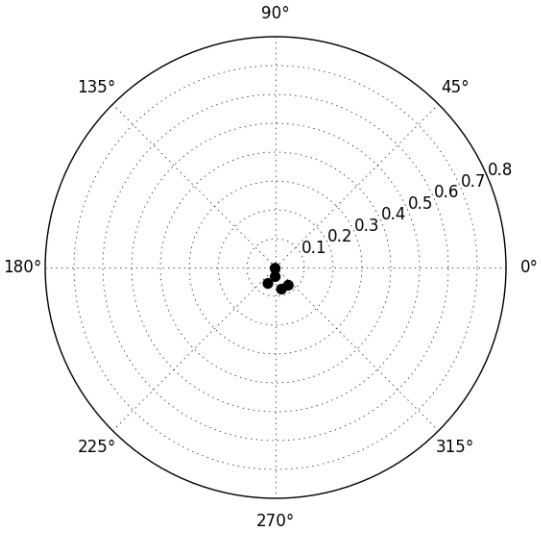

Figure 5.112: Random Array 5 Element Configuration

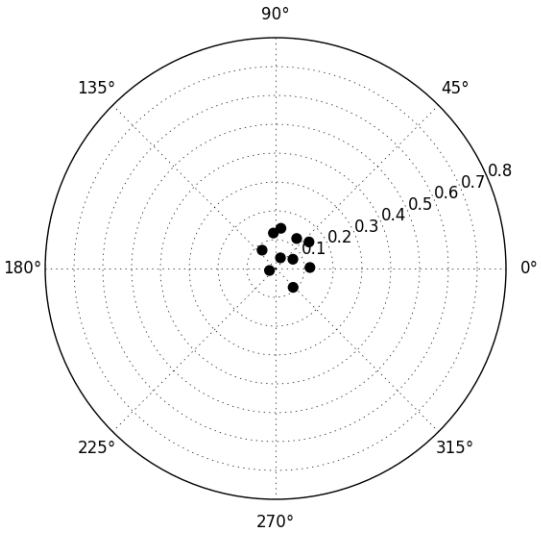

Figure 5.113: Random Array 10 Element Configuration

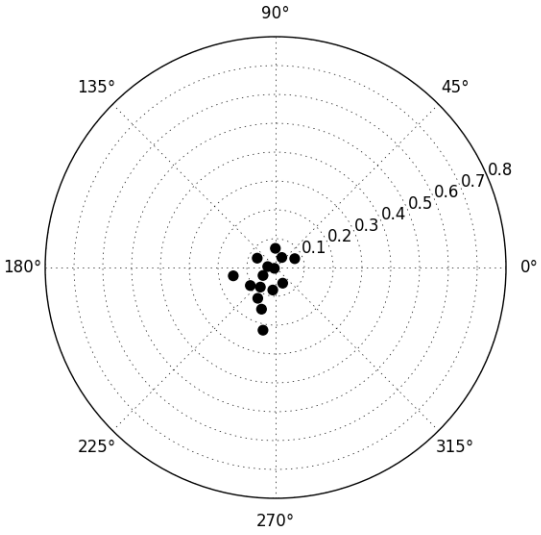

Figure 5.114: Random Array 15 Element Configuration

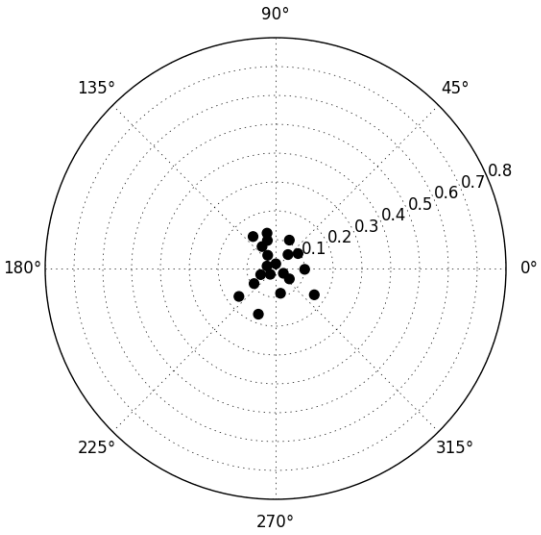

Figure 5.115: Random Array 20 Element Configuration

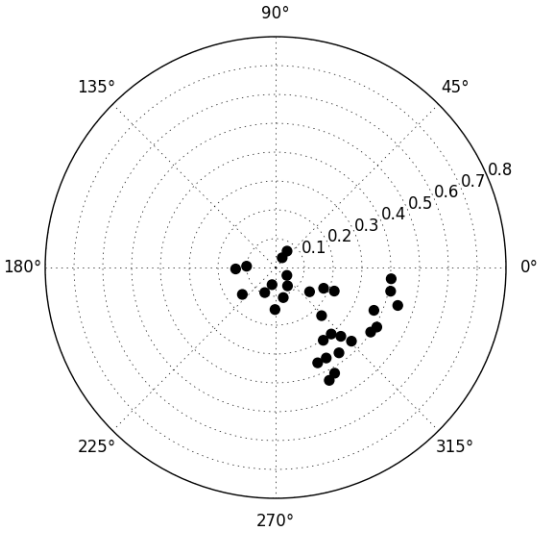

Figure 5.116: Random Array 30 Element Configuration

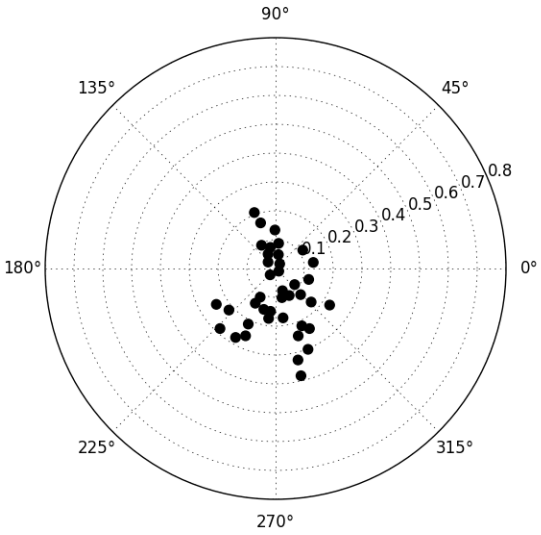

Figure 5.117: Random Array 40 Element Configuration

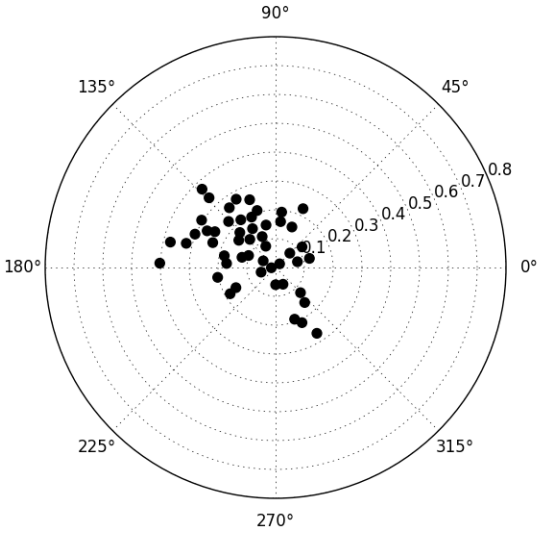

Figure 5.118: Random Array 50 Element Configuration

5.6.4.2 Array Size

The circular area encompassed by the array from 2 elements to 50 in m^2 is shown in Figure 5.119. As expected the array size increases with additional elements and is highest for the maximum tolerance $T_{max} = \lambda$.

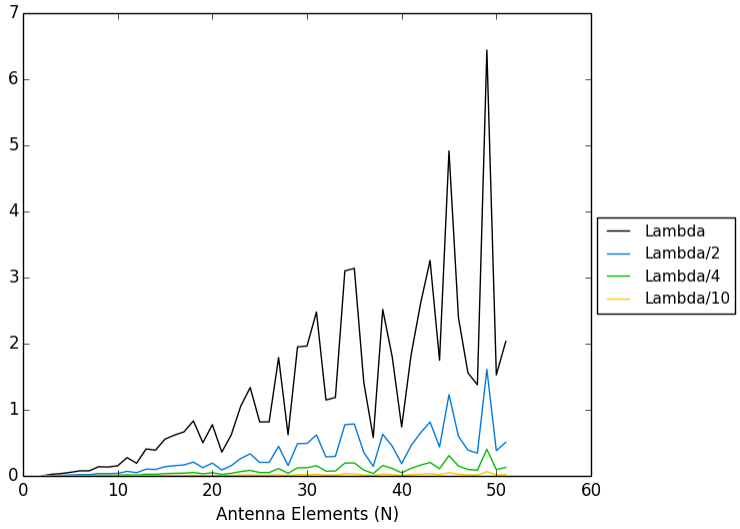

Figure 5.119: Array Size for λ, $\lambda/2$, $\lambda/4$, $\lambda/10$ Array Spacing in Circular Area in m^2 for Random Array

5.6.4.3 Directivity

Directivity is a measure of the concentration of an array beam. The directivity for the Random Array is shown in Figure 5.120. As expected the directivity increases for all tolerances of T_{max} simulated.

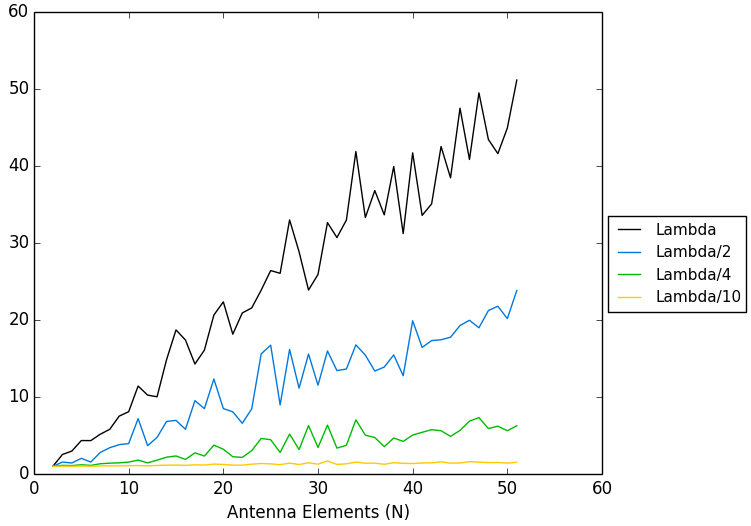

Figure 5.120: Directivity for λ, $\lambda/2$, $\lambda/4$, $\lambda/10$ Array Spacing for Random Array

5.6.4.4 Random Array Factor

The Random Array is characterized by a random main beam and random null structure as depicted in Figures 5.121 - 5.133 for a tolerance of $T_{max} = \lambda/2$. The random structure beamsteering in the direction of $(\theta, \phi) = (60.0821, 374.6239)$ of a single source is also shown in Figures 5.122 - 5.134. The focus of the main beam mirrors the increase in directivity shown in Figure 5.120.

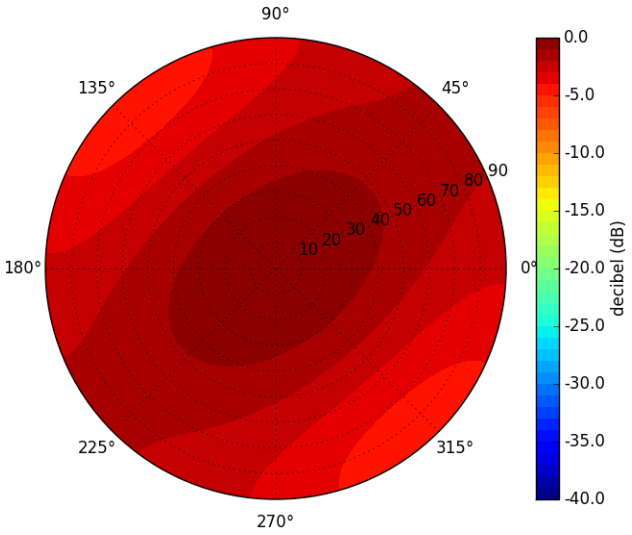

Figure 5.121: Array Factor Contour of 5 Element Random Array in Decibels

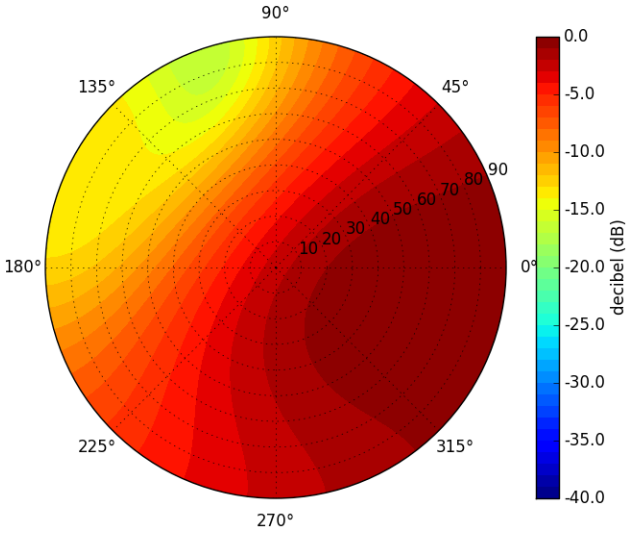

Figure 5.122: Array Factor Contour of 5 Element Random Array with Beamsteering in Decibels

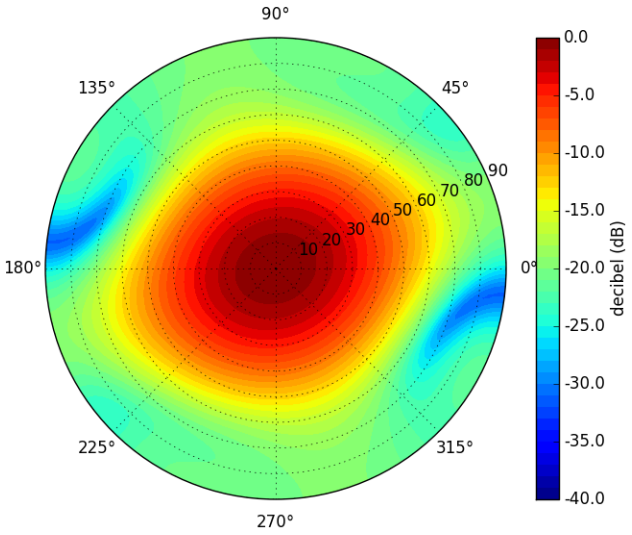

Figure 5.123: Array Factor Contour of 10 Element Random Array in Decibels

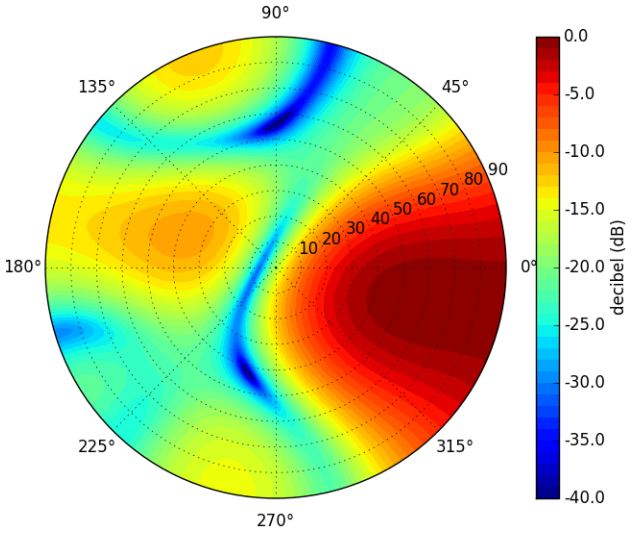

Figure 5.124: Array Factor Contour of 10 Element Random Array with Beamsteering in Decibels

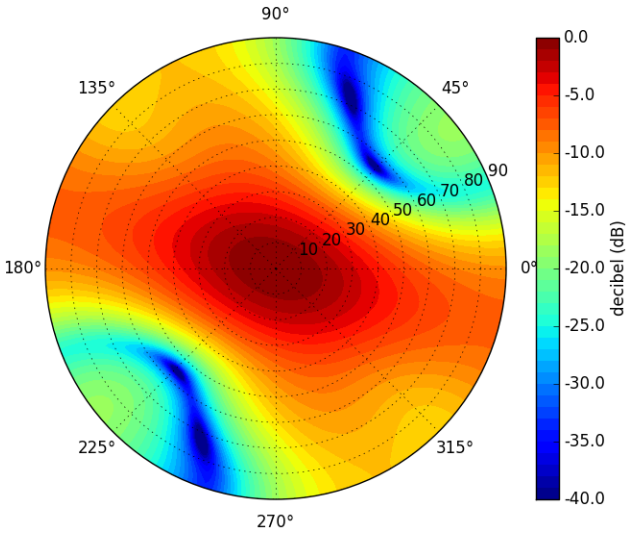

Figure 5.125: Array Factor Contour of 15 Element Random Array in Decibels

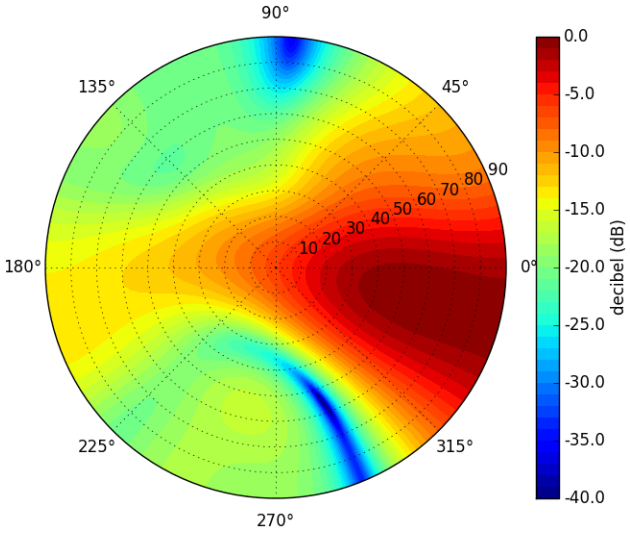

Figure 5.126: Array Factor Contour of 15 Element Random Array with Beamsteering in Decibels

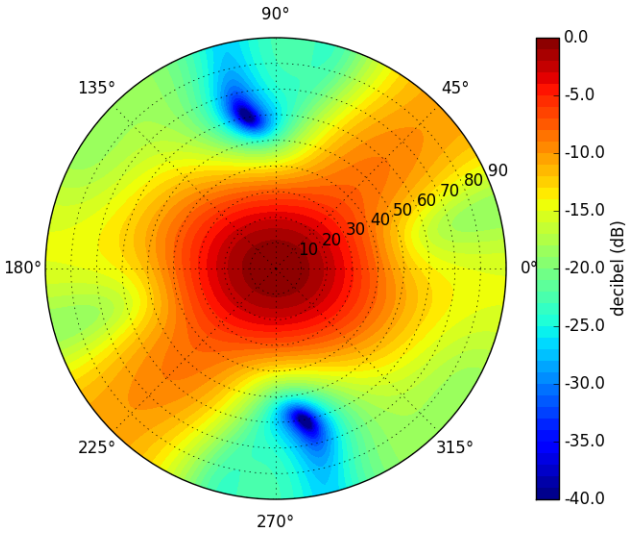

Figure 5.127: Array Factor Contour of 20 Element Random Array in Decibels

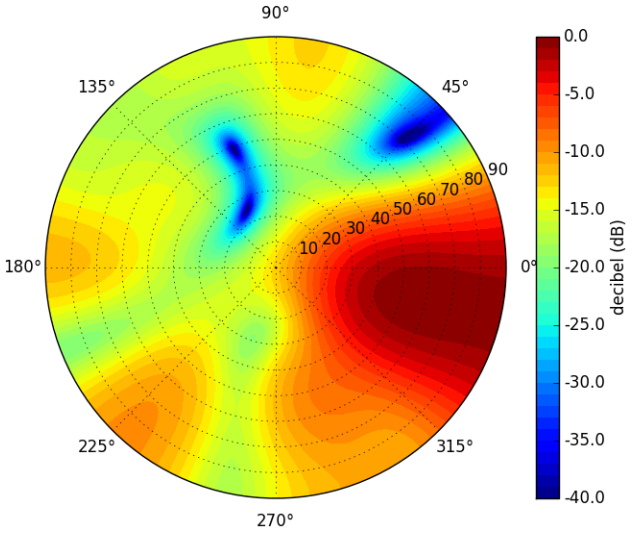

Figure 5.128: Array Factor Contour of 20 Element Random Array with Beamsteering in Decibels

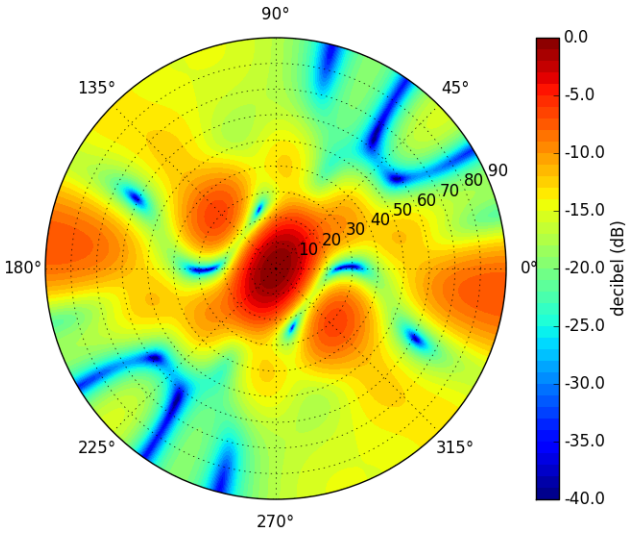

Figure 5.129: Array Factor Contour of 30 Element Random Array in Decibels

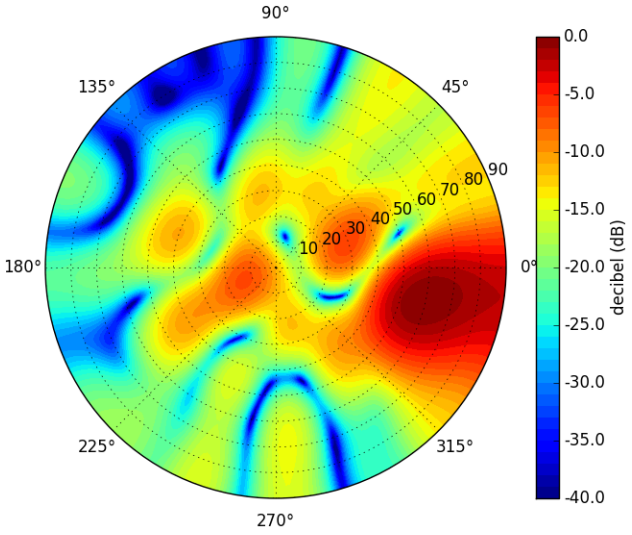

Figure 5.130: Array Factor Contour of 30 Element Random Array with Beamsteering in Decibels

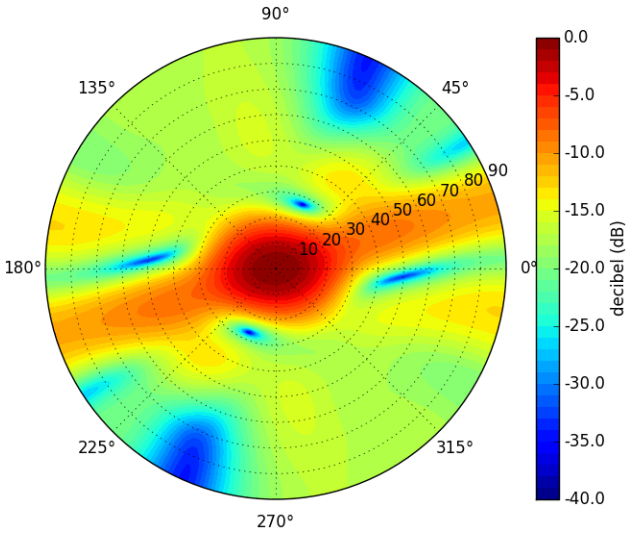

Figure 5.131: Array Factor Contour of 40 Element Random Array in Decibels

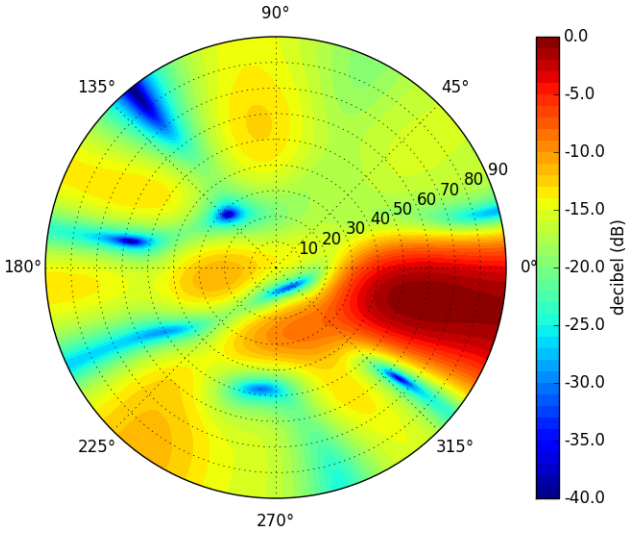

Figure 5.132: Array Factor Contour of 40 Element Random Array with Beamsteering in Decibels

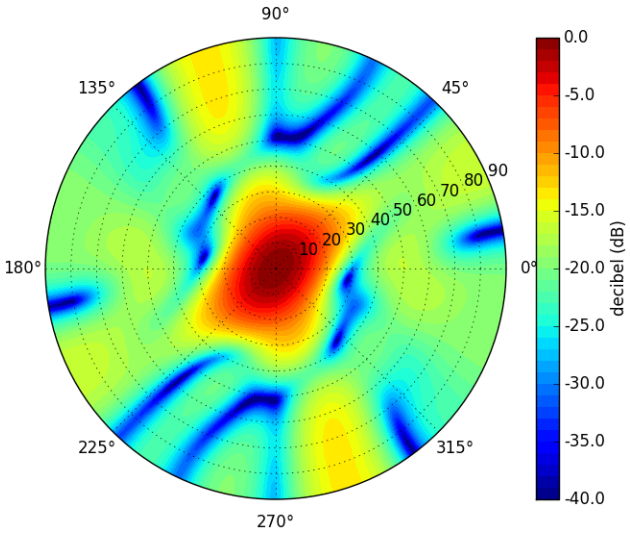

Figure 5.133: Array Factor Contour of 50 Element Random Array in Decibels

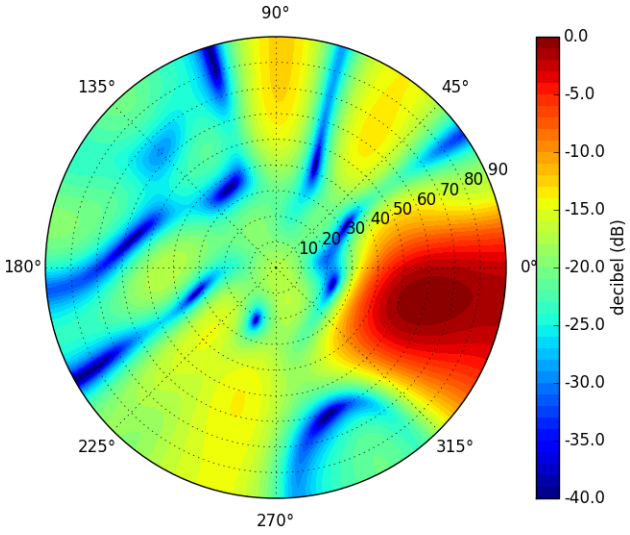

Figure 5.134: Array Factor Contour of 50 Element Random Array with Beamsteering in Decibels

5.6.4.5 Random Direction of Arrival

The MUSIC DoA estimation algorithm with a maximum resolution of .5° processed the synthetic aperture array data after despreading each incident signal with its PRN sequence and prior to combining or beamsteering. A peak detection algorithm was used to determine the predicted signal direction of origin. Figure 5.135 shows the DoA error under CW interference CW_0 and CW_1, where CW_0 is near the horizon and CW_1 is near a satellite signal. Regardless of the presence of interference or the interference's proximity to the signal source the DoA error flattens around an array of size 25.

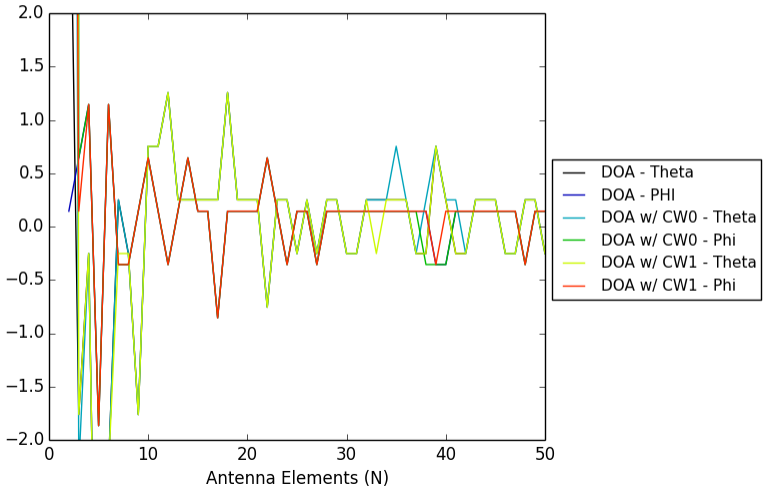

Figure 5.135: DoA error for different interference sources for $\lambda/2$ spacing

5.6.4.6 Nominal SNR and SINR Comparison

A comparison of the SNR and SINR ratios under ideal or nominal DoA information from signal PRN_7 for beamsteering, MUSIC DoA information from signal PRN_7, and all signals of interest DoA generated by MUSIC estimation averaged together. The comparison occurred at $\lambda/2$ spacing, and the results are shown in Figure 5.136 and Figure 5.137. From these two graphs it is apparent that the DoA error generated by the MUSIC algorithm is very small, which is shown by the PRN_7 signal tracking the nominal or ideal signal as the number array elements increased. The averaged signal power shows that all six signals of interest follow PRN_7 with a small variance.

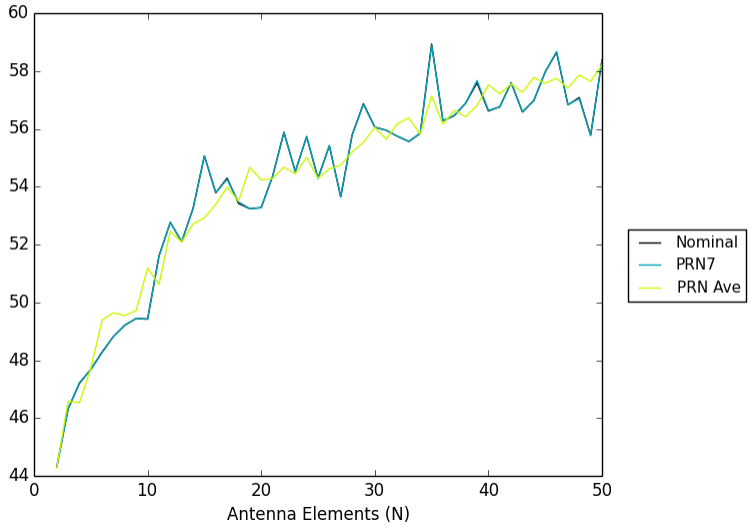

Figure 5.136: Random Array SNR for Nominal, PRN_7, and Averaged PRN Signal DoA at $\lambda/2$ Spacing

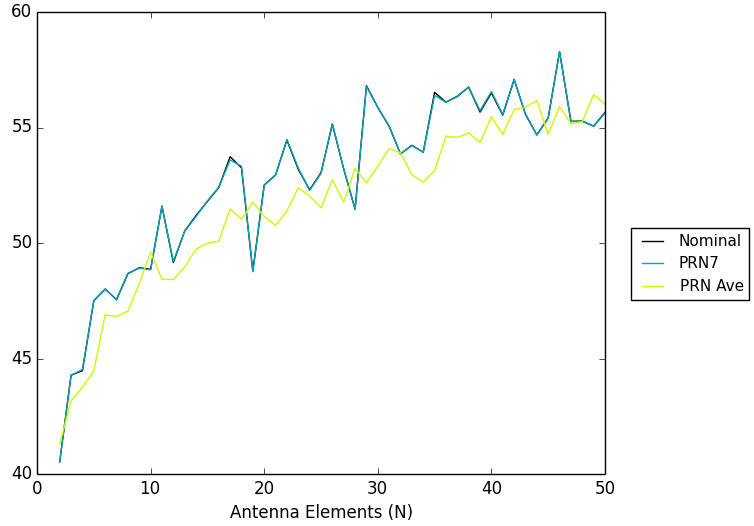

Figure 5.137: Random Array SINR for Nominal, PRN_7, and Averaged PRN Signal DoA at $\lambda/2$ Spacing, with CW_0 Interference

5.6.4.7 Noise Level Comparison

The noise level was evaluated for $\lambda/2$ spacing with a noise temperature of 513 K and 2052 K with interference source CW_0. The SNR and SINR are shown in Figure 5.138 and Figure 5.139 respectively. From the figures it is apparent that a higher noise floor has a negative impact on the SNR and SINR, but the size of the array has a limited impact on complex AWGN as expected. The two noise curves are identical only differing in magnitude.

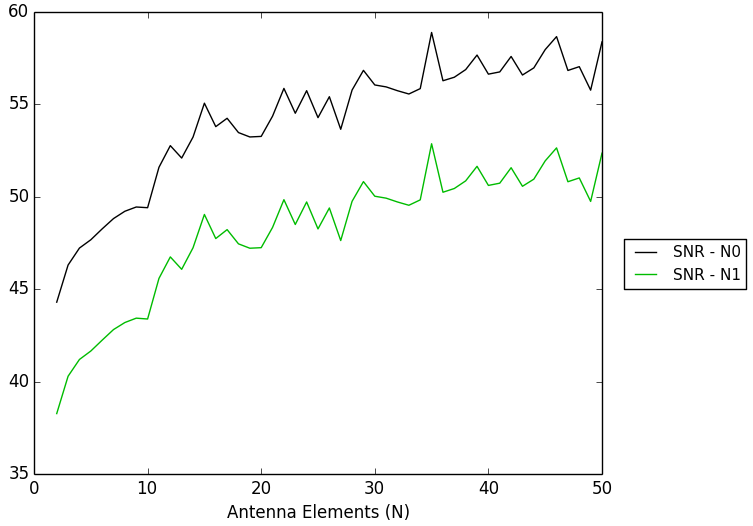

Figure 5.138: Random Array SNR for noise levels N_0 and N_1 at $\lambda/2$ spacing

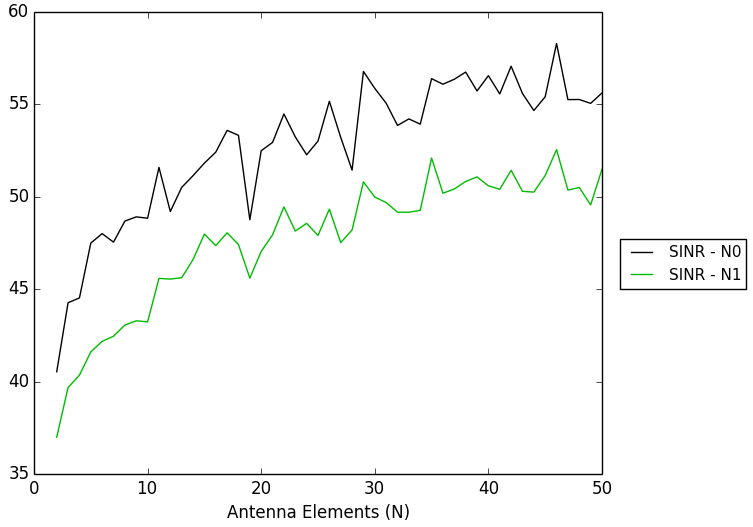

Figure 5.139: Random Array SINR for noise levels N_0 and N_1 at $\lambda/2$ spacing

5.6.4.8 Interference Position Comparison

Figure 5.140 shows the SINR under CW interference CW_0 and CW_1, where CW_0 is near the horizon and CW_1 is near a satellite signal. The interference source near the satellite signal has a smaller gain as expected. When beamsteering near the signal of interest a highly focused pattern is moving near the interference source placing it near a gain rather than a null. This results in increased interference power and a decreased SINR.

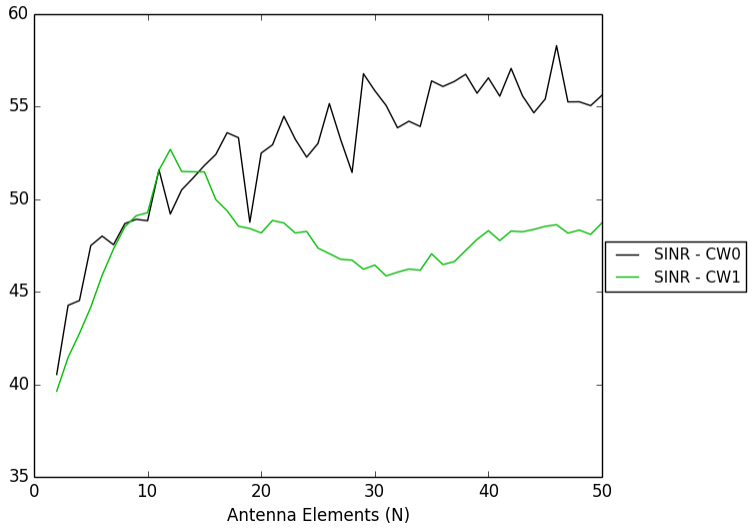

Figure 5.140: Random Array SINR for Different Interference Sources at $\lambda/2$ Spacing

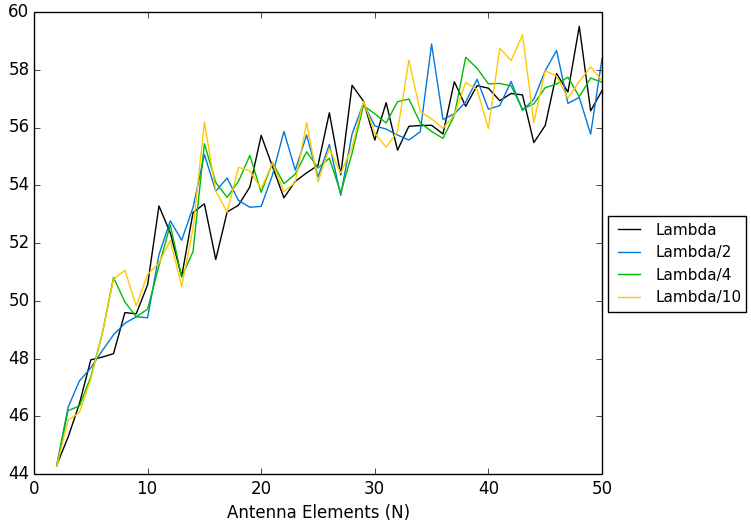

Figure 5.141: Random Array SNR for λ, $\lambda/2$, $\lambda/4$, $\lambda/10$ spacing

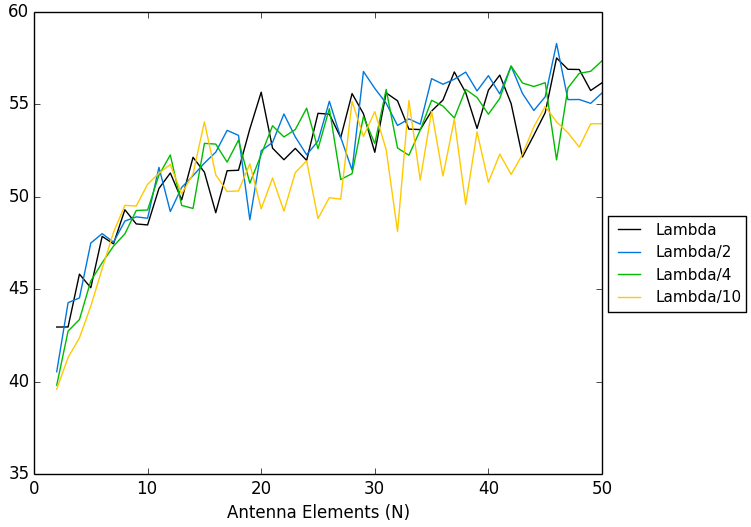

Figure 5.142: Random Array SINR for λ, $\lambda/2$, $\lambda/4$, $\lambda/10$ spacing

5.6.4.9 Array Inter-Element Spacing Comparison

A little surprising is the effect of the array spacing or lack of a significant effect on the SNR and SINR ratios respectively for λ, $\lambda/2$, $\lambda/4$, $\lambda/10$ array spacing. This is captured in Figure 5.141 and Figure 5.142. The comparable ratios are likely the result of the communication despreading process selecting only the signal of interest. In the scenario with CW and a small array spacing of $\lambda/10$ a decrease in SINR occurred as the array size increased. The cause for this decrease is likely a smaller directivity compared to the other array spacings and aliasing placing sidelobes near the interference source.

5.6.5 Random Full Aperture Array Placement

The random full aperture array is made of antenna elements that are randomly placed using a uniformly distributed random number within a circle of a certain radius. The full aperture is obtained by ignoring the inter-element tolerance and maintaining the circle radius provided by the same formula as the UCA that is described in Equation 5.45. After element generation shown in Equation 5.51 and Equation 5.52, the coordinates were converted from Polar to Cartesian coordinates.

$$\vec{\theta} = rand(n) \cdot 2\pi \tag{5.51}$$

$$\vec{r} = rand(n) \cdot r \tag{5.52}$$

$$\vec{X} = \vec{r} \cdot \cos(\vec{\theta}) \tag{5.53}$$

$$\vec{Y} = \vec{r} \cdot \sin(\vec{\theta}) \tag{5.54}$$

$$\vec{Z} = \vec{0} \tag{5.55}$$

5.6.5.1 Random Full Aperture Element Configuration

Following the array placement described in Section 5.6.5 where $T_{max} = \lambda/2$ for array sizes of 5, 10, 15, 20, 30, 40, and 50 result in the configurations shown in Figures 5.143 - 5.149.

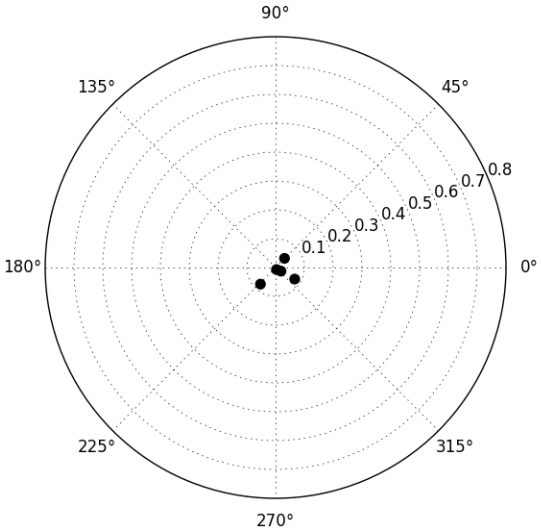

Figure 5.143: Random Full Aperture Array 5 Element Configuration

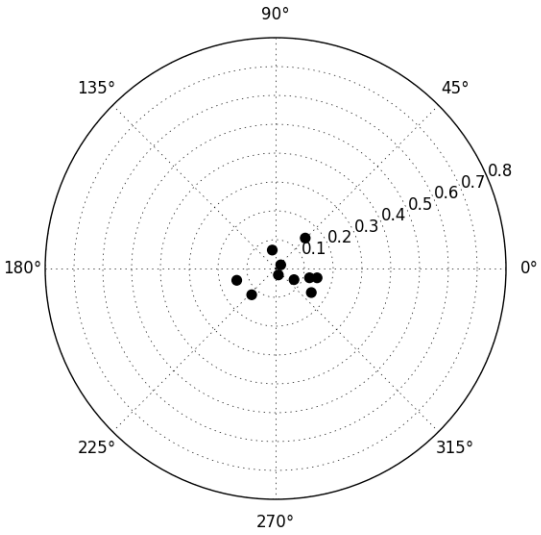

Figure 5.144: Random Full Aperture Array 10 Element Configuration

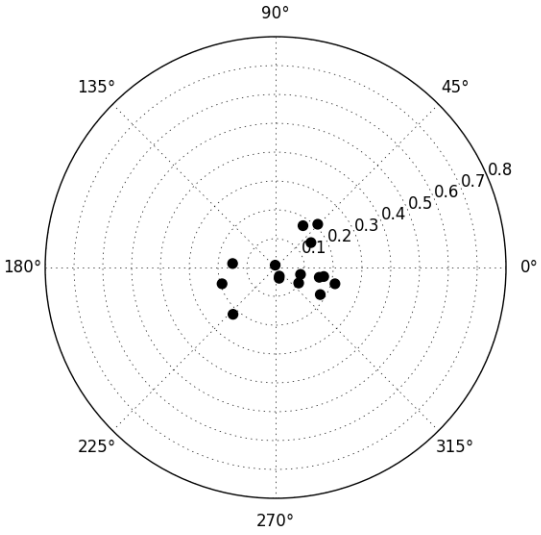

Figure 5.145: Random Full Aperture Array 15 Element Configuration

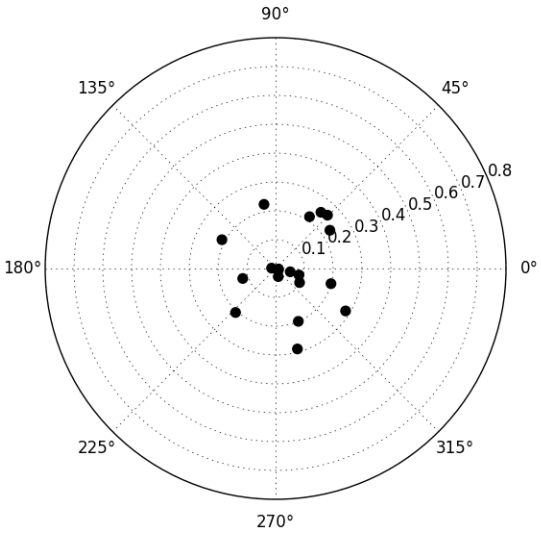

Figure 5.146: Random Full Aperture Array 20 Element Configuration

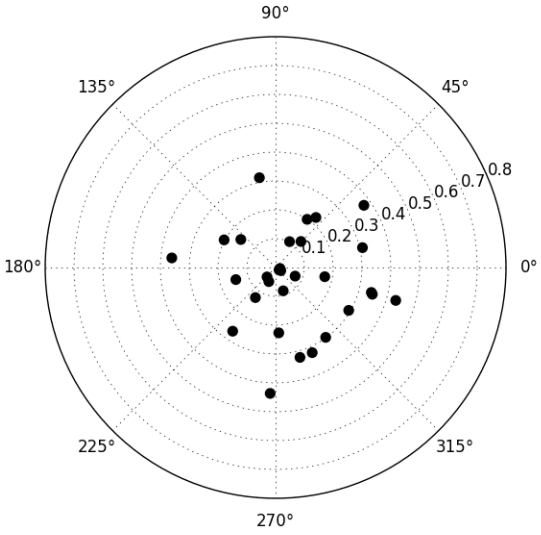

Figure 5.147: Random Full Aperture Array 30 Element Configuration

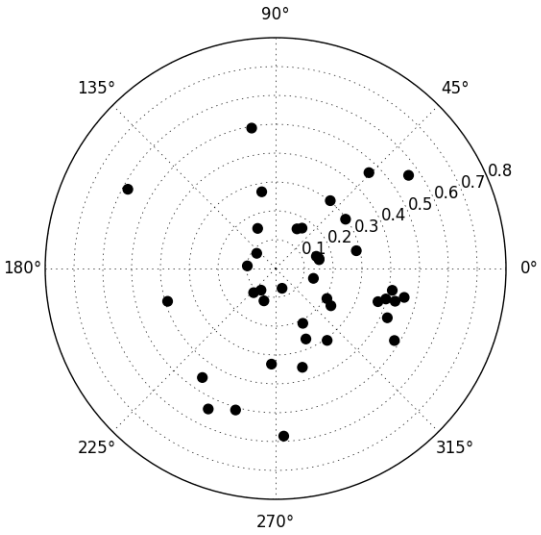

Figure 5.148: Random Full Aperture Array 40 Element Configuration

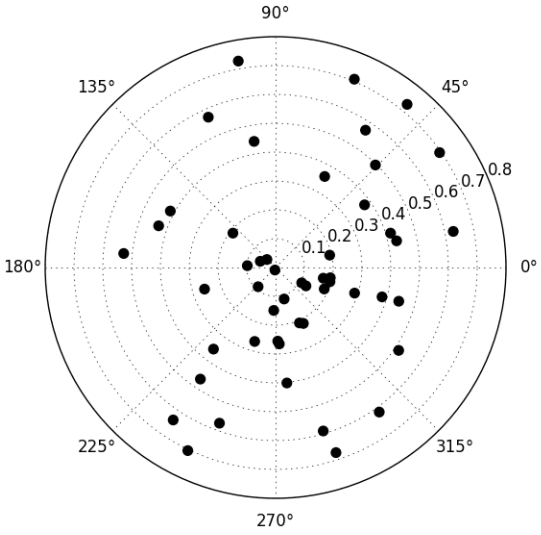

Figure 5.149: Random Full Aperture Array 50 Element Configuration

5.6.5.2 Array Size

The circular area encompassed by the array from 2 elements to 50 in m^2 is shown in Figure 5.150. As expected the array size increases with additional elements and is highest for the maximum tolerance $T_{max} = \lambda$ determined radius.

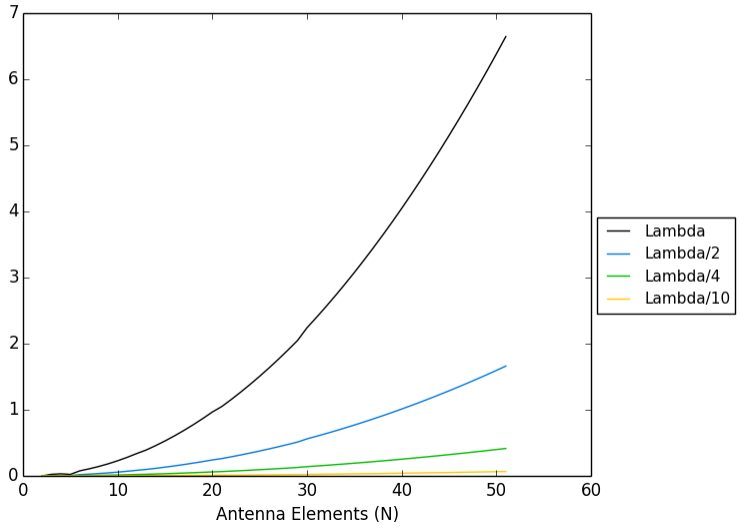

Figure 5.150: Array Size for λ, $\lambda/2$, $\lambda/4$, $\lambda/10$ Array Spacing in Circular Area in m^2 for Random Full Aperture Array

5.6.5.3 Directivity

Directivity is a measure of the concentration of an array beam. The directivity for the Random Full Aperture Array is shown in Figure 5.151. As expected the directivity increases for all tolerances of T_{max} simulated.

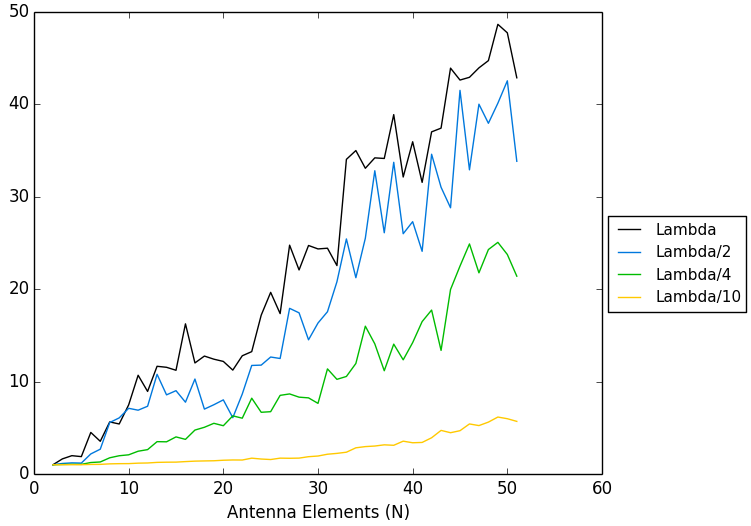

Figure 5.151: Directivity for λ, $\lambda/2$, $\lambda/4$, $\lambda/10$ Array Spacing for Random Full Aperture Array

5.6.5.4 Random Full Aperture Array Factor

The Random Full Aperture Array is characterized by a random main beam and random null structure as depicted in Figures 5.152 - 5.164 for a tolerance of $T_{max} = \lambda/2$. The random structure beamsteering in the direction of $(\theta, \phi) = (60.0821, 374.6239)$ of a single source is also shown in Figures 5.153 - 5.165. The focus of the main beam mirrors the increase in directivity shown in Figure 5.151.

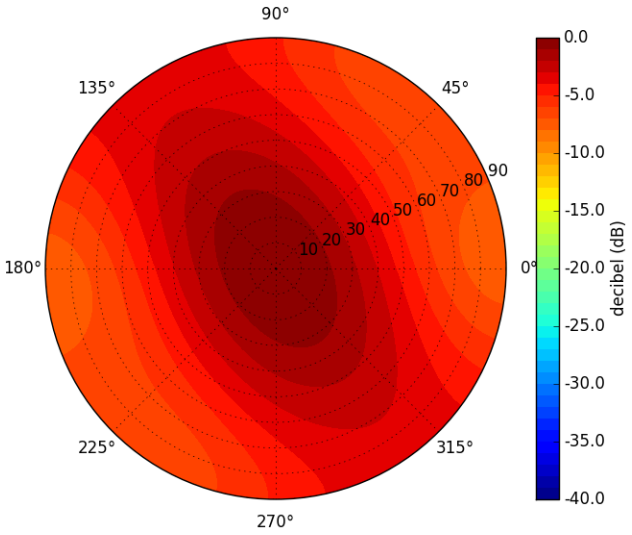

Figure 5.152: Array Factor Contour of 5 Element Random Full Aperture Array in Decibels

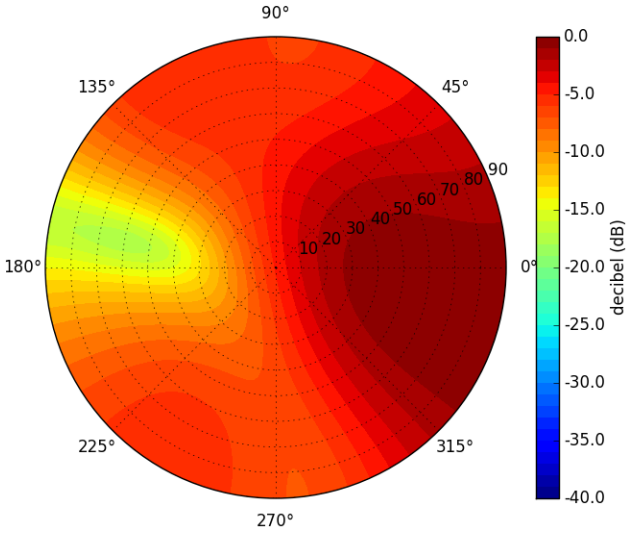

Figure 5.153: Array Factor Contour of 5 Element Random Full Aperture Array with Beamsteering in Decibels

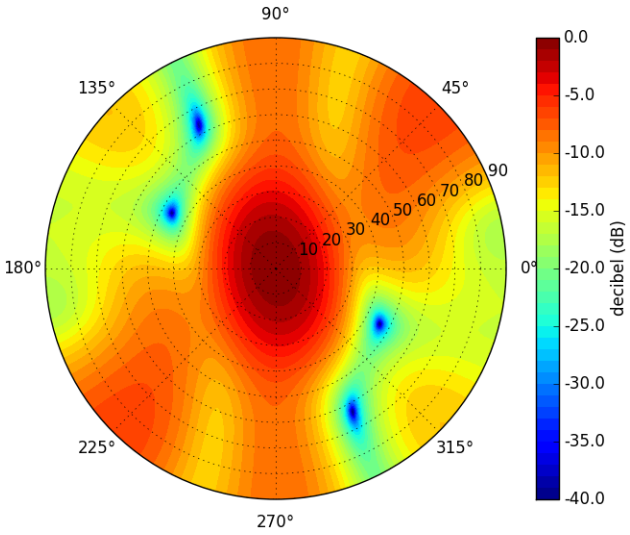

Figure 5.154: Array Factor Contour of 10 Element Random Full Aperture Array in Decibels

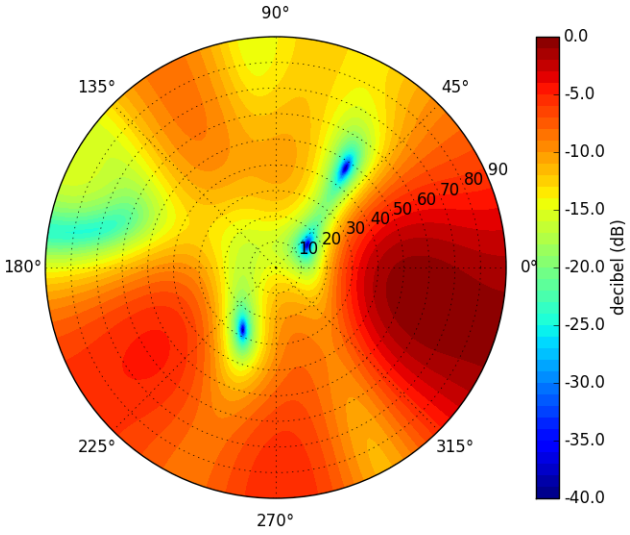

Figure 5.155: Array Factor Contour of 10 Element Random Full Aperture Array with Beamsteering in Decibels

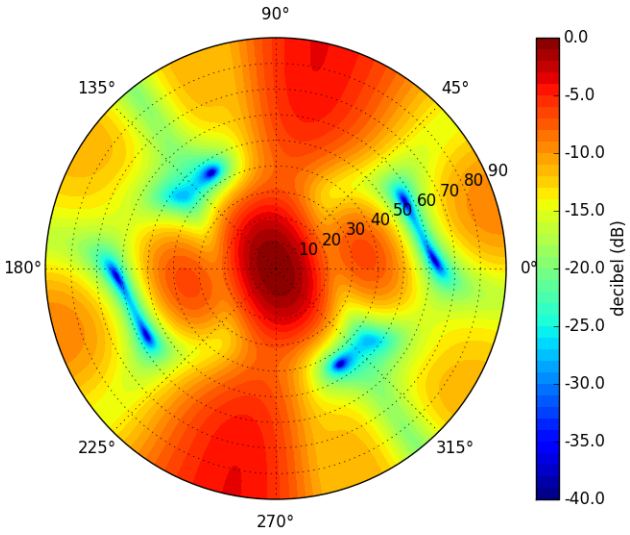

Figure 5.156: Array Factor Contour of 15 Element Random Full Aperture Array in Decibels

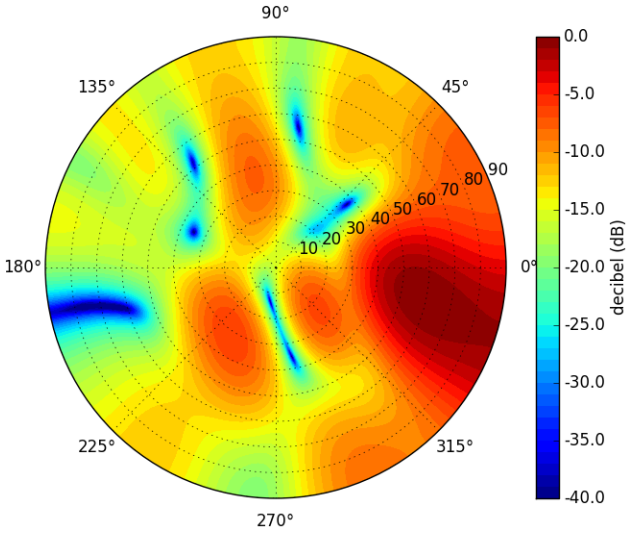

Figure 5.157: Array Factor Contour of 15 Element Random Full Aperture Array with Beamsteering in Decibels

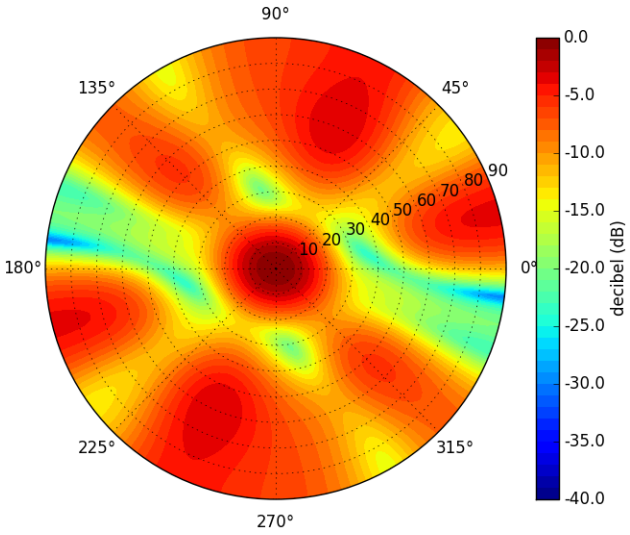

Figure 5.158: Array Factor Contour of 20 Element Random Full Aperture Array in Decibels

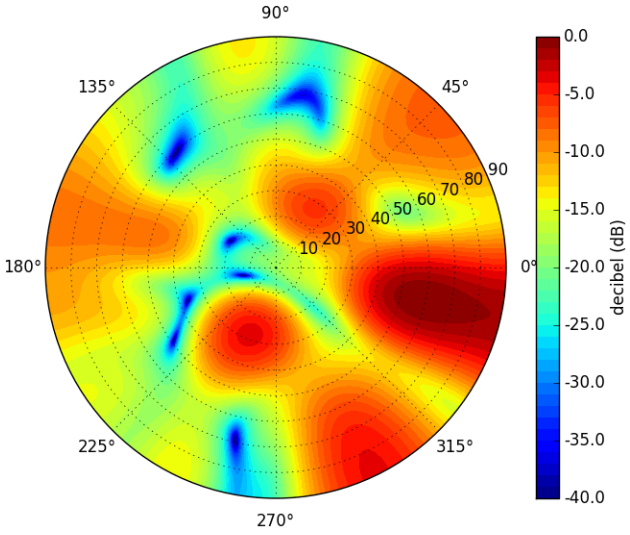

Figure 5.159: Array Factor Contour of 20 Element Random Full Aperture Array with Beamsteering in Decibels

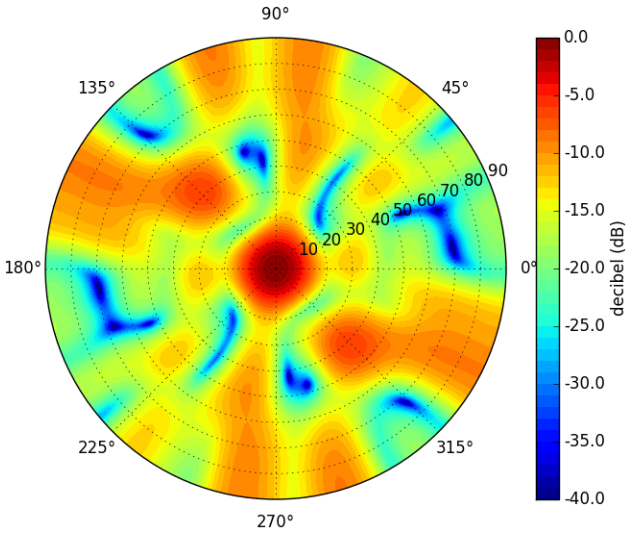

Figure 5.160: Array Factor Contour of 30 Element Random Full Aperture Array in Decibels

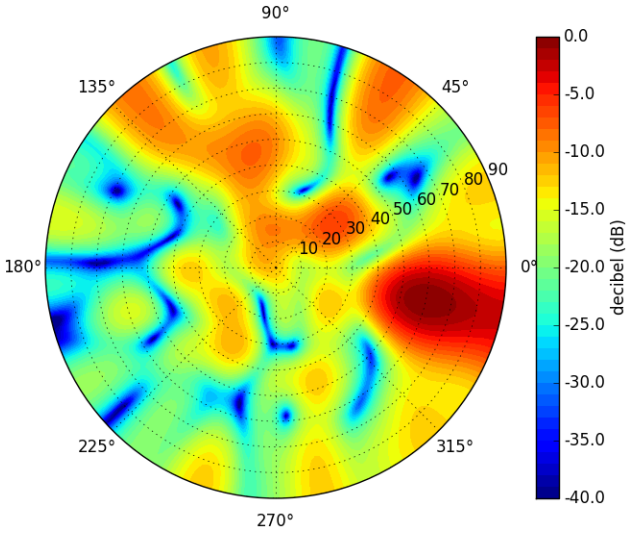

Figure 5.161: Array Factor Contour of 30 Element Random Full Aperture Array with Beamsteering in Decibels

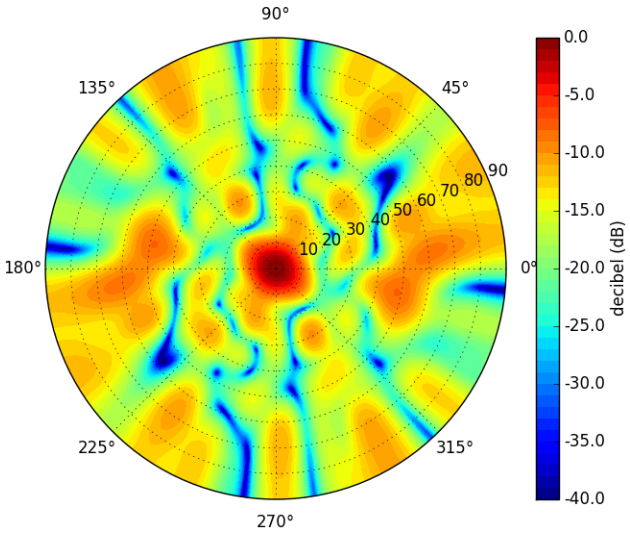

Figure 5.162: Array Factor Contour of 40 Element Random Full Aperture Array in Decibels

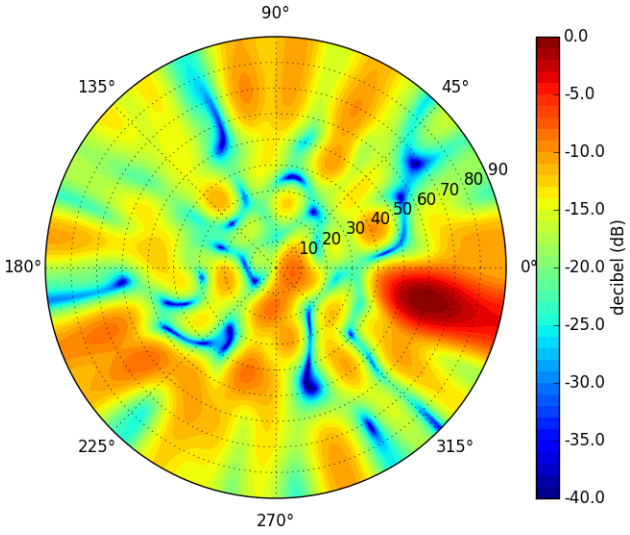

Figure 5.163: Array Factor Contour of 40 Element Random Full Aperture Array with Beamsteering in Decibels

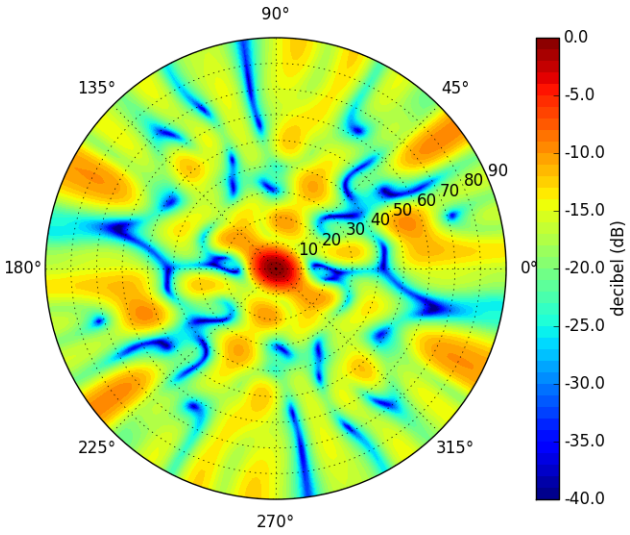

Figure 5.164: Array Factor Contour of 50 Element Random Full Aperture Array in Decibels

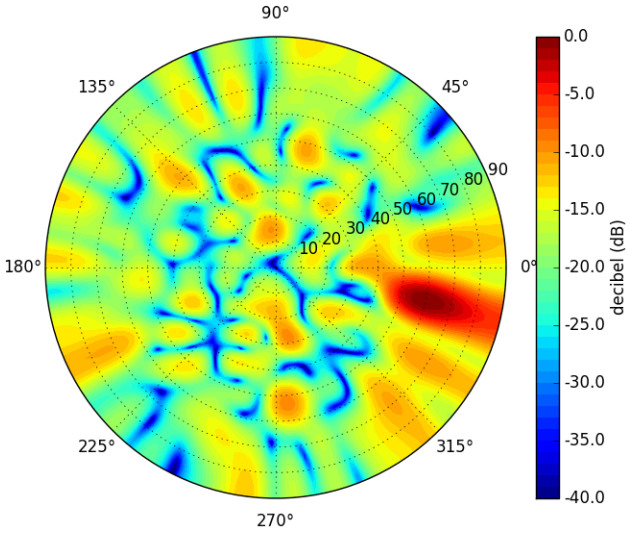

Figure 5.165: Array Factor Contour of 50 Element Random Full Aperture Array with Beamsteering in Decibels

5.6.5.5 *Random Full Aperture Direction of Arrival*

The MUSIC DoA estimation algorithm with a maximum resolution of .5° processed the synthetic aperture array data after despreading each incident signal with its PRN sequence and prior to combining or beamsteering. A peak detection algorithm was used to determine the predicted signal direction of origin. Figure 5.166 shows the DoA error under CW interference CW_0 and CW_1, where CW_0 is near the horizon and CW_1 is near a satellite signal. Regardless of the presence of interference or the interference's proximity to the signal source the DoA error flattens around an array of size 20.

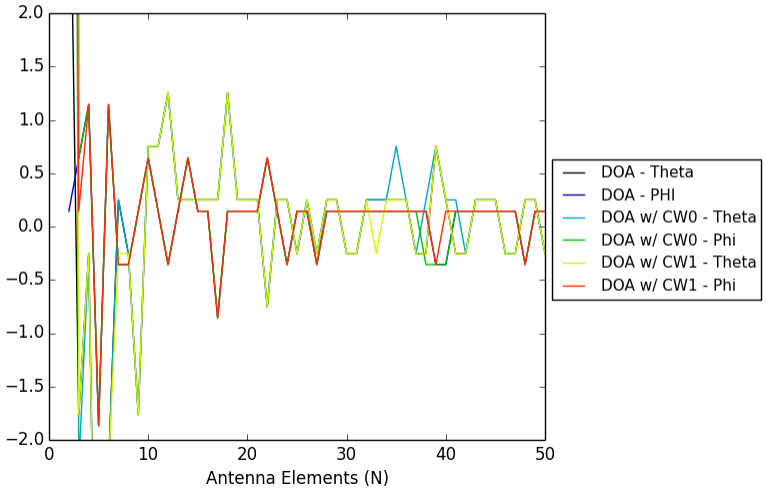

Figure 5.166: DoA error for different interference sources for $\lambda/2$ spacing

5.6.5.6 Nominal SNR and SINR Comparison

A comparison of the SNR and SINR ratios under ideal or nominal DoA information from signal PRN_7 for beamsteering, MUSIC DoA information from signal PRN_7, and all signals of interest DoA generated by MUSIC estimation averaged together. The comparison occurred at $\lambda/2$ spacing, and the results are shown in Figure 5.167 and Figure 5.168. From these two graphs it is apparent that the DoA error generated by the MUSIC algorithm is very small, which is shown by the PRN_7 signal tracking the nominal or ideal signal as the number array elements increased. The averaged signal power shows that all six signals of interest follow PRN_7 with a small variance.

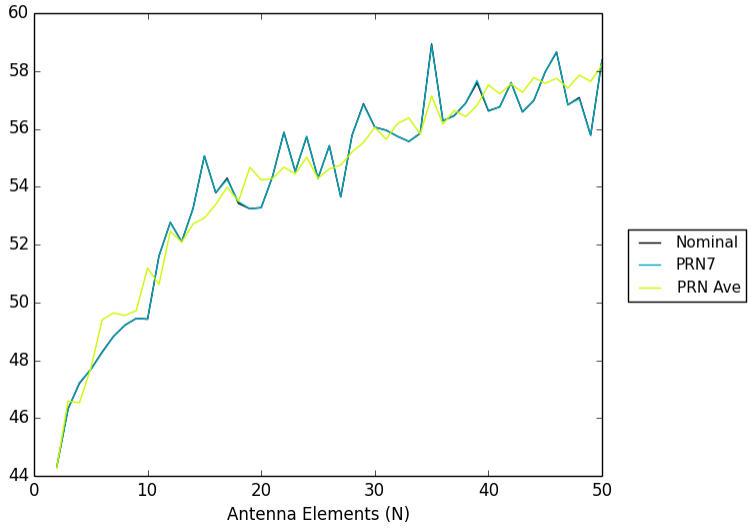

Figure 5.167: Random Full Aperture Array SNR for Nominal, PRN_7, and Averaged PRN Signal DoA at $\lambda/2$ Spacing

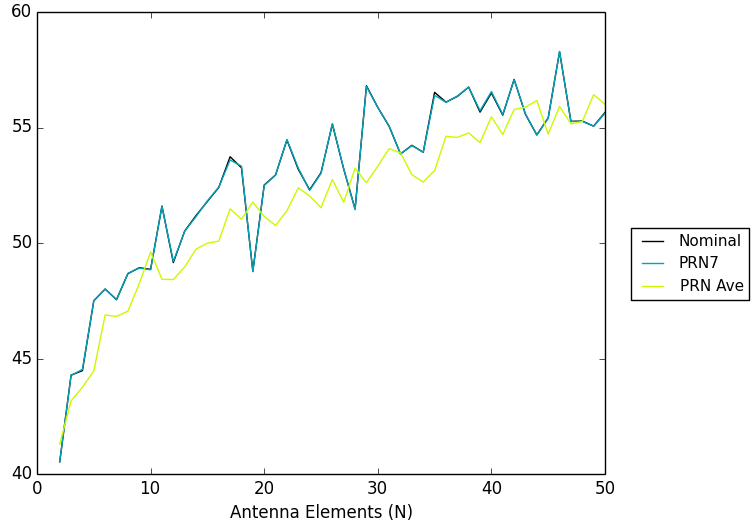

Figure 5.168: Random Full Aperture Array SINR for Nominal, PRN_7, and Averaged PRN Signal DoA at $\lambda/2$ Spacing, with CW_0 Interference

5.6.5.7 Noise Level Comparison

The noise level was evaluated for $\lambda/2$ spacing with a noise temperature of 513 K and 2052 K with interference source CW_0. The SNR and SINR are shown in Figure 5.169 and Figure 5.170 respectively. From the figures it is apparent that a higher noise floor has a negative impact on the SNR and SINR, but the size of the array has a limited impact on complex AWGN as expected. The two noise curves are identical only differing in magnitude.

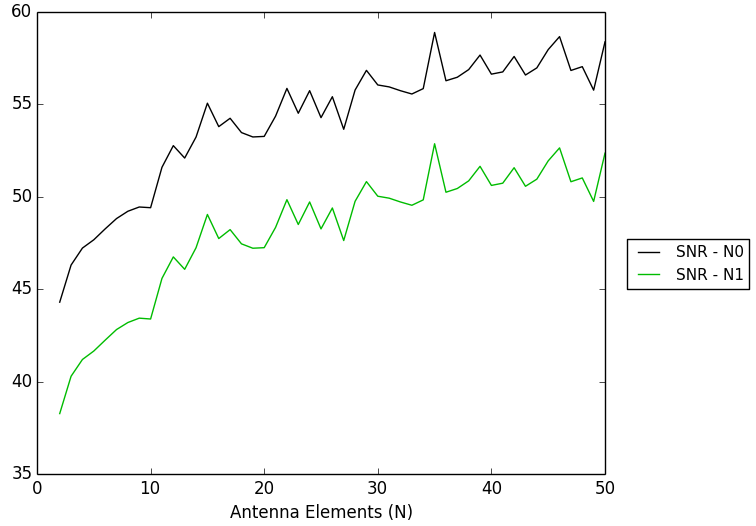

Figure 5.169: Random Full Aperture Array SNR for noise levels N_0 and N_1 at $\lambda/2$ spacing

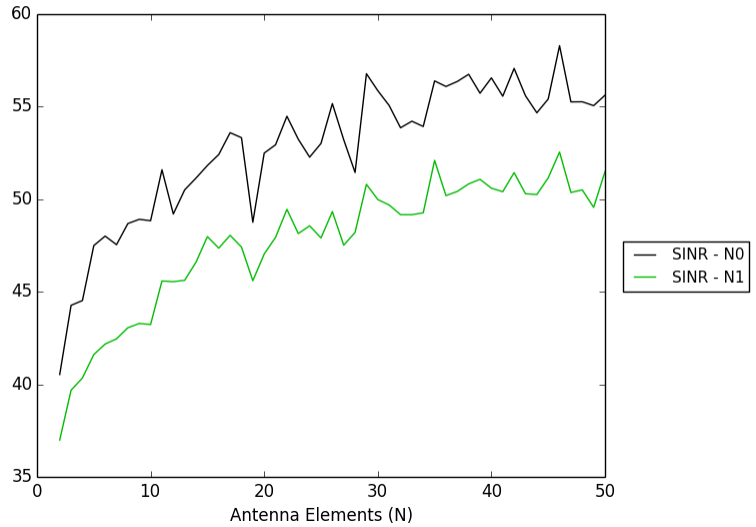

Figure 5.170: Random Full Aperture Array SINR for noise levels N_0 and N_1 at $\lambda/2$ spacing

5.6.5.8 Interference Position Comparison

Figure 5.171 shows the SINR under CW interference CW_0 and CW_1, where CW_0 is near the horizon and CW_1 is near a satellite signal. The interference source near the satellite signal has a smaller gain as expected. When beamsteering near the signal of interest a highly focused pattern is moving near the interference source placing it near a gain rather than a null. This results in increased interference power and a decreased SINR.

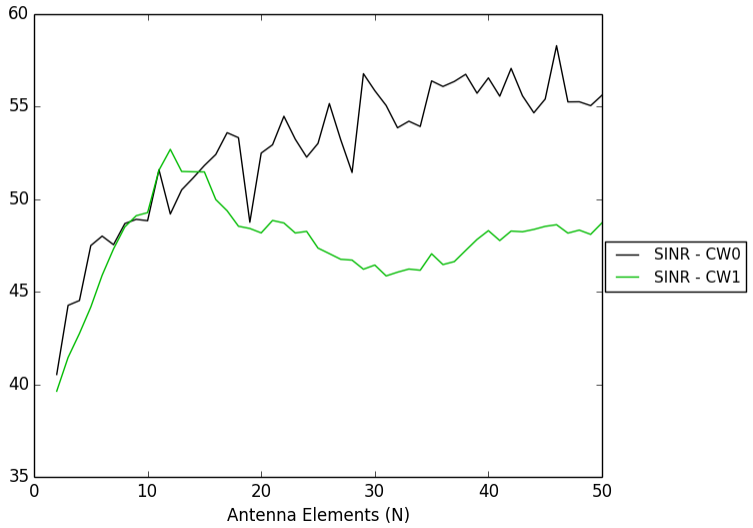

Figure 5.171: Random Full Aperture Array SINR for Different Interference Sources at $\lambda/2$ Spacing

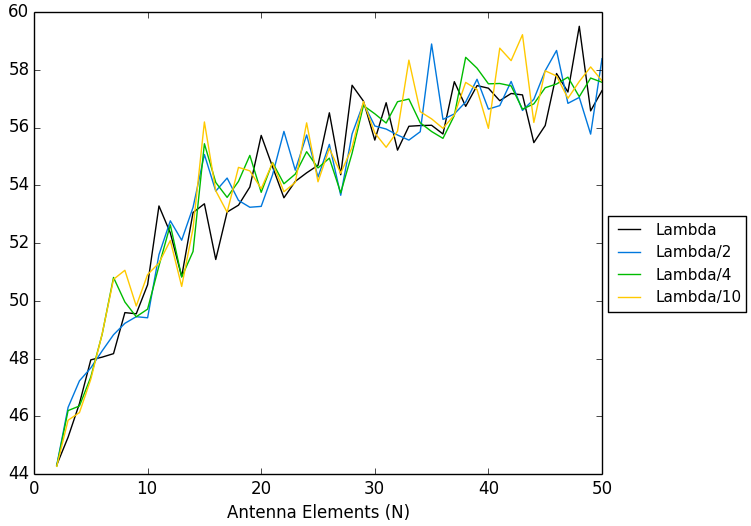

Figure 5.172: Random Full Aperture Array SNR for λ, $\lambda/2$, $\lambda/4$, $\lambda/10$ spacing

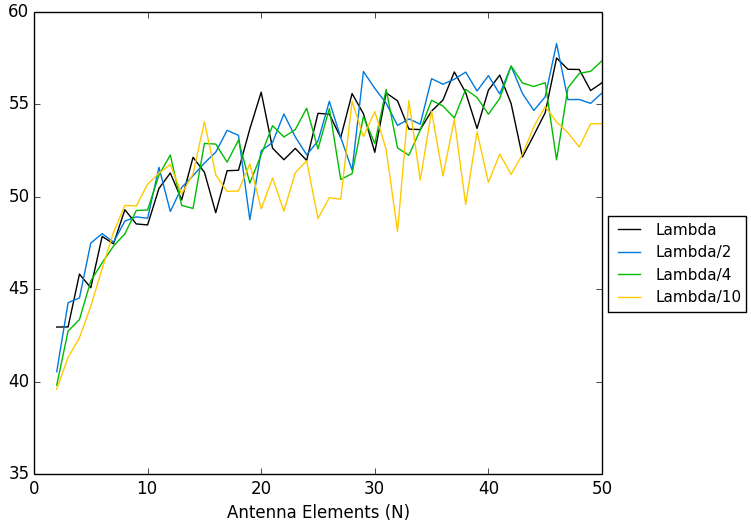

Figure 5.173: Random Full Aperture Array SINR for λ, $\lambda/2$, $\lambda/4$, $\lambda/10$ spacing

5.6.5.9 Array Inter-Element Spacing Comparison

A little surprising is the effect of the array spacing or lack of a significant effect on the SNR and SINR ratios respectively for λ, $\lambda/2$, $\lambda/4$, $\lambda/10$ array spacing. This is captured in Figure 5.172 and Figure 5.173. The comparable ratios are likely the result of the communication despreading process selecting only the signal of interest. In the scenario with CW and a small array spacing of $\lambda/10$ a decrease in SINR occurred as the array size increased. The cause for this decrease is likely a smaller directivity compared to the other array spacings and aliasing placing sidelobes near the interference source.

5.6.6 Ring Array

A ring array combines the UCA with a random array inside the circle by shrinking the circle's radius to maintain the tolerance of each element within T_{max}. In inter number of randomly selected elements is governed by $\lceil \frac{n}{2} \rceil$ and the uniform normal distribution. The radius of the UCA was adjusted by:

$$\theta = \frac{2\pi}{\lfloor \frac{n}{2} \rfloor} \tag{5.56}$$

$$r = \sqrt{\frac{T_{max}^2}{2(1 - \cos(\theta))}} \tag{5.57}$$

5.6.6.1 Ring Array Element Configuration

Following the array placement described in Section 5.6.1 where $T_{max} = \lambda/2$ for array sizes of 5, 10, 15, 20, 30, 40, and 50 result in the configurations shown in Figures 5.174 - 5.180.

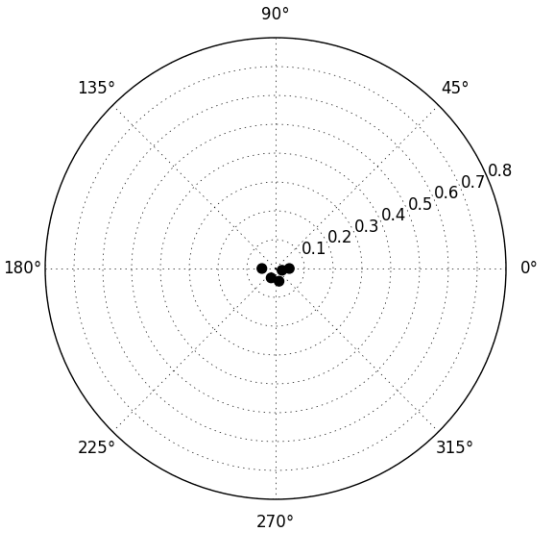

Figure 5.174: Ring Array 5 Element Configuration

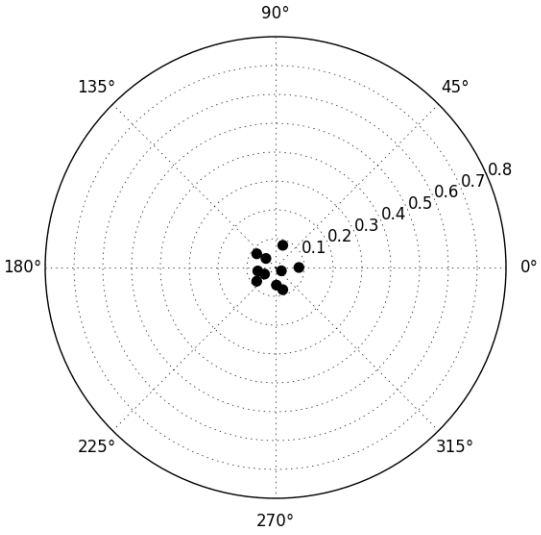

Figure 5.175: Ring Array 10 Element Configuration

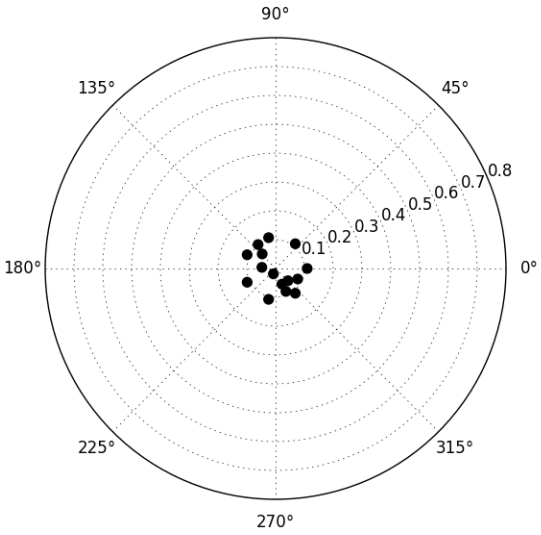

Figure 5.176: Ring Array 15 Element Configuration

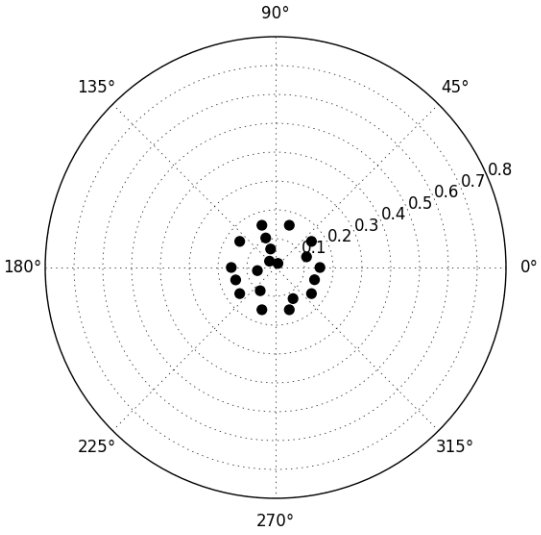

Figure 5.177: Ring Array 20 Element Configuration

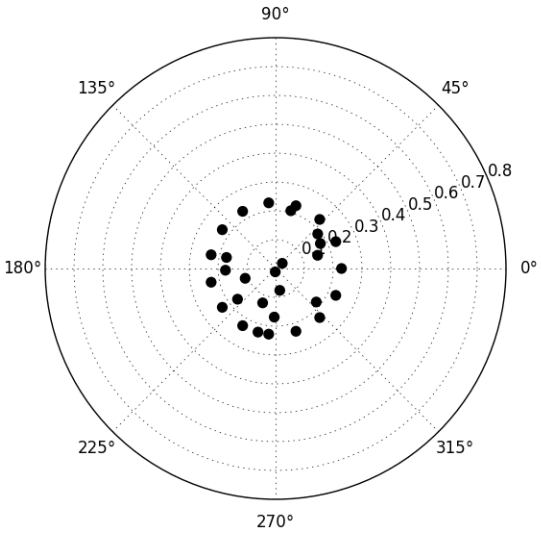

Figure 5.178: Ring Array 30 Element Configuration

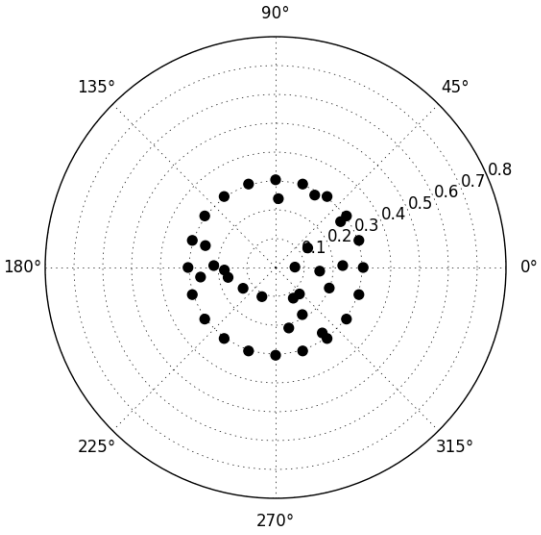

Figure 5.179: Ring Array 40 Element Configuration

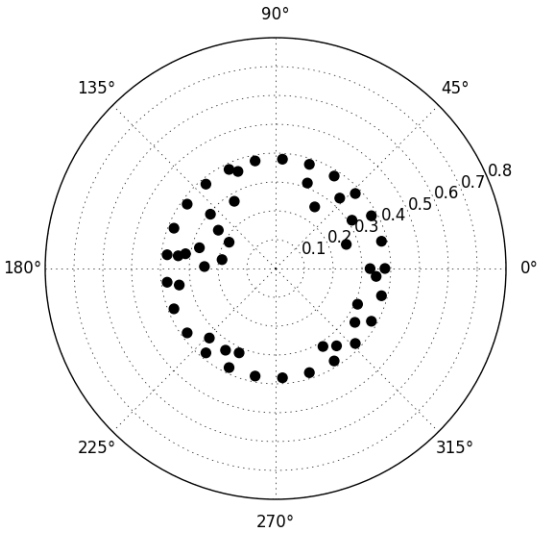

Figure 5.180: Ring Array 50 Element Configuration

5.6.6.2 Array Size

The circular area encompassed by the array from 2 elements to 50 in m^2 is shown in Figure 5.181. As expected the array size increases with additional elements and is highest for the maximum tolerance $T_{max} = \lambda$.

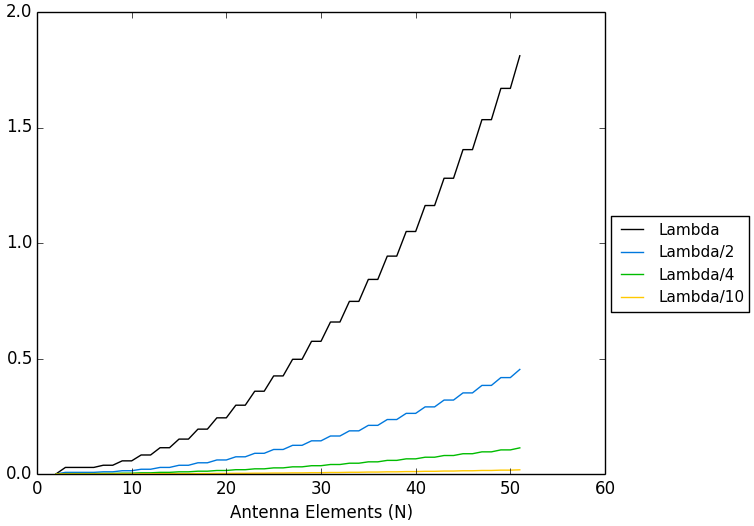

Figure 5.181: Array Size for λ, $\lambda/2$, $\lambda/4$, $\lambda/10$ Array Spacing in Circular Area in m^2 for Ring Array

5.6.6.3 Directivity

Directivity is a measure of the concentration of an array beam. The directivity for the ring array is shown in Figure 5.182. As expected the directivity increases for all tolerances of T_{max} simulated.

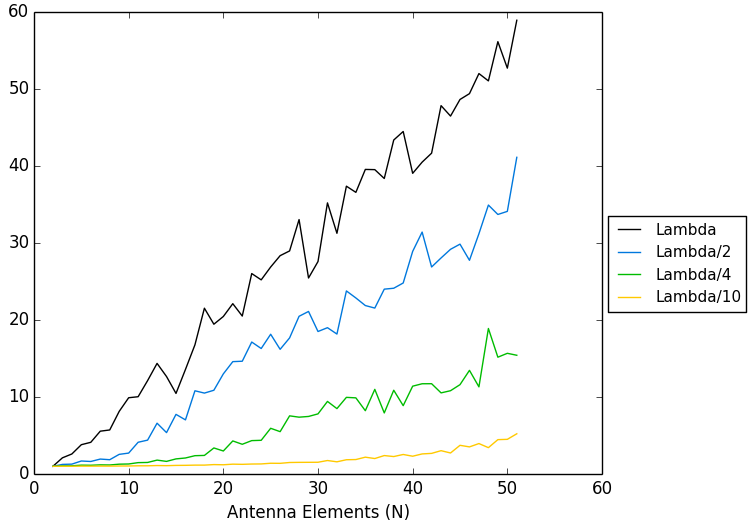

Figure 5.182: Directivity for λ, $\lambda/2$, $\lambda/4$, $\lambda/10$ Array Spacing for Ring Array

5.6.6.4 Uniform Circular Array (UCA) Array Factor

The ring array is characterized by main beam with a hybrid random ring null structure as depicted in Figures 5.183 - 5.195 for a tolerance of $T_{max} = \lambda/2$. The beamsteered structure in the direction of $(\theta, \phi) = (60.0821, 374.6239)$ of a single signal source is also shown in Figures 5.184 - 5.196. The focus of the main beam mirrors the increase in directivity shown in Figure 5.182.

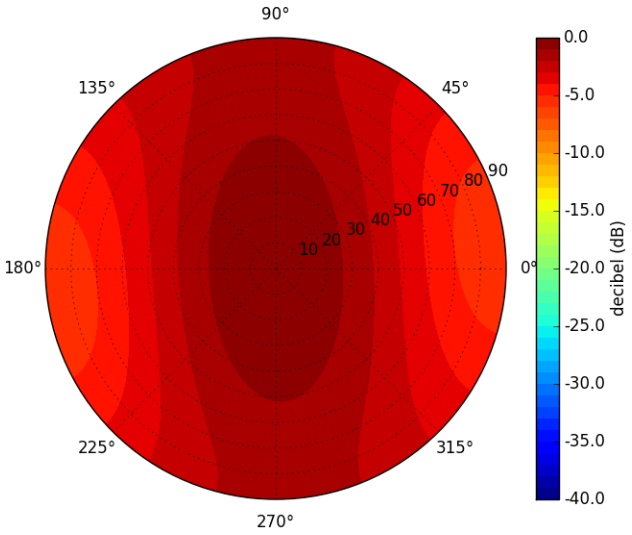

Figure 5.183: Array Factor Contour of 5 Element Ring Array in Decibels

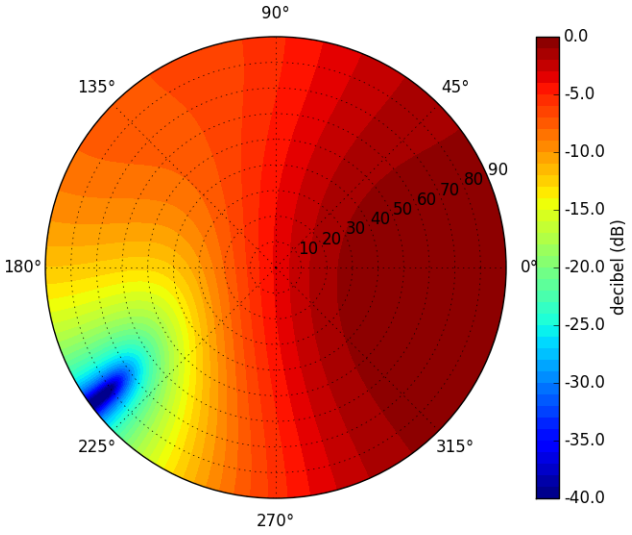

Figure 5.184: Array Factor Contour of 5 Element Ring Array with Beamsteering in Decibels

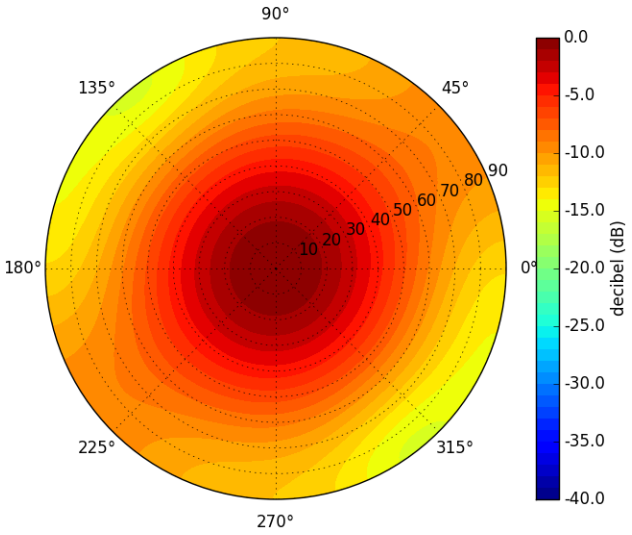

Figure 5.185: Array Factor Contour of 10 Element Ring Array in Decibels

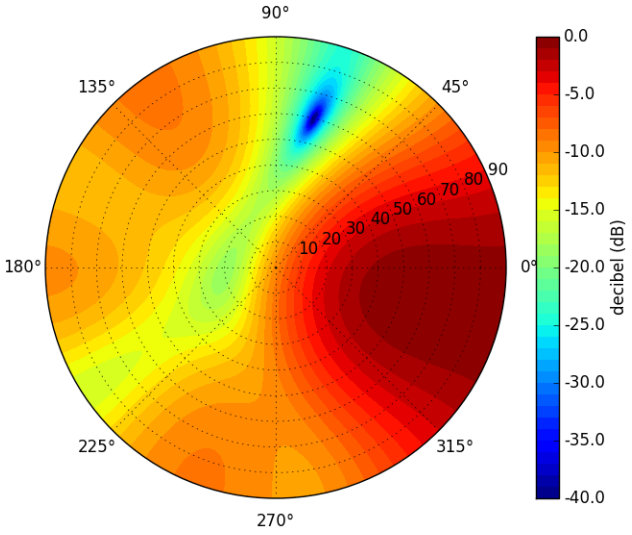

Figure 5.186: Array Factor Contour of 10 Element Ring Array with Beamsteering in Decibels

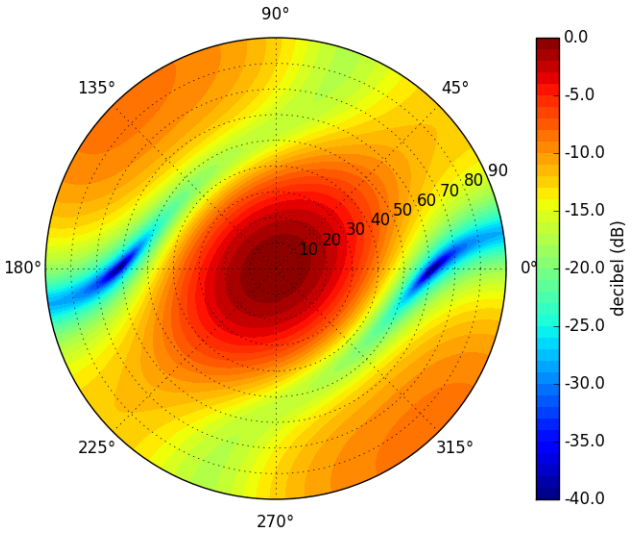

Figure 5.187: Array Factor Contour of 15 Element Ring Array in Decibels

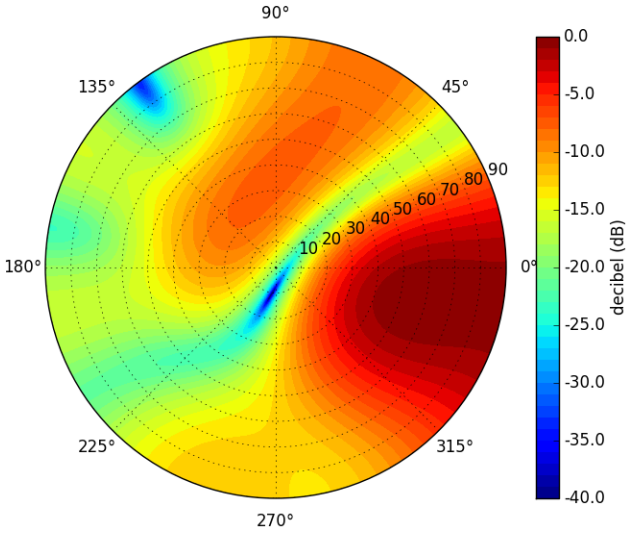

Figure 5.188: Array Factor Contour of 15 Element Ring Array with Beamsteering in Decibels

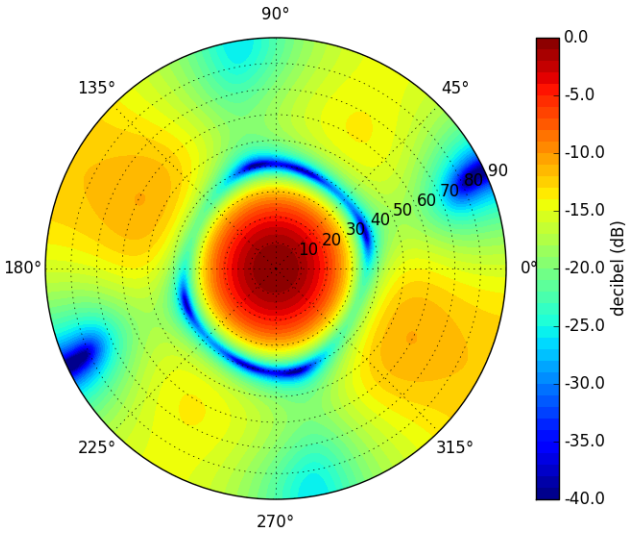

Figure 5.189: Array Factor Contour of 20 Element Ring Array in Decibels

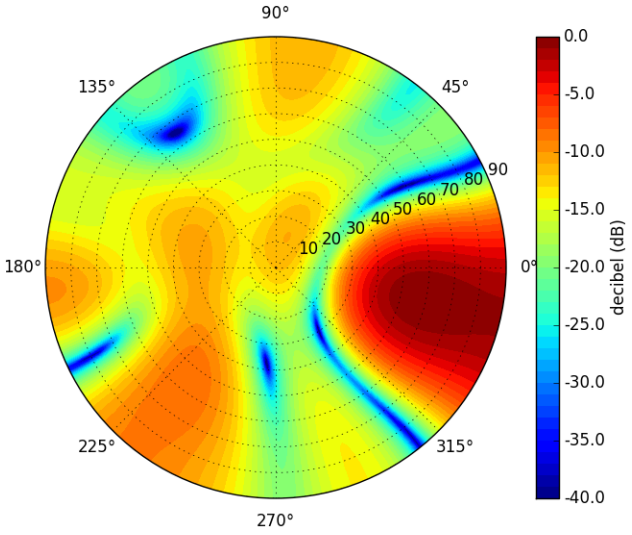

Figure 5.190: Array Factor Contour of 20 Element Ring Array with Beamsteering in Decibels

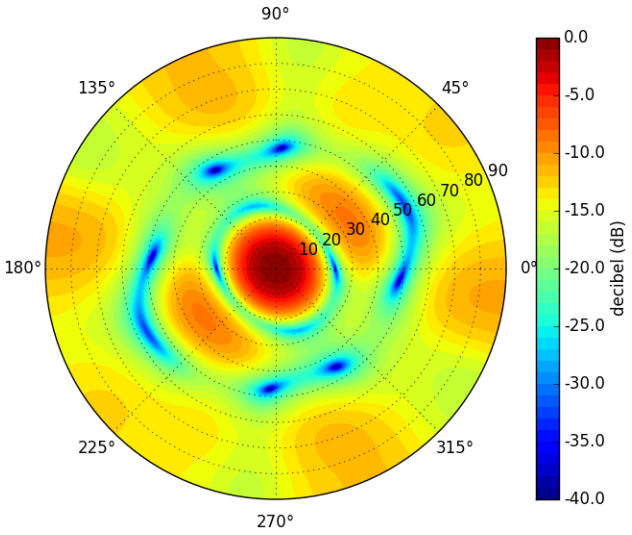

Figure 5.191: Array Factor Contour of 30 Element Ring Array in Decibels

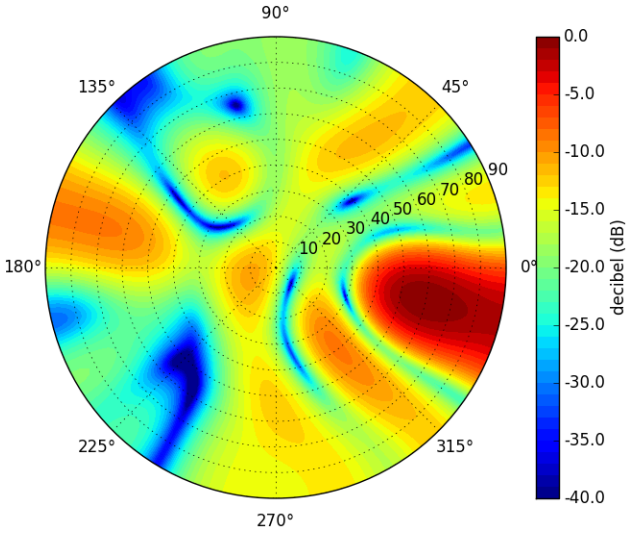

Figure 5.192: Array Factor Contour of 30 Element Ring Array with Beamsteering in Decibels

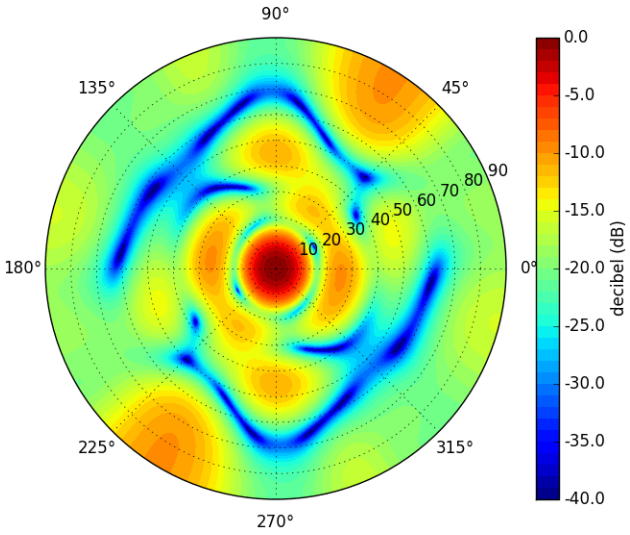

Figure 5.193: Array Factor Contour of 40 Element Ring Array in Decibels

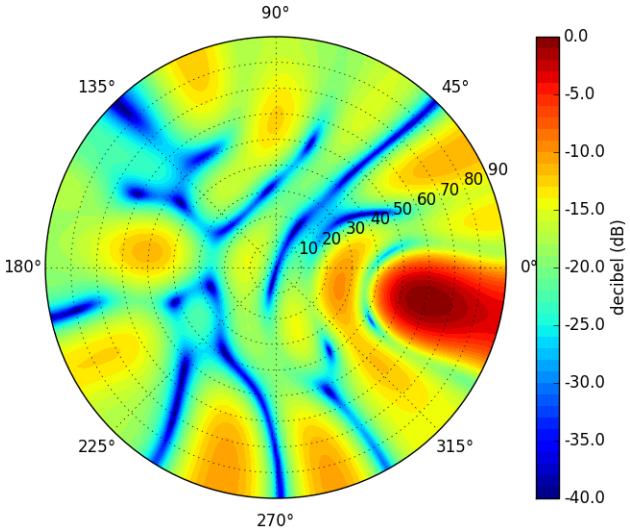

Figure 5.194: Array Factor Contour of 40 Element Ring Array with Beamsteering in Decibels

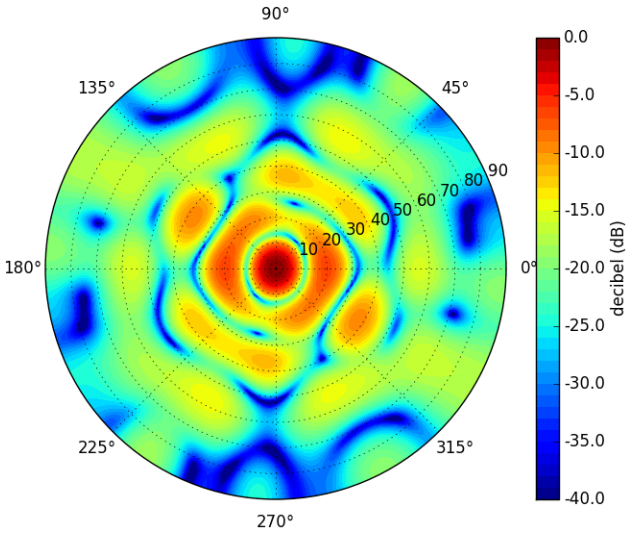

Figure 5.195: Array Factor Contour of 50 Element Ring Array in Decibels

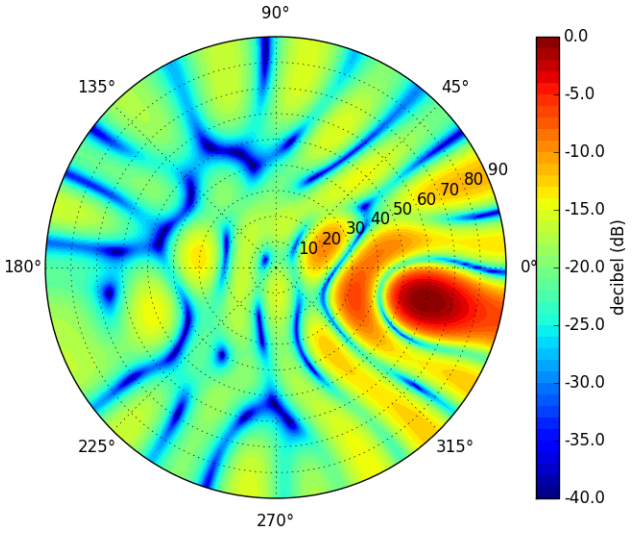

Figure 5.196: Array Factor Contour of 50 Element Ring Array with Beamsteering in Decibels

5.6.6.5 *Uniform Circular Array Direction of Arrival*

The MUSIC DoA estimation algorithm processed the synthetic aperture array data after despreading each incident signal with its PRN sequence and prior to combining or beamsteering with a maximum resolution of .5°. A peak detection algorithm was used to determine the predicted signal direction of origin. Figure 5.197 shows the DoA error under CW interference CW_0 and CW_1, where CW_0 is near the horizon and CW_1 is near a satellite signal. Regardless of the presence of interference or the interference's proximity to the signal source the DoA error flattens around an array of size 10.

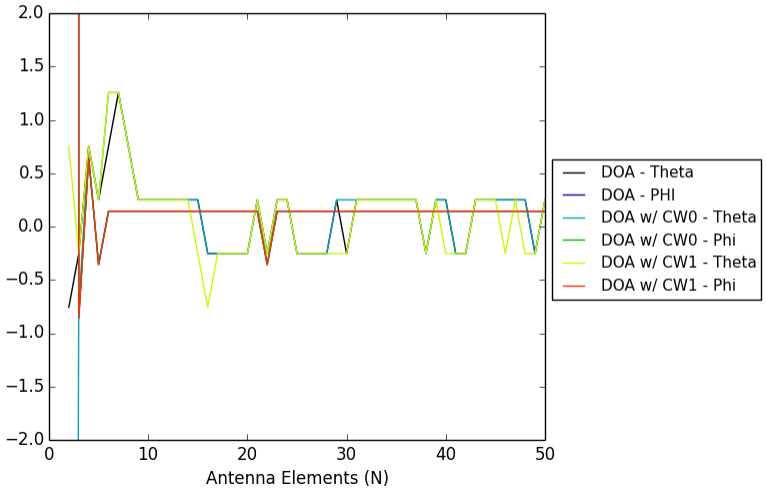

Figure 5.197: DoA error for different interference sources for $\lambda/2$ spacing

5.6.6.6 Nominal SNR and SINR Comparison

A comparison of the SNR and SINR ratios under ideal or nominal DoA information from signal PRN_7 for beamsteering, MUSIC DoA information from signal PRN_7, and all signals of interest DoA generated by MUSIC estimation averaged together. The comparison occurred at $\lambda/2$ spacing, and the results are shown in Figure 5.198 and Figure 5.199. From these two graphs it is apparent that the DoA error generated by the MUSIC algorithm is very small, which is shown by the PRN_7 signal tracking the nominal or ideal signal as the number array elements increased. The averaged signal power shows that all six signals of interest follow PRN_7 with a small variance.

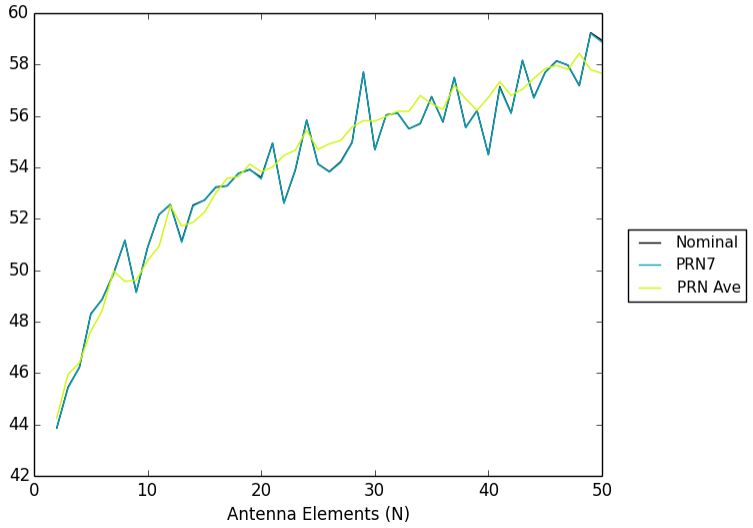

Figure 5.198: Ring Array SNR for Nominal, PRN_7, and Averaged PRN Signal DoA at $\lambda/2$ Spacing

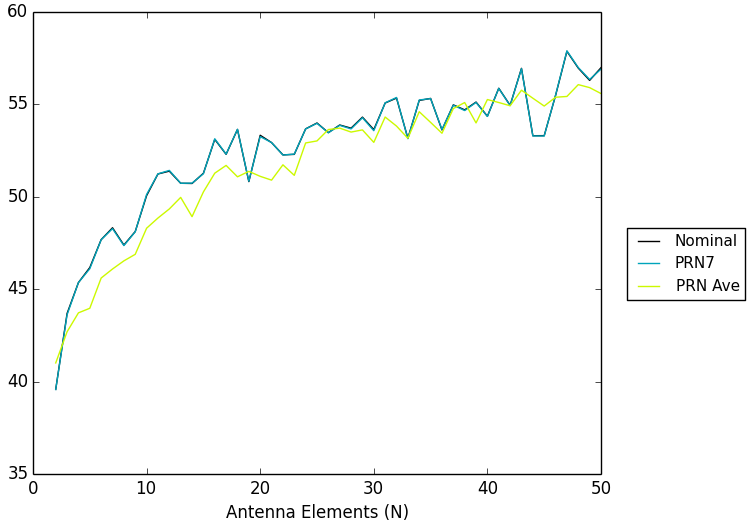

Figure 5.199: Ring Array SINR for Nominal, PRN_7, and Averaged PRN Signal DoA at $\lambda/2$ Spacing, with CW_0 Interference

5.6.6.7 Noise Level Comparison

The noise level was evaluated for $\lambda/2$ spacing with a noise temperature of 513 K and 2052 K with interference source CW_0. The SNR and SINR are shown in Figure 5.200 and Figure 5.201 respectively. From the figures it is apparent that a higher noise floor has a negative impact on the SNR and SINR, but the size of the array has a limited impact on complex AWGN as expected. The two noise curves are identical only differing in magnitude.

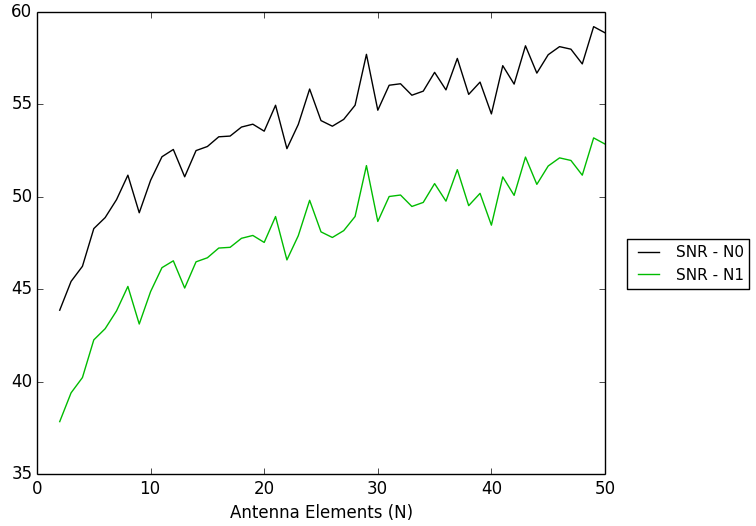

Figure 5.200: Ring Array SNR for noise levels N_0 and N_1 at $\lambda/2$ spacing

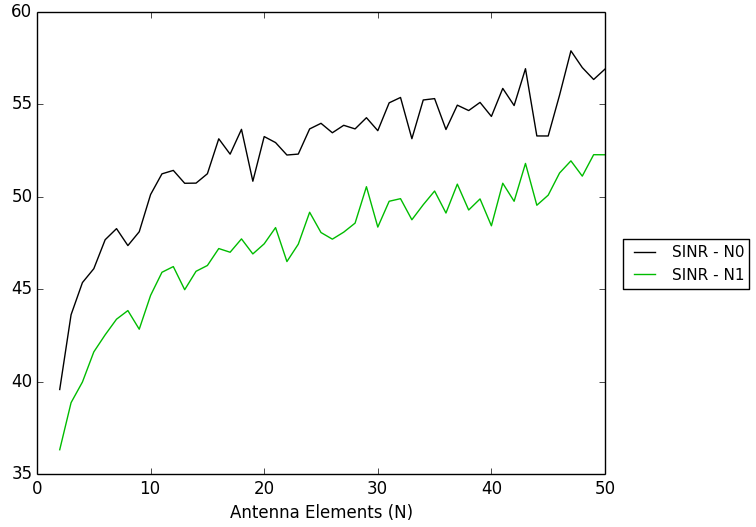

Figure 5.201: Ring Array SINR for noise levels N_0 and N_1 at $\lambda/2$ spacing

5.6.6.8 *Interference Position Comparison*

Figure 5.202 shows the SINR under CW interference CW_0 and CW_1, where CW_0 is near the horizon and CW_1 is near a satellite signal. The interference source near the satellite signal has a smaller gain as expected. When beamsteering near the signal of interest a highly focused pattern is moving near the interference source placing it near a gain rather than a null. This results in increased interference power and a decreased SINR.

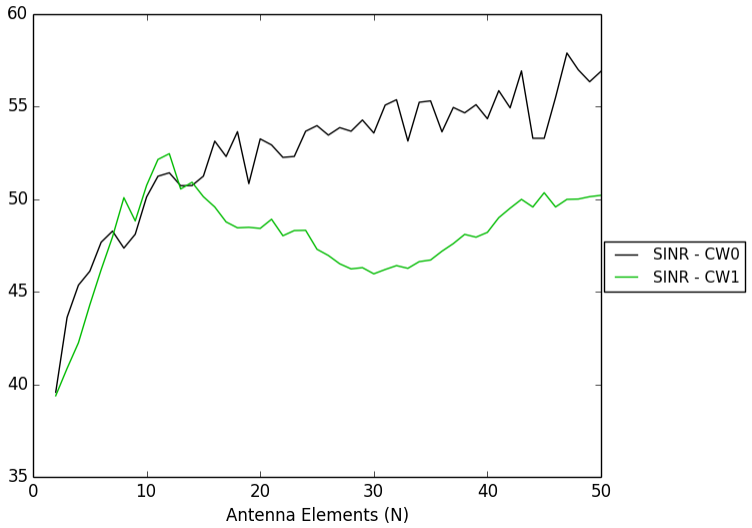

Figure 5.202: Ring Array SINR for Different Interference Sources at $\lambda/2$ Spacing

5.6.6.9 *Array Inter-Element Spacing Comparison*

The effect on the SNR and SINR ratios respectively for λ, $\lambda/2$, $\lambda/4$, $\lambda/10$ array spacing. This is captured in Figure 5.203 and Figure 5.204. The comparable ratios are likely the result of the communication despreading process selecting only the

signal of interest. The presence of one signal would cause aliasing or a decrease in directivity to have a marginal affect.

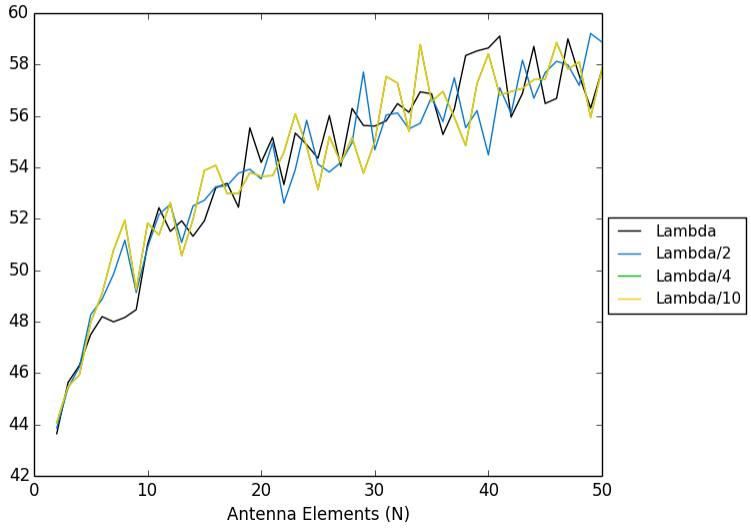

Figure 5.203: Ring Array SNR for λ, $\lambda/2$, $\lambda/4$, $\lambda/10$ spacing

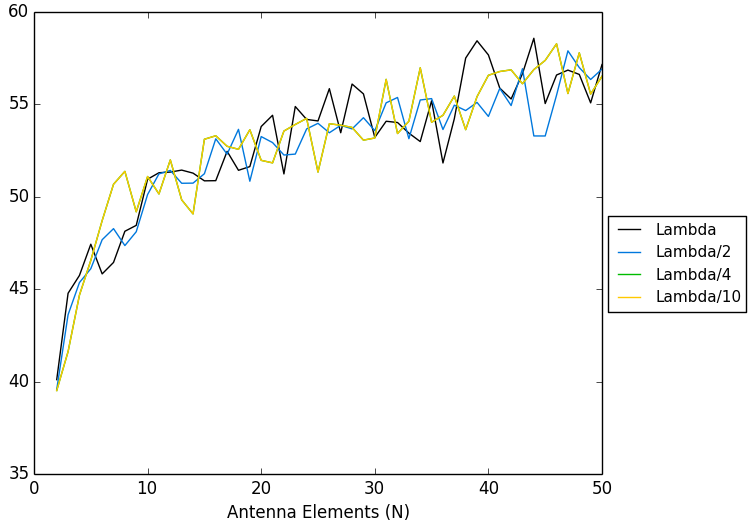

Figure 5.204: Ring Array SINR for λ, $\lambda/2$, $\lambda/4$, $\lambda/10$ spacing

5.7 Combined Comparison

The following section reviews the UCA, rectangular, random, random sequential, random full aperture, and ring arrays at a maximum spacing of $\lambda/2$.

5.7.1 Directivity and Array Size

Due to the extreme differences in array configurations a common area metric of the smallest circle containing all array elements was used from elements 2 to 50 in m^2. The area for all array configurations for $\lambda/2$ spacing is shown in Figure 5.205. The main beam concentration or directivity for all array configurations at $\lambda/2$ spacing is shown in Figure 5.206.

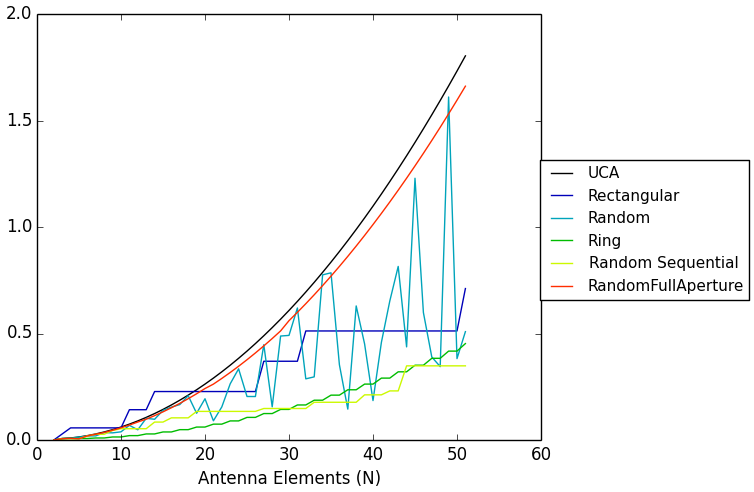

Figure 5.205: Array size for $\lambda/2$ Array Spacing in Circular Area in m^2 for Different Arrays

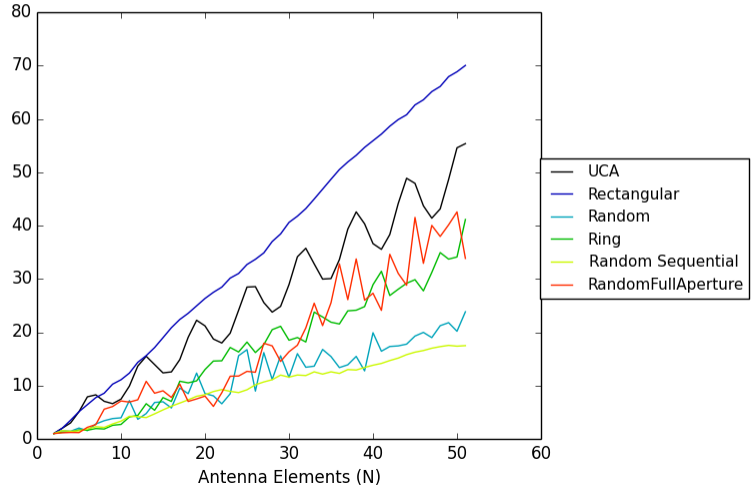

Figure 5.206: Directivity for $\lambda/2$ Array Spacing for Different Arrays

5.7.2 Signal to Noise Ratio (SNR) and Signal to Interference Noise Ratio (SINR)

Based on the previous antenna specific section the SNR for Figure 5.207 for all array types at $\lambda/2$ spacing following the same pattern is not surprising. This phenomena is likely the result of the effectiveness of the despreading process in removing external noise. Figure 5.208 and Figure 5.209 show the SINR for CW_0 and CW_1 respectively.

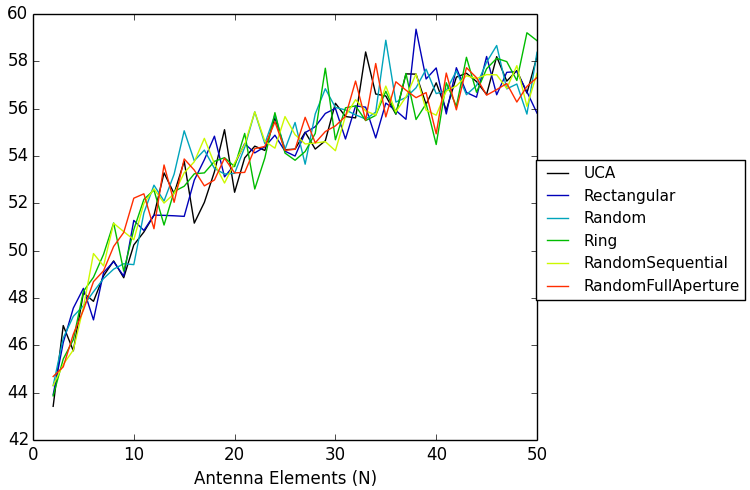

Figure 5.207: SNR for Different Arrays using $\lambda/2$ Spacing

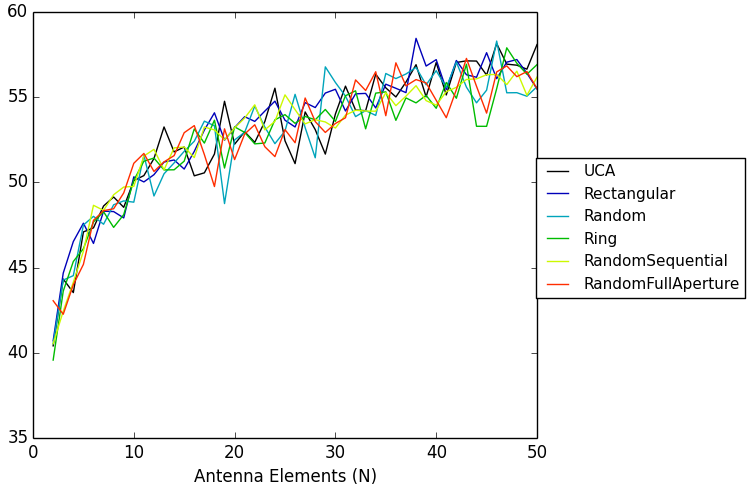

Figure 5.208: SINR for Different Arrays using $\lambda/2$ Spacing with CW_0 Interference

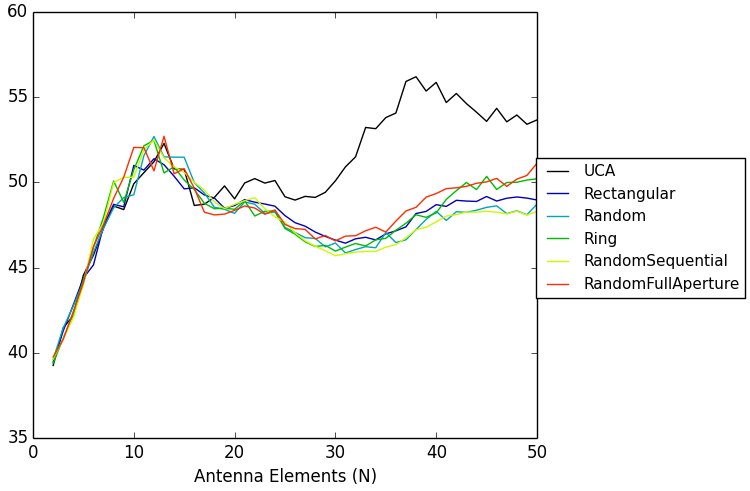

Figure 5.209: SINR for Different Arrays using $\lambda/2$ Spacing with CW_1 Interference

5.7.3 Evaluation

The UCA maintained a stable DoA at approximately 10 elements. The rectangular array required approximately 15 elements to achieve the same level of stability, the random sequential, random full aperture, and ring arrays both required about 20 array elements, and the pure random array required approximately 25 elements. At the minimum number of elements to achieve a high accuracy DoA, the UCA array maintains the smallest spatial footprint and the highest directivity.

In the presence of highly directional CW interference with a scenario power of -120 dBW the different arrays performed at same level for CW_0 as shown in Figure 5.208. Only in the presence of an interference source near the locality of a signal of interest do the different array topologies show a performance distinction. The SINR with CW_1, shown in Figure 5.209, for all arrays is the same until around 20 array elements. At this point, the UCA's high directivity surrounded by close spatial nulls brings the performance back up to SNR levels.

If size were a limiting factor, which is commonly the case in civilian applications, in the presence of a single CW interference source the UCA provides the best compromise between size and performance in the given scenarios due to its highly directive main beam and alternating sidelobe null structure. Given a different scenario looking purely at the highest sidelobe, the random full aperture array provides high gain with non-uniform relatively low sidelobes. This configuration, especially when coupled with spatial nulling, is likely to perform well in a variety of interference location scenarios.

Research thus far tends toward the conclusion that the array topology has little impact on the system performance as long as some spatial diversity exists. However, this evaluation does not take into consideration the different array's ability to place

spatial nulls or performance in differing interference types. Once these factors are considered, the compromise in performance between array size and the array type may change.

5.8 Future Tasks

Several research items remain to be completed to truly evaluate the effectiveness of the switch feed synthetic aperture array for GPS interference mitigation. These include but are not limited to:

- Incorporate temporal diversity
- Analyze the performance of spatial nulling
- Analyze immunity to several different noise/jamming models
- Analyze effects of spoofing and incorporate mitigation methods
- Build and test physical system

6. CONCLUSION

To better understand the operation of a GPS receiver, antenna arrays, and the affect of CW interference sources on a receiver, a simulation model was constructed with the assistance of the SoftGPS software. The synthetic aperture array was used to provide a signal gain and improve receiver performance. The simulation model departed from mechanically based synthetic aperture arrays or synthetic aperture arrays dependent on trajectory by utilizing a switch feed antenna network. The lack of moving parts blends the design to incorporate the array elements into the physical receiver design or receiver housing and removes the requirement to incorporate accelerometers to monitor the antenna location.

Unexpectedly, in the presence of a single CW interference source the different array topologies analyzed maintained a very similar performance with respect to DoA, SNR and SINR. Only when the interference source was placed near a signal of interest did the topologies show a performance difference. Finding a compromise between the array physical size and performance the UCA array required the smallest number of elements to achieve a stable DoA and helped to restore the SINR to SNR levels with a large array due to the interference source falling within a null near the highly directive main beam. The random full aperture array did not achieve as high of gains compared to the UCA, however, its low overall sidelobes with a comparable directivity has the potential to perform very well when spatial nulling is applied. Further study is required to very this hypothesis.

Although the proposed synthetic aperture digital beamsteering will not necessarily assist a GPS receiver combat interference during startup where the true incident satellite signals are not know, during the acquisition and tracking phases once the

receiver gains lock on legitimate SV it will provide a boost in SINR where the performance enhancement is not dependent on the receiver's trajectory.

REFERENCES

[1] Andeggs, "3d spherical coordinates," http://en.wikipedia.org/wiki/File:3D_Spherical.svg, 2009, from Wikipedia.

[2] D. P. Bertsekas and J. N. Tsitsiklis, *Introduction to Probability*, 2nd ed. Belmont, Massachusetts: Athena Scientific, July 2008.

[3] K. Borre, D. M. Akos, N. Bertelsen, P. Rinder, and S. H. Jensen, *A Software-Defined GPS and Galileo Receiver: A Single-Frequency Approach.* Boston, Massachusetts: Birkhäuser Boston, 2007.

[4] A. Broumandan, T. Lin, A. Moghaddam, D. Lu, J. Nielsen, and G. Lachapelle, "Direction of arrival estimation of gnss signals based on synthetic antenna array," in *Proceedings of the 20th International Technical Meeting of the Satellite Division of The Institute of Navigation (ION GNSS 2007).* Fort Worth, Texas: ION GNSS, 2007, pp. 727–738.

[5] K. Buchanan and G. Huff, "A comparison of geometrically bound random arrays in euclidean space," in *Antennas and Propagation (APSURSI), 2011 IEEE International Symposium on*, 2011, pp. 2008–2011.

[6] G. Charvat, L. C. Kempel, E. Rothwell, C. Coleman, and E. Mokole, "An ultrawideband (uwb) switched-antenna-array radar imaging system," in *Phased Array Systems and Technology (ARRAY), 2010 IEEE International Symposium on*, 2010, pp. 543–550.

[7] Y.-H. Chen, J. Juang, D. De Lorenzo, J. Seo, S. Lo, P. Enge, and D. Akos, "Real-time software receiver for gps controlled reception pattern antenna array processing," in *Proceedings of the 23rd International Technical Meeting of the*

Satellite Division of the Institute of Navigation (ION GNSS 2010), Portland, Oregon, 2010, pp. 1932–1941.

[8] Z. Chen, G. Gokeda, and Y. Yu, *Introduction to Direction-of-arrival Estimation*. Boston, Massachusetts: Artech House, 2010.

[9] S.-C. Cheng and K.-C. Lee, "Reducing the array size for doa estimation by an antenna mode switch technique," *Progress In Electromagnetics Research*, vol. 131, pp. 117–134, 2012.

[10] V. Dehghanian, A. Broumandan, M. Zaheri, and J. Nielsen, "Dual-polarized synthetic antenna array for gnss handheld applications," *ISRN Communications and Networking*, vol. 2013, no. Article ID 985401, p. 11, 2013.

[11] Economist Newspaper Limited, "Out of sight," *The Economist*, July 2013.

[12] A. El-Rabbany, *Introduction to GPS: the Global Positioning System*, 2nd ed., ser. Artech House mobile communications. Boston Massachusetts: Artech House, 2006.

[13] M. G. Ellis, "Using mixers in radio communications," http://michaelgellis.tripod.com/mixerscom.html, 1999.

[14] GNSS at Colorado Center for Astrodynamics Research, "Front end hardware module," University of Colorado at Boulder website, October 2011, http://ccar.colorado.edu/gnss/.

[15] M. S. Grewal, L. R. Weill, and A. P. Andrews, *Global positioning systems, inertial navigation, and integration*, 2nd ed. Hoboken, New Jersey: John Wiley & Sons, 2007.

[16] T. T. Ha, *Theory and design of digital communication systems*. New York: Cambridge University Press, 2010.

[17] T. E. Humphreys, "Statement on the vulnerability of civil unmanned aerial vehicles and other systems to civil gps spoofing," July 2012, submitted to the Subcommittee on Oversight, Investigations, and Management of the House Committee on Homeland Security.

[18] T. E. Humphreys, B. M. Ledvina, M. L. Psiaki, B. W. O'Hanlon, and J. Paul M. Kintner, "Assessing the spoofing threat: Development of a portable gps civilian spoofer," in *Proceedings of the 21st International Technical Meeting of the Satellite Division of The Institute of Navigation (ION GNSS 2008)*. Savannah, GA: ION GNSS, 2008, pp. 2314–2325.

[19] V. P. Ipatov, *Spread Spectrum and CDMA: Principles and Applications*. Chichester: John Wiley & Sons, 2005.

[20] E. D. Kaplan and C. J. Hegarty, *Understanding GPS: Principles And Applications*, 2nd ed., ser. Artech House Mobile Communications. Boston, Massachusetts: Artech House, 2006.

[21] J. D. Kraus and R. J. Marhefka, *Antennas For All Applications*, 3rd ed. New York: McGraw-Hill, 2002.

[22] M. Li, A. Dempster, A. Balaei, C. Rizos, and F. Wang, "Switchable beam steering/null steering algorithm for cw interference mitigation in gps c/a code receivers," *Aerospace and Electronic Systems, IEEE Transactions on*, vol. 47, no. 3, pp. 1564–1579, July 2011.

[23] T. Lin, A. Broumandan, J. Nielsen, C. O'Driscoll, and G. Lachapelle, "Robust beamforming for gnss synthetic antenna arrays," in *Proceedings of the 22nd International Technical Meeting of The Satellite Division of the Institute of Navigation (ION GNSS 2009)*, Savannah, Georgia, 2009, pp. 387–401.

[24] M. Lu, J. Wang, R. Babu, D. Li, and Z. Feng, "A novel antenna array for gps/ins/pl integration," *Scientific Research Publishing*, vol. 4, no. 1, pp. 160–165, 2005.

[25] P. Y. Montgomery, T. E. Humphreys, and B. M. Ledvina, "A multi-antenna defense: Receiver-autonomous gps spoofing detection," *InsideGNSS*, pp. 40–46, March/April 2009.

[26] R. A. Monzingo and T. W. Miller, *Introduction to Adaptive Arrays*, 2nd ed. Raleigh, North Carolina: SciTech Publishing, 2011.

[27] NOAA, "Antenna diversity," http://www.gps.gov, January 2014.

[28] S. J. Orfanidis, *Electromagnetic waves and antennas*. New Brunswick, New Jersey: Rutgers University, 2008.

[29] T. Pany and B. Eissfeller, "Demonstration of a synthetic phased array antenna for carrier/code multipath mitigation," *Proceedings of the 21st International Technical Meeting of the Satellite Division of the Institute of Navigation (ION GNSS 2008)*, pp. 663–668, September 2008.

[30] P. Papadimitratos and A. Jovanovic, "Gnss-based positioning: Attacks and countermeasures," in *Military Communications Conference, 2008. MILCOM 2008. IEEE*, 2008, pp. 1–7.

[31] D. Plausinaitis, "Softgps," Accompanied A Software-Defined GPS and Galileo Receiver, 2007, http://kom.aau.dk/project/softgps/.

[32] B. R. Rao, W. Kunysz, and R. L. Fante, *GPS/GNSS Antennas*, ser. GNSS technology and applications series. Boston, Massachusetts: Artech House, October 2012.

[33] D. P. Shepard, J. A. Bhatti, and T. E. Humphreys, "Drone hack: Spoofing attack demonstration on a civilian unmanned aerial vehicle," *GPS World*, August 2012.

[34] D. P. Shephard and T. E. Humphreys, "Characterization of receiver response to spoofing attacks," in *Proceedings of the 24th International Technical Meeting of The Satellite Division of the Institute of Navigation (ION GNSS 2011)*. Portland, Oregon: ION GNSS, September 2011.

[35] B. Sklar, *Digital Communications: fundamentals and applications*, 2nd ed. Upper Saddle River, New Jersey: Prentice Hall, 2001.

[36] A. Soloviev and F. Van Graas, "Beam steering in global positioning system receivers using synthetic phased arrays," *Aerospace and Electronic Systems, IEEE Transactions on*, vol. 46, no. 3, pp. 1513–1522, July 2010.

[37] Sparkfun, "Sige gn3s sampler v3," https://www.sparkfun.com/products/10981, April 2014.

[38] T. Stansell and L. Scott, "Gnss jamming and interference: Causes, consequences, solutions," InsideGNSS webinar, August 2012.

[39] J. B.-Y. Tsui, *Fundamentals of Global Positioning System Receivers: A Software Approach*, 2nd ed., ser. Microwave and Optical Engineering. Hoboken, New Jersey: John Wiley & Sons, Inc., 2005.

[40] u-blox AG, "Gps essentials of satellite navigation," http://www.u-blox.com/images/stories/Resources/gps_compendiumgps-x-02007.pdf, 2009.

[41] J. S. Warner and R. G. Johnston, "Gps spoofing countermeasures," *Journal of Homeland Security*, December 2003.

[42] W.-D. Wirth, *Radar Techniques Using Array Antennas*, ser. IEE radar, sonar, navigation and avionics series. London, England: Institution of Electrical Engineers, 2001, vol. 10.

[43] L. S. Wu and T. Lo Yuen, *Antenna Handbook: Theory, Applications and Design*. New York: Van Nostrand Reinhold, 1988.

[44] S. Zaragoza, "Spoofing a superyacht at sea," http://www.utexas.edu/know/2013/07/30/spoofing-a-superyacht-at-sea/, July 2013.